Dissertation zur Erlangung des Doktorgrades

der Fakultät für Chemie und Pharmazie

der Ludwig-Maximilians-Universität München

Low Sensitivity Energetic Materials

Vorgelegt von

Jan Matthew Welch

Aus

Albany, New York, Vereinigte Staaten von Amerika

2008

<u>Erklärung</u>

Diese Dissertation wurde im Sinne von § 13 Abs. 3 bzw. 4 der Promotionsordnung vom 29. Januar 1998 von Prof. Dr. Thomas M. Klapötke betreut.

<u>Ehrenwörtliche Versicherung</u>

Diese Dissertation wurde selbständig, ohne unerlaubte Hilfsmittel erarbeitet.

München, den ……………………………………

………………………………………

(Jan M. Welch)

Dissertation eingereicht am:

1. Gutachter   Prof. Dr. Thomas M. Klapötke

2. Gutacher   Prof. Dr. Jürgen Evers

Mündliche Prüfung am

Acknowledgement

"You have to ask yourself, 'are you feeling lucky?' well are you punk?"

(Clint Eastwood, in 'Dirty Harry')

And yes I do, very.

1 General Introduction

1.1 Background and Terminology.

Development of energetic materials, in other words, substances that burn, combust rapidly or explode under certain conditions constitutes one of mankind's early scientific investigations. Although, explosive materials were developed later than other early human technologies (2nd century BC), combustion and the ability to control it is considered, one of the defining technological achievements of early humans. The history of energetic materials is well chronicled elsewhere and therefore mentioned here only in passing.[1,2] Early energetic materials were used primarily for entertainment (fireworks), but their potential in the realm of armed conflict was also recognized. An understanding and application of energetic materials in conflict has served, throughout history, as the key technological advantage of one civilization over another. In modern times, however, the manifold application of energetic materials reaches well beyond those original uses in entertainment and warfare. Today, energetic materials find use in mining, construction, demolition, safety equipment (signal flares, fire suppression systems, etc.), rocketry and space exploration among other civil and military applications.

Having established the utility and wide area of application of "energetic materials," definition of the terms used above is helpful for the sake of clarity. As suggested above, "energetic materials" can be divided into several classes, namely, explosives, propellants and pyrotechnics, each of which requires a definition of its own. Explosives are most often vaguely defined as "a solid or liquid substance (or mixture of substances) which is in itself capable by chemical reaction of producing gas at such a temperature and pressure and at such a speed as to cause damage to the surroundings." Propellants may be defined as substances or mixtures of substances that burn rapidly or deflagrate (deflagrate is defined specifically below) releasing a significant volume of gas at a rate sufficient to raise pressure and provide propulsive force (or impulse). Whereas the purpose of explosives and propellants is the

transfer of stored chemical energy to macroscopic kinetic energy, the purpose of pyrotechnic substances and mixtures is to use this stored chemical energy to generate defined visual and acoustic effects.[1,2]

The primary objectives of this work are in the area of explosives and to a lesser extent propellants. Therefore, further discussion of pyrotechnics is omitted. However, several more scientific definitions of terms concerning explosives and propellants may be useful. Firstly, in order to more precisely define the term "explosives" a definition of an "explosion" is necessary. Unfortunately, "explosion" is another term lacking a specific, scientific definition. An explosion is vaguely defined as occurring when a large amount of accumulated energy is released suddenly. The source of the energy released maybe physical, chemical or nuclear.[1,2] Therefore, rather than defining chemical explosive materials redundantly as those that, under certain conditions, release their energy suddenly, perhaps it is useful to discuss "explosions" in terms of the rate at which chemical energy is released.

Detonation is the fastest release of chemical energy and is propagated, not by heat transfer, but by a supersonic shockwave traveling though the materials. The shockwave propagation is maintained by the rapid release of chemical energy immediately behind the wave front. The shockwave exiting the material results in the destructive or propulsive force of the material. Deflagration reactions proceed through energetic materials at slightly subsonic linear velocities and are propagated principally by heat transfer. Deflagration can be considered an intermediate state between detonation and combustion. Combustion or simple burning reactions occur at slower rates and are defined as complex self-sustaining exothermic oxidation reactions. Therefore, in this work, chemical explosives are treated as compounds capable releasing their energy in the form of a detonation and these materials will be discussed principally in terms of their detonation properties. Propellants on the other hand, may be explosive materials, but release their energy principally through gas generation as the result of a deflagration.[1,2]

As evidenced by their definitions, explosives and propellants have different and varied applications. Explosive and propellant materials and mixtures can be further classified depending on ease of initiation to detonation or deflagration. The principal feature of primary explosives is facile initiation to detonation due to a very rapid intrinsic transition from burning to deflagration to detonation. Detonation of primary explosive materials is most often initiated by mechanical, electrostatic or thermal stimulus. Secondary explosives, on the other hand require a much larger stimulus to initiate detonation. Normally the stimulus initiating detonation of a secondary explosive is the detonation shockwave generated by a primary explosive. Although they are more difficult to detonate, secondary explosives generally have significantly higher performances (in other words release far more energy, more rapidly) than primary explosives. Within the secondary explosive class, two further types (classifications) of explosives (High Energy Density Materials, HEDMs and Low Performance Energetic Materials, LPEMs) have been heavily investigated in recent years. The purpose of HEDMs is to produce the highest performance possible, while the purpose of LPEMs is to sacrifice a small amount of performance to obtain the lowest sensitivity possible.[1, 2]

Propellants may also be divided into several classes and categories on the basis of application and composition including single, double and triple base solid propellants, composite propellants as well as liquid mono- and bipropellants. Single, double and triple base solid propellants contain one, two or three energetic components, respectively. The main ingredient used in solid propellant mixtures is nitrocellulose (NC). Double base propellants add nitroglycerin (NG) to the NC base and triple base propellants add both NG and nitroguanidine (NQ) to the NC base. Supplementing the energetic component(s) in classical solid propellants are a variety of substances including stabilizers, plasticizers, coolants, surface moderants and lubricants, flash inhibitors and decoppering and anti-wear agents. In addition to NC based propellants solid propellants, modern composite propellants

based on a secondary explosive mixed with a plasticizer and binder are also in common use. Solid propellants are found in a variety of applications ranging from small and large caliber firearms to rocketry. In addition to solid propellants, liquid propellants are often used in rocketry and space exploration. As stated above liquid propellants may either be single component monopropellants such as hydrogen peroxide or anhydrous hydrazine or bipropellents which are mixtures of a liquid fuel and liquid oxidizer.[1, 2]

1.2 Chemistry and Energetic Materials.

Having defined the terminology specific to "explosions" and established the various classifications of energetic materials, the physical and chemical properties of energetic materials can easily be discussed. Sensitivity and performance are two of the most important physical properties of energetic materials and have already been mentioned above. Specifically, the sensitivity of an explosive substance may be defined as the ease with which detonation or deflagration is initiated by physical stimuli. These stimuli include friction (thermal and kinetic energy), impact (kinetic energy), electrostatic discharge (electrical energy) and thermal shock (thermal energy). Depending on the particular physical stimulus, the magnitude of the stress on the material required for ignition is more or less quantifiable. Performance of energetic materials may also quantified, although the physical quantities used depend on the type of reaction (detonation or deflagration), and are sometimes difficult to assess experimentally. Measures of detonation performance include detonation pressure (P_{det}, the pressure at front of the detonation shockwave) and velocity (D, rate of propagation of detonation shockwave), heat (Q_{det}, thermal energy released during detonation at constant pressure) and temperature (T_{det}, temperature of the detonation products) of detonation and the volume of gas produced by the detonation (V_{gas}). Deflagration (propellant) performance is most often gauged by specific impulse (I_s, related to pressure and velocity of gas exiting a rocket motor), the volume of gas produced by the deflagration (V_{gas}) and linear burning rate of the material.

Detonation and deflagration are largely defined by physical quantities which are ultimately related to the chemical properties of the material. The simplest chemical properties of the material, chemical composition (most often discussed in terms of percentage of nitrogen, N%, and oxygen balance (Ω)) and molecular structure (atomic connectivity), largely determine the density (ρ) and energy of formation ($\Delta_f U$) of the material. Since the rate at which the detonation shockwave is limited by the density of the material through which it is propagating and is sustained by the energy released immediately behind the wave front, density and energy of formation (which are largely determined by chemical composition and molecular connectivity) underlie all of the above mentioned measures of energetic performance. Energy of formation also directly influences heat of detonation and the composition of the material determines the volume and type of gas released.

Just as performance is related to the chemical properties of energetic materials, so is sensitivity. The sensitivity of an explosive substance is a direct reflection of the ability of that substance to dissipate sudden energetic input, without undergoing decomposition (detonation, deflagration or combustion). The ability to dissipate energy without breaking chemical bonds (decomposition) is directly related to the density (lower density materials can dissipate energy more efficiently), molecular structure (certain functional groups are more susceptible to decomposition) and intermolecular interactions within the material (strong interactions between molecules lead to more efficient dissipation of energy).

As stated above modern energetic materials have a myriad of both military and civilian applications. Knowledge of the relationships between chemical and energetic properties can thus be used to develop new energetic materials tailored to specific applications. Modern, practical research and development of such materials has, in particular, three focuses. Classically as well as currently, the development of more powerful energetic materials, primarily for military application, is a principal aim of this field. Although an interest in safety and ease of handling has been more or less continuously present since the development

of commercial explosive materials, in recent times the interest in developing low sensitivity and insensitive materials with long shelf-lives has become considerable. The most recent development in this field is that of "green" energetic materials, in other words, compounds that can be used or disposed of with the least possible environmental impact aside from that of the initial detonation.

Since this work focuses on secondary explosives and propellants, a detailed discussion of developments and properties of primary explosives will not be undertaken. Classically, secondary explosives have been based on molecules such as NG (nitroglycerin), TNT (2,4,6-trinitrotoluene) and RDX (1,3,5-trinitro-1,3,5-triazacyclohexane) containing $O-NO_2$, $C-NO_2$ and $N-NO_2$ functional groups, respectively. In the case of NG and TNT the energy of detonation is obtained primarily from oxidation of carbon and the energies of formation of both compounds are negative. For RDX the energy of detonation is obtained by both the oxidation of carbon and the formation of molecular nitrogen. Due to the presence of the N-N bonds in the nitramine moieties, the energy of formation of RDX is positive and in addition to a high density, this results in a significantly higher performance than that of NG or TNT. The structures, properties and performance of these classical CHNO explosives are shown in Figure 1.1.[3]

O$_2$NO— —ONO$_2$ / —ONO$_2$ CH$_3$ O$_2$N   NO$_2$ NO$_2$ NO$_2$ N O$_2$N—N   N—NO$_2$
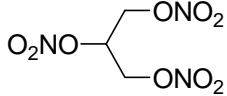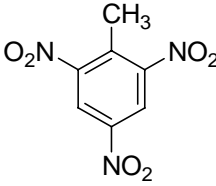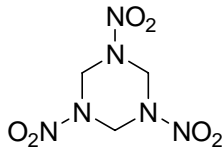
Systematic Name (Abbreviation)	1,2,3-propanetrioltrinitrate (NG)	2,4,6-trinitrotoluene (TNT)	1,3,5-trinitro-1,3,5-triazinane (RDX)
T_m (°C)	13	80	~200
T_{dec} (°C)	200	300	213
N (%)[c]	18.5	18.5	37.8
Ω (%)[d]	3.5	-73.9	-21.6
ρ (g/cm^3)[e]	1.59	1.654	1.82
$\Delta_f H_m^\circ$ (kJ/mol)	-370	-67	67
Impact (J)	0.2	15	7.4
Friction (N)	>360	353	120
D (m/s)	7600	6900	8750

Figure 1.1. Properties of NG, TNT and RDX.

To improve on the performance of any of these materials, it is necessary to increase density, change the chemical composition or the molecular structure in order to increase the energy of formation. From a synthetic chemical stand point, new molecular structures with more oxygen balanced formulae, higher nitrogen contents and thus higher heats of formation are simpler to design and synthesize than compounds that will pack more efficiently leading to higher densities. Therefore most recently developed HEDMs use one or both of the following strategies to increase energy of formation: the use of strained cage structures as in molecules such as TEX (4,10-dinitro-2,6,8,12-tetraoxa-4,10-diazaisowurtzitane), CL-20 (2,4,6,8,10,12-hexanitro-hexaazaisowurtzitane) and TNAZ (1,3,3-trinitroazetine) or the use of molecules containing large numbers of covalently bonded nitrogen atoms (nitrogen catenation) as in the primary explosive tetrazene (1(5-tetrazolyl)-4-guanyl tetrazene hydrate).
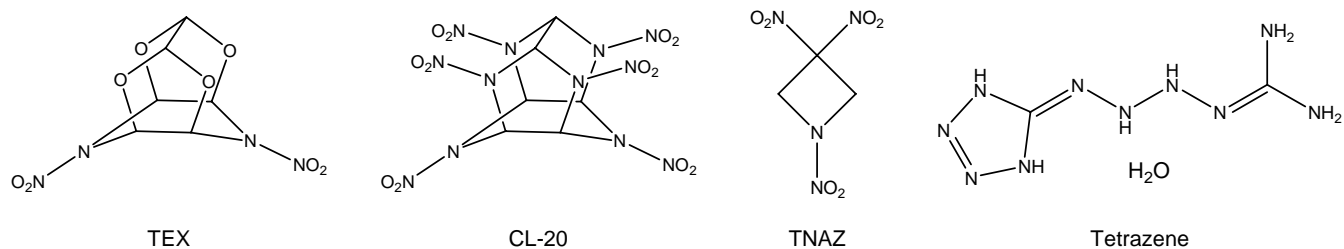
Figure 1.2. Molecular structures of TEX, CL-20, TNAZ and tetrazene.

The concept of nitrogen catenation is also being utilized in the new area of "green" energetic materials. Since classical nitro CHNO explosives are not particularly environmentally benign, one of the major goals of green energetic materials research is the development of nitro-free energetic materials. Another major goal is the replacement of hydrazine containing liquid mono and bipropellants and of environmentally detrimental liquid (N_2O_4) and solid (NH_4ClO_4) oxidizers by more benign materials. The by-products of more environmentally friendly, nitrogen-rich energetic materials should be mainly, if not exclusively, molecular nitrogen, carbon dioxide and water.[4]

Insensitive or low sensitivity secondary explosives are not a new concept, but are attracting increasing interest due to a need for stable, storable and transportable materials which are resistant to accidental ignition. The problem of accidental initiation has been present in the explosives industry from the time of Nobel's first NG factories. Although advances in safety have been considerable, accidents still occur during production, transport and storage of energetic materials. The primary goal of research and development in the area of low sensitivity and insensitive energetic materials is reduce sensitivity to a minimum while sacrificing as little performance as possible. To this end the LPEM class of materials has developed. Although 1,3,5-triamino-2,4,6-trinitrobenzene (TATB) was first synthesized nearly 120 years ago, it is currently the industry standard for a lower performance insensitive material.[5] However, several new materials have been developed for low sensitivity applications in recent years and research is still expanding.[4]

O_2N NH_2 NO_2

H_2N NH_2

NO_2

1,3,5-triamino-2,4,6-trinitrobenzene
(TATB)

O

HN   NH

N

NO_2

3-nitro-1,2,4-triazole-5-one
(NTO)

H_2N NO_2

H_2N NO_2

1,1-diamino-2,2-dinitroethene
(FOX-7)

H_2N N NH_2

O_2N N^+ NO_2

O^-

2,6-diamino-3,5-dinitropyrazin-1-oxide
(LLM-105)
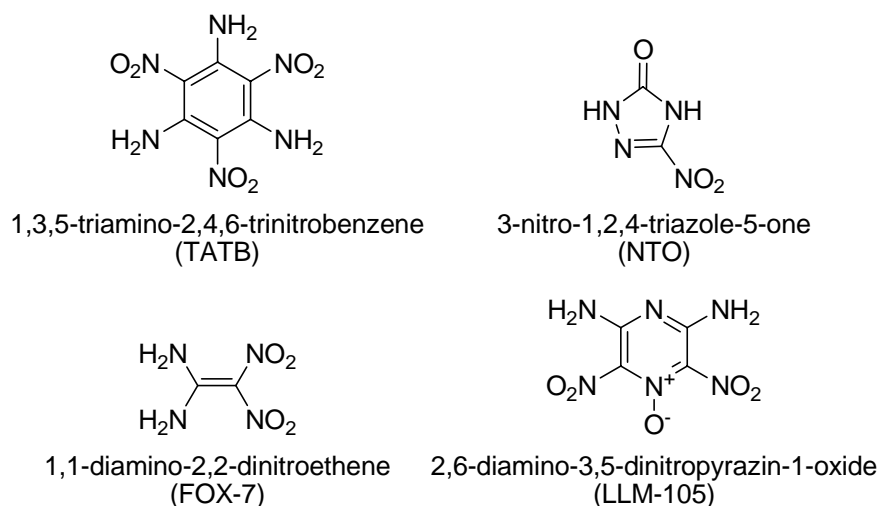
Figure 1.3. Low sensitivity energetic materials

1.3 Goals of this Study.

The general area of this thesis is that of low- and insensitive secondary explosive materials and potential propellant compositions thereof. The development of new low sensitivity ionic materials incorporating the above outlined concepts of high nitrogen content, in order to improve performance as well as environmental compatibility (Chapter 1), is one of the two specific aims of this work. The second specific aim is the thorough structural investigation of FOX-7, a recently developed insensitive energetic material in the early stages of production, and its behavior as the physical extremes of detonation (high temperature and pressure) are approached (Chapter 2).

1.3.1   Chapter 1: Energetic Salts.

Two new families of energetic nitrogen-rich ionic energetic materials have been developed. The first family of salts utilizes combinations of cations based on 1-methyl-5-amino-2*H*-tetrazole (**4**) and 1,4-dimethyl-5-iminotetrazole (**5**) and simple oxygen- or nitrogen-rich anions. The second family of ionic materials utilizes simple nitrogen-rich cations in combination with the anion of 5-nitro-2*H*-tetrazole. In addition, the cation of **5** was combined with the anion of 5-nitro-2*H*-tetrazole generating a novel tetrazolium tetrazolate energetic salt. Each material studied, has been synthesized by scalable means from inexpensive readily

available laboratory chemicals, fully characterized in bulk (by spectroscopic and analytical methods) and its molecular structure determined by X-ray crystallography. In addition to standard chemical characterization, the physical, thermochemical and energetic properties of each compound have also been thoroughly investigated and verified by computationally based methods when possible. The performance of each new substance has also been predicted using the EXPLO5 hydrodynamic code in order to identify compounds of particular interest.

1.3.2   Chapter 2: Temperature dependent studies of FOX-7.

The behavior of FOX-7 upon heating has been thoroughly investigated using differential scanning calorimetry (DSC), temperature resolved Raman spectroscopy, temperature resolved X-ray powder diffraction and temperature resolved single crystal X-ray diffraction. The occurrence of two solid-state phase transitions on heating has been verified and the structures of two high temperature polymorphs of FOX-7 (β- and γ-FOX-7) have been determined. On the basis of DSC measurements, diffraction data and structure determinations the mechanism and nature of the both transitions has been elucidated. Lastly, the physical changes caused by and motivating the phase transformations were examined.

1.4 References.

(1)   *Chimia*, **2004,** *58*, 351-429.

(2)   Akhavan, J., *The chemistry of explosives*. Royal Society of Chemistry: Cambridge, UK, 1998.

(3)   Köhler, J.; Mayer, R., *Explosivstoffe*. Wiley-VCH: Weinheim, Germany, 1998.

(4)   Sikder, A. K.; Sikder, N., *J. Haz. Mater.*, **2004,** *112*, 1-15.

(5)   Pagoria, P. F.; Lee, G. S.; Mitchell, A. R.; Schmidt, R. D., *Thermochim. Acta*, **2002,** *384*, 187-204.

2 Ionic Energetic Materials

2.1 Introduction to ionic energetic materials

As discussed in the general introduction, the primary goal of research concerning low sensitivity or insensitive energetic materials is to couple reasonable performance with decreased sensitivity. Unfortunately, as also mentioned in the general introduction, performance and sensitivity are linked both to each other and to the general physical and chemical properties of a substance. The primary chemical method of counteracting the correlation of high performance with high sensitivity is the synthesis of compounds which form extensive hydrogen bonding networks in the solid state such as FOX-7[1] or TATB[2]. Hydrogen bonded networks (especially between amino and nitro groups) stabilize, by several means, the material substantially. In addition to lower sensitivities, the performance of such materials is generally adequate since chemical composition is unaffected by strong hydrogen bonding (FOX-7, for example, shares a common empirical formula, $CH_2N_2O_2$, with HMX and RDX), density is generally increased and heat of formation only slightly decreased (less positive). Since the performance of an energetic material is most heavily dependent on density, increases in density tend to outweigh the adverse affect on heat of formation caused by strong hydrogen bonding. The density of such materials also benefits from the higher packing efficiency achieved through stronger intermolecular interactions.

Thus far, the examples of low sensitivity energetic materials presented have generally been covalent molecular species, however, ionic energetic materials and compositions based on ionic materials are also known and widely used (ammonium nitrate/oil, ammonium nitrate/nitromethane). Several properties of ionic energetic materials might make them attractive choices as new low sensitivity energetic materials. Firstly, ionic materials are often made from inexpensive components through simple metathesis and acid-base reactions leading to low cost and a minimum of side products [the syntheses of both TNT and RDX results in several side products]. The ease of synthesis means that many permutations are

possible and chemical constitution and therefore density and energy of formation are thus easily adjusted by combining cations and anions with different compositions. In addition to ease of synthesis, ionic materials are defined by strong electrostatic interionic interactions in the solid state and often form strong hydrogen bonding networks, the result of which should be considerable stability as well as insensitivity. Furthermore, ionic energetic materials tend to exhibit lower vapor pressure (essentially eliminating the risk of exposure through inhalation) than their neutral non-ionic analogues. In short, ionic energetic materials should be cheaper, more flexible, safer and perform at least as well as their molecular counterparts. [3-5] With these properties in mind, two families of nitrogen-rich ionic materials were synthesized. One family utilizes methylated 5-amino-1H-tetrazoles as cations with simple nitrogen- and oxygen-rich anions (ClO_4^-, NO_3^-, N_3^-, $(NO_2)_2N^-$) and the other 5-nitrotetrazolate in combination with simple, nitrogen-rich cations (ammonium, hydrazinium, guanidinium and amino- and polyaminoguanidinium).

The choice of methylated 5-amino-1H-tetrazoles is motivated by recent studies of salts of 5-amino-1H-tetrazole **1** (5-AT)[6] and 1,5-diamino-1H-tetrazole **2** (DAT)[7], which showed promising performance but suffer several shortcomings. Firstly, in the case of DAT salts, synthesis of the parent compound is difficult and hazardous.[8] Secondly, in spite of their large number of electron pairs, **1** and **2** are both only weakly basic and therefore are only protonated by strong acids, thus precluding their direct combination with slightly basic nitrogen and oxygen rich anions (e.g. dinitramide and azide). Therefore, in the case of **2**, the tetrazole ring was selectively methylated at the N4 position, generating the N5 protonated form of **3** with no strongly acidic protons and allowing for combination with a far greater variety of anions. Since 1-methyl-5-amino-1H-tetrazole (**4**) is easily synthesized from inexpensive reagents with no hazardous side products[9, 10] and the hydroiodide of **5**, 1,4-dimethyl-5-aminotetrazolium iodide (**8**), is simply prepared from **4**[11], a new family of

energetic salts based on protonated and methylated **4**, analogous to those of **2** and **3** which showed promising properties, can be envisioned.

| **1** | **2** | **3** | **4** | **5** |
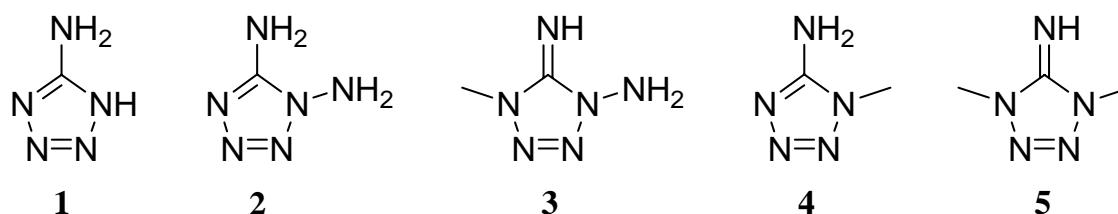
The second class of ionic energetic materials studied is based on the 5-nitrotetrazolate anion (NT⁻), which was first synthesized over 75 years ago by von Herz.[12] Since its discovery, the metal and heavy metal salts of NT⁻ have attracted much interest as primary explosives.[12-16] More recently metal complexes (Zn and Fe) have been presented as potential "green" replacements for lead azide in initiators.[17] In 1998 the free acid of the NT⁻ anion (5-nitro-2*H*-tetrazole, HNT) was isolated and characterized for the first time along with a series of functionalized derivatives.[18] Additional, neutral energetic derivatives have also appeared over the last few years.[19] Finally, also in recent years, new energetic heterocycle based salts of HNT have appeared in the literature, many of which display promising ionic liquid properties.[3, 5, 20-23]

Considering the amount of literature concerning HNT and its derivatives and the recent interest in the area of ionic energetic materials, it is surprising that the simplest metal-free nitrogen-rich salts of HNT, remained largely uninvestigated. Further motivation for the investigation of simple, nitrogen-rich (ammonium, hydrazinium, guanidinium and amino- and polyaminoguanidinium) salts of HNT is provided by the promising properties of recently investigated simple nitrogen-rich salts of other tetrazole-based anions (e.g. 5,5'-azotetrazolate, ZT^{2-}).[24] Lastly, in light of the above mentioned interest in heterocyclic cation-NT⁻ anion salts, the dimethylated cation of **5** was combined with the NT⁻ anion and the resulting compound, which bridges the two series of salts, was also studied.

2.2 Results and Discussion

2.2.1 Synthesis.

4 was prepared by methylation of the sodium salt of 5-aminotetrazole with methyl iodide or dimethyl sulfate as described in literature.[9, 10] The nitrate (**6**) and perchlorate (**7**) salts of **4** were prepared by protonation with the corresponding acid. Compound **8** was prepared by regioselective methylation of **4** at N4 in acetonitrile with excess methyl iodide by a method analogous to that used for the preparation of the iodide salt of **3**.[7] The salts of **5** were initially prepared by exchange of iodide for nitrate (**9**), perchlorate (**10**), azide (**11**), dinitramide (**12**) or 5-nitrotetrazolate (**21**) using the respective silver salt of the desired anion as shown in Scheme 2.1. For the purposes of scale-up, alternative methods were utilized for the syntheses of **11**, **12** and **21** due to the sensitivity of the silver salts of azide, dinitramide and 5-nitrotetrazolate. For **11** ion-exchange chromatography (as described by Christe, et al. in reference [25]) was utilized, for **12** the bis-pyridine silver dinitramide reagent described by Franek et al.[26] was used and for **21**, **5** was reacted with ammonium 5-nitrotetrazolate hemihydrate (**13**) under loss of ammonia. The reaction of **5** with free acid or ammonium salts of the desired anion should yield salts of **5** in scaleable quantities with excellent yields (Scheme 2.2). However, **5** was isolated by treatment of **8** with potassium hydroxide in methanol and subsequent sublimation only after salts **9 - 12** had been thoroughly investigated. Therefore such a method was utilized only for the large scale synthesis of **21**.

$$X = NO_3^-,\ ClO_4^-,\ N_3^-,\ N(NO_2)_2^-,\ CN_5O_2^-$$
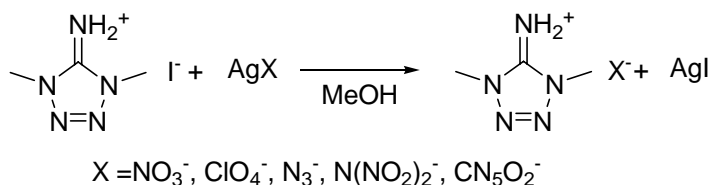
Scheme 2.1. Synthesis of salts of **5** by silver salt metathesis reactions.

$X = NO_3^-, ClO_4^-, N_3^-, N(NO_2)_2^-, CN_5O_2^-$
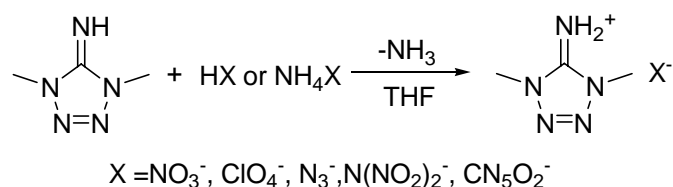
Scheme 2.2. Synthesis of salts of **5** from **5** and free acids or ammonium salts.

Compound **13** used above, was prepared by a slightly modified literature method. Lee et al. describe the material obtained as compound ammonium 5-nitrotetrazolate (**14**).[27] In the author's experience, the preparation loosely described by Lee et al. and described in detail here yielded exclusively **13** as identified by elemental analysis and X-ray structure determination. Lee et al. reported isolated yields of >70 %, whereas yields of ~50 % were obtained in this study. On scale-up (quadruple the procedure reported here) a yield of just over 60 % of **13** was obtained. In addition, Lee et al. also reported several properties of the bulk material generated (density, heat of formation, sensitivity to impact, friction and electrostatic discharge as well as predicted energetic performance), which we found either to be in reasonable agreement with either values measured for **13** (sensitivities and density) or values calculated based on the assumption that the material generated was **14** (heat of formation, predicted energetic performance). Therefore, the author suggests that the material isolated by Lee et al. was **13** in slightly lower yield than reported.

Initially, compounds **13** - **19** (hydrazinium 5-nitrotetrazolate, **15**, guanidinium 5-nitrotetrazolate, **16**, aminoguanidinium 5-nitrotetrazolate, **17**, diaminoguanidinium 5-nitrotetrazolate, **18** and triaminoguanidinium 5-nitrotetrazolate monohydrate, **19**) were prepared by metathesis of silver 5-nitrotetrazolate with the corresponding bromide or iodide salts as shown in Scheme 2.3. However, the synthesis of energetic salts for study using silver 5-nitrotetrazolate as the 5-nitrotetrazole transfer reagent was unsuitable for several reasons. Firstly, silver 5-nitrotetrazolate is extremely sensitive to impact, friction and electrostatic discharge and manipulation of it on a small scale (250 - 500 mg) requires extreme caution and

large scale (>1 g) manipulation of dry material is not advisable. Secondly, silver salts tend to be reduced by aminated guanidines and hydrazines to elemental silver. Therefore, even with short reaction times substantial decomposition of hydrazine and amino-, diamino- and triaminoguanidine moieties is observed.

$$X = Br^- \text{ or } I^-$$
$$Cat = NH_4^+, N_2H_5^+, CH_6N_3^+, CH_7N_4^+, CH_8N_5^+, CH_9N_6^+ \text{ or } CN_5O_2^-$$
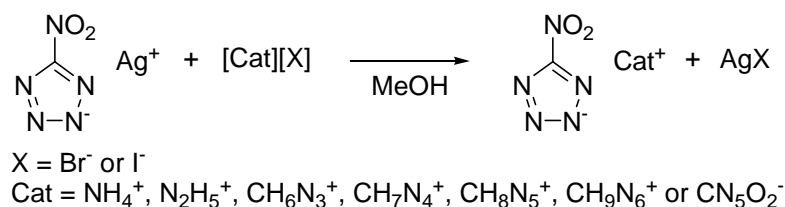
Scheme 2.3. Synthesis of NT salts by silver salt metathesis reactions

It is also foreseeable to use 5-nitrotetrazole itself as the transfer reagent. However the free-acid 5-nitrotetrazole is reported to be both significantly friction and impact sensitive as well as hygroscopic and is, therefore, not suitable for larger scale manipulation. Therefore, **13**, generated as discussed above, was used as a starting material. To generate compounds **15** – **17** free bases (hydrazine hydrate and guanidine) and hydrogen carbonates (aminoguanidinium hydrogen carbonate, AGHCO$_3$) were combined with **13** under loss of ammonia and in the case of compound **17** carbon dioxide. In practice, compound **16** crystallizes preferentially from a warm aqueous mixture of **13** and guanidinium nitrate (GNO$_3$) and is thus most easily generated by this method. Compounds **18** and **19** can be generated using barium 5-nitrotetrazolate and the corresponding aminated guanidinium hemisulfate. However, this method is also undesirable because barium nitrotetrazolate is a sensitive explosive material which forms with variable hydration. Diamino- and triaminoguanidinium hemisulfates are also not conveniently prepared on a laboratory or larger scale.[28] Moreover, anhydrous triaminoguandinium 5-nitrotetrazolate (**20**) cannot be prepared directly by this method (**19** is dehydrated over P$_4$O$_{10}$ to form **20**), since water is the only available, practical solvent in which triaminoguanidinium hemsulfate dihydrate is soluble. Compound **18** was thus generated from **13**, sodium carbonate and 1-amino-3-ammonioguanidinium sulfate, under loss

of ammonia, carbon dioxide water and sodium sulfate. A similar synthesis should be possible

for **19** and possibly **20** directly from 1,2-diamino-3-ammonioguanidinium sulfate and **13,** as

suggested in

Scheme **2.4**, but has not yet been applied. Methods suitable for scale-up are shown in

Scheme **2.4** and all but those for the sensitive explosive materials **15** and **20** have been

applied on at least a ~5 g scale.
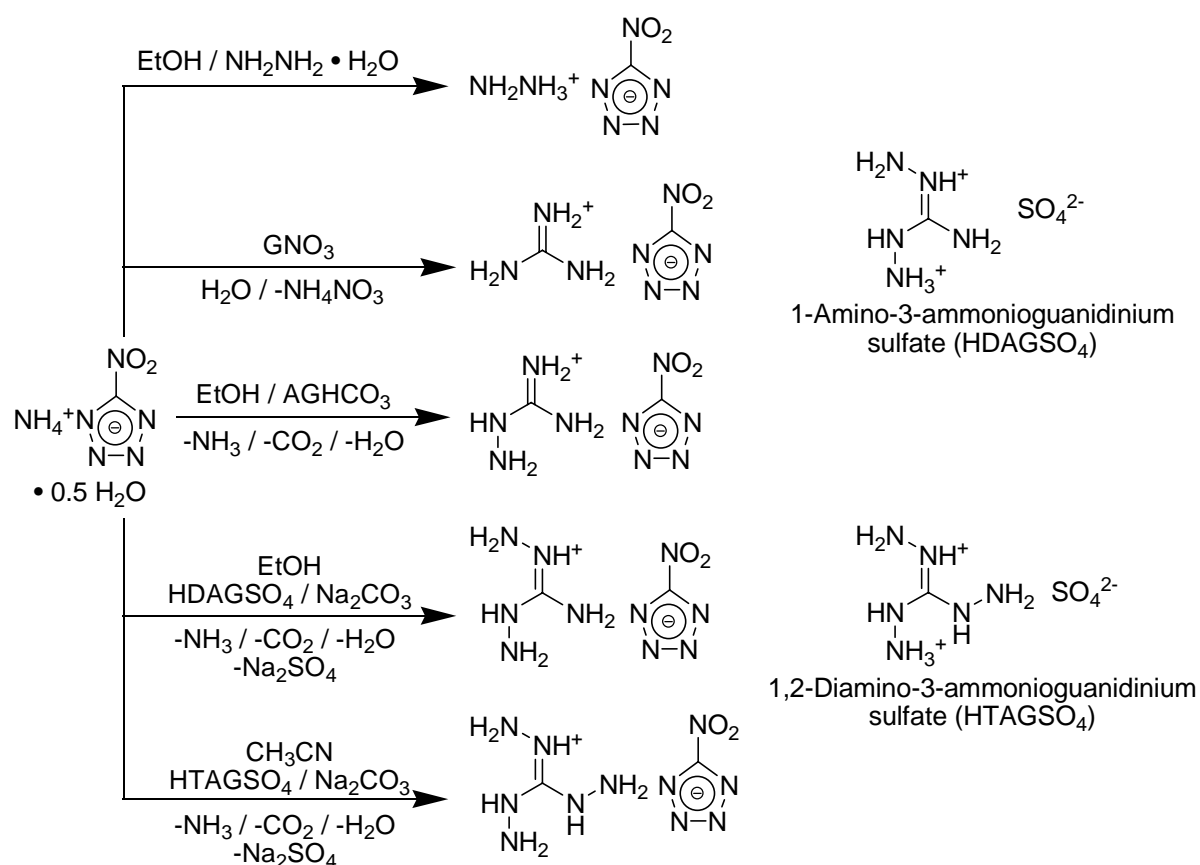
Scheme 2.4. Applied and proposed scalable syntheses of simple, nitrogen-rich NT salts

from **13.**

2.2.2 Vibrational Spectroscopy

Both families of energetic salts were qualitatively identified by vibrational spectroscopy

(infrared and Raman). Each spectrum shows the characteristic bands of the respective

energetic cations (1-methyl-5-aminotetrazolium, HMAT[+], 1,4-dimethyl-5-aminotetrazolium,

DMAT[+], ammonium, hydrazinium, guanidinium, 1-aminoguananidinium, 1,3-

diaminoguanidinium and 1,2,3-triaminoguanidinium) and anions (nitrate, perchlorate, azide, dinitramide and 5-nitrotetrazolate).

The IR and Raman spectra of compounds **6 – 12** and **21** contain the following set of bands which can be assigned to the cations: 3400 - 3100 cm^{-1} [v(N-H)], 3000 - 2850 cm^{-1} [v(C-H)], ~1680 cm^{-1} [v(C1=N5) + δ(N5H$_2$)], 1550 - 1350 cm^{-1} [v(tetrazole ring), δ_{as}(CH$_3$), δ(N4-H)], ~1380 cm^{-1} [δ(CH$_3$)], 1350 - 700 cm^{-1} [v(N1-C1-N4), v(N-N), γ(CN), δ(tetrazole ring)], <700 cm^{-1} [δ out-of-plane bend (N-H), ω(N5H$_2$)].[29] The cations in salts **14 - 20** display well-known sets of vibrations in the IR and Raman spectra. All of these salts show a set of strong absorptions in the IR and weak bands in the Raman spectra between 3500 - 2800 cm^{-1} corresponding to N–H stretching modes. N–H deformation vibrations are observed in their expected ranges as intense bands in the IR and weak bands in the Raman (1490 - 1390 cm^{-1} for **13** and **14** and 1700 - 1500 cm^{-1} for **15 - 20**). In the case of **16 - 20**, the N–H deformation vibrations are strongly coupled to the C=N stretching modes, increasing both IR and Raman intensities. Additionally, in **15 - 20**, an N–N stretching band is observed between 800 - 1000 cm^{-1} in both IR and Raman spectra.[29]

The nitrate anion, NO$_3^-$, shows a strong, broad IR absorption centered at ~1350 cm^{-1} and a sharp band near 1050 cm^{-1} in the Raman.[30, 31] Compounds **6** and **9** show a broad IR signal masked by cation absorptions with maxima at 1312 cm^{-1} and 1307 cm^{-1} respectively. In the Raman sharp, intense NO$_3^-$ bands are observed in **6** and **9** at 1049 cm^{-1} and 1041 cm^{-1} respectively, as expected. Salts of the perchlorate anion, ClO$_4^-$, show a strong broad signal with its maximum around 1090 cm^{-1} in the infrared spectra, and strong, sharp bands around 940 and 460 cm^{-1} in the Raman spectra.[32, 33] As in the cases of **6** and **9**, the perchlorate stretch in the IR spectra of **7** and **10** is masked to a certain extent by tetrazolium cation absorptions with two strong absorptions appearing in each spectrum at 1072 and 1033 cm^{-1} and 1108 and 1053 cm^{-1}, respectively. Once again, Raman spectroscopy unambiguously confirms the presence of the perchlorate anion in both **7** and **10**, showing strong bands at 938 and 935 cm^{-1}

and at 457 and 461 cm^{-1}, respectively. The antisymmetric stretch of ionic azides is observed as a strong absorption at around 2000 cm^{-1} and the symmetric stretch as a weak absorption around 1300 cm^{-1} in the IR. In the Raman only the symmetric stretch is observed for ionic azides as a strong band around 1300 cm^{-1}.[25] Interestingly, in both the IR and Raman spectra of **11** both azide vibrations are observed (2018 and 1329 cm^{-1} in the IR and 2027 and 1331 cm^{-1} in the Raman). The presence of both bands in both IR and Raman spectra seems to indicate strong cation-anion interactions. The dinitramide anion N(NO$_2$)$_2^-$ has strong absorptions at around 1530, 1445, 1345, 1183, and 1025 cm^{-1} in the infrared and strong bands in the Raman spectrum at 1335 and 830 cm^{-1}.[34] The IR and Raman spectra of **12** confirm the presence of the dinitramide anion as evidenced by bands at 1529, 1446, 1183 and 1011 cm^{-1} in the IR and bands at 1329 and 825 cm^{-1} in the Raman.

The characteristic vibrations of the NT anion are either incompletely described in the literature in the case of the IR absorptions or wholly unknown in the case of the Raman bands. Therefore, in order to establish a characteristic set of vibrations for the NT anion, the vibrational frequencies and associated intensities and activities for the NT anion were calculated by quantum chemical methods, as described in the experimental section. In addition to establishing a characteristic set of bands in the vibrational spectra of compounds **13 - 21**, quantum chemical calculations also facilitate the assignment of bands observed in the experimental spectra to individual and coupled vibrational modes, which can in turn be used to derive structural information about the NT anion and its surroundings in the solid state.

The scaled, calculated IR and Raman frequencies calculated IR intensities and Raman activities are summarized in Table 2.1, along with average measured frequencies, qualitative IR intensities and averaged Raman activities (quantitative) from the vibrational spectra of **13 - 21**. The experimentally observed vibrations were thus assigned by comparison to the computed vibrational energies and are also tabulated in Table 2.1. The characteristic set of IR and Raman bands observed for the NT anion is thus established as listed in Table 2.1.

Table 2.1. Calculated and measured IR and Raman frequencies, intensities (IR) and activities (Raman) for the 5-nitrotetrazolate (NT) anion.

	ν_{calc} (cm^{-1})^a	ν_{meas} (cm^{-1})^b (IR / Raman)	IR intensity (Calc / Obs)	Raman activity (Calc / Obs)	Approximate Mode Assignment
1	1538	1533(6) / 1538(8)	74.1 / s	3.8 / 7.3	$\nu_{asymm}(NO_2)$
2	1396	1442(5) / 1443(3)	19.5 / s	0.18 / 6	$\nu_{asymm}(N1 - C5 - N4)$
3	1383	1417(3) / 1418(4)	100 / vs	100 / 100	$\nu_{symm}(NO_2) + \nu_{symm}(N1 - C5 - N4)$, "in phase"
4	1294	1316(3) / 1317(2)	12.6 / s	0.4 / 5.6	$\nu_{symm}(NO_2) + \nu_{symm}(N1 - C5 - N4)$, "out of phase"
5	1182	1181(9) / 1180(3)	2.0 / m	2.6 / 3.7	$\nu_{asymm}(Tetrazole)$
6	1163	1158(9) / 1164(7)	19.7 / m	4.0 / 4.6	$\nu_{symm}(Tetrazole) + \nu_{symm}(NO_2)$, "in phase"
7	1024	1058(7) / 1059(7)	0.2 / w	8.0 / 50.9	$\delta(N1 - C5 - N4) + \nu_{symm}(NO_2)$, "in phase"
8	1018	1042(5) / 1044(5)	1.2 / vw	3.8 / 40.3	$\delta_{asymm}(Tetrazole)$
9	966	1029(3) / 1030(6)	19.0 / w	64.4 / 7.6	$\nu(N2 - N3) + \delta_{symm}(Tetrazole)$, "out of phase"
10	821	836(2) / 839(3)	14.4 / s	5.0 / 9.3	$\delta(NO_2) + \delta(N1 - C5 - N4)$, "in of phase"
11	763	765(13) / 773(1)	2.4 / vw	0.8 / 3.3	$\gamma(NO_2) + \gamma(N1 - C5 - N4)$, "out of phase"
12	718	725(13) / 730(11)	0 / vw	0.001 / 1.1	$\gamma(Tetrazole)$ "in phase"
13	664	667(2) / 669(3)	3.3 / w	0.2 / 1	$\gamma(Tetrazole)$ "out of phase"
14	522	n.o. / 540(4)	0.02 / n.o.	2.3 / 4.9	$\omega(NO_2) + \omega(Tetrazole)$, "out of phase"
15	439	n.o. / 451(4)	0.2 / n.o.	1.8 / 2.9	$\nu(C5 - N5) + \delta(NO_2)$
16	242	n.o. / 245(3)	0.2 / n.o.	0.3 / 3.4	$\omega(NO_2) + \omega(Tetrazole)$, "in phase"
17	218	n.o. / 208(8)	1.9 / n.o.	0.3 / 1.3	$\gamma(N1 - C5 - N4)$
18	57	n.o. / 62(5)	0 / n.o.	0.03 / 1	$\tau(C5 - N5)$

^{a} B3LYP / aug-cc-pVDZ Calculated frequencies; scaled by 0.9613.[35] ^{b} Measured frequencies; average values from IR and Raman spectra of compounds **13 - 21**, with standard deviations shown in parentheses; n.o. not observed. ^{c} Calculated intensities; percentages of the most intense signal; qualitative observed intensities; n.o. not observed. ^{d} Activities as percentage of the most intense signal; measured intensities are average values from **13 - 21**. ^{e} Approximate description of vibrational modes; ν, stretching, δ, in-plane bending, γ, out-of-plane bending, ω, in plane rocking, τ, torsion; asymm, asymmetric and symm symmetric; for atom numbering see X-ray section.

Remarkably, all 18 frequencies obtained from the computational results were observed in the vibrational spectra of compounds **13 - 21** with reasonably good agreement between the observed and calculated frequencies. The largest differences between calculated and observed frequencies were for those vibrations involving deformation of the tetrazole ring (vibrations 2 – 4 and 7 – 8). The scaled values for the energies of this type of vibration are always underestimated, which is consistent with the greater rigidity of the tetrazole moiety in the solid state. Also of note, is that the observed frequencies assigned to the NT anions in the

vibrational spectra of **13 - 21** occur at fairly consistent energies as indicated by the reasonably narrow range of standard deviations observed for the average experimental frequencies (maximum 13 cm^{-1}). As can been seen from the tabulated IR and Raman bands in the experimental section, some variation is observed in the observed vibrational frequencies for NT containing salts. Such variations are most likely due to differences in anion surroundings in the solid-state. In spite of these small differences, the IR and Raman data suggest that the observed geometry of the NT anion should be practically identical in all compounds in this study. This prediction is confirmed by X-ray crystallography (see Table 2.7).

In the case of compounds containing the HMAT^{+} and DMAT^{+} cations, IR spectroscopy can also provide detailed insight into cation structure and interionic interactions including hydrogen bonding, which in turn reflect the properties of the counter anions.[36] A comparison of the IR spectrum of **4** to those of **6** and **7** shows substantial changes, shifts and broadening of the bands observed in **4** when it is protonated at N4. The bands at 3328 and 3151 cm^{-1} in **4** are split and shifted to slightly higher wavenumbers in both **6** (bands at 3357, 3306, 3236 and 3159 cm^{-1}) and **7** (bands at 3411, 3330, 3269, 3188 cm^{-1}) indicating a strengthening (shortening) of the N–H bonds in the exocyclic amino group. In the case of **6**, two broad signals appear at 2620 and 2360 cm^{-1} indicating the presence of strong hydrogen bonding involving the proton at the N4 position on the tetrazole ring. No such broad, lower energy N-H absorptions are observed for **7** indicating that only weaker hydrogen bonding should be observed. Differences in N–H stretching band shifts observed in the IR spectra of **6** and **7** also seem to indicate the well known difference in basicity between nitrate and perchlorate. In **6** a smaller increase in amino N-H stretching frequencies is observed than in **7** because the ring proton is more weakly bound in **6** and therefore places less electronic demand on the amino group. In addition to this effect, stronger hydrogen bonding between the amino group protons and the nitrate anion seem to result in weaker amino N–H bonds in **6** and thus lower energy amino N–H stretching vibrations than observed in **7**.

In addition to providing information about hydrogen bonding and N–H bond strengths, IR spectra also indicate other structural differences between neutral **4** and the HMAT$^+$ cation. The IR spectrum of **4** shows a strong band at 1667 cm^{-1} (with a shoulder at 1677 cm^{-1}) and another at 1596 cm^{-1} corresponding to amino group deformation and C=N ring stretch, respectively. [16] In spectra of salts **6** and **7** a single, higher energy band corresponding to the coupled amino group deformation and exocyclic C=N stretch is observed at 1687 and 1684 cm^{-1} with a shoulder at 1702 cm^{-1}, respectively and the C=N ring stretch band is no longer observed. These observations are explained perfectly by the structural changes expected on protonation of the tetrazole ring. The exocyclic C–NH$_2$ bond length should decrease (increase in stretching energy) and the endocyclic C-N bond length should increase (shift to lower wavenumbers). The observations of hydrogen bond strength and structural changes within the cation are verified by the crystal structures of these two materials (see X-ray discussion).

IR spectra of the salts of **5** also provide insight into the cation structure, hydrogen bonding and the nature of the anions. Quaternization of **4** with methyl iodide yields **8**. IR spectra show a splitting of the asymmetric amino group stretching absorption observed at 3329 cm^{-1} for **4** into two bands (3249 and 3216 cm^{-1}) for **8**. The symmetric NH$_2$ stretch remains a single discrete band shifted to slightly lower energy (3082 cm^{-1}, from 3155 cm^{-1} for **4**) for **8**. One might expect quaternization of **4** to lead to higher energy NH$_2$ stretching vibrations in **8**. However, this is not observed in the case of **8**. Cation-anion hydrogen-bonding would seem to explain the lower than expected NH$_2$ stretching energies. Strong cation-anion hydrogen-bonding is observed in the x-ray structure of **8**. [10] An overview of the IR spectra of salts of **5** in this study shows that the energies of amino group stretching vibrations are almost entirely dependent on the counter anion. The highest energy NH$_2$ stretching bands (3378, 3328, 3265 and 3191 cm^{-1}) and thus weakest interionic interactions are observed, as expected in the perchlorate salt, **10**. The dinitramide salt, **12**, exhibits the next highest energy set of NH$_2$

stretching bands (3341, 3314, 3254 and 3139 cm^{-1}) and thus the next weakest interionic interactions. **9** and **21** exhibit slightly stronger interionic interactions than those observed for **8** with broader, more intense amino group stretching vibrations appearing at 3276, 3223, 3166 and 3040 cm^{-1} and 3350, 3267, 3175 and 3031 cm^{-1}, respectively. Lastly, the NH_2 stretching band in the IR spectrum of **11** is a, broad, intense signal with a maximum at 2874 cm^{-1} indicating the strongest cation-anion interactions found in for a salt of **5**. The significant strength of the interactions observed in **11** is also evidenced by the above mentioned observation of the azide group antisymmetric stretch in the Raman spectrum, which, in purely ionic compounds, should not be observed. All of the observations of interionic hydrogen bond strength are confirmed by X-ray crystallography (see Table 2.6).

Further structural comparison of the HMAT$^+$ and DMAT$^+$ cations can be made by IR spectroscopy. The spectra of salts **6** and **7** show the above mentioned coupled amino group deformation exocyclic C=N stretching vibration at 1687 and 1684 cm^{-1}, respectively. The IR spectra of **8**, **9**, **10**, **11**, **12** and **21** all show the amino group deformation exocyclic C=N stretching vibration as a single band at 1677, 1685, 1686, 1685, 1683 and 1690 cm^{-1}, respectively, indicating that the ring and exocyclic amino group geometries in HMAT$^+$ and DMAT$^+$ should be very similar. Once again, X-ray crystallography confirms this suggestion (see Table 2.6).

2.2.3   NMR Spectroscopy

Both families of energetic salts and their precursors were fully characterized by multinuclear (^{1}H, ^{13}C, $^{14/15}$N and when possible ^{35}Cl) NMR spectroscopy. The chemical shifts recorded for all nuclei as well as ^1J, ^2J and ^3J (^{1}H-^{15}N) coupling constants, when measured, are reported in the experimental section. In the case of **4** all recorded signals and $^1J(^1$H-^{15}N) couplings are in excellent agreement with previously published results[37] and the ^{1}H and ^{13}C resonances are also observed as expected.[9] The ^1J, ^2J and $^3J(^1$H-^{15}N) coupling constants for **4**

(see experimental), reported here for the first time, and those for compounds **6**, **7** and **8 - 12** are in good agreement with typical values for ^2J and $^3J(^1H-^{15}N)$ coupling constants.[38]

In addition to providing a quick method to uniquely identify the compounds synthesized, protonation (**6** and **7**, PIS) and methylation (**8 - 12**, MIS) induced shifts (calculated as a difference in ^{15}N shift between analogous nitrogen signals in neutral **4** and salts of **4** and **5**) can be used to derive information about the structure in solution and hydrogen bonding (interionic interactions) of the salts of **4** and **5**. In the literature, PIS and MIS values have shown to be useful in unequivocally determining the site of protonation or methylation for a variety of heterocyclic compounds.[7] So, for salts **6** and **7** as well as **8 - 12** the substantial protonation and methylation induced shifts observed are tabulated in Table 2.2 (similar measurements of salts of **2** are shown for comparison).

Table 2.2. ^{15}N and ^{13}C Chemical Shifts (ppm) and Protonation (PIS) / Methylation (MIS) Induced Shifts[a]

	N1	N2	N3	N4	N5	C5[j]	C1/C4[j]
1[b,h]	-137.1	-13.1	-13.1	-137.1	-338.9	157.2	
1a[c,h]	-165.2 (-28.1)	-24.5 (-11.4)	-24.5 (-11.4)	-165.2 (-28.1)	-329.1 (9.8)	152.4	
2[d,h]	-167	-5.5	-20.8	-97.5	-338.3	155	
2a[eih]	-164.9 (2.1)	-21.9 (-16.4)	-33.1 (-12.3)	-170.4 (-72.9)	-333.3 (5.0)	152.8	
3a[f,h]	-167.9 (-0.9)	-24.0 (-18.5)	-35.3 (-14.5)	-186.0 (-88.5)	-319.0 (19.3)	148.1	33.6
4[h]	-185	-23.2	2.2	-92.7	-338.2	156.4	32.0
6[h]	-184.0 (1.0)	-24.0 (-0.8)	-13.5 (-15.7)	-129.7 (-37.0)	-331.4 (6.8)	153.6	32.9
7[h]	-183.8 (1.2)	-24.3 (-1.1)	-17.4 (-19.6)	-139.1 (-46.4)	-329.5 (8.7)	155.2	31.6
8[g,i]	-182.9 (2.1)	-29.9 (-6.7)	-29.9 (-32.1)	-182.9 (-90.2)	-318.0 (20.2)	149.1	34.7
9[h]	-182.8 (2.2)	-29.5 (-6.3)	-29.5 (-31.7)	-182.8 (-90.1)	-320.4 (17.8)	148.9	34.2
10[h]	-182.9 (2.1)	-29.5 (-6.3)	-29.5 (-31.7)	-182.9 (-90.2)	-320.0 (18.2)	148.5	34.0
11[h]	-185.8 (-0.8)	-30.7 (-7.5)	-30.7 (-32.9)	-185.8 (-93.1)	-307.2 (31.0)	148.8	33.4
12[h]	-182.7 (2.3)	-29.4 (-6.2)	-29.4 (-31.6)	-182.7 (-90.0)	-320.1 (18.1)	148.5	34.0
21[i]	-182.6 (2.4)	-29.6 (-6.4)	-29.6 (-31.8)	-182.6 (-89.9)	-320.3 (17.9)	148.9	34.5

[a] PIS and MIS shifts in parentheses. [b] From Ref 5a. [c] 5-amino-1*H*-tetrazolium nitrate from Ref 5a. [d] From Ref 5a. [e] 1,5-diamino-1*H*-tetrazolium nitrate from Ref 5a. [f] 1,5-diamino-4-methyl-1*H*-tetrazolium Iodide from Ref 5a. [g] 1,4-dimethyl-5-amimotetrazolium iodide from Ref 5c. [h] DMSO-d_6. [i] CD$_3$OD. [j] ^{13}C NMR shifts.

The PIS data for **6** and **7** show, as expected from the literature, the most significantly negative (-37.0 and -46.4 ppm, respectively) shifts at N4 indicating that protonation in solution occurs exclusively at N4. Additionally, slight, positive PIS shifts for N5 (6.8 ppm for **6** and 8.7 ppm for **7**) show a decrease in electron density at N5 as compared to neutral **4**

and thus indicate a strengthening of the $C-NH_2$ and N-H bonds. Such an observation is in excellent agreement with the solid state IR and Raman data as discussed above. The differences in cation structure due to differences in counter anion basicity observed in the vibrational spectra are also corroborated by the differences in PIS shifts for **6** and **7** at N4 and N5. **6** shows less dramatic PIS shifts (greater structural similarity to **4**) and thus stronger interactions between $HMAT^+$ (especially the acidic proton at N4) and nitrate than **7** for which more dramatic PIS shifts (lesser structural similarity to **4**) are observed indicating weaker cation-anion interactions (hydrogen bonding) in **7**.

The ^{15}N NMR spectrum of the reaction mixture of **4** with methyl iodide shows only 3 resonances thus indicating selective methylation at N4 forming **8**. In addition, the N1 (the N1 and N4 resonances are the same due to molecular symmetry) resonance observed is identical to that of N1 in **7** and shows an MIS of -90.2 relative to N4 of **4**. The observed resonances and MIS values observed and calculated for all salts of **5** except for **11** are all very nearly equal within the tolerances of the measurement. The largest differences in resonances and MIS values are observed for N5, a fact which is explained by the NH_2^+ protons that interact to varying degrees with the counter anions. **11** shows the strongest cation-anion interactions and thus the largest positive MIS at N5 and slight but significant shifts throughout the entire spectrum. Such shifts for **11** fit nicely with vibrational data showing strong azide-NH_2^+ interactions in the solid state. For the remaining salts of **5** the MIS data are less conclusive than vibrational methods, showing only similar amounts of interaction between the cations and anions.

The NMR shifts corresponding to the other simple, nitrogen-rich cations in this study are in perfect agreement with previously recorded shifts for the appropriate cations.[24, 39] The ^{13}C NMR resonance observed for C5 of the NT anion is found between 169.0 and 169.5 ppm, which is consistent both with previous reports[3, 5, 11, 21-23, 40] and with other known tetrazolate anions with electron withdrawing substituents at the 5 position of the tetrazole ring.[39]

Interestingly, in the ^{14}N NMR spectra of **13 - 20** signals corresponding to all three chemically inequivalent nitrogen atoms in the NT anion are observed. The sharpest of the resonances, corresponding to the nitro group nitrogen, N5, is observed around -23 ppm with a line width between 60 and 110 Hz. The remaining two resonances are much broader ($v_{1/2}$ up to 990 Hz) but no less characteristic and are observed at around 20 ppm (N2/3) and -60 ppm (N1/4). The observation and shifts of resonances for the tetrazole ring nitrogen atoms in the ^{14}N spectra of **13 - 20** are consistent with those recorded for 5-trifluoromethyltetrazolate salts.[39] The ^{14}N NMR spectrum of **13** is shown in Figure 2.1.
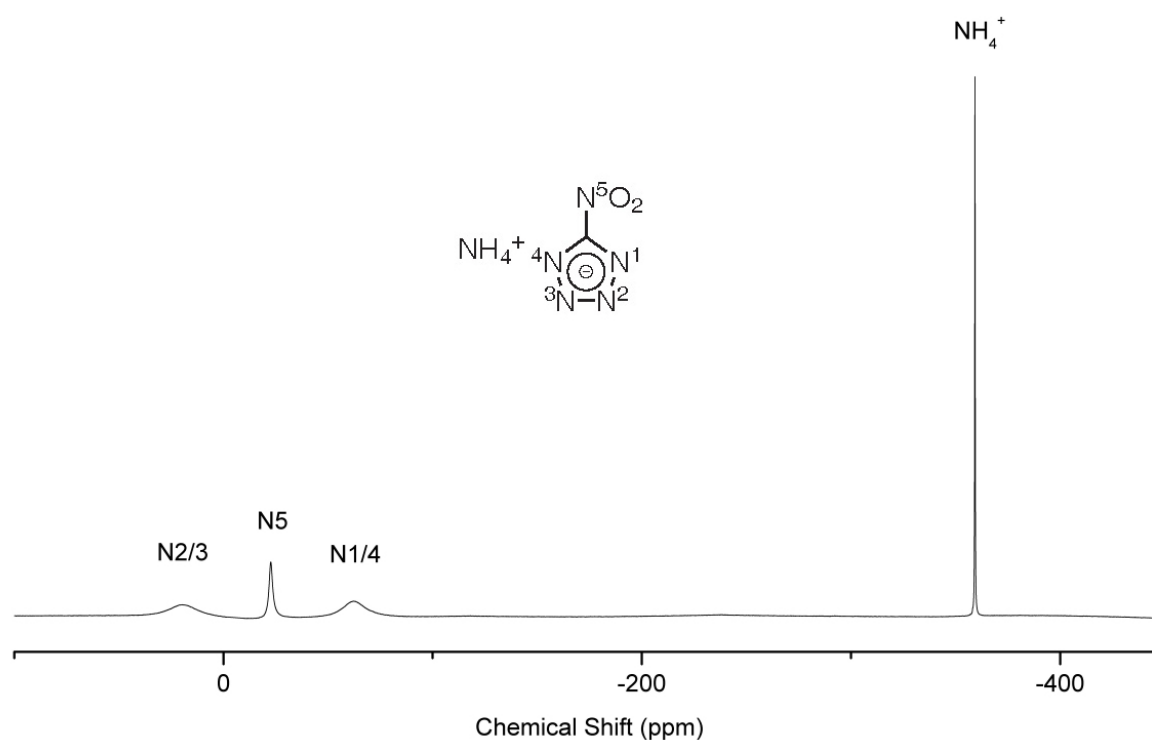
Figure 2.1. [14]Nitrogen NMR spectrum of **13**

2.2.4 X-ray Structures

Each compound synthesized was characterized by X-ray structure determination. Crystallographic data and structure determination details are presented in Table 2.3 (**6** and **7**), Table 2.4 (**8 - 12** and **21**) and Table 5 (**13 - 20**). Selected interatomic distances and angles for

6 - 12 and **21** are shown in Table 2.6 and for **13 - 21** in Table 2.7. Hydrogen bond geometric parameters are tabulated in Table 2.8 for **6 - 12** and **21** and Table 2.9, Table 2.11, Table 2.13, Table 2.15, Table 2.17, Table 2.19, Table 2.20 and Table 2.22 for **13 - 20.** Hydrogen bond pattern graph-set matrices for **13 - 17**, **19** and **20** are included in the text as Table 2.10, Table 2.12, Table 2.14, Table 2.16, Table 2.18, Table 2.21 and Table 2.23. **6** and **7** crystallize in the same monoclinic space group $P2_1/n$ but differences in the lengths of the crystallographic axes and monoclinic angles indicate that the packing in the two structures is certainly different. Although both structures are composed of three dimensional hydrogen bonded networks consisting of seven crystallographically independent hydrogen bonds each, the packing around the planar nitrate anion in **6** is, for geometric reasons, different than the packing around the tetrahedral perchlorate anion in **7**.

Table 2.3. Crystallographic Data and Structure Determination Details for **6** and **7**.

	6	7
formula	$C_2H_6N_5{}^+NO_3{}^-$	$C_2H_6N_5{}^+ClO_4{}^-$
formula weight (g/mol)	162.13	199.57
crystal system	monoclinic	monoclinic
space group	$P2_1/n$	$P2_1/n$
a (Å)	10.6122(3)	5.2741(8)
b (Å)	5.3606(2)	20.696(3)
c (Å)	11.5508(4)	7.149(2)
α (°)	90	90
β (°)	97.663(2)	106.60(2)
γ (°)	90	90
V (Å^3)	651.23(4)	747.8(2)
Z	4	4
ρ_{calcd} (g/cm^3)	1.653	1.773
μ (mm^{-1})	0.149	0.499
λ (Mo Kα, Å)	0.71073	0.71073
T (K)	200(2)	200(2)
reflections collected	8969	3813
independent reflections	1484	1465
R_{int}	0.0554	0.0372
observed reflections	1150	1333
F(000)	336	408
$R_1{}^a$	0.0355	0.0484
$wR_2{}^b$	0.1017	0.1061
weighting scheme^c	0.0483, 0.1647	0.0267, 1.2214
GOOF	1.076	1.161
number of parameters	125	133

^{a} $R_1 = \Sigma \, ||F_o| - |F_c|| \, / \, \Sigma \, |F_o|$. ^{b} $R_w = [\Sigma \, (F_o{}^2 - F_c{}^2) \, / \, \Sigma \, w \, (F_o)^2]^{1/2}$. ^{c} $w = [\sigma_c{}^2 \, (F_o{}^2) + (xP)^2 + yP]^{-1}$, $P = (F_o{}^2 - 2F_c{}^2) \, / \, 3$.

8 and **11** both crystallize in the orthorhombic space group *Fddd* and are closely related structurally. Both structures crystallize in planar layers within which cations and anions hydrogen bond to one another forming dimeric pairs (two cations and two anions), which interact with one another through non-polar interaction of the methyl groups (see Figure 2.2 and Figure 2.3). Not surprisingly, the a-axes in these two structures differ the least (~0.07 Å) since this is the direction normal to the planar cation-anion layers in both structures and the only interaction between the layers in both cases are weak van der Waals forces. The b- and c-axes are slightly more dissimilar (~0.9 Å and ~0.5 Å, respectively). However, these differences are easily rationalized, by the different sizes and geometries of the iodide and

azide anions. In the case of the monatomic iodide anion in **8**, the b-axis is slightly longer than that of the azide anion in **11** since iodine has a larger van der Waals radius (2.15 Å) than nitrogen (1.5 Å). [26] For the c-axis the situation is reversed with **11** having a longer axis than **8** since the linear azide anions in **11** are arranged parallel to the c-axis. Compound **10** (Figure 2.4) also forms dimeric pairs similar to those observed in **8** and **11**, however due to the tetrahedral shape of the perchlorate anion the compound crystallizes in the monoclinic space group $P2_1/n$ rather than the orthorhombic *Fddd*, with substantially different lattice parameters (Table 2.4). Lastly, structures **9**, **12** and **21** crystallize in the non-centrosymmetric (chiral) monoclinic space group $P2_12_12_1$ with similar lattice parameters. As in the case of **8** and **11**, the packing patterns of these compounds are also related (Table 2.4). **9**, **12** and **21** all form infinite hydrogen bonded (3 H-bonds each, see Table 5), helical (source of chirality) chains of cations and anions. Interactions between the chains are once again limited weak van der Waals interactions. Although the dimensions of the crystallographic axes are similar for all three compounds, the axis of the helix is parallel to the a-axis in **9** and **21** and parallel to the b-axis in **12**, suggesting similarities between the preferred packing patterns of the NT anion and the nitrate anion.
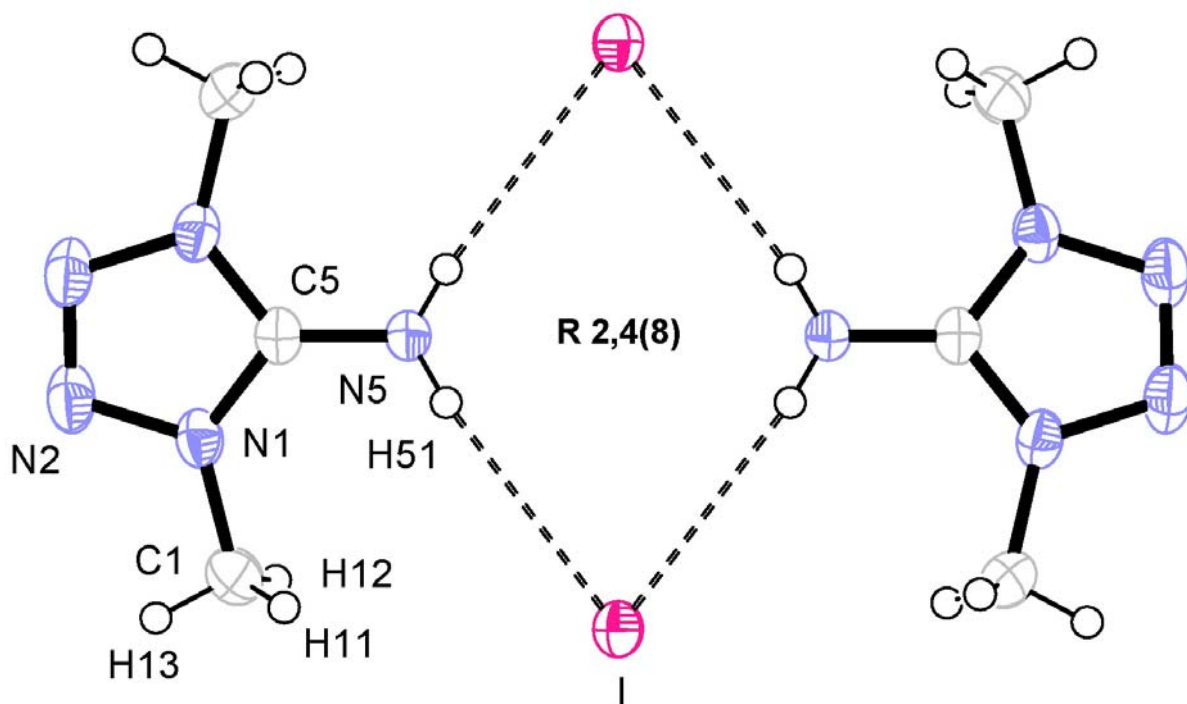
Figure 2.2. View of a hydrogen-bonded dimer of 1,4-dimethyl-5-aminotetrazolium iodide (**8**) with atom labels for one asymmetric unit and thermal ellipsoids shown for 50 % probability along the crystallographic a-axis.
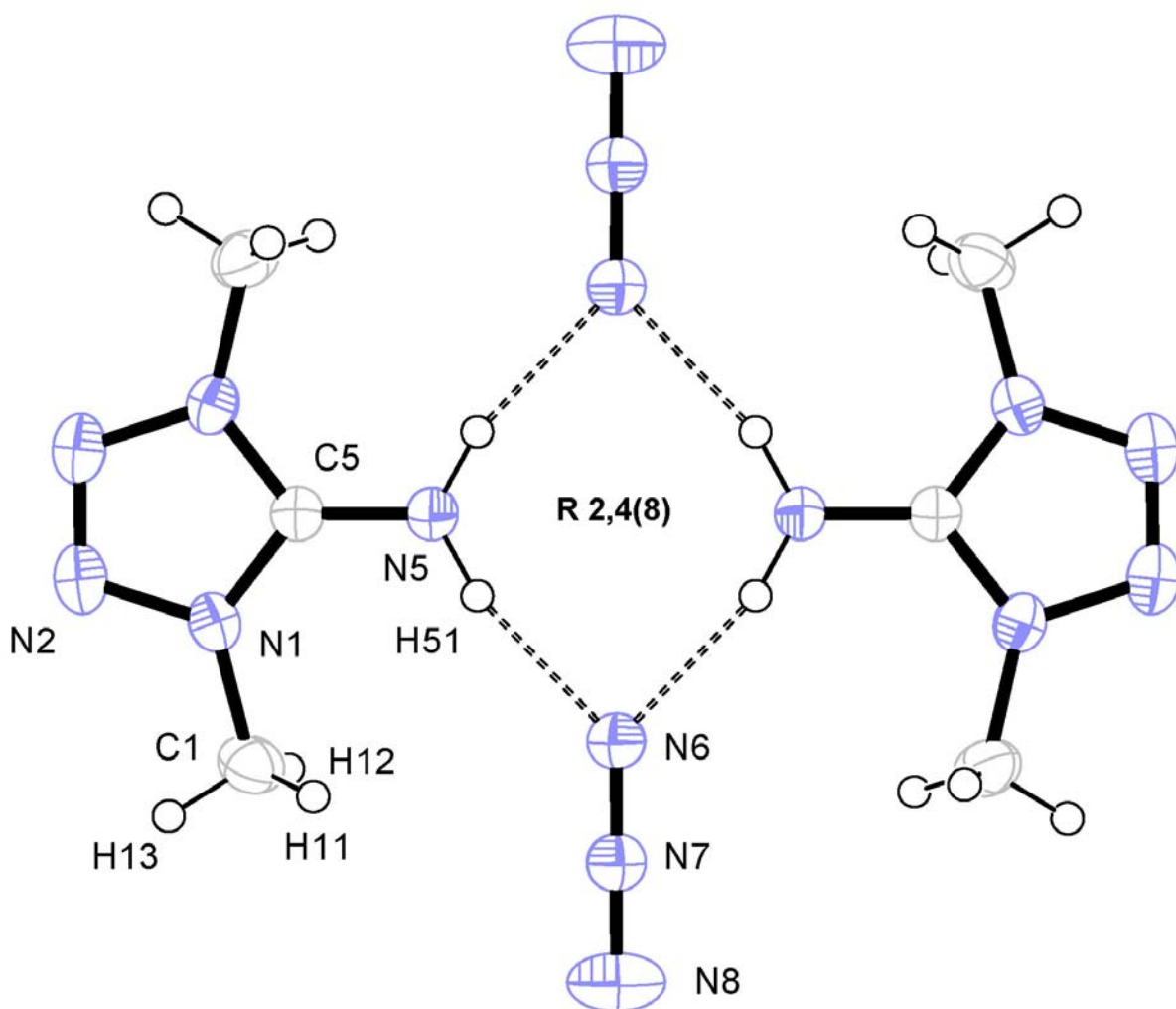
Figure 2.3. View of a hydrogen-bonded dimer of 1,4-dimethyl-5-aminotetrazolium azide (**11**) with atom labels for one asymmetric unit and thermal ellipsoids shown for 50% probability along the crystallographic a-axis.
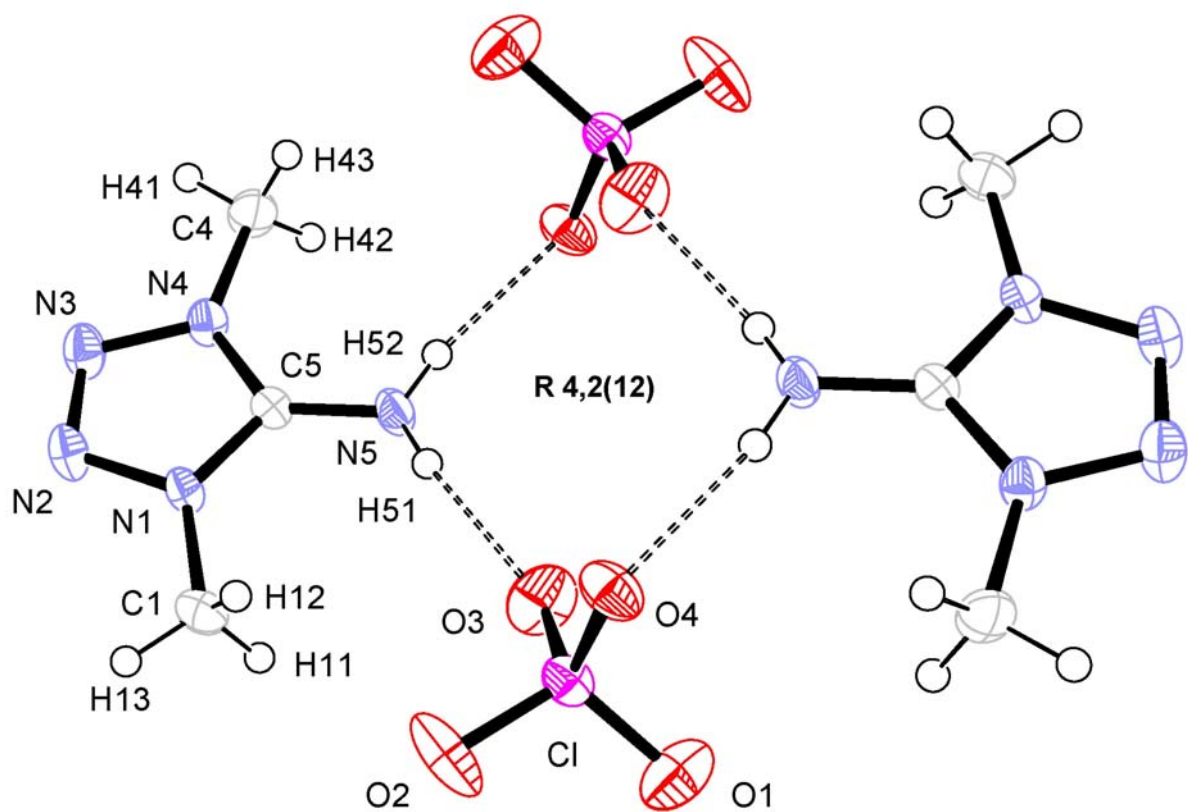
Figure 2.4. Hydrogen-bonded dimer of 1,4-dimethyl-5-aminotetrazolium perchlorate (**10**) with atom labels for one formula unit and thermal ellipsoids shown for 50% probability.

Table 2.4. Crystallographic Data and Structure Determination Details for **8 - 12** and **21**.

	8	9	10	11	12	21
formula	$C_3H_8N_5^+I^-$	$C_3H_8N_5^+NO_3^-$	$C_3H_8N_5^+ClO_4^-$	$C_3H_8N_5^+N_3^-$	$C_3H_8N_5^+N_3O_4^-$	$C_3H_8N_5^+CN_5O_2^-$
mass (g/mol)	241.03	176.15	213.59	156.17	220.17	228.2
crystal system	orthorhombic	orthorhombic	monoclinic	orthorhombic	orthorhombic	orthorhombic
space group	*Fddd*	*P$2_12_12_1$*	*P2_1/n*	*Fddd*	*P$2_12_12_1$*	*P$2_12_12_1$*
a (Å)	13.718(2)	5.3855(2)	5.7280(7)	12.351(2)	5.3985(6)	5.7089(10)
b (Å)	14.486(2)	10.8511(5)	10.9681(8)	13.952(2)	12.926(2)	12.8661(16)
c (Å)	16.281(2)	12.9152(6)	13.499(2)	17.180(2)	13.336(2)	13.3277(19)
α (°)	90	90	90	90	90	90
β (°)	90	90	92.24(2)	90	90	90
γ (°)	90	90	90	90	90	90
V (Å^3)	3235.4(5)	754.75(6)	847.4(2)	2960.5(4)	930.6(2)	978.8(3)
Z	16	4	4	16	4	4
ρ_{calcd} (g/cm^3)	1.979	1.550	1.674	1.403	1.572	1.548
μ (mm^{-1})	3.891	0.135	0.446	0.106	0.14	0.127
λ (Mo Kα, Å)	0.71073	0.71073	0.71073	0.71073	0.71073	0.71073
T (K)	200(2)	100(2)	200(2)	200(2)	200(2)	200(2)
reflns collected	6527	4277	7096	6973	4786	6729
indep. reflns	964	1290	2001	730	1087	1650
R_{int}	0.036	0.0432	0.0438	0.062	0.062	0.0334
obsd. reflns.	786	886	1391	725	973	1523
F(000)	1824	368	440	1312	456	472
$R_1{}^a$	0.0169	0.0367	0.0333	0.0409	0.0488	0.0399
$wR_2{}^b$	0.0352	0.0903	0.0801	0.1069	0.1257	0.0990
weighting scheme^c	0.0137, 3.5456	0.0503, 0.0000	0.0469, 0.0000	0.0579, 2.4663	0.0762, 0.0516	0.0660, 0.0323
GOOF	1.128	0.969	0.897	1.165	1.087	1.091
parameters	59	141	150	69	146	177

^{a} $R_1 = \Sigma ||F_o| - |F_c|| / \Sigma |F_o|$. ^{b} $R_w = [\Sigma (F_o{}^2 - F_c{}^2) / \Sigma w (F_o)^2]^{1/2}$. ^{c} $w = [\sigma_c{}^2 (F_o{}^2) + (xP)^2 + yP]^{-1}$, $P = (F_o{}^2 - 2F_c{}^2) / 3$.

Compounds **13 - 18** crystallize in a variety (*P2_1/c*, *C2/c*, *P2_1/n* and *P2_1*) of monoclinic space groups whereas **20** crystallizes in the orthorhombic space group *P$2_12_12_1$* and **19** crystallizes in triclinic *P*-1. From the unit cell parameters, no close relationships in packing may be deduced (no similar unit-cell parameters in structures with the same space groups). All salts of the NT anion studied here crystallize either in layered structures as in **14**, **16** and **19** or, in the case of the remaining compounds, as complex, three dimensional hydrogen bonded networks of cations and anions.

Table 2.5. Crystallographic data and structure determination details for compounds **13 - 20**.

	13	14	15	16	17	18	19	20
weight (g/mol)	141.11	132.1	147.12	174.15	189.17	204.18	237.22	219.20
crystal system	Monoclinic	Monoclinic	Monoclinic	Monoclinic	Monoclinic	Monoclinic	Triclinic	Orthorhombic
space group	$C2/c$	$P2_1/c$	$P2_1/c$	$C2/c$	$P2_1/n$	$P2_1$	P-1	$P2_12_12_1$
a (Å)	10.4860(13)	4.8436(2)	8.0124(3)	9.8240(3)	6.9447(5)	6.8162(9)	6.9805(9)	4.4024(4)
b (Å)	8.1461(10)	13.7981(6)	10.3237(5)	11.7601(4)	6.3716(6)	7.3468(10)	8.1249(9)	9.5261(7)
c (Å)	13.8381(17)	8.0853(4)	7.1531(3)	6.8736(2)	17.3196(12)	17.001(2)	9.1040(10)	21.6851(14)
α (°)	90	90	90	90	90	90	88.480(9)	90
β (°)	104.207(11)	97.2558(17)	106.186(3)	117.6043(13)	99.152(8)	92.774(11)	74.880(10)	90
γ (°)	90	90	90	90	90	90	81.314(10)	90
V (Å^3)	1145.9(3)	536.03(4)	568.23(4)	703.72(4)	756.62(10)	850.4(2)	492.70(10)	909.42(12)
Z	4	4	4	4	4	4	2	4
ρ_{calcd} (g/cm^3)	1.636	1.637	1.72	1.644	1.661	1.595	1.599	1.601
μ (mm^{-1})	0.149	0.147	0.153	0.141	0.142	0.136	0.139	0.136
λ (Mo Kα, Å)	0.71069	0.71073	0.71073	0.71073	0.71073	0.71069	0.71069	0.71069
T (K)	140(2)	200(2)	200(2)	200(2)	200(2)	200(2)	140(2)	100(2)
reflns collected	2875	6065	6560	5932	6344	6000	5044	11757
ind. reflections	1120	1229	1294	804	1492	2645	1926	1579
R_{int}	0.0292	0.1018	0.0806	0.0922	0.0493	0.0516	0.0366	0.0984
obs. reflections	1001	959	997	738	1721	1711	1749	921
F(000)	584	272	304	360	392	424	248	456
$R_1{}^a$	0.0329	0.0559	0.0576	0.0395	0.0499	0.0665	0.0406	0.0417
$wR_2{}^b$	0.088	0.1144	0.1124	0.1039	0.0872	0.1091	0.0963	0.0812
weighting scheme^c	0.0499, 0.6428	0.0641, 0.0000	0.0594, 0.0801	0.0545, 0.2774	0.0544, 0.0000	0.0327, 0.0000	0.04010, 0.1780	0.0301, 0.0000
GOOF	1.05	1.057	1.047	1.08	1.131	1.046	1.093	0.99
no. of parameters	107	99	112	69	146	301	189	172

^{a} $R_1 = \Sigma \ ||F_o| - |F_c|| \ / \ \Sigma \ |F_o|$. ^{b} $R_w = [\Sigma \ (F_o{}^2 - F_c{}^2) \ / \ \Sigma \ w \ (F_o)^2]^{1/2}$. ^{c} $w = [\sigma_c{}^2 \ (F_o{}^2) + (xP)^2 + yP]^{-1}$, $P = (F_o{}^2 - 2F_c{}^2) \ / \ 3$.

In the structures of **6** and **7** the HMAT$^+$ cations are nearly identical within the limits of structure determination accuracy as suggested by IR and Raman observations (Table 2.6). The HMAT$^+$ cation is planar with exception of the methyl group protons which are staggered with respect to the ring in both **6** and **7** (Figure 2.5 and Figure 2.6). Unfortunately, we were unable to determine the structure of **4** for comparison, however all bond lengths and angles in **6** and **7** are quite similar to those found in analogous salts of **1** and **2**. The differences observed are no greater than 0.01 A for analogous interatomic distances and no greater than 5 degrees for analogous angles.[7] As in salts of **1** and **2**, protonation is observed exclusively at the N4 position, which is in excellent agreement with NMR observations and as mentioned above, the only slight variation in the HMAT$^+$ cations observed is in the location of H4. Although the determination of absolute hydrogen atom position by X-ray methods is prone to large systematic errors stemming from the electronegativity of the atom to which the H atom is bonded,[41] the HMAT$^+$ cations in **6** and **7** are very nearly identical, so a comparison of the

relative lengths of the N4-H4 bond should provide pertinent information about hydrogen bonding in these structures. Stronger hydrogen bonding is observed in **6** because the calculated length of the N4-H4 bond (0.93(2) Å) is greater than that of the same bond (0.84(4) Å) in **7**. As stated above, vibrational spectroscopy, as well as the acid-base properties of nitrate and perchlorate suggest that exactly such a trend in hydrogen bond strength should be present (a more in depth discussion of hydrogen bonding in all salts of **4** and **5** follows below).

Figure 2.5. Formula unit of 1-methyl-5-aminotetrazolium nitrate (**6**) with atom labels and thermal ellipsoids shown for 50% probability.

Figure 2.6. Formula unit of 1-methyl-5-aminotetrazolium perchlorate (**7**) with atom labels and thermal ellipsoids shown for 50% probability.

Table 2.6. Selected bond lengths (Å) and angles (°) in compounds **6 - 12** and **21**.

	6	7	8	9	10	11	12	21
				Bond Lengths				
N1-C5	1.3386(19)	1.337(3)	1.330(3)	1.338(3)	1.328(2)	1.3373(15)	1.341(4)	1.339(2)
N1-N2	1.3652(17)	1.370(3)	1.358(3)	1.362(2)	1.359(2)	1.3640(15)	1.356(4)	1.357(2)
N1-C1	1.457(2)	1.463(4)	1.451(4)	1.450(3)	1.452(2)	1.4530(18)	1.466(4)	1.450(3)
N2-N3	1.2739(18)	1.274(4)	1.277(5)	1.270(3)	1.274(2)	1.268(2)	1.270(4)	1.273(3)
N3-N4	1.3604(18)	1.352(4)	1.358(3)	1.367(2)	1.361(2)	1.3640(15)	1.372(4)	1.361(2)
N4-C5	1.3364(19)	1.337(4)	1.330(3)	1.337(3)	1.335(2)	1.3373(15)	1.345(4)	1.336(2)
N5-C5	1.3173(19)	1.311(4)	1.311(4)	1.315(3)	1.314(3)	1.311(2)	1.304(4)	1.314(2)
N4-R^a	0.93(2)	0.84(4)	1.451(4)	1.458(3)	1.456(3)	1.4530(18)	1.452(4)	1.456(3)
				Bond Angles				
C5-N1-N2	109.54(12)	109.6(2)	109.99(19)	109.32(17)	109.70(15)	109.31(11)	110.0(3)	109.51(16)
C5-N1-C1	129.16(14)	129.6(3)	128.79(19)	129.64(19)	128.81(16)	128.80(12)	127.4(3)	128.16(16)
N2-N1-C1	121.18(13)	120.7(3)	121.2(2)	121.02(19)	121.45(17)	121.65(11)	122.2(3)	122.30(15)
N3-N2-N1	108.00(12)	107.7(2)	107.75(13)	108.52(17)	108.01(16)	108.22(7)	108.6(3)	108.15(15)
N2-N3-N4	108.02(12)	108.1(2)	107.75(13)	107.77(17)	107.91(14)	108.22(7)	107.6(3)	108.15(16)
C5-N4-N3	109.84(13)	110.3(2)	109.99(19)	109.58(18)	109.43(15)	109.31(11)	109.7(3)	109.39(15)
N5-C5-N4	127.89(14)	128.2(3)	127.73(12)	127.7(2)	127.61(18)	127.54(8)	127.7(3)	127.43(16)
N5-C5-N1	127.50(14)	127.6(3)	127.73(12)	127.5(2)	127.44(17)	127.54(8)	128.3(3)	127.78(18)
N4-C5-N1	104.60(13)	104.3(2)	104.5(2)	104.80(19)	104.95(15)	104.92(15)	104.1(3)	104.79(16)
C5-N4-R^a			128.79(19)	128.13(19)	128.90(17)	128.80(12)	128.9(3)	128.22(16)
N3-N4-R^a			121.2(2)	122.25(18)	121.60(15)	121.65(11)	121.3(3)	122.35(16)

^{a} R = H (**6** and **7**) and R = CH$_3$ (**8 - 12** and **21**).

The structures of **8 - 12** and **21** also show nearly identical DMAT$^+$ cations within the structure determination tolerances and only slight differences in the rotational configuration of the methyl groups are also observed (Figure 2.2 – Figure 2.4, Figure 2.7 – Figure 2.9). The

geometry of the DMAT$^+$ cations, aside from their higher symmetry, is also very nearly identical to that observed for HMAT$^+$ cations and they are therefore planar with the exception of the methyl group protons. Only the N5-H calculated distance in the DMAT$^+$ cation of **11** varies significantly (~0.1 Å) from those found for the other salts of **5**. The formation of strong interionic hydrogen bonds, as observed by both vibrational and NMR spectroscopy, explains this deviation nicely. Lastly, all of the anions, aside from the NT anion, employed in this study are crystallographically identical to those observed in numerous other studies and discussion thereof is thus omitted.
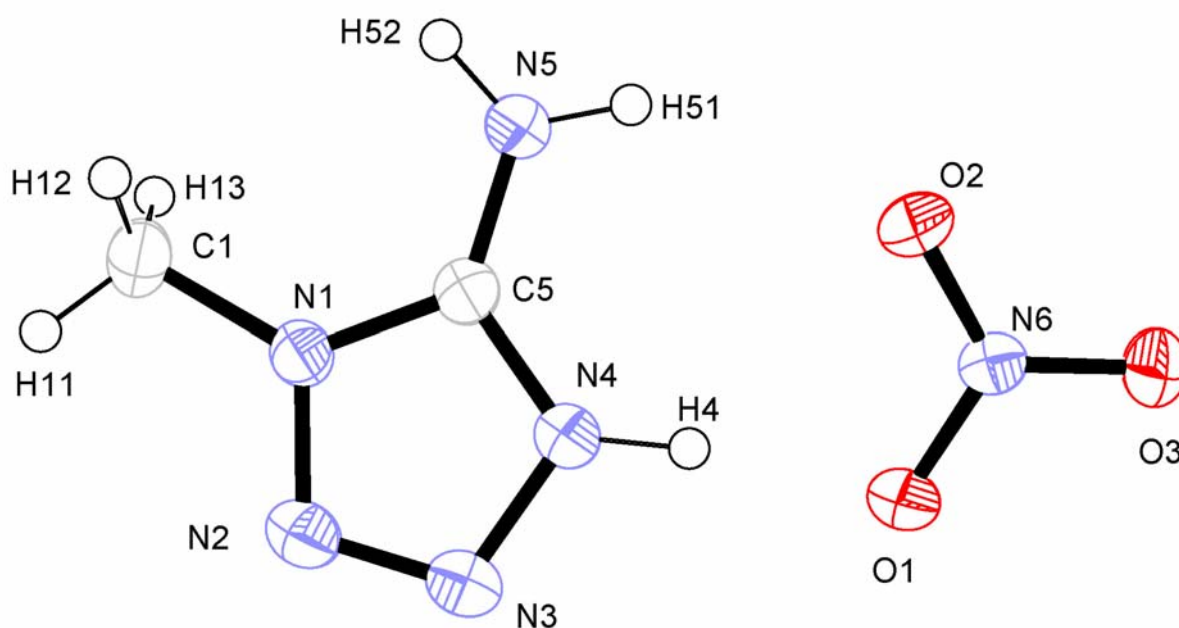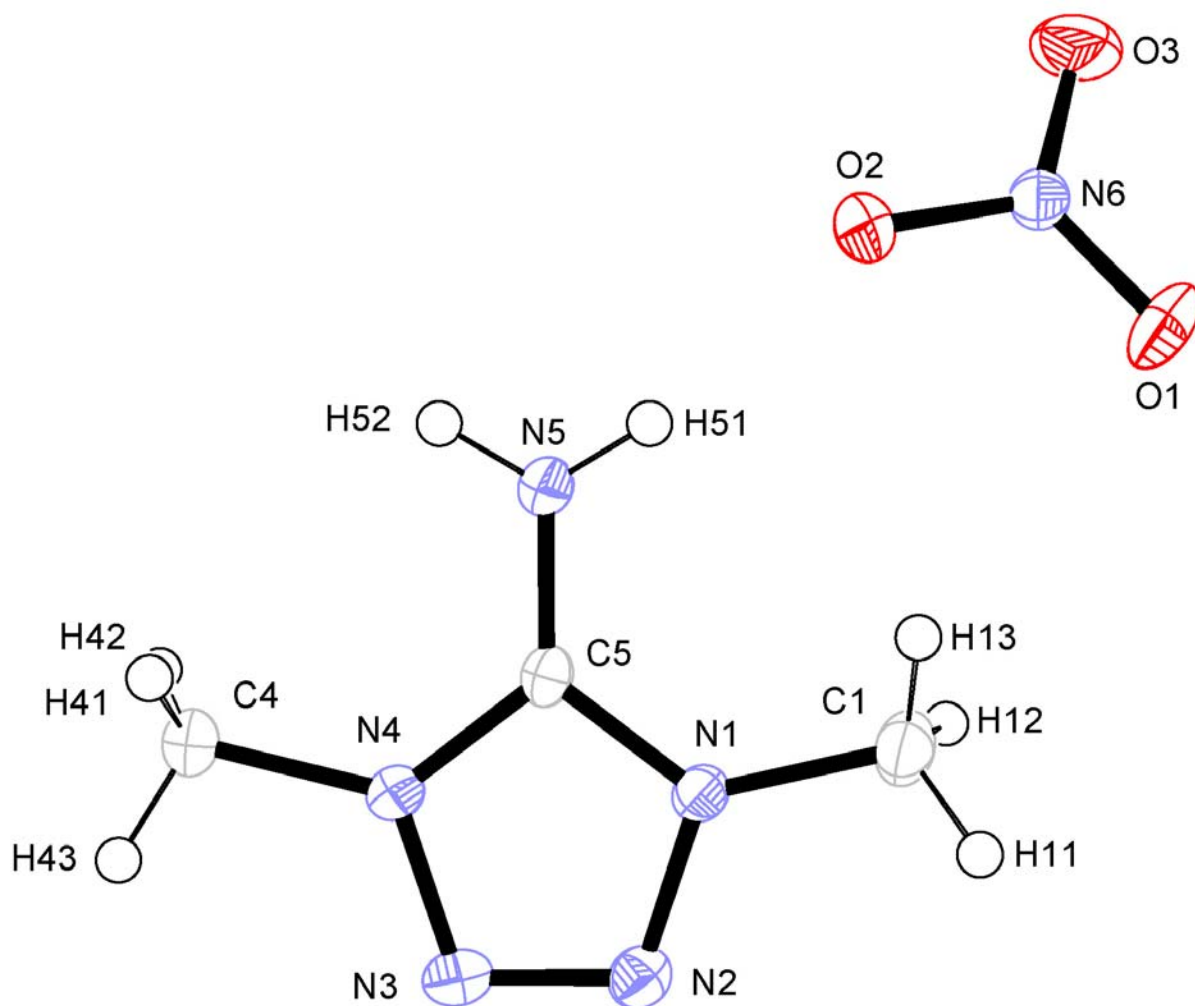

Figure 2.7. Formula unit of 1,4-dimethyl-5-aminotetrazolium nitrate (**9**) with atom labels and thermal ellipsoids shown for 50% probability.
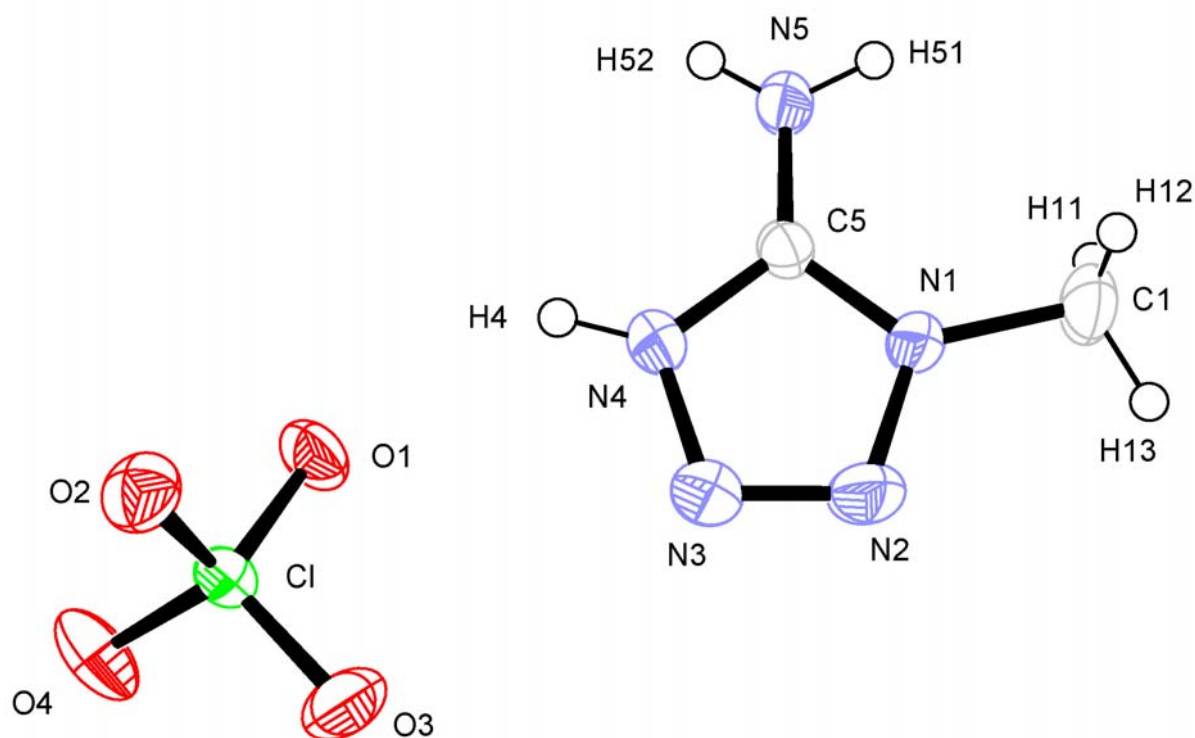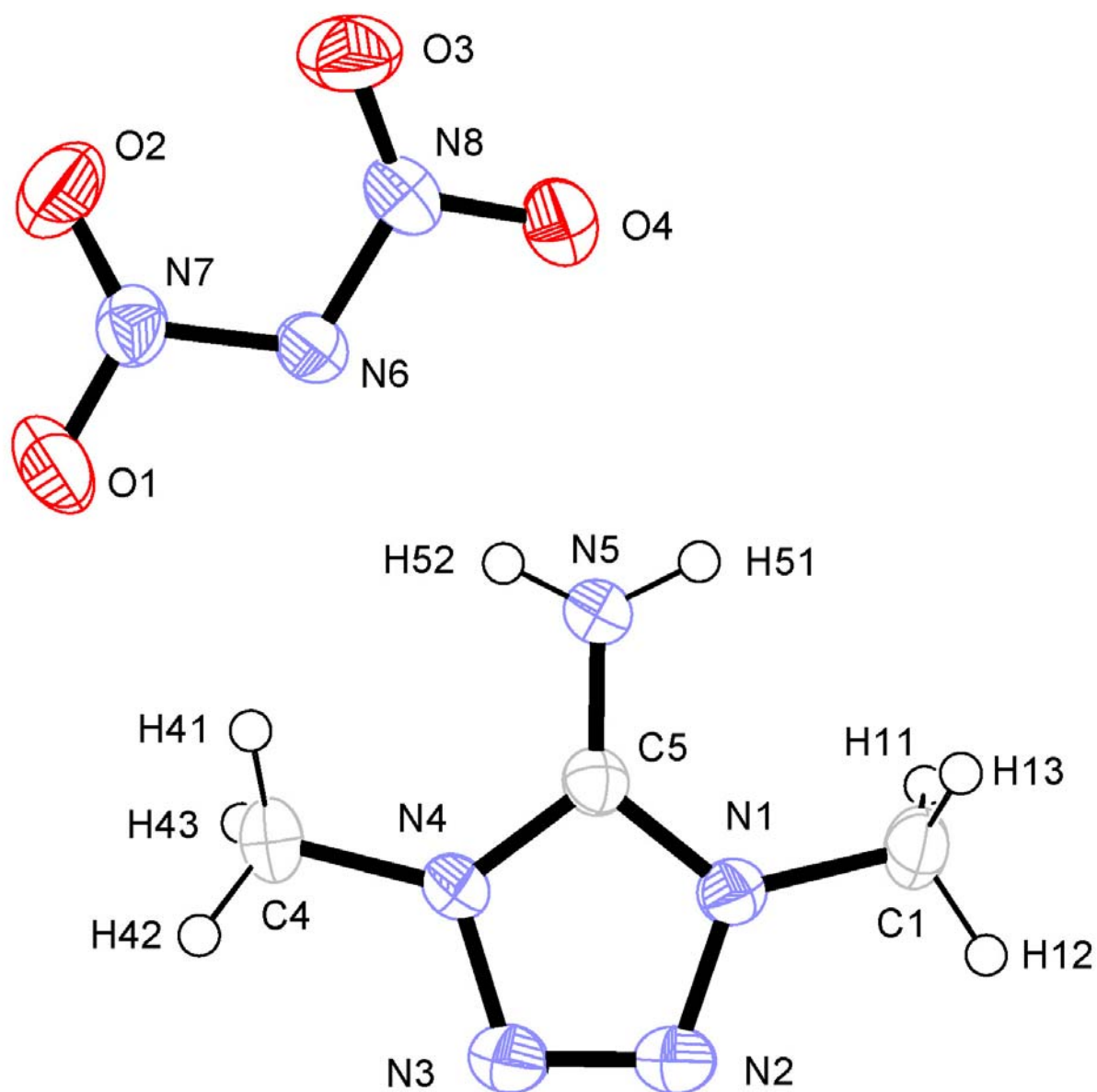
Figure 2.8. Formula unit of 1,4-dimethyl-5-aminotetrazolium dinitramide (**12**) with atom labels and thermal ellipsoids shown for 50% probability.
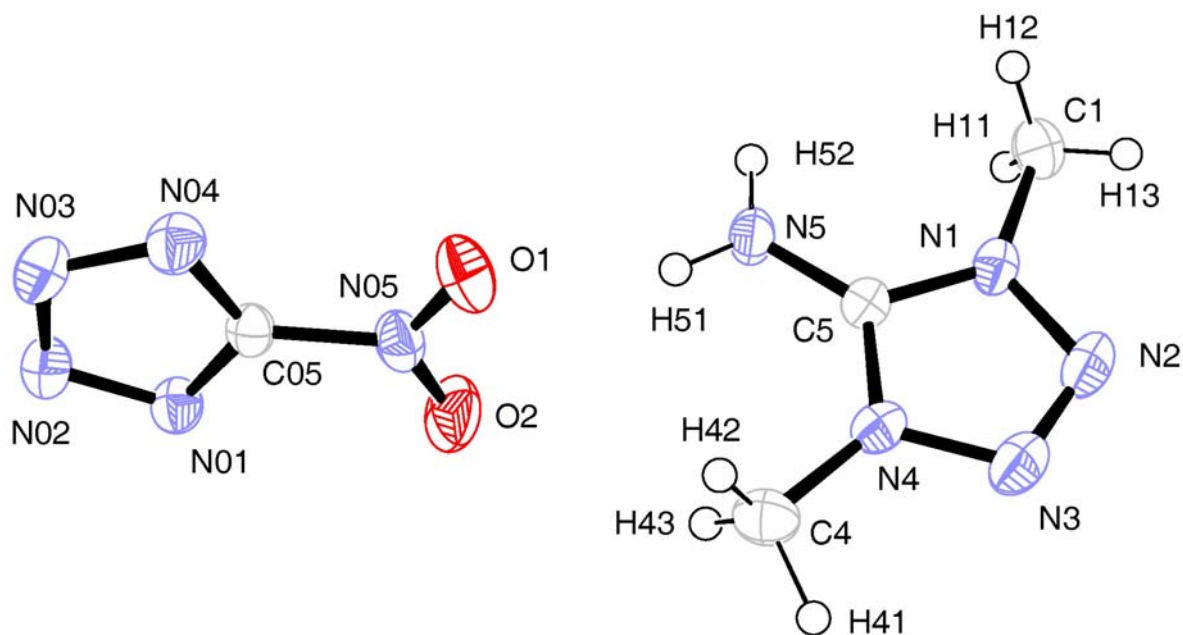
Figure 2.9. Formula unit of 1,4-dimethyl-5-aminotetrazolium 5-nitrotetrazolate (**21**) with atom labels and thermal ellipsoids shown for 50% probability.

The nitrogen-rich cations employed in this study are also the subject of many X-ray studies and are therefore structurally well characterized. The ammonium cation in **13** and **14** is tetrahedral, as ammonium is well-known to be. The geometry of the hydrazinium ($N_2H_5^+$) cation in **15** is also as it is reported previously in the literature[42] as are the geometries of the guanidinium cation[43-45] in **16** and the geometries of the cations in **17 - 20**.[24, 39, 46]

As suggested by vibrational spectroscopy, the NT anions in **13 - 21** are, within the limits of structure determination precision, nearly identical. From Table 2.7, it is also evident that the NT anion has the same geometry as was identified in previous structure determinations of NT containing salts.[11, 23, 40, 47-50] The geometry of the tetrazole portion of the NT anion in **13 - 21** is also very similar to other 5-substituted tetrazolate anions with electron-withdrawing substituents, including $-CF_3$[39, 51, 52] and $-CN$.[53, 54] The tetrazole bond lengths in such tetrazolate anions are all $\approx$ 1.33 Å and angles as expected for a slightly (symmetrically) distorted planar pentagon. As expected, the tetrazole ring bond lengths in 5-substituted tetrazolate anions with electron-withdrawing groups, such as NT, are slightly shorter than

those in 5-substituted tetrazolate anions with electron-donating substituents, such as –NH$_2$.[55] The only geometric parameter in which significant variation is observed from one NT containing salt or metal complex to another, both in this study and in the literature, is in the "out-of-tetrazole-ring-plane" torsion of the nitro group. In Table 3 all four torsion angles describing the nitro group are listed for compounds **13 - 21** and "out-of-tetrazole-ring-plane" torsions vary from 0º (**18**, NT moiety B) and 10º (**17**).

Table 2.7. Selected bond lengths (Å), angles (º) and torsion angles (º) in compounds **13 - 21**.[a]

	13	14	15	16	17	18[b]	19	20	21
					Bond Lengths				
C5-N1	1.3215(17)	1.3219(15)	1.3232(18)	1.3261(11)	1.3220(16)	1.314(5) / 1.317(5)	1.3260(19)	1.330(3)	1.316(2)
C5-N4	1.3236(17)	1.3216(16)	1.3185(17)	1.3261(11)	1.3112(18)	1.313(5) / 1.319(5)	1.3275(19)	1.332(3)	1.322(2)
C5-N5	1.4515(17)	1.4398(17)	1.4414(19)	1.4410(19)	1.4437(16)	1.453(6) / 1.452(5)	1.448(2)	1.445(3)	1.442(2)
N1-N2	1.3422(16)	1.3341(17)	1.3389(17)	1.3366(13)	1.3387(16)	1.342(5) / 1.341(5)	1.3413(19)	1.350(3)	1.337(2)
N2-N3	1.3278(16)	1.3256(15)	1.3202(18)	1.3263(19)	1.3167(18)	1.323(5) / 1.330(5)	1.3363(19)	1.341(3)	1.326(2)
N3-N4	1.3450(16)	1.3391(16)	1.3419(17)	1.3366(13)	1.3378(16)	1.339(5) / 1.340(5)	1.336(2)	1.351(3)	1.346(2)
N5-O1	1.2265(15)	1.2199(15)	1.2271(16)	1.2254(10)	1.2218(15)	1.218(5) / 1.224(4)	1.2241(18)	1.235(3)	1.222(2)
N5-O2	1.2306(15)	1.2297(14)	1.2265(17)	1.2254(10)	1.2190(15)	1.226(4) / 1.226(4)	1.2264(18)	1.236(3)	1.222(2)
					Bond Angles				
N1-C5-N4	114.94(11)	114.10(11)	114.75(13)	115.14(12)	114.75(11)	115.3(4) / 115.4(4)	114.75(14)	114.9(2)	114.86(15)
N1-C5-N5	123.17(12)	123.15(11)	122.50(12)	122.43(6)	123.23(12)	122.0(4) / 122.7(3)	123.27(13)	122.7(2)	123.06(16)
N4-C5-N5	121.87(11)	122.75(13)	122.76(12)	122.43(6)	122.02(11)	122.7(4) / 121.9(3)	121.96(13)	122.3(3)	122.06(16)
C5-N1-N2	102.97(11)	103.68(10)	103.03(11)	102.47(8)	102.78(11)	102.7(3) / 103.0(3)	103.05(12)	103.1(2)	103.32(14)
N3-N2-N1	109.67(11)	109.31(11)	109.53(11)	109.96(6)	109.67(11)	109.5(3) / 109.1(3)	109.36(13)	109.3(2)	109.31(14)
N2-N3-N4	109.57(10)	109.70(11)	109.91(11)	109.96(6)	109.67(11)	109.6(3) / 110.0(3)	109.87(12)	109.7(2)	109.76(15)
C5-N4-N3	102.84(10)	103.21(11)	102.78(11)	102.47(8)	103.13(11)	102.9(3) / 102.5(3)	102.97(12)	102.9(2)	102.75(15)
O1-N5-O2	125.23(12)	125.15(12)	124.50(14)	124.24(13)	124.76(12)	126.2(4) / 124.4(4)	124.42(15)	124.4(2)	123.96(16)
O1-N5-C5	117.55(11)	117.89(12)	117.74(12)	117.88(7)	117.14(12)	118.1(4) / 118.1(3)	117.34(14)	118.4(2)	118.23(16)
O2-N5-C5	117.20(11)	116.96(12)	117.76(13)	117.88(7)	118.10(11)	115.7(4) / 117.5(4)	118.23(13)	117.2(2)	117.81(16)
					Torsion Angles				
O1-N5-C5-N4	-169.04(12)	176.47(11)	175.48(12)	-177.22(7)	-172.04(12)	-176.8(4) / 178.7(4)	-176.71(14)	-176.2(2)	-174.14(16)
O2-N5-C5-N4	9.59(18)	-3.95(16)	-4.86(19)	2.78(7)	8.23(18)	3.7(6) / 0.6(5)	1.9(2)	3.7(4)	6.0(3)
O1-N5-C5-N1	9.61(18)	-3.20(16)	-4.28(19)	2.78(7)	7.49(18)	2.0(6) / 1.1(5)	2.5(2)	3.3(4)	4.6(3)
O2-N5-C5-N1	-171.75(12)	176.38(11)	175.38(12)	-177.22(7)	-172.23(13)	-177.5(4) / -177.0(4)	-178.96(14)	-176.7(3)	-175.28(18)

[a] Bond lengths, angles and torsion angles from the NT anion [b] Parameters for both anions in the asymmetric unit of **18** are shown (A / B).

As suggested above, intermolecular (or interionic) hydrogen bonding plays a pivotal role in determining the properties of energetic materials and is also a defining element in the structures of salts of **4** and **5**. As might be expected, salts of **4** show more extensive hydrogen bonding than salts of **5** for the simple reason that more and better proton donors are available in salts of **4** (see Table 2.8). **6** and **7** form seven hydrogen bonds each ranging in strength from strong (D-H···A, 2.660(2) Å) to weak (D-H···A 3.361(2) Å) which, in both cases, form extensive networks within the lattice. The extensive hydrogen bond network is probably responsible for the low sensitivity of **6** to friction and impact as well as its reasonably high density. Complete description of the reasonably complex hydrogen bonding networks in **6** and **7** is facilitated by the use of graph-set analysis as described by Berstein et al.[56] For a brief description of graph set analysis see the appropriate chapter 1 appendix section. For **6** the computer program *RPLUTO*[57-59] identifies several characteristic two bond (binary) ring graph-set patterns including R 2,2(4), R 1,2(6), R 2,2(6), R 2,1(4) as shown in Figure 2.10. Similarly, the structure of **7** is characterized by a hydrogen bond network built principally of two hydrogen bond ring R 2,2(4), R 1,2(6) and R 4,4(12) graph-sets (Figure 2.11).

Table 2.8. Hydrogen-bonding geometry in **6** - **12** and **21**.

D–H•••A[a]	D–H (Å)	H•••A (Å)	D•••A (Å)	D–H•••A (°)
		6		
N5–H51•••O2	0.88(2)	2.352(19)	3.1215(18)	146.1(15)
N5–H51•••O2[i]	0.88(2)	2.369(19)	3.1106(18)	142.1(15)
N5–H52•••O1[ii]	0.88(3)	2.60(3)	3.3606(18)	145(2)
N5–H52•••O3[i]	0.88(3)	2.63(2)	3.0697(17)	111.7(19)
N5–H52•••O3[ii]	0.88(3)	2.17(3)	3.0176(19)	161(2)
N4–H4•••O1	0.93(2)	1.74(2)	2.6598(17)	169.3(18)
N4–H4•••O2	0.93(2)	2.41(2)	3.0741(17)	128.5(15)
		7		
N4–H4•••O1[vi]	0.84(4)	2.28(4)	2.952(4)	137(3)
N4–H4•••O2[vii]	0.84(4)	2.51(4)	3.009(4)	119(3)
N4–H4•••O2[v]	0.84(4)	2.29(4)	2.929(3)	133(3)
N5–H52•••O1[iv]	0.77(4)	2.34(4)	3.020(4)	149(3)
N5–H52•••O2[vii]	0.77(4)	2.71(3)	3.152(4)	118(3)
N5–H52•••O2[v]	0.77(4)	2.65(3)	3.216(4)	132(3)
N5–H51•••O4[iii]	0.84(4)	2.07(4)	2.887(4)	162(4)
		8		
N5–H51•••I[viii]	0.77(3)	2.87(3)	3.6381(16)	172(3)
		9		
N5–H51•••O2[ix]	0.84(3)	1.99(3)	2.821(3)	169(2)
N5–H52•••O2[x]	0.86(3)	2.05(3)	2.868(3)	158(3)
N5–H52•••O3[x]	0.86(3)	2.65(3)	3.422(3)	149(3)
		10		
N5–H51•••O4[xi]	0.81(3)	2.13(3)	2.926(2)	171(2)
N5–H52•••O3[xii]	0.82(3)	2.12(3)	2.931(2)	171(3)
		11		
N5–H51•••N6[xiii]	0.909(18)	1.955(19)	2.8429(18)	165.0(18)
		12		
N5–H51•••O4[xv]	0.86(5)	2.03(4)	2.876(4)	165(4)
N5–H52•••N6[xiv]	0.82(5)	2.21(4)	3.004(4)	161(3)
N5–H51•••O4[xiv]	0.86(5)	2.85(5)	3.034(4)	94(4)
		21		
N5–H51•••O1	0.85(3)	2.21(3)	3.014(2)	157(3)
N5–H51•••O2	0.85(3)	2.70(3)	3.448(2)	148(2)
N5–H52•••N01[xvi]	0.93(3)	1.98(3)	2.900(2)	171(3)

[a] Symmetry codes for **6**: (i) -x, -y +2, -z; (ii) x+1/2, -y+3/2, z+1/2. **7**: (iii) x-1, y, z; (iv) -x, -y, -z; (v) -x+1, -y, -z; (vi) x, y, z-1 (vii) x-1, y, z-1. **8**: (viii) -x+1, -y, -z+1. **9**: (ix) -x+3/2, -y, z+1/2; (x) -x+2, y+1/2, -z+3/2. **10**: (xi) -x, -y+1, -z+2; (xii) x+1, y, z. **11**: (xiii) -x+1/2, -y, -z+1/2. **12**: (xiv) x-1/2, -y+3/2, -z; (xv) x, y, z-1. **21**: (xvi) x-1/2, -y+3/2, -z
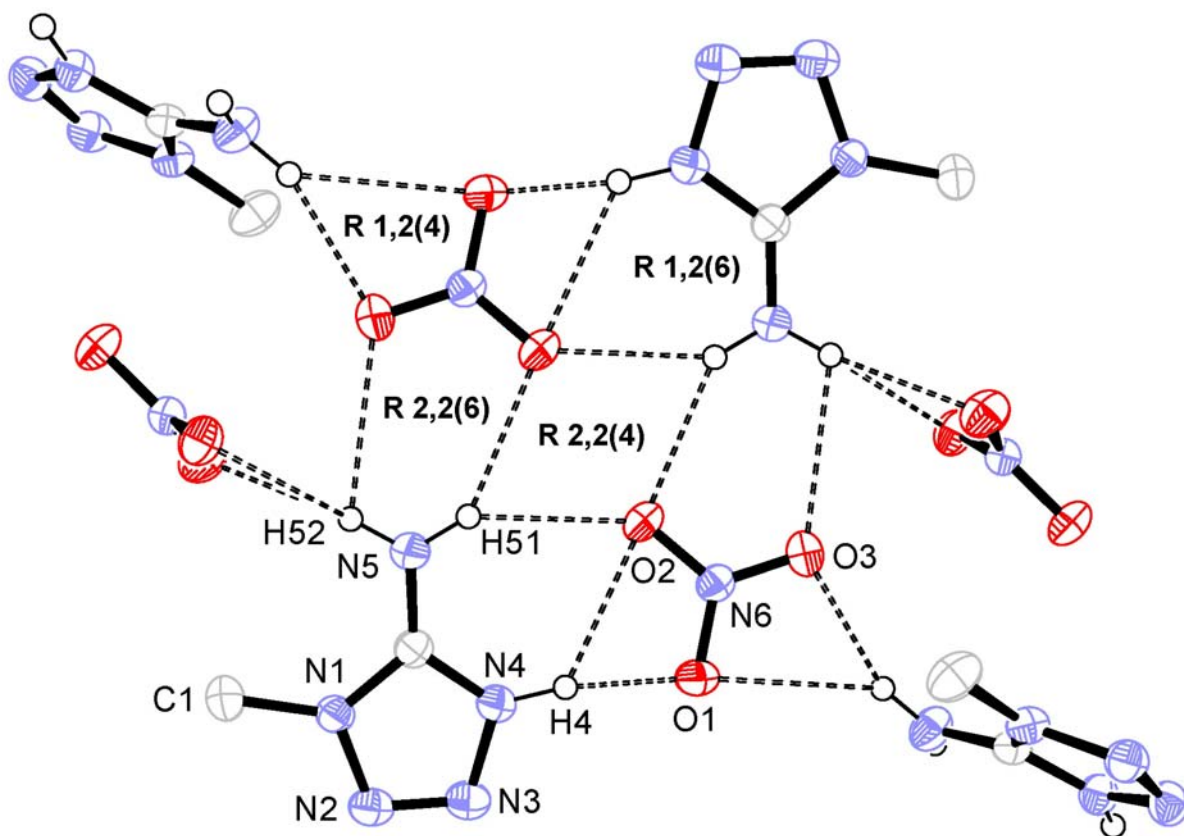
Figure 2.10. Ring hydrogen-bonding graph-sets in 1-methyl-5-aminotetrazolium nitrate (**6**). Methyl-group protons are omitted for clarity.
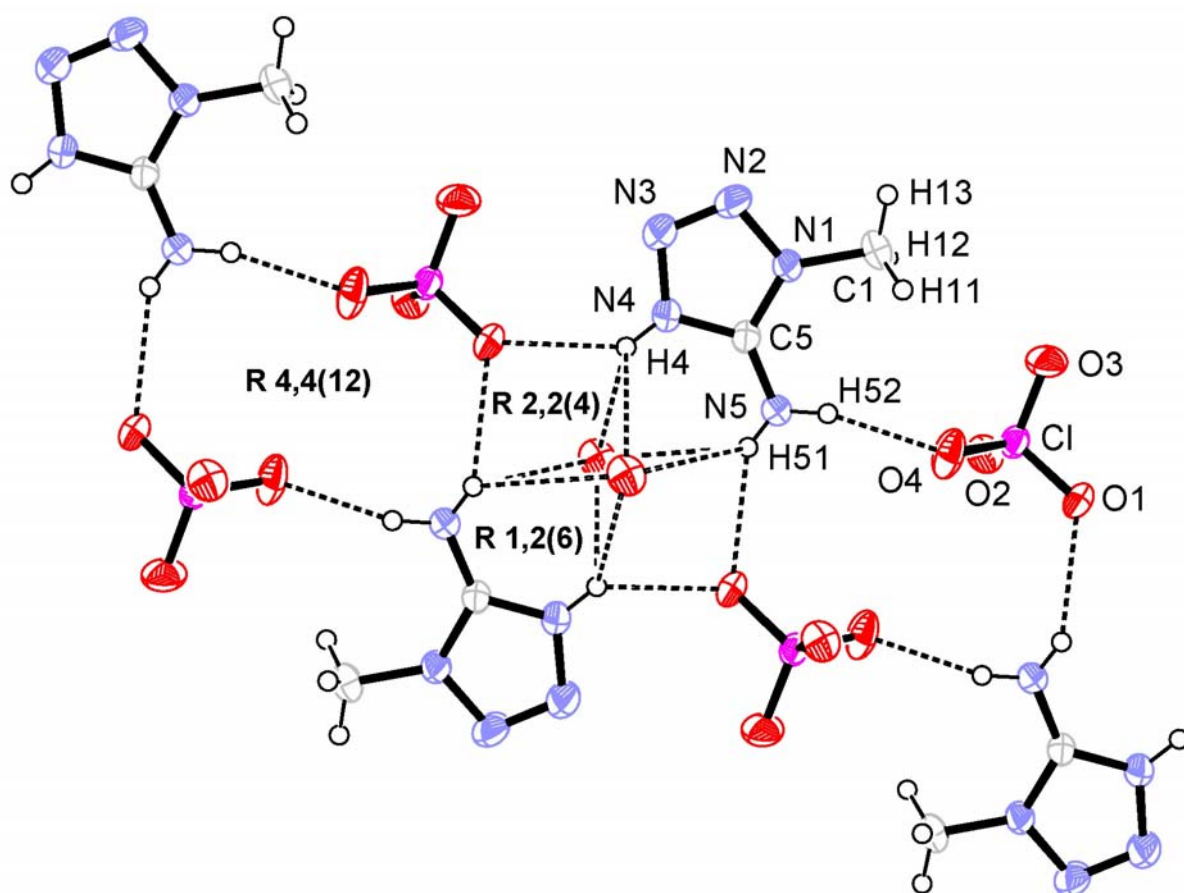
Figure 2.11. Ring hydrogen-bond graph-sets in 1-methyl-5-aminotetrazolium perchlorate (**7**).

As mentioned above, salts of **5** build fewer hydrogen bonds than those of **4**. The most extreme case is that found in **8** and **11** in which a single, crystallographically independent hydrogen bond, N5-H51···N03, is observed. Due to symmetry, this single hydrogen bond links the planar cation-anion pair dimers forming a common R 2,4(8) motif (Figure 2.2 and Figure 2.3). Non-planar dimeric pairs linked in a ring motif (binary R 4,2(12)) are also observed in the structure of **10** as seen in Figure 2.4. In the case of **9**, **12** and **21**, the infinite helices observed are described as chain graph-sets C 1,2(4) (**9** and **12**, Figure 2.12 and Figure 2.13) and C 2,2(7) (**21**, Figure 2.14). The hydrogen bonds composing the helices range in length from short (strong) to medium. Additionally, in all three cases one proton is chelated by the anion resulting in an R 2,1(4) ring motif.
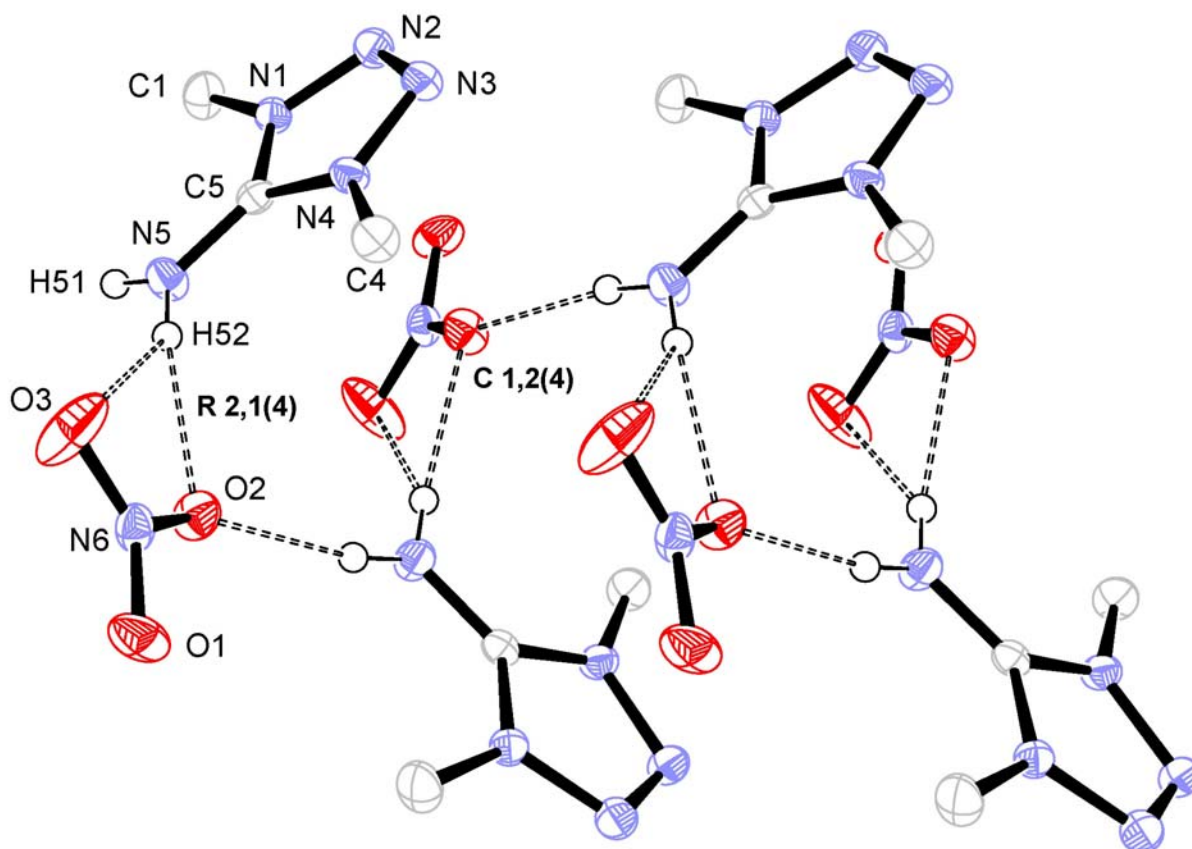
Figure 2.12. Hydrogen-bonding in 1,4 dimethyl-5-aminotetrazolium nitrate (**9**) with atom labels and thermal ellipsoids shown for 50% probability. Methyl-group protons are omitted for clarity.
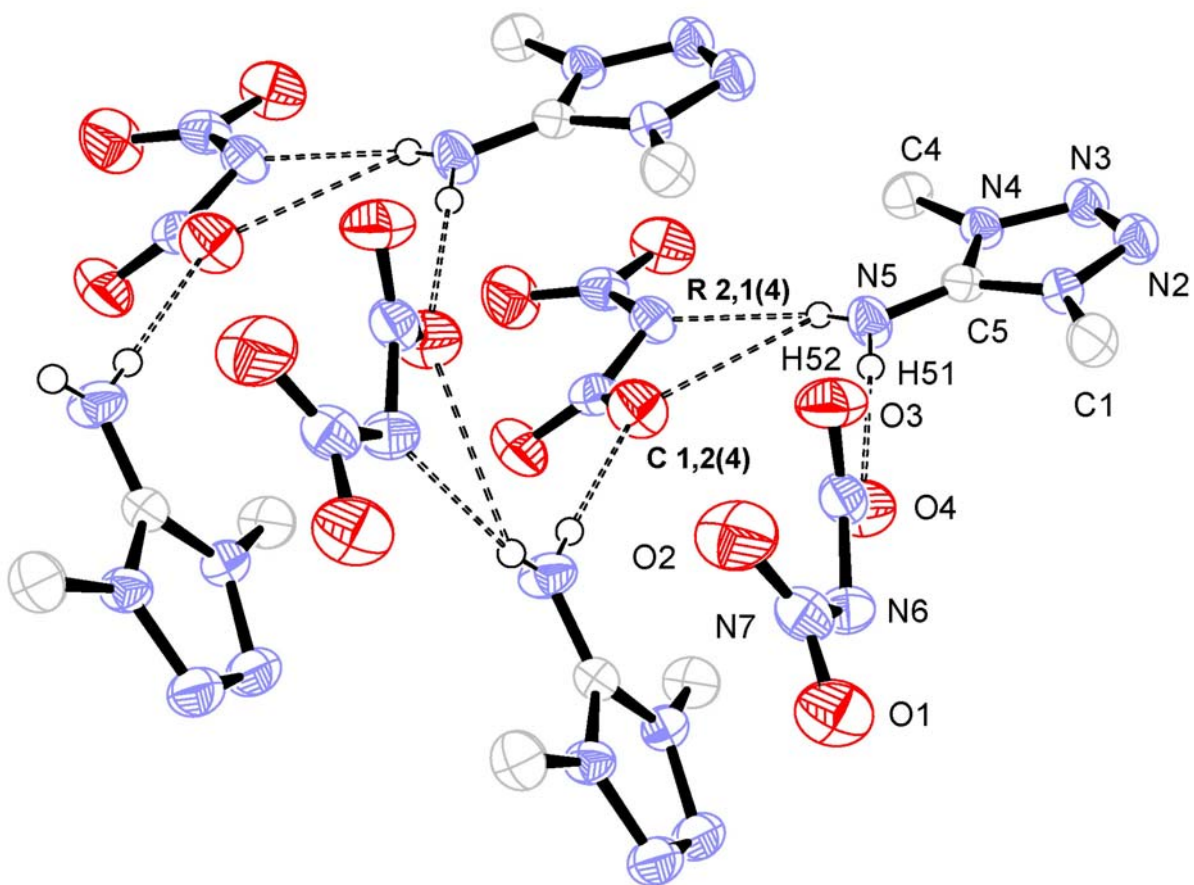
Figure 2.13. Hydrogen-bonding in 1,4 dimethyl-5-aminotetrazolium dinitramide (**12**). Methyl-group protons are omitted for clarity.
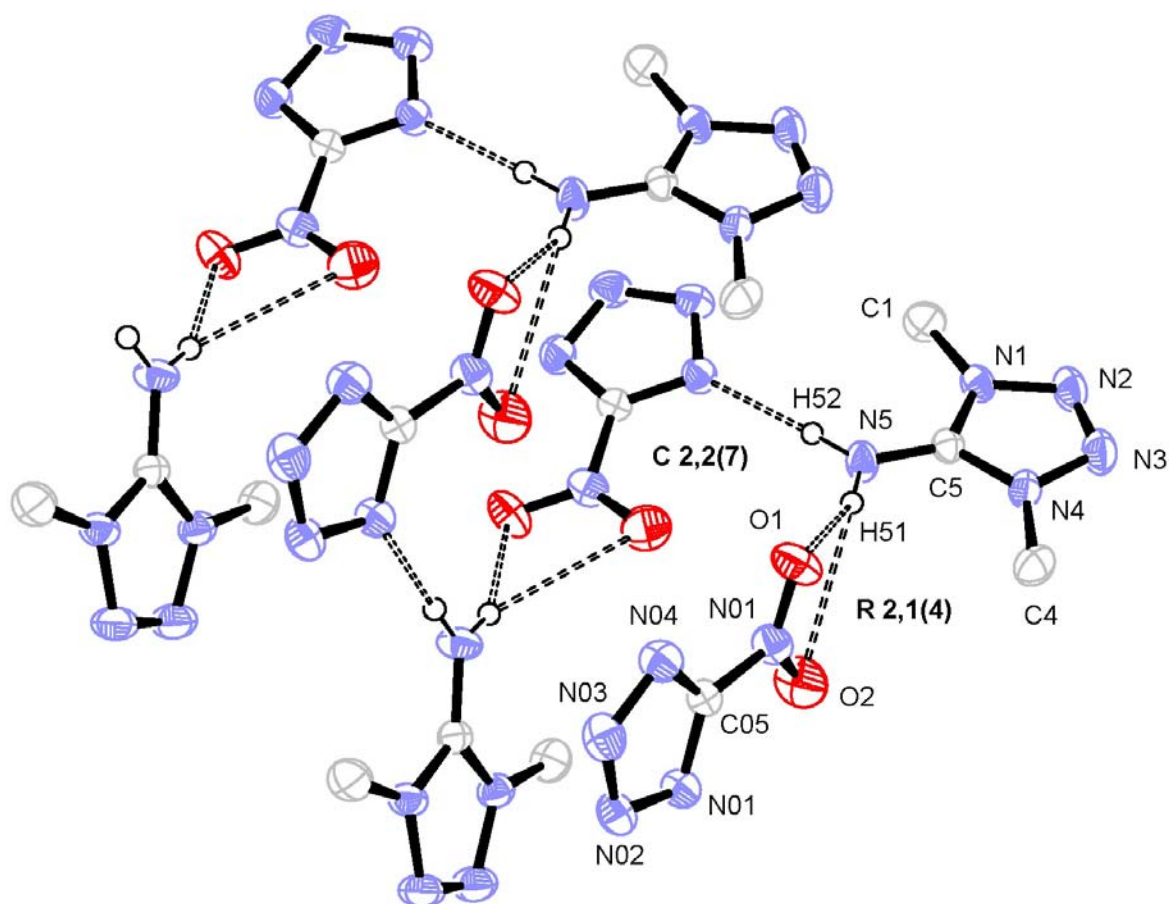
Figure 2.14. Hydrogen-bonding in 1,4 dimethyl-5-aminotetrazolium 5-nitrotetrazolate (**21**). Methyl-group protons are omitted for clarity.

Interionic hydrogen bonding is also present in the structures of salts **13 - 20** and seems to contribute highly to the stability and density of these salts. Although compounds **15** and **20** are reasonably sensitive to friction and impact (Table 2.27), they are both much less sensitive than the heavy metal salts of HNT (used as primary explosives) and considerably less sensitive than the alkali and alkaline earth metal salts and their hydrates.[60] Additionally, although the densities of **13 - 20** (~1.6 - 1.7 g/cm^3) are not optimal (1.8 - 2.0 g/cm^3) for energetic materials, they are still reasonably high for salts composed of bulky organic cations and anions. In light of these points, once again, a detailed description and discussion of the hydrogen-bonding and packing in **13 - 20**, facilitated by graph-set analysis may provide explanations for some of the phenomena observed.

Compound **14** crystallizes as described in Table 2.5 with planar layers of NT anions parallel to the crystallographic b-axis. Within the layers, the anions are joined to the tetrahedral ammonium cations (H1, H2 and H3 are also situated in the plane) by three strong hydrogen bonds (N6–H1•••N1[i], N6–H2•••N4[ii] and N6–H3•••N3[iii] [symmetry codes: (i) x, -y+1/2, z+1/2, (ii) -x+2, -y, -z+1, (iii) x-1, y, z+1]). The layers of NT anions are joined by three weaker hydrogen bonds all involving H4 (N6–H4•••N2[iv], N6–H4•••O2[v] and N6–H4•••O1 [symmetry codes: (iv) x-1, -y+1/2, z+1/2, (v) -x+1, -y, -z+1]). The view normal to one layer is shown in Figure 2.15 and the hydrogen bonding geometry for **14** can be found in Table 2.9. Table 2.10 shows a complete graph-set matrix describing the unitary and binary hydrogen bonding patterns formed by the 6 crystallographically independent hydrogen bonds in **14**. The most prominent patterns within the layer shown are also labeled in Figure 2.15. Such patterns include (at the binary level) chains described as C 2,2(6) and C 2,1(6) as well as two ring patterns, R 4,4(10) and R 4,2(8). Hydrogen bonds linking the layers form, in combination with those within the layers, a variety of binary chain patterns with the form C 2,2(X), where X is 5, 6 or 7 and larger binary ring patterns (R 4,4(14) and R 4,4(16)).

Table 2.9. Hydrogen-bonding geometry in **14**.

D–H•••A[a]	D–H (Å)	H•••A (Å)	D•••A (Å)	D–H•••A (°)
N6–H1•••N1[i]	0.898(18)	2.028(18)	2.9025(16)	164.2(13)
N6–H2•••N4[ii]	0.87(2)	2.09(2)	2.9516(17)	171.5(17)
N6–H3•••N3[iii]	0.86(2)	2.10(2)	2.9486(18)	172.6(16)
N6–H4•••N2[iv]	0.820(19)	2.389(17)	2.9892(16)	130.7(14)
N6–H4•••O2[v]	0.820(19)	2.550(16)	3.0184(16)	117.6(14)
N6–H4•••O1	0.820(19)	2.591(19)	3.1050(17)	122.0(15)

[a] Symmetry codes for **14**: (i) x, -y+1/2, z+1/2, (ii) -x+2, -y, -z+1, (iii) x-1, y, z+1, (iv) x-1, -y+1/2, z+1/2, (v) -x+1, -y, -z+1.

Table 2.10. Unitary and binary hydrogen bond pattern graph-set matrix for **14**.[a]

	N6–H1•••N1[i]	N6–H2•••N4[ii]	N6–H3•••N3[iii]	N6–H4•••N2[iv]	N6–H4•••O2[v]	N6–H4•••O1
N6–H1•••N1[i]	D 1,1(2)					
N6–H2•••N4[ii]	C 2,2(6)	D 1,1(2)				
N6–H3•••N3[iii]	C 2,2(6)	R 4,4(10)	D 1,1(2)			
N6–H4•••N2[iv]	C 2,2(5)	C 2,2(6)	C 2,2(5)	D 1,1(2)		
N6–H4•••O2[v]	C 2,2(7)	R 4,4(14)	C 2,2(8)	C 2,1(6)	D 1,1(2)	
N6–H4•••O1	C 2,2(7)	C 2,2(7)	R 4,4(16)	C 2,1(6)	R 4,2(8)	D 1,1(2)

^{a} Symmetry codes: (i) x, -y+1/2, z+1/2, (ii) -x+2, -y, -z+1, (iii) x-1, y, z+1, (iv) x-1, -y+1/2, z+1/2, (v) -x+1, -y, -z+1.
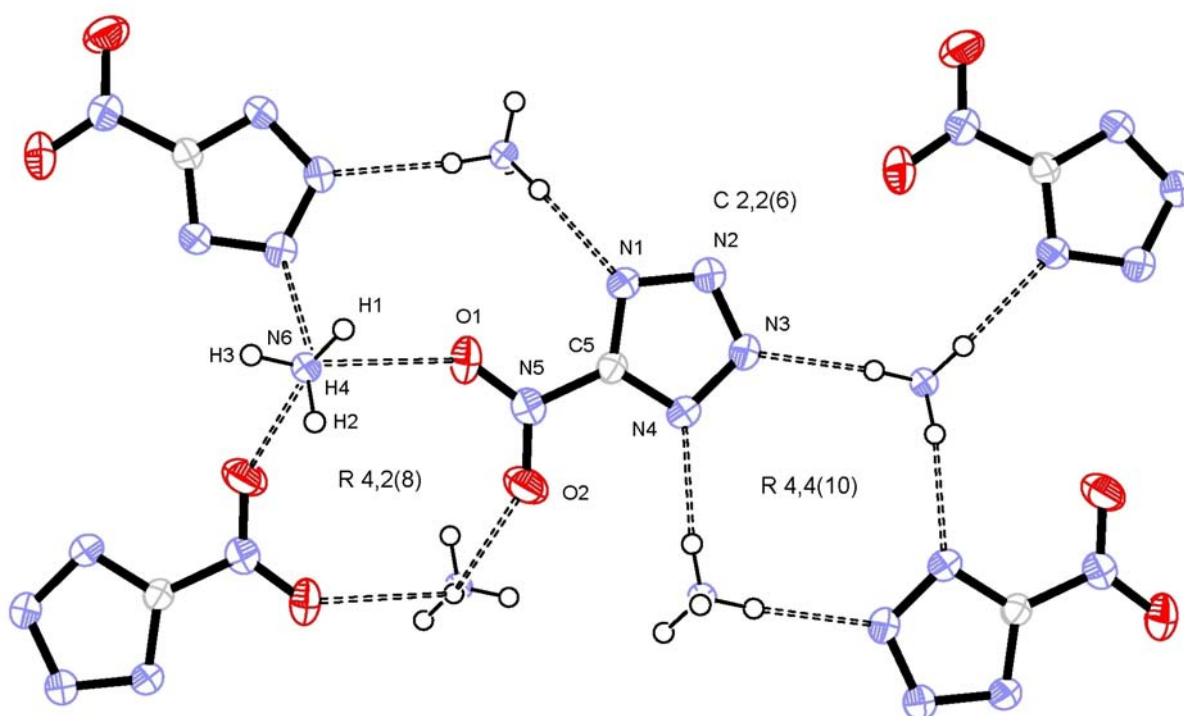
Figure 2.15. View normal to one layer of NT anions in **14**, including atom labels for relevant atoms, graph-set descriptors and thermal ellipsoids showing 50% probability.

As opposed to anhydrous **14**, the hydrate **13** crystallizes in the higher symmetry monoclinic space group *C*/2*c* with 0.5 water molecules in the asymmetric unit. Although the packing of the cations, anions and crystal water in **13** maintains several of the features described for **14**, the packing of **13** is considerably more complex. The most prominent feature of the packing are "stacks" of NT anions arranged such that planes defined by the tetrazole rings are parallel

to one another but the orientation of the nitro group alternates by ~180° between neighboring anions within the stack. The NT anions in the stacks are surrounded by three ammonium cations and one water molecule as opposed to four ammonium cations in **14**. The stacks are thus connected to one another through hydrogen bonding to water and ammonium cations. However, the planes of tetrazole rings in neighboring stacks of NT anions are rotated ~70° from each other, such that the stacks are not parallel to one another. A representation of the orientation of the NT anions in the unit cell of **13** is shown in Figure 2.16.
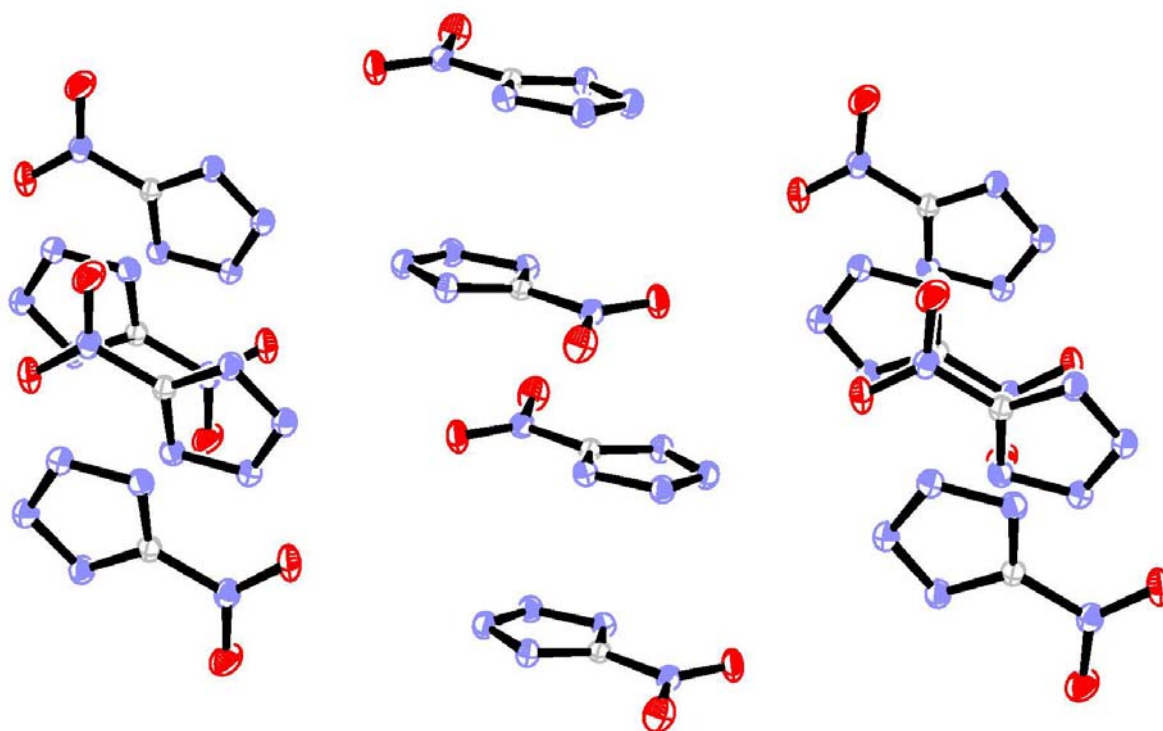
Figure 2.16. Packing of NT anions in the unit cell of **13**.

As in **14**, a strong, directional, three dimensional hydrogen bonding network is the defining element of the crystallographic packing in **13**. Although fewer hydrogen bonds are observed in **13** due to increased symmetry, the interactions observed are slightly stronger than those in **14**, as can be seen in Table 2.11. A sixth, weak interaction (N6–H4•••O2[i] [symmetry code: (i) 1/2-x, 1/2-y, 1-z],) is present in the structure, but is neglected due to the relatively long H4•••O2[i] distance (2.64(2) Å) and relatively low N6–H4•••O2[i] angle (107(2)°). The hydrogen bond patterns observed for **13** are similar to those observed for **14** although, due to symmetry,

D 2,2(X) type patterns, where X = 4 or 5, are prevalent as opposed to the C 2,2(X) chains observed in **14**. At the first level, two prominent dimer interactions (D 1,2(3) and D 2,2(5)) occur across the water molecule, which lies on a special position in the structure. C 2,2(5) and C 2,2(6) chain patterns are also observed in **13** and the ring pattern R 4,4(10) is also present in **13** in exactly the same configuration as it is found in **14** (N3 and N4 of one NT anion linked to N4 and N3, respectively, of a second NT anion over two ammonium cations, see Figure 2.15 and Figure 2.17). A full graph-set matrix for the hydrogen bonding in **13** can be found in Table 2.12.

Table 2.11. Hydrogen-bonding geometry in **13**.

D–H•••A[a]	D–H (Å)	H•••A (Å)	D•••A (Å)	D–H•••A (°)
N6–H1•••N3[vi]	0.940(18)	2.073(19)	3.0051(17)	171.0(15)
N6–H2•••N2	0.91(2)	2.09(2)	2.9704(17)	162.6(17)
N6–H3•••N4[vii]	0.89(2)	2.11(2)	2.9919(17)	175.6(16)
N6–H4•••O3[viii]	0.88(2)	2.03(2)	2.8867(15)	163.8(16)
O3–H5•••N1	0.87(2)	2.04(2)	2.8745(15)	158.8(17)

[a] Symmetry codes for **13**: (vi) -x+1/2, y+1/2, -z+1/2, (vii) x, -y, z-1/2, (viii) x+1/2, y-1/2, z.

Table 2.12. Unitary and binary hydrogen bond pattern graph-set matrix for **13**.[a]

	O3–H5•••N1	N6–H4•••O3[viii]	N6–H1•••N3[vi]	N6–H3•••N4[vii]	N6–H2•••N2
O3–H5•••N1	D 2,2(5)				
N6–H4•••O3[viii]	D 2,2(4)	D 1,2(3)			
N6–H1•••N3[vi]	D 2,2(5)	D 2,2(5)	D 1,1(2)		
N6–H3•••N4[vii]	D 2,2(5)	D 2,2(5)	R 4,4(10)	D 1,1(2)	
N6–H2•••N2	D 2,2(4)	D 2,2(5)	C 2,2(5)	C 2,2(6)	D 1,1(2)

[a] Symmetry codes: (vi) -x+1/2, y+1/2, -z+1/2, (vii) x, -y, z-1/2, (viii) x+1/2, y-1/2, z.

Figure 2.17. Hydrogen bonding in **13** including atom labels for relevant atoms, graph-set descriptors and thermal ellipsoids showing 50% probability.

The crystal packing of **15** is also defined by "stacks" of NT anions arranged within the stacks as described for **13**. However, in the case of **15**, the stacks formed are all parallel to the crystallographic c-axis as well as to the hydrogen bonded (C 1,1(3) motif) chains of hydrazinium cations, which serve to connect (also by strong hydrogen bonding) the stacks of NT anions. The geometric parameters for the seven strong and medium strength hydrogen bonds observed are tabulated in Table 2.13. In addition, three weaker contacts are also observed but are, for the same reasons discussed for **13**, as well as simplicity and clarity omitted from further discussion. As seen in Figure 2.18, the hydrogen bonding network of **15** is composed of a variety of ring, chain and dimer graph-sets. As in **14** and **13** multiple binary C 2,2(X) (X = 6 – 8 for **15**) patterns are observed. Also similar to **13** are the presence, at the second level, of multiple dimer patterns by combination of the aforementioned unitary C 1,1(3) motif with other hydrogen bonds. Lastly, and most characteristic are the R 2,1(5) ring

showing chelation of H61 by an NT anion, the R 2,2(8) ring formed by the hydrazinium

cation generated by symmetry operation 1+x, y, z (H donors) and O1 and N1 (H acceptors)

and the R 4,4(12) ring shown in Figure 2.18. A full graph-set matrix for **15** is provided in

Table 2.14.

Table 2.13. Hydrogen-bonding geometry in **15**.

D–H•••A[a]	D–H (Å)	H•••A (Å)	D•••A (Å)	D–H•••A (º)
N6–H61•••N4	0.888(18)	2.406(18)	3.1046(18)	135.7(14)
N6–H61•••O2	0.888(18)	2.481(18)	3.3035(17)	154.1(15)
N6–H62•••N2[ix]	0.952(19)	2.229(19)	3.1343(17)	158.7(13)
N6–H62•••O1[x]	0.952(19)	2.644(15)	3.2223(18)	119.6(12)
N7–H71•••N6[xi]	0.95(2)	1.98(2)	2.9291(19)	175.4(18)
N7–H72•••N1[x]	0.967(19)	1.943(19)	2.9058(17)	173.4(16)
N7–H73•••N3[xii]	0.913(19)	2.089(19)	2.9420(17)	155.0(15)

[a] Symmetry codes for **15**: (ix) -x+1, y+1/2, -z+1/2, (x) x-1, y, z, (xi) x, -y+1/2, z-1/2, (xii) -x+1, -y, -z+1.

Table 2.14. Unitary and binary hydrogen bond pattern graph-set matrix for **15**.[a]

	N6–H61•••O2	N6–H61•••N4	N6–H62•••N2[ix]	N7–H71•••N6[xi]	N7–H72•••N1[x]	N7–H73•••N3[xii]	N6–H62•••O1[x]
N6–H61•••O2	D 1,1(2)						
N6–H61•••N4	R 2,1(5)	D 1,1(2)					
N6–H62•••N2[ix]	C 2,2(8)	C 2,2(6)	D 1,1(2)				
N7–H71•••N6[xi]	D 3,3(8)	D 3,3(8)	D 3,3(8)	C 1,1(3)			
N7–H72•••N1[x]	C 2,2(8)	C 2,2(7)	C 2,2(6)	D 3,3(8)	D 1,1(2)		
N7–H73•••N3[xii]	R 4,4(18)	R 4,4(12)	C 2,2(6)	D 3,3(8)	R 4,4(12)	D 1,1(2)	
N6–H62•••O1[x]	C 2,2(6)	C 2,2(7)	C 2,1(6)	D 3,3(8)	R 2,2(8)	R 4,4(18)	D 1,1(2)

[a] Symmetry codes: (ix) -x+1, y+1/2, -z+1/2, (x) x-1, y, z, (xi) x, -y+1/2, z-1/2, (xii) -x+1, -y, -z+1.

Figure 2.18. Hydrogen bonding in **15** including atom labels for relevant atoms, graph-set descriptors and thermal ellipsoids showing 50% probability.

The simplest packing in this study is found in the planar layer structure of **16**. The layers formed lie in the crystallographic b-c plane and with anion orientation alternating by 180º from layer to layer. Only four hydrogen bonds are present, due to symmetry, which connect the cations and anions within the layers (Table 2.15). Between layers only weak van der Waals interactions predominate. The layered nature of the structure and the hydrogen bonding patterns in the structure of **16** bear a strong but not wholly unexpected similarity to those found in guanidinium nitrate.[43, 44] The hydrogen bonding network in **16** is shown in Figure 2.19 and, at the unitary level, is composed of two C 2,2(8) motifs and two R 2,2(X) motifs, where X = 6 and 7. At the binary level, a variety of further C 2,2 (X) patterns (X = 5, 8, 9 and 10), a C 1,2(6) pattern and the same chelating R 2,1(5) pattern as found in **15** as part

of an extended C 2,2(9)[R 2,1(5)] pattern are observed. A full graph-set matrix for **16** is shown in Table 2.16.

Table 2.15. Hydrogen-bonding geometry in **16**.

D–H•••A^a	D–H (Å)	H•••A (Å)	D•••A (Å)	D–H•••A (°)
N3–H3•••N2^{xiii}	0.874(19)	2.154(19)	3.0203(13)	171.1(14)
N3–H2•••N1	0.895(19)	2.23(2)	3.1221(14)	176.6(17)
N3–H2•••O1	0.895(19)	2.448(18)	2.8963(13)	111.3(15)
N4–H1•••O1^{xiv}	0.848(19)	2.43(2)	3.0132(17)	126.2(17)

^{a} Symmetry codes for **16**: (xiii) -x+1/2, y+1/2, -z+3/2, (xiv) x-1/2, y-1/2, z.

Table 2.16. Unitary and binary hydrogen bond pattern graph-set matrix for **16**.^{a}

	N3–H2•••O1	N4–H1•••O1^{xiv}	N3–H3•••N2^{xiii}	N3–H2•••N1
N3–H2•••O1	C 2,2(8)			
N4–H1•••O1^{xiv}	C 1,2(6)	R 2,2(6)		
N3–H3•••N2^{xiii}	C 2,2(8)	C 2,2(10)	R 2,2(7)	
N3–H2•••N1	C 2,2(9)[R 2,1(5)]	C 2,2(9)	C 2,2(5)	C 2,2(8)

^{a} Symmetry codes: (xiii) -x+1/2, y+1/2, -z+3/2, (xiv) x-1/2, y-1/2, z.
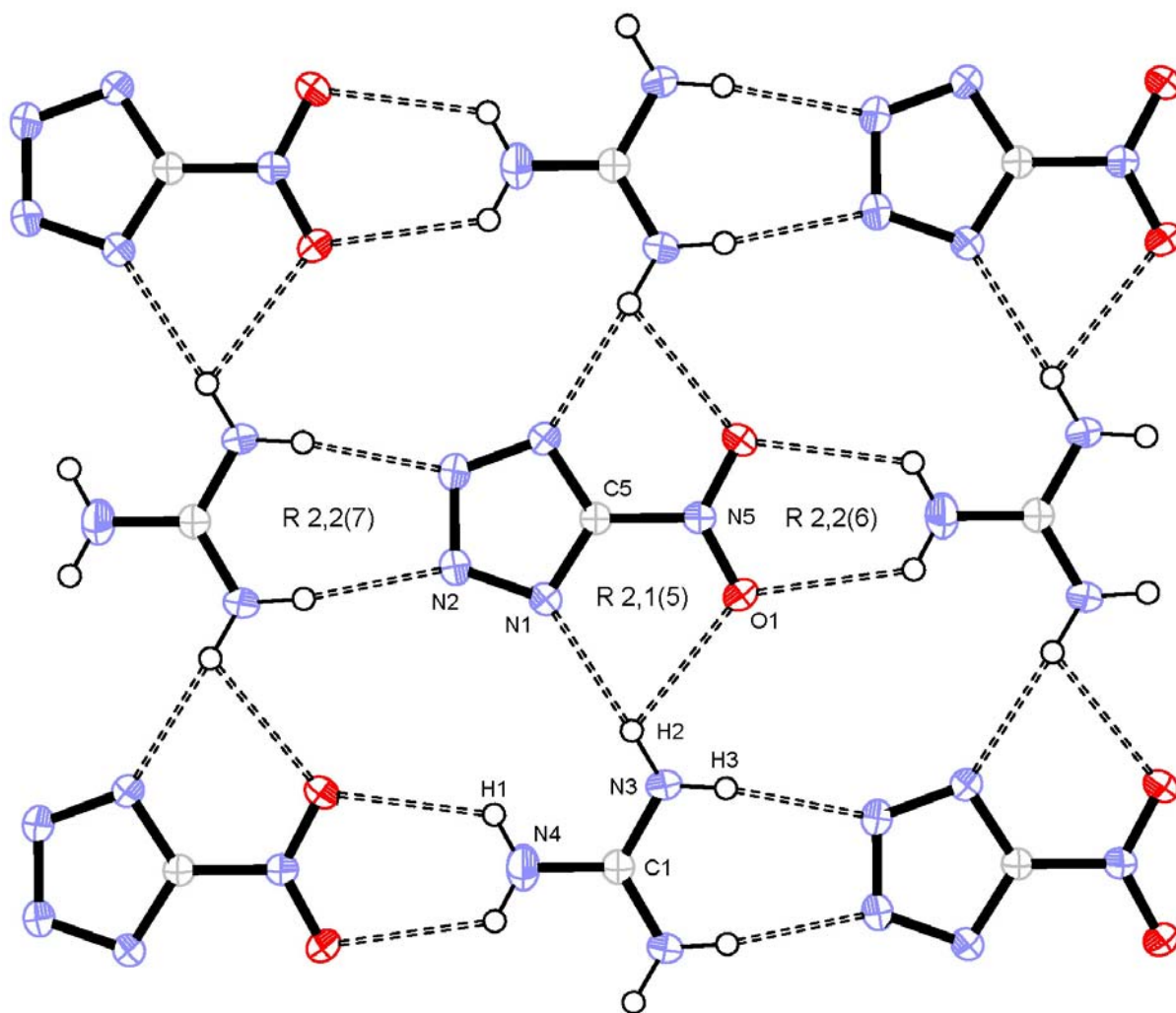
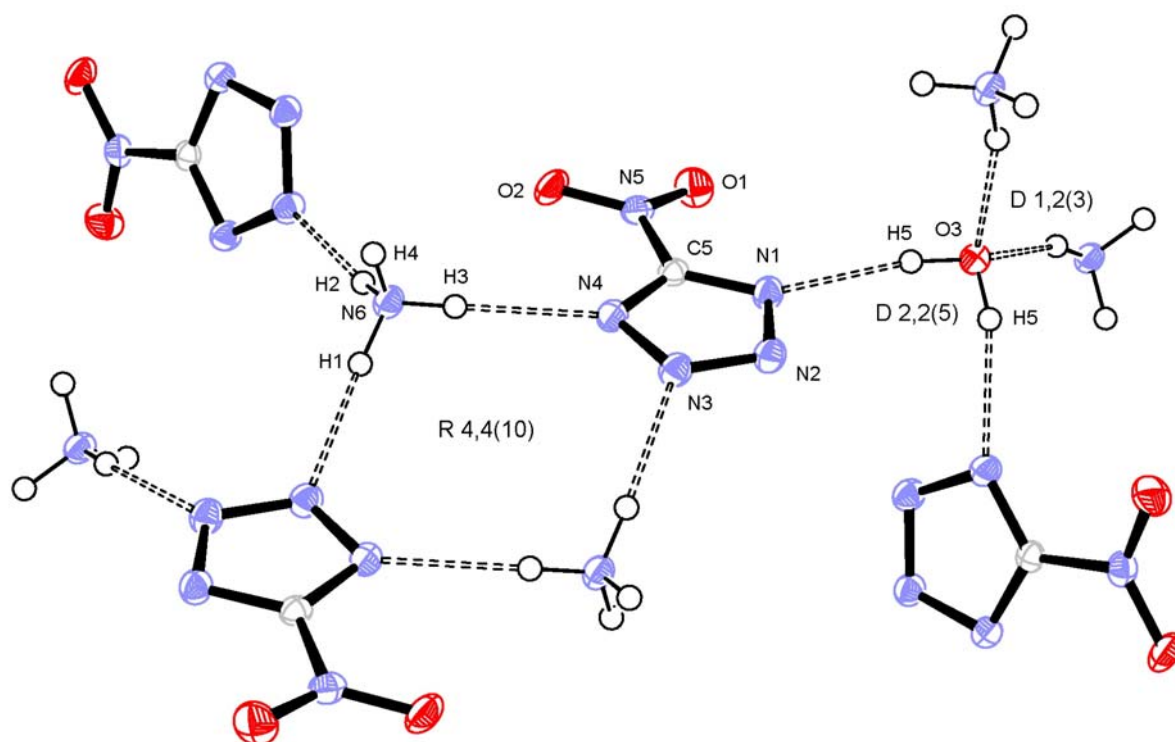**Figure 2.19.** View normal to the b-c plane of a single layer of **16**, including atom labels for relevant atoms, graph-set descriptors and thermal ellipsoids showing 50% probability.

Compound **17** exhibits complex packing, composed of neither layers nor stacks, in which each cation hydrogen bonds to six anions and vice versa. The cations and anions are either roughly parallel to or rotated ~50° out-of-plane from one another (see Figure 2.20 for packing details). Seven strong crystallographically independent hydrogen bonds between the guanidinium and NT moieties (including the intramolecular hydrogen bond found in the aminoguanidinium cation) and 2 additional weaker contacts are found between neighboring cations and O1 of the NT anion (Table 2.17). The weaker contacts are included here because they appear to be significant in fixing the orientation of the nitro-group, which may explain the aforementioned ~10° out-of-tetrazole-ring-plane twist of the nitro group from the plane of

56

the tetrazole ring in the anion in **17**. Hydrogen bonding surrounding the cation and anion is shown in Figure 2.21. The structure of **17** exhibits many binary hydrogen bonded chain patterns of the familiar C 2,2(X) type (X = 6 – 11). Smaller binary ring patterns such as R 2,2(7) and R 2,2(9) are shown in Figure 8 and larger ring patterns involving both 2 and 4 donor - acceptor systems incorporating up to 16 atoms are also observed. A full graph-set matrix summarizing the unitary and binary hydrogen bonding patterns observed in **17** can be found in Table 2.18.

Table 2.17. Hydrogen-bonding geometry in **17**.

D–H•••A[a]	D–H (Å)	H•••A (Å)	D•••A (Å)	D–H•••A (°)
N6–H61•••N2[xv]	0.852(18)	2.307(17)	3.0103(16)	140.0(16)
N6–H61•••O1[xvi]	0.852(18)	2.567(18)	3.1343(18)	125.0(14)
N7–H71•••O1[xvii]	0.857(17)	2.397(17)	3.1665(16)	149.7(15)
N9–H91•••N3[xviii]	0.870(18)	2.382(18)	3.2433(18)	170.3(15)
N9–H92•••O1[xix]	0.918(18)	2.501(19)	3.3035(16)	146.2(15)
N6–H62•••N3[xxi]	0.84(2)	2.35(2)	3.185(2)	170.6(17)
N8–H8•••N4[xxi]	0.826(18)	2.166(19)	2.9635(17)	162.3(16)
N7–H72•••N1[xvi]	0.887(19)	2.075(19)	2.9615(17)	179.0(16)
N7–H71•••N9	0.857(17)	2.288(17)	2.6602(17)	106.4(13)

[a] Symmetry codes for **17**: (xv) x, y-1, z, (xvi) -x+1/2, y-1/2, -z+3/2, (xvii) -x+1/2, y+1/2, -z+3/2 (xviii) -x, -y+1, -z+1, (xix) x+1/2, -y+1/2, z-1/2, (xx) -x+1, -y, -z+1, (xxi) -x, -y, -z+1.

Table 2.18. Unitary and binary hydrogen bond pattern graph-set matrix for **17** excluding intraionic hydrogen bonds.[a]

		a	b	c	d	e	f	g	h
N6–H61•••N2[xv]	a	D 1,1(2)							
N9–H91•••N3[xviii]	b	R 4,4(16)	D 1,1(2)						
N6–H62•••N3[xxi]	c	R 4,4(10)	C 1,2(7)	D 1,1(2)					
N8–H8•••N4[xxi]	d	R 4,4(16)	C 2,2(6)	R 2,2(7)	D 1,1(2)				
N7–H72•••N1[xvi]	e	C 2,2(7)	C 2,2(9)	C 2,2(8)	C 2,2(8)	D 1,1(2)			
N6–H61•••O1[xvi]	f	C 2,1(6)	C 2,2(11)	C 2,2(8)	C 2,2(9)	R 2,2(9)	D 1,1(2)		
N7–H71•••O1[xvii]	g	C 2,2(10)	C 2,2(11)	C 2,2(10)	C 2,2(9)	C 2,2(7)	C 1,2(6)	D 1,1(2)	
N9–H92•••O1[xix]	h	C 2,2(11)	C 2,2(8)	C 2,2(11)	C 2,2(8)	R 4,4(20)	R 2,4(14)	R 2,4(14)	D 1,1(2)

[a] Symmetry codes: (xv) x, y-1, z, (xvi) -x+1/2, y-1/2, -z+3/2, (xvii) -x+1/2, y+1/2, -z+3/2 (xviii) -x, -y+1, -z+1, (xix) x+1/2, -y+1/2, z-1/2, (xx) -x+1, -y, -z+1, (xxi) -x, -y, -z+1.
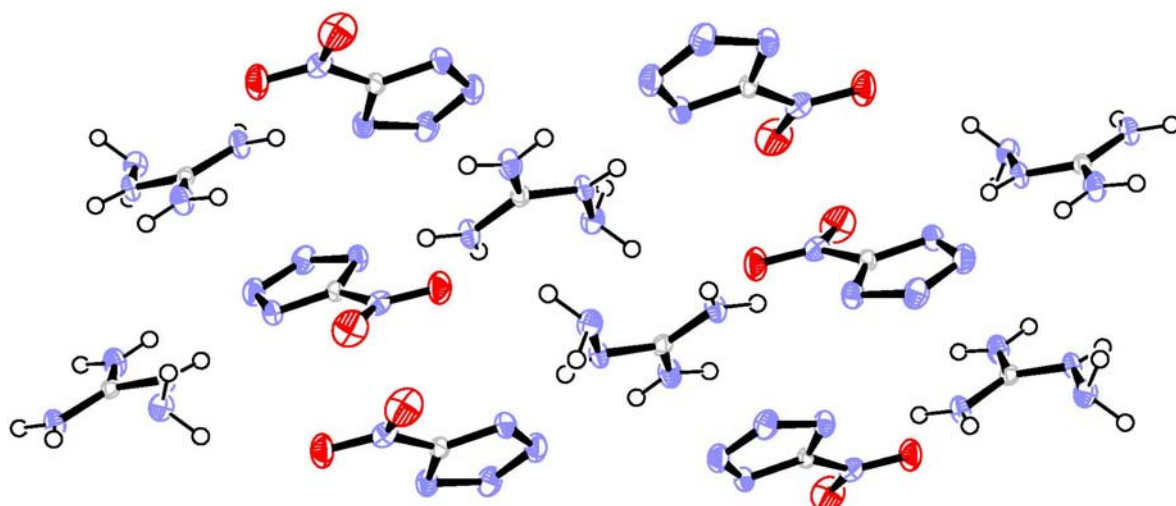
Figure 2.20. View of the packing in the unit cell of **17** along the crystallographic b-axis.
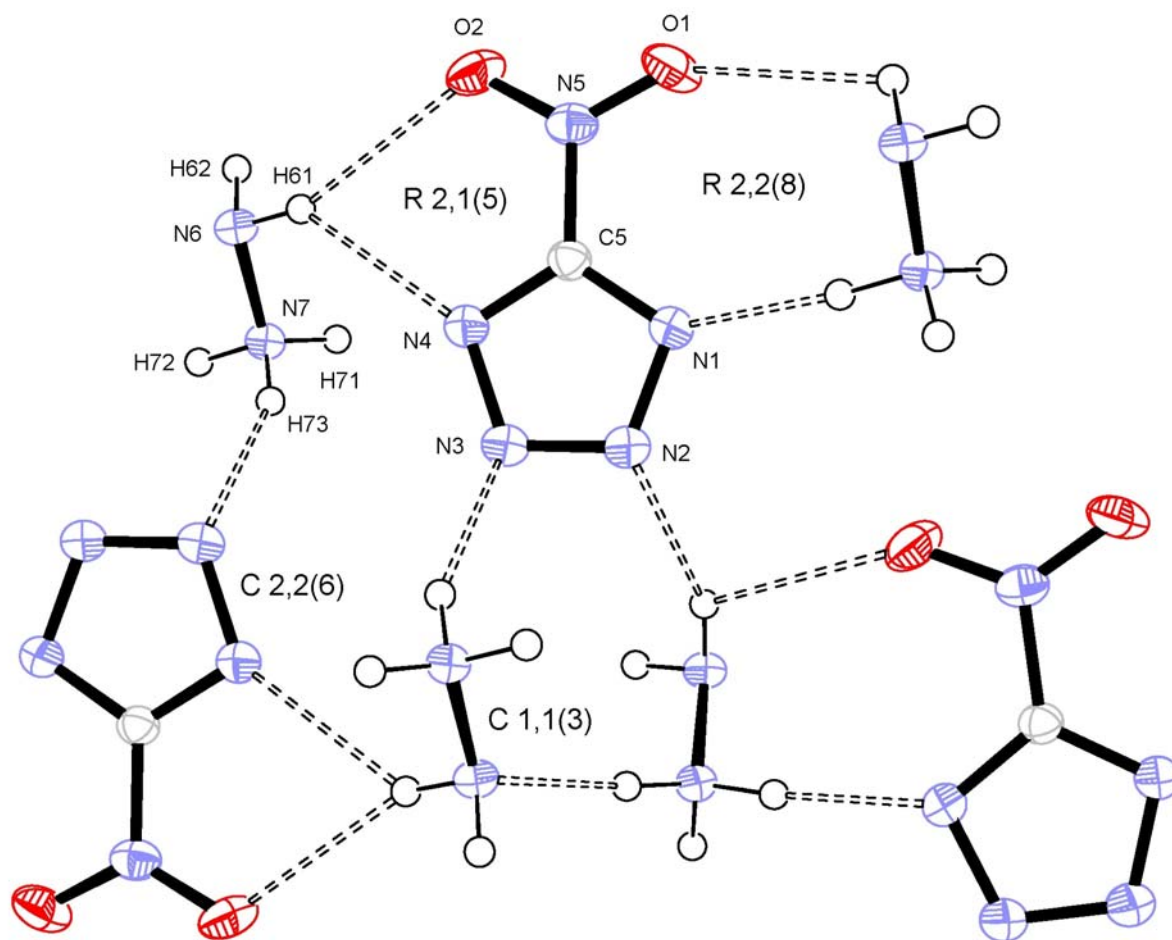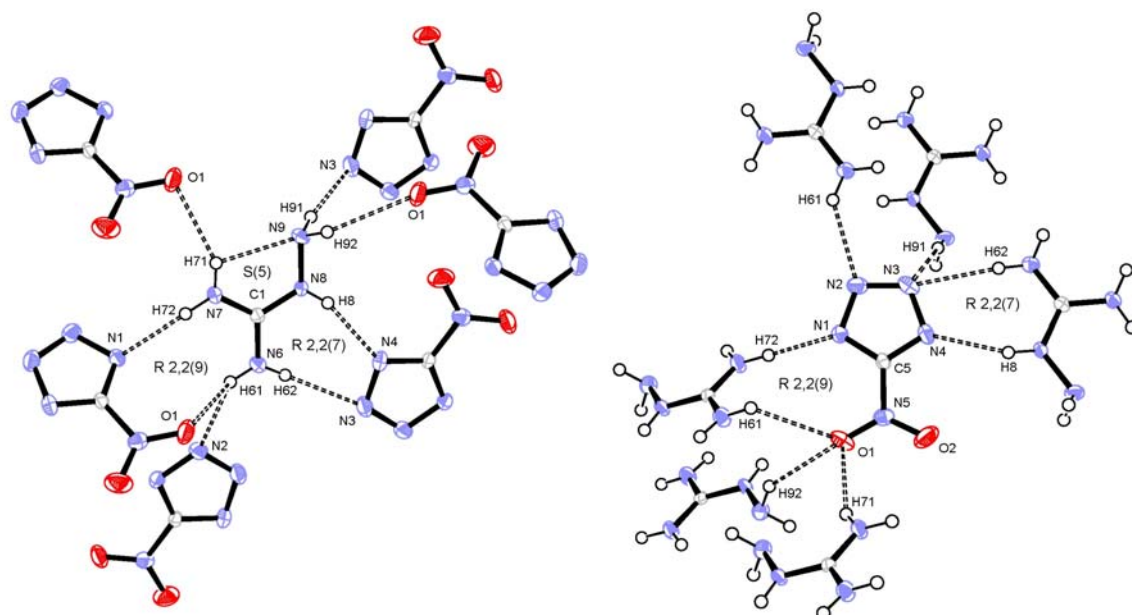

Figure 2.21. Hydrogen bonding around the cation (left) and anion (right) of **17**, including atom labels for relevant atoms, graph-set descriptors and thermal ellipsoids showing 50% probability.

18 crystallizes in the non-centrosymmetric space group $P2_1$ with 2 formula units per asymmetric unit (two cations and two anions). The two crystallographically independent cations are nearly parallel to one another and lie in the plane normal to the crystallographic b-axis. The planes of the tetrazole rings of the two anions are not parallel (twisted from each

other by ~24 °) and lie approximately in the plane normal to the crystallographic a-axis.

Therefore, the packing can be roughly described as being composed of perpendicular cations

and anions. As in the structures of **13 – 17**, hydrogen bonding is the dominant feature of the

packing in **18**. However, due to the complexity and sheer number of crystallographically

inequivalent hydrogen bonds (>17 depending on tolerances) a complete analysis of the

hydrogen bonding network in **18** is not undertaken here. Also of importance is that with a

doubled asymmetric unit, many characteristic graph-set patterns for **18** may not appear until

fourth level (combinations of 4 independent hydrogen bonds). Analysis beyond the binary

level is not possible with *RPLUTO* (up to 20 bonds) and a third or fourth level analysis of a

17 bond network by hand would be a very involved undertaking. Therefore, a full graph-set

matrix has also not been generated, although a table of the 17 strongest intra- and interionic

hydrogen bonds is provided in Table 2.19.

Table 2.19. Hydrogen-bonding geometry in **18**.

D–H•••A[a]	D–H (Å)	H•••A (Å)	D•••A (Å)	D–H•••A (°)
N8A–H8A•••N9A	0.79(5)	2.31(5)	2.648(5)	107(4)
N8B–H8B•••N9B	0.90(5)	2.28(4)	2.637(5)	103(3)
N7A–H72A•••N10A	0.86(5)	2.31(5)	2.680(5)	106(4)
N7B–H72B•••N10B	0.84(5)	2.32(5)	2.711(5)	109(4)
N6A–H6A•••N3A	0.79(4)	2.29(5)	2.925(5)	138(5)
N6B–H6B•••N1B	0.84(4)	2.57(5)	3.257(5)	139(4)
N8B–H8B•••N4A	0.90(5)	2.22(5)	2.987(5)	142(4)
N7B–H71B•••N1B	0.81(5)	2.22(5)	2.986(5)	158(5)
N10A–H11A•••O1B	0.87(5)	2.43(5)	3.079(5)	132(4)
N6B–H6B•••N3B[xxii]	0.84(4)	2.38(5)	2.971(5)	128(4)
N8A–H8A•••N4B[xxii]	0.79(5)	2.37(5)	3.035(5)	143(5)
N7A–H71A•••N1A[xxiii]	0.84(5)	2.14(5)	2.972(5)	173(5)
N7A–H72A•••O2B[xxiv]	0.86(5)	2.49(5)	3.251(5)	147(4)
N9B–H91B•••N10B[xxv]	0.85(5)	2.64(5)	3.056(5)	111(4)
N9A–H92A•••O2A[xxvi]	0.82(5)	2.41(5)	3.045(5)	136(4)
N10B–H11B•••N2A[xxvii]	0.91(5)	2.17(5)	3.065(6)	171(4)
N10A–H12A•••N2B[xxvi]	0.84(5)	2.25(5)	3.094(5)	177(5)

[a] Symmetry codes for **18**: (xxii) -x-1, y-1/2, -z, (xxiii) -x, y-1/2, -z+1, (xxiv) -x, y-1/2, -z, (xxv) x-1, y, z, (xxvi) x, y-1, z, (xxvii) -x, y+1/2, -z+1.
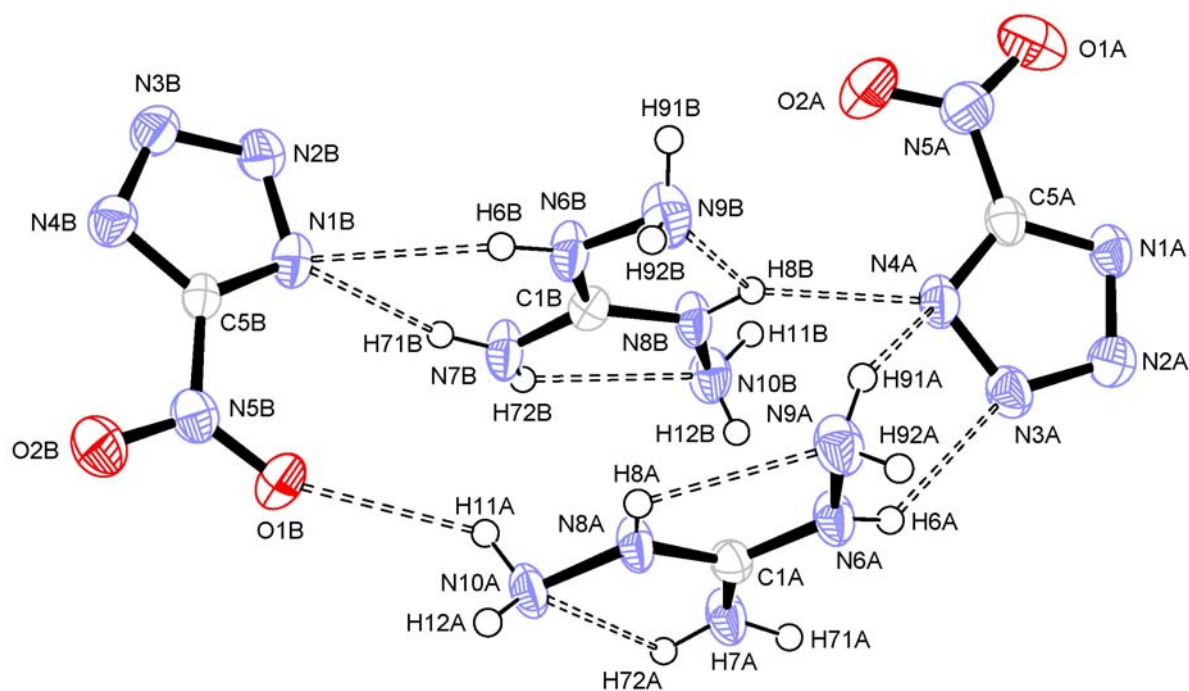
Figure 2.22. Hydrogen bonding in the asymmetric unit of **18**, including atom labels and thermal ellipsoids showing 50% probability.

For **18**, at the unitary level, two hydrogen bond patterns are of note. Firstly, the four S(5) motifs formed by the intraionic hydrogen bonds of the diaminoguanidinium cations and secondly a C 1,1(6) motif formed by the hydrogen bond N9B–H91B•••N10B[xxv] [symmetry code: x-1, y, z] linking the "b" cations, similar to the C 1,1(3) motif observed for **15**. Within the asymmetric unit, at the binary level, two six membered ring patterns, R 1,2(6) and R 2,2(6) as well as a variety of dimer and chain patterns are observed (see Figure 2.22).

As in **17** and **18**, the packing of **20** is composed of a complex three dimensional hydrogen bonded network of cations and anions and is shown in Figure 2.23. The eleven crystallographically independent medium and strong hydrogen bonds observed form three S(5) motifs, identical to those found in **17** and **18**, and one C 1,1(6) motif linking the cations (N11–H112•••N10[xxxiv] [symmetry code: -x+2,y+1/2,-z+1/2]), similar to that observed for the cations in moiety "b" of **18** and for the cations in **15** (as discussed above for **18**), at the unitary level. Interestingly, at the binary level only chain patterns, mainly of the C 2,2(X), where X =

60

6 – 11, variety and dimer patterns of the D 3,3(X), where X = 11, 13 or 15, type are observed.

The hydrogen bonding geometry found in **20** is shown in Table 2.20 and a full graph-set

matrix describing the hydrogen bond patterns in **20** is provided in Table 2.21.

Table 2.20. Hydrogen-bonding geometry in **20**

D–H•••A[a]	D–H (Å)	H•••A (Å)	D•••A (Å)	D–H•••A (°)
N6–H6•••N11	0.92(3)	2.36(3)	2.654(3)	98(2)
N7–H7•••N9	0.89(3)	2.22(3)	2.621(4)	107(2)
N8–H8•••N10	0.86(4)	2.36(4)	2.722(3)	106(3)
N9–H92•••N4	0.94(3)	2.51(3)	3.181(4)	128(2)
N6–H6•••N3[xxviii]	0.92(3)	2.08(4)	2.899(4)	149(3)
N7–H7•••O1[xxix]	0.89(3)	2.15(3)	2.916(3)	144(3)
N8–H8•••N2[xxx]	0.86(4)	2.23(4)	2.954(3)	141(3)
N9–H91•••O1[xxxi]	0.88(4)	2.57(4)	3.243(4)	134(3)
N10–H101•••N1[xxxii]	0.97(4)	2.12(4)	3.085(4)	176(3)
N11–H111•••N1[xxxiii]	0.97(3)	2.16(3)	3.108(3)	167(2)
N11–H112•••N10[xxxiv]	0.88(4)	2.51(3)	3.271(4)	144(3)

[a] Symmetry codes for **20**: (xxviii) x-1, y, z, (xxix) x+1/2, -y+3/2, -z, (xxx) -x+2, y-1/2, -z+1/2, (xxxi) x-1/2, -y+3/2, -z, (xxxii) x, y-1, z, (xxxiii) -x+1, y-1/2, -z+1/2, (xxxiv) -x+2,y+1/2,-z+1/2.

Table 2.21. Unitary and binary hydrogen bond pattern graph-set matrix for **20** excluding

intraionic hydrogen bonds.[a]

		a	b	c	d	e	f	g	h
N6–H6•••N3[xxviii]	a	D 1,1(2)							
N8–H8•••N2[xxx]	b	C 2,2(7)	D 1,1(2)						
N9–H92•••N4	c	C 2,2(6)	C 2,2(9)	D 1,1(2)					
N10–H101•••N1[xxxii]	d	C 2,2(9)	C 2,2(8)	C 2,2(10)	D 1,1(2)				
N11–H111•••N1[xxxiii]	e	C 2,2(9)	C 2,2(6)	C 2,2(10)	C 1,2(8)	D 1,1(2)			
N11–H112•••N10[xxxiv]	f	D 3,3(13)	D 3,3(11)	D 3,3(15)	D 3,3(11)	D 3,3(11)	C 1,1(6)		
N7–H7•••O1[xxix]	g	C 2,2(10)	C 2,2(10)	C 2,2(10)	C 2,2(8)	C 2,2(10)	D 3,3(11)	D 1,1(2)	
N9–H91•••O1[xxxi]	h	C 2,2(9)	C 2,2(11)	C 2,2(7)	C 2,2(11)	C 2,2(11)	D 3,3(15)	C 1,2(7)	D 1,1(2)

[a] Symmetry codes: (xxviii) x-1, y, z, (xxix) x+1/2, -y+3/2, -z, (xxx) -x+2, y-1/2, -z+1/2, (xxxi) x-1/2, -y+3/2, -z, (xxxii) x, y-1, z, (xxxiii) -x+1, y-1/2, -z+1/2, (xxxiv) -x+2,y+1/2,-z+1/2.
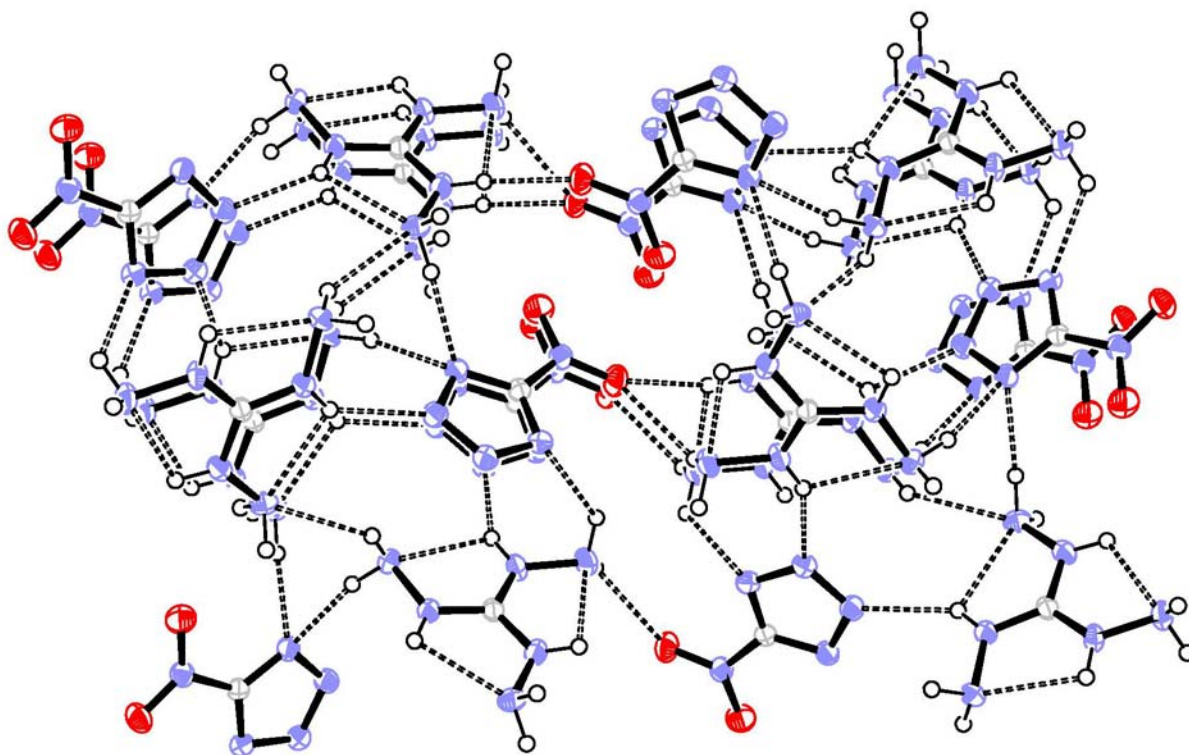
Figure 2.23. Packing and hydrogen bonding in **20** with thermal ellipsoids showing 50% probability

In contrast to anhydrous **20**, the hydrate **19** forms a layer structure with six strong hydrogen bonds joining the cations, anions and crystal water within the layer, three weaker hydrogen bonds linking the layers and three intraioninc hydrogen bonds forming S(5) motifs identical to those in **20**. Within the layer, two symmetry related anions are joined by two water molecules through two hydrogen bonds forming a binary R 4,4(10) graph-set. These pairs of anions are in turn hydrogen-bonded to pairs of cations, which are joined by a single hydrogen bond forming a unitary R 2,2(10). The cation pairs also hydrogen bond to the crystal water molecule in the layers. The hydrogen bonding within one layer of **19** is shown in Figure 2.24. The hydrogen-bonding geometry found in **19** is tabulated in Table 2.22 and a full graph-set matrix describing the hydrogen bonding in **19** can be found in Table 2.23.

Table 2.22. Hydrogen-bonding geometry in **19**.

D–H•••A[a]	D–H (Å)	H•••A (Å)	D•••A (Å)	D–H•••A (°)
N6–H6•••N1[xxxv]	0.898(19)	2.423(19)	3.0297(19)	125.1(15)
N7–H7•••O3[xxxvi]	0.88(2)	1.98(2)	2.8013(19)	155.6(18)
N8–H8•••N9[xxxvii]	0.85(2)	2.28(2)	3.0209(19)	145.3(16)
N9–H91•••O1[xxxv]	0.90(2)	2.45(2)	3.1441(19)	134.8(15)
N9–H91•••N1[xxxviii]	0.90(2)	2.595(19)	3.215(2)	126.7(15)
N9–H91•••N1[xxxv]	0.90(2)	2.666(19)	3.1881(19)	118.0(14)
N11–H111•••O3[xxxviii]	0.86(2)	2.30(2)	3.096(2)	152.7(18)
N11–H112•••N2[xxxix]	0.91(2)	2.475(19)	3.236(2)	141.8(15)
O3–H10•••N4	0.86(2)	2.09(2)	2.9222(18)	163(2)
O3–H11•••N3[xxxix]	0.84(3)	2.05(3)	2.8834(19)	172(2)
N6–H6•••N10	0.898(19)	2.252(18)	2.635(2)	105.3(14)
N7–H7•••N11	0.88(2)	2.423(19)	2.694(2)	98.3(15)
N8–H8•••N9	0.85(2)	2.361(19)	2.6892(18)	103.3(14)

[a] Symmetry codes for **19**: (xxxv) -x, -y-1, -z+1, (xxxvi) -x, -y, -z+2, (xxxvii) -x+1, -y, -z+1, (xxxviii) x+1, y, z, (xxxix) -x, -y, -z+1.

Table 2.23. Unitary and binary hydrogen bond pattern graph-set matrix for **19** excluding intraionic hydrogen bonds.[a]

		a	b	c	d	e	f	g	h	i	j
N6–H6•••N1[xxxv]	a	D 1,1(2)									
N8–H8•••N9[xxxvii]	b	D 3,3(10) [R 2,2(10)]	R 2,2(10)								
N9–H91•••N1[xxxv]	c	R 2,4(10)	D 3,3(10) [R 2,2(10)]	D 1,1(2)							
N9–H91•••N1[xxxviii]	d	R 1,2(5)	D 3,3(10) [R 2,2(10)]	R 2,2(4)	D 1,1(2)						
N11–H112•••N2[xxxix]	e	C 2,2(8)	D 3,3(12) [R 2,2(10)]	R 4,4(18)	C 2,2(9)	D 1,1(2)					
N9–H91•••O1[xxxv]	f	R 2,2(8)	D 3,3(10) [R 2,2(10)]	R 4,2(10)	R 2,1(5)	C 2,2(12)	D 1,1(2)				
N11–H111•••O3[xxxviii]	g	D 2,2(8)	D 3,3(12) [R 2,2(10)]	D 2,2(9)	D 2,2(9)	D 2,2(5)	D 2,2(9)	D 1,1(2)			
O3–H10•••N4	h	D 2,2(5)		D 2,2(5)	D 2,2(5)	D 2,2(5)	D 2,2(6)	D 2,2(4)	D 1,1(2)		
O3–H11•••N3[xxxix]	i	D 2,2(5)		D 2,2(5)	D 2,2(5)	D 2,2(4)	D 2,2(7)	D 2,2(4)	R 4,4(10)	D 1,1(2)	
N7–H7•••O3[xxxvi]	j	D 2,2(7)	D 3,3(12) [R 2,2(10)]	D 2,2(8)	D 2,2(8)	D 2,2(8)	D 2,2(8)	R 2,4(14)	D 2,2(4)	D 2,2(4)	D 1,1(2)

[a] Symmetry codes: (xxxv) -x, -y-1, -z+1, (xxxvi) -x, -y, -z+2, (xxxvii) -x+1, -y, -z+1, (xxxviii) x+1, y, z, (xxxix) -x, -y, -z+1.
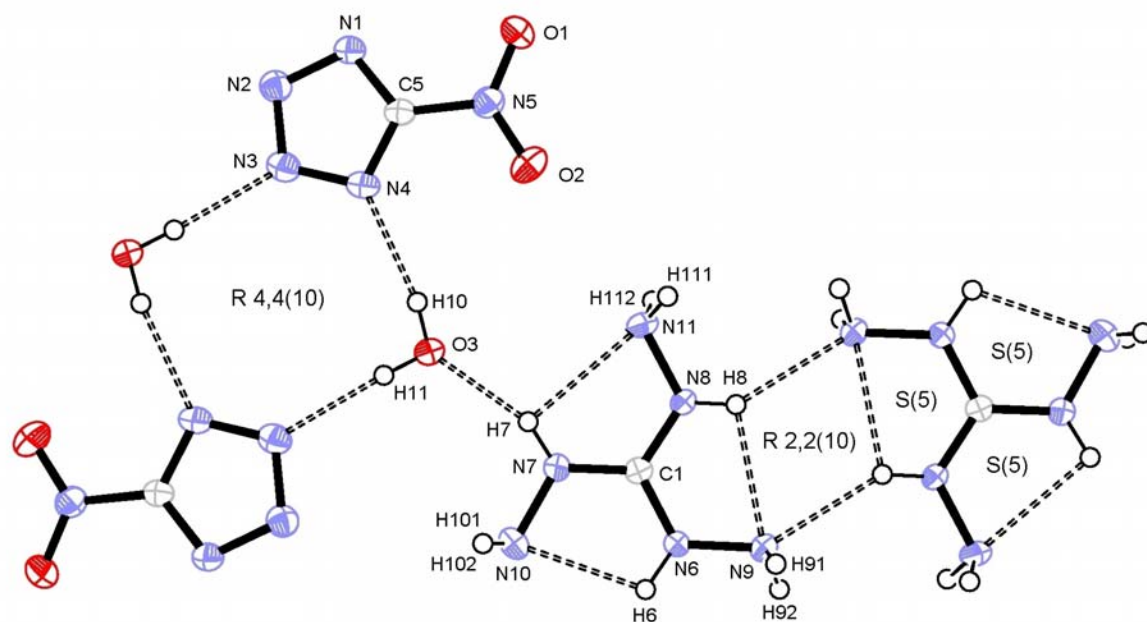
Figure 2.24. Some hydrogen bonding within a layer of **19**, including atom labels, graph-set descriptors and thermal ellipsoids showing 50% probability.

2.2.5 Energetic Properties

In order to assess the energetic properties of compounds **6 - 21**, the thermal stability (dehydration, melting and decomposition temperatures from DSC measurements) and relevant physical properties (density, nitrogen content and oxygen balance) for each compound are tabulated in Table 2.24 and Table 2.25. The sensitivities of each compound to friction, impact, electrostatic discharge and thermal shock were experimentally determined and are included in Table 2.26 and Table 2.27. For each salt the constant volume energy of combustion $\Delta_c U$ was determined experimentally using oxygen bomb calorimetry and also predicted on the basis of theoretical electronic energies (see computational methods section and Appendix Table 1) and an estimation of lattice enthalpy[61, 62] (Appendix Table 2). Details of the method used here are provided in the experimental section (Scheme 2.9). The measured and predicted thermochemical properties of **6 - 12** and **21** are summarized in Table 2.28 and those for **13 - 20** in Table 2.29. From constant volume energies of formation (back-calculated from experimental combustion data), molecular formulas and densities (from X-

ray) the detonation performance parameters (pressure and velocity) for each compound were estimated using the EXPLO5 computer code.[63]

DSC measurements were made on samples of ~1 mg of each energetic compound in this study (**6 - 21**) the results of which are summarized Table 2.24 and Table 2.25. Except the hydrate, **19**, all salts in this study melt near or above 100 ºC and all salts decompose above 170 ºC. Also, several salts show a significant separation of melting and decomposition temperatures of ≥90 ºC (**7**, **9**, **10**, **18 - 20**) whereas salts **6**, **13 - 15** and **21** show melting followed by almost immediate decomposition. The remaining materials studied showed reasonable separations of T_m and T_d of ~50 ºC. In comparison to commonly used explosives such as TNT and RDX, the compounds in this study generally have higher melting points than TNT (81 °C)[64] and lower melting points than RDX (204 °C)[64]. Compounds **6**, **12** and **13 - 21** decompose at a lower temperature than RDX (230 °C) and the remaining energetic compounds decompose higher temperatures. Only **10** exhibits a higher thermal stability than TNT. In addition to DSC analysis, all compounds were tested for sensitivity to thermal shock by placing a small sample (~0.5-1 mg) of compound in a Bunsen burner flame. This resulted in an explosion in the case of **7**, **10**, **12 - 15** and **20** and in all other cases, the compound burned or deflagrated without exploding (both TNT and RDX explode under similar conditions). From these "flame test" observations it would seem that the compounds in this study with less negative oxygen balances and / or higher nitrogen contents are more sensitive to thermal shock as might be expected.

Several trends in melting and decomposition behavior can also be observed from the DSC data. Salts of **4** are generally more stable (higher T_m and T_d) than salts of **5**. Within the series of salts of **5**, a stability trend is also observed with **10** being most stable followed by **9** and **11** which have similar stabilities, then **21** and the least thermally stable member of the family is **12**. The trend in melting and decomposition points observed for salts of the NT anion (**13** >

15 and **16** > **17** > **18** > **20**) is in keeping with known trends for simple nitrogen rich salts.[24, 39, 46]

Table 2.24. Physical Properties of **6** - **12** and **21**.

	6	7	9	10	11	12	21
formula	$C_2H_6N_6O_3$	$C_2H_6N_5O_4Cl$	$C_3H_8N_6O_3$	$C_3H_8N_5O_4Cl$	$C_3H_8N_8$	$C_3H_8N_8O_4$	$C_4H_8N_{10}O_2$
T_m (°C)[a]	162	125	181	225	186	120	190
T_d (°C)[b]	178	245	270	315	>250	174	200
N (%)[c]	51.8	35.1	47.7	32.8	71.8	50.9	61.2
Ω (%)[d]	-39.5	-20.0	-63.6	-41.2	-102.5	-43.6	-61.2
ρ (g/cm³)[e]	1.654	1.773	1.523	1.674	1.403	1.572	1.548

[a] Chemical melting point (DSC onset) from measurement with β = 10 °C / min. [b] Decomposition point (DSC onset) from measurement with β = 10 °C / min. [c] Percentage nitrogen. [d] Oxygen balance. [e] Density from X-ray measurements.

Table 2.25. Physical Properties of **13** - **20**.

	13	14	15	16	17	18	19	20
formula	$CH_5N_6O_{2.5}$	$CH_4N_6O_2$	$CH_5N_7O_2$	$C_2H_6N_8O_2$	$C_2H_7N_9O_2$	$C_2H_8N_{10}O_2$	$C_2H_{11}N_{11}O_3$	$C_2H_9N_{11}O_2$
T_m (°C)[a]	207	207	135	212	147	108	63	96
ΔH_{fus} (kJ/mol)[b]	–	–	-19.4	–	-33.4	-31.84	-33.2	-26.6
T_{deh} (°C)[c]	68	–	–	–	–	–	95	–
ΔH_{deh} (kJ/mol)[d]	10.7	–	–	–	–	–	1.43*	–
T_d (°C)[e]	217	217	188	217	211	216	191	191
N (%)[f]	59.6	63.6	66.7	64.4	66.7	68.7	65.0	70.3
Ω (%)[g]	-24.2	-24.2	-27.2	-45.9	-46.5	-47	-47.4	-47.4
ρ (g/cm³)[h]	1.636	1.637	1.720	1.644	1.661	1.595	1.599	1.601

[a] Chemical melting point (DSC onset) from measurement with β = 10 °C / min. [b] Enthalpy of fusion from DSC measurement with β = 10 °C / min. [c] Temperature at which crystal water is lost (dehydration, DSC onset) from measurement with β = 10 °C / min. [d] Enthalpy of crystal water loss (dehydration) from DSC measurement with β = 10 °C / min. [e] Decomposition point (DSC onset) from measurement with β = 10 °C / min. [f] Percentage nitrogen. [g] Oxygen balance. [h] Density from X-ray measurements.

Data collected for friction, impact and electrostatic discharge sensitivity testing are summarized in Table 2.26 and Table 2.27. Within the series of salts based on **4** and **5** the trend of increasing sensitivity with decreasingly negative oxygen balance is observed as was the case for the "flame test." For salts **13** - **20**, a trend of increasing sensitivity to friction and impact with increasing nitrogen content is observed which is also in accordance with the results of the "flame test." Each compound was roughly tested for sensitivity to electrostatic discharge by spraying sparks across a small (3-5 crystals) sample of material using a tesla coil (ESD testing, ~20 kV electrostatic discharge from an HF-Vacuum-Tester type VP 24). All compounds except **7** and **15** failed to explode under these conditions. Once again, a

comparison with the properties of TNT and RDX is useful to assess the energetic salts in this study. Compounds **6**, **9, 11**, **16**, **17** and **19** are less sensitive to both friction and impact than TNT (15 J) and RDX (7.4 J).[64] **17** is less sensitive to friction but more sensitive to impact than both TNT and RDX. The remaining materials (**7**, **13 - 15** and **19**) are as or more sensitive to impact and friction than RDX. Lastly, all of the compounds in this study, except **7**, **15** and **19** are safe for transport under the UN Recommendations on the Transport of Dangerous Goods as described in reference [65].

Table 2.26. Initial safety testing results and predicted energetic performance of **6 - 12** and **21**, using the EXPLO5 code.

	P_{det} (GPa)[a]	D (m/s)[b]	Impact (J)[c]	Friction (N)[c]	ESD (+/-)[d]	Thermal Shock
6	25.6	8100	>30	>360	-	Burns
7			3	10	+	Explodes
9	20.2	7500	>30	>360	-	Burns
10			5.5	96	-	Deflagrates
11	21.7	8200	>30	>360	-	Burns
12	21.2	7500	5	360	-	Deflagrates
21	23.0	7960	30	>360	-	Deflagrates

[a] Detonation pressure. [b] Detonation velocity. [c] Impact and friction sensitivities determined by standard BAM methods.[65] [d] Rough sensitivity to 20 kV electrostatic discharge (ESD), + sensitive, - insensitive from an HF-Vacuum-Tester type VP 24.

Table 2.27. Initial safety testing results for and predicted energetic performance of (EXPLO5 code) **13 - 20**, TNT and RDX.

	P_{det} (GPa)[a]	D (m/s)[b]	Impact (J)[c]	Friction (N)[c]	ESD (+/-)[d]	Thermal Shock
13	22.5	7740	4	120	-	explodes
14	23.9	7950		**14** was not tested in bulk		
15	30.1	8750	2	16	+	explodes
16	20.1	7500	>30	>360	-	burns
17	24.7	8190	30	360	-	deflagrates
18	24.4	8230	4	360	-	deflagrates
19	26.0	8480	2	48	-	explodes
20	20.7	7680	>30	>360	-	deflagrates
TNT	20.5	7100 (6900)	15	353	+	explodes
RDX	34.0	8900 (8700)	7.4	120	+	explodes

[a] Detonation pressure. [b] Detonation velocity, experimental values in parentheses.[64] [c] Impact and friction sensitivities determined by standard BAM methods[65]. [d] Rough sensitivity to 20 kV electrostatic discharge (ESD), + sensitive, - insensitive from an HF-Vacuum-Tester type VP 24.

In addition to safety considerations, performance of new energetic materials is of utmost interest. Using the molecular formula, density (from X-ray) and energy of formation ($\Delta_f U^{\circ}{}_{(exp)}$), the EXPLO5 computer code can be used to calculate the detonation velocity and pressure of CHNO explosives. Therefore, the energies of formation of **6 - 21** were back-calculated from constant volume energies of combustion by first converting to standard enthalpy of combustion and then on the basis of the general combustion equation, Equation **2.1**, Hess's Law as applied in Equation **2.2**, incorporating the known standard heats formation for water, carbon dioxide and aqueous hydrogen chloride[66] and a correction for change in gas volume during formation (Equation **2.3**). Due to the reasonably large standard deviations for several sets of experimental combustion measurements, the thermochemical data ($\Delta_c U, \Delta_c H^{\circ}_m, \Delta_f H^{\circ}_m$ and $\Delta_f U^{\circ}$) for each compound were predicted on the basis of the method described in the experimental section in an attempt to validate the experimentally determined values.

$$C_a H_b N_c O_d Cl_{e\,(s)} + \frac{4a - 2d + b - e}{4} O_{2\,(g)} \rightarrow a CO_{2\,(g)} + \frac{b - e}{2} H_2 O_{(l)} + \frac{c}{2} N_{2\,(g)} + e HCl_{(g)} \tag{2.1}$$
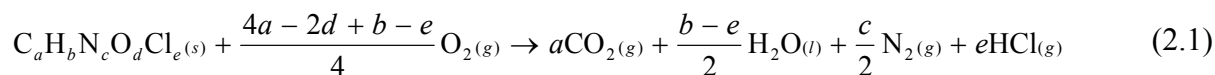
$$a\Delta_f H^{\circ}_m(CO_{2\,(g)}) + \frac{b}{2}\Delta_f H^{\circ}_m(H_2 O_{(l)}) + e\Delta_f H^{\circ}_m(HCl_{(aq)}) - \Delta_c H^{\circ}_m(C_a H_b N_c O_{d\,(s)}) = \Delta H^{\circ}_f(C_a H_b N_c O_d Cl_{e\,(s)}) \tag{2.2}$$

$$\Delta_f H^{\circ}_m(C_a H_b N_c O_d Cl_{e\,(s)}) - \Delta n_g RT = \Delta_f U^{\circ}_m \tag{2.3}$$

The predicted and experimental thermochemical data for compounds **6 - 12** and **21** were calculated as outlined above and are tabulated in Table 2.28 and Table 2.29 with experimental uncertainties (standard deviations for the sets of five individual measurements). As noted above, the standard deviations of the several of the sets of five measurements used to experimentally determine the heat of combustion of each compound are quite large. The substantial uncertainties stem from several sources. Firstly, and perhaps most significantly, all compounds in this study contain a large percentage of nitrogen and relatively little carbon

or hydrogen, therefore, upon combustion relatively little energy is released and very sensitive equipment would be required to detect such minute energy changes. To compensate for this, larger sample sizes would seem logical, but for safety reasons as well as practical ones, the use of larger samples is not an effective solution. When larger samples or "concentrated" mixtures of compound and diluting agent (benzoic acid) are used for oxygen bomb calorimetric measurements, the samples tend not to combust cleanly, but rather to explode. The explosion results in incomplete combustion and thus to less reliable measurements.

Table 2.28. Thermochemical properties of **6 - 12** and **21**.

	6	7	9	10	11	12	21
$\Delta_c U_{(exp)}$ (cal/g)[a]	-2510(10)	-2000	-3190(30)	-2600	-4500(100)	-2570(70)	
$\Delta_c U_{(pred)}$ (cal/g)[b]	-2620.87	-2563.1	-3306.81	-3128.21	-4424.19	-2879.19	-3443.44
$\Delta_c H^o_{m\,(exp)}$ (kJ/mol)[c]	-1695.0	-1664.2	-2348.0	-2319.4	-2908.4	-2358.3	
$\Delta_c H^o_{m\,(pred)}$ (kJ/mol)[d]	-1771.4	-2133.4	-2432.4	-2790.5	-2887.5	-2643.9	-3279.7
$\Delta_f H^o_{m\,(exp)}$ (kJ/mol)[e]	50(10)	150	20(30)	120	580(80)	30(70)	
$\Delta_f H^o_{m\,(pred)}$ (kJ/mol)[f]	127.0	614.4	108.7	592.2	563.8	320.2	562.5
$\Delta_f U^o_{(exp)}$ (kJ/kg)[g]	430(60)	830	260(130)	670	3870(470)	270(300)	

[a] Measured constant volume energy of combustion with standard deviations in brackets. [b] Predicted constant volume energy of combustion. [c] Standard molar enthalpy of combustion computed from experimental data with uncertainties in brackets. [d] Standard molar enthalpy of combustion computed from predicted data. [e] Standard molar enthalpy of formation computed from experimental data with uncertainties in brackets. [f] Standard molar enthalpy of formation computed from predicted data. [g] Standard energy of formation computed from experimental data with uncertainties in brackets.

Table 2.29. Thermochemical properties of **13 – 20**.

	13	14	15	16	17	18	19	20
$\Delta_c U_{(exp)}$ (cal/g)[a]	-1770(30)	-1860(30)	-2110(150)	-2250(40)	-2470(30)	-2620(50)	-2510(50)	-2690(50)
$\Delta_c U_{(pred)}$ (cal/g)[b]	-1975.7	-2095.9	-2362.4	-2526.6	-2654.6	-2778.6	-2741.4	-2924.0
$\Delta_c H^o_{m\,(exp)}$ (kJ/mol)[c]	-1050(20)	-1030(20)	-1290(90)	-1630(30)	-1940(20)	-2230(40)	-2500(40)	-2460(40)
$\Delta_c H^o_{m\,(pred)}$ (kJ/mol)[d]	-1167.1	-1156.6	-1451.83	-1835.72	-2095.36	-2367.58	-2710.6	-2675.03
$\Delta_f H^o_{m\,(exp)}$ (kJ/mol)[e]	-70(20)	60(20)	180(90)	-10(30)	160(20)	300(40)	120(40)	390(40)
$\Delta_f H^o_{m\,(pred)}$ (kJ/mol)[f]	51.6	191.4	343.7	191.2	307.9	437.2	352.7	601.8
$\Delta_f U^o_{(exp)}$ (kJ/kg)[g]	-380(130)	540(130)	1360(600)	30(160)	940(100)	1580(180)	650(180)	1890(180)

[a] Measured constant volume energy of combustion with standard deviations in brackets. [b] Predicted constant volume energy of combustion. [c] Standard molar enthalpy of combustion computed from experimental data with uncertainties in brackets. [d] Standard molar enthalpy

of combustion computed from predicted data. [e] Standard molar enthalpy of formation computed from experimental data with uncertainties in brackets. [f] Standard molar enthalpy of formation computed from predicted data. [g] Standard energy of formation computed from experimental data with uncertainties in brackets.

For compounds **6 - 13** and **15 – 18** and **20** $\Delta_f U^{\circ}{}_{(exp)}$ may be calculated by the simple method described above. However, for the hydrate **19**, for which no combustion measurements were made, and anhydrous **14**, which was not studied in bulk, some additional information is required to extract the energies of formation of these materials. In the case of **14**, the enthalpy of combustion is calculated from that of **13**, the enthalpy of dehydration (as determined by DSC) and the heat of vaporization of water[66] as described by the Born-Haber energy cycle shown in Scheme 2.5.

$$\mathbf{14}_{(s)} + O_{2\,(g)} + 0.5\,H_2O_{(l)} \xrightarrow{\Delta_c H^{\circ}_{m\,(exp)}\ \mathbf{(14)}} CO_{2\,(g)} + 2.5\,H_2O_{(l)} + 3\,N_{2\,(g)}$$

$$+ 0.5\,\Delta H_{vap}(H_2O) \qquad\qquad \Delta_c H^{\circ}_{m\,(exp)}\ \mathbf{(13)}$$

$$\mathbf{14}_{(s)} + O_{2\,(g)} + 0.5\,H_2O_{(g)} \xrightarrow{-\,0.5\,\Delta H_{dehydration}\ \mathbf{(13)}} \mathbf{13}_{(s)} + O_{2\,(g)}$$
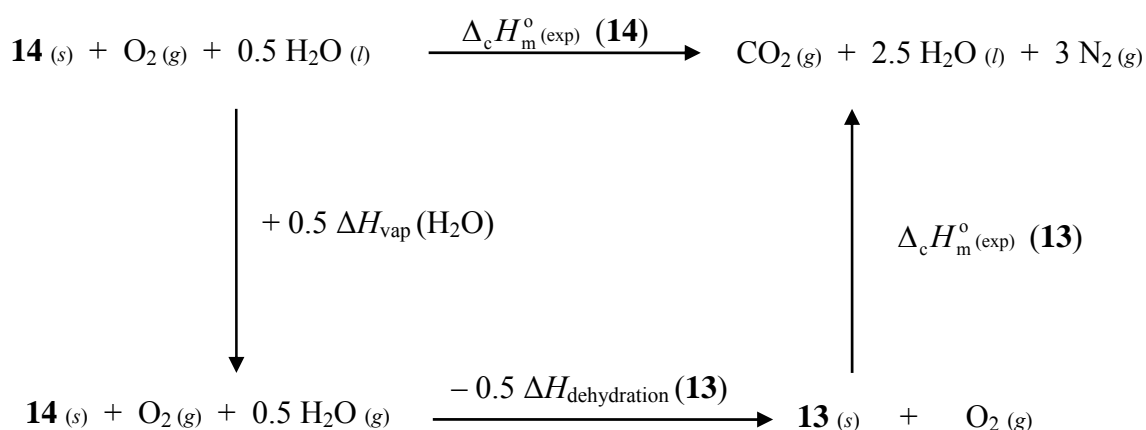
Scheme 2.5. Born-Haber energy cycle for the calculation of the molar heat of combustion of **14**.

The calculation of the heat of combustion of **19** from that of **20** is similar to that of **14** from **13** but complicated further by the fact that **19** melts before it loses crystal water. Therefore, the heat of combustion of **19** is calculated from that of **20**, the heats of fusion of both **20** and **19** (from DSC), the enthalpy of dehydration of molten **19** (also from DSC) and the heat of vaporization of water as described by the Born-Haber energy cycle shown in Scheme 2.6.

70

$$19_{(s)} + 3.25\ O_{2\,(g)} \xrightarrow{\Delta_c H^{\circ}_{m\,(exp)}\ \mathbf{(19)}} 2\ CO_{2\,(g)} + 5.5\ H_2O_{(l)} + 5.5\ N_{2\,(g)}$$

$\downarrow -\Delta H_{fus}\,\mathbf{(19)}$

$$19_{(l)} + 3.25\ O_{2\,(g)}$$

$\downarrow \Delta H_{dehydration}\,\mathbf{(19)}$

$$20_{(l)} + 3.25\ O_{2\,(g)} + H_2O_{(g)} \xrightarrow{-\Delta H_{vap}\,(H_2O)}$$

$\downarrow \Delta H_{fus}\,\mathbf{(20)}$

$$20_{(s)} + 3.25\ O_{2\,(g)} \xrightarrow{\Delta_c H^{\circ}_{m\,(exp)}\ \mathbf{(20)}} 2\ CO_{2\,(g)} + 4.5\ H_2O_{(l)} + 5.5\ N_{2\,(g)}$$
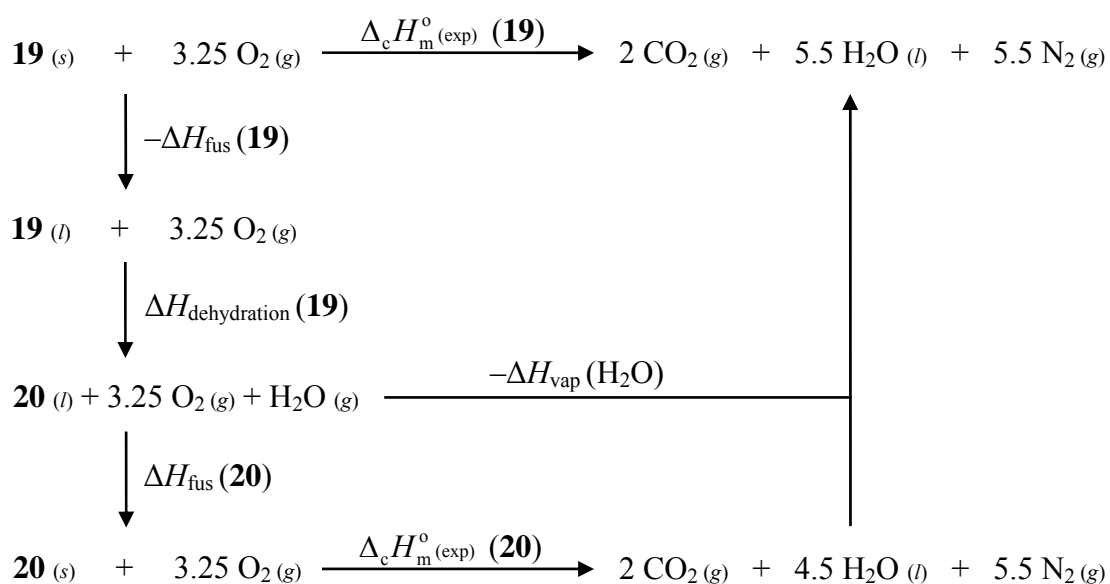
Scheme 2.6. Born-Haber energy cycle for the calculation of the heat of combustion of **19**

Using the heats of combustion for **14** and **19** obtained as described above, the energy of formation is easily calculated by application of the gas volume change correction given in Equation 2.3.

The thermochemical properties of the anhydrous compounds in this study are easily predicted using the method outlined in the experimental section. However, values for the thermochemical properties of the hydrates **13** and **19** must be calculated taking into account the effect of crystal water on the lattice enthalpy. To this end, the enthalpy of water loss obtained from DSC measurements is again useful. The heats of combustion of **13** and **19** are thus predicted using the lattice and gas-phase combustion reaction enthalpies calculated for **14** and **20**, the enthalpies of dehydration for **13** and **19** and the heat of vaporization of water, following the Born-Haber energy cycles shown in Scheme 2.7 and Scheme 2.8. All predicted values overestimate the measured enthalpy of combustion by ~100 − 280 kJ/mol. The presence of significant hydrogen bonding seems to explain this rather large margin of

overestimation, since the approximation of lattice enthalpy used in the calculation of the predicted values does not account for the energetic effects of hydrogen bonding.

$$\textbf{13}_{(s)} \quad + \quad O_{2\,(g)} \quad \xrightarrow{\Delta_c H^{\circ}_{m\,(pred)}\,\textbf{(13)}} \quad CO_{2\,(g)} \quad + \quad 2.5\,H_2O_{(l)} \quad + \quad 3\,N_{2\,(g)}$$

$$\downarrow \Delta H_{dehydration}\,\textbf{(13)}$$

$$\textbf{14}_{(s)} + O_{2\,(g)} + 0.5\,H_2O_{(g)} \quad \xrightarrow{-0.5\,\Delta H_{vap}\,(H_2O)}$$

$$\uparrow -2\,\Delta H_{vap}\,(H_2O)$$

$$\downarrow +\Delta H_L\,\textbf{(14)}$$

$$NH_4^{+}{}_{(g)} + NT^{-}{}_{(g)} + O_{2\,(g)} \quad \xrightarrow{\Delta_r H\,\textbf{(14)}} \quad CO_{2\,(g)} + 2\,H_2O_{(g)} + 3\,N_{2\,(g)}$$
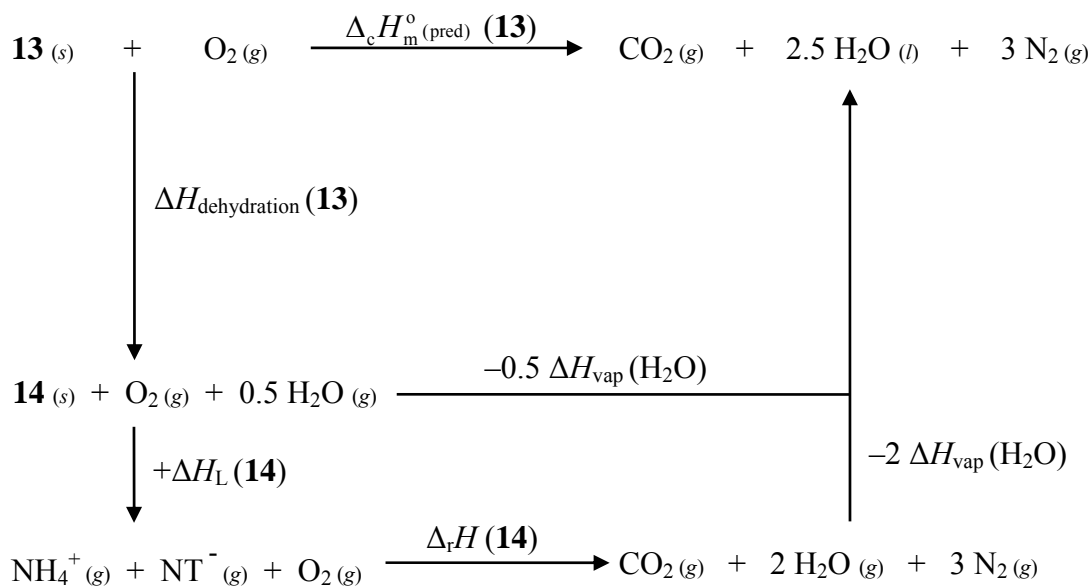
Scheme 2.7. Born-Haber energy cycle for the prediction of the combustion enthalpy of **13**.

19 $_{(s)}$ + 3.25 $O_{2\,(g)}$ $\xrightarrow{\Delta_c H^o_{m\,(pred)}\ \textbf{(19)}}$ 2 $CO_{2\,(g)}$ + 5.5 $H_2O_{\,(l)}$ + 5.5 $N_{2\,(g)}$

$\downarrow -\Delta H_{fus}\,\textbf{(19)}$

19 $_{(l)}$ + 3.25 $O_{2\,(g)}$

$\downarrow \Delta H_{dehydration}\,\textbf{(19)}$

20 $_{(l)}$ + 3.25 $O_{2\,(g)}$ + $H_2O_{\,(g)}$ $\xrightarrow{-\Delta H_{vap}\,(H_2O)}$

$\downarrow \Delta H_{fus}\,\textbf{(20)}$

$-4.5\,\Delta H_{vap}\,(H_2O)$

20 $_{(s)}$ + 3.25 $O_{2\,(g)}$

$\downarrow \Delta H_L\,\textbf{(20)}$

$TAG^+_{\,(g)}$ + $NT^-_{\,(g)}$ + 3.25 $O_{2\,(g)}$ $\xrightarrow{\Delta_r H\,\textbf{(20)}}$ 2 $CO_{2\,(g)}$ + 4.5 $H_2O_{\,(g)}$ + 5.5 $N_{2\,(g)}$
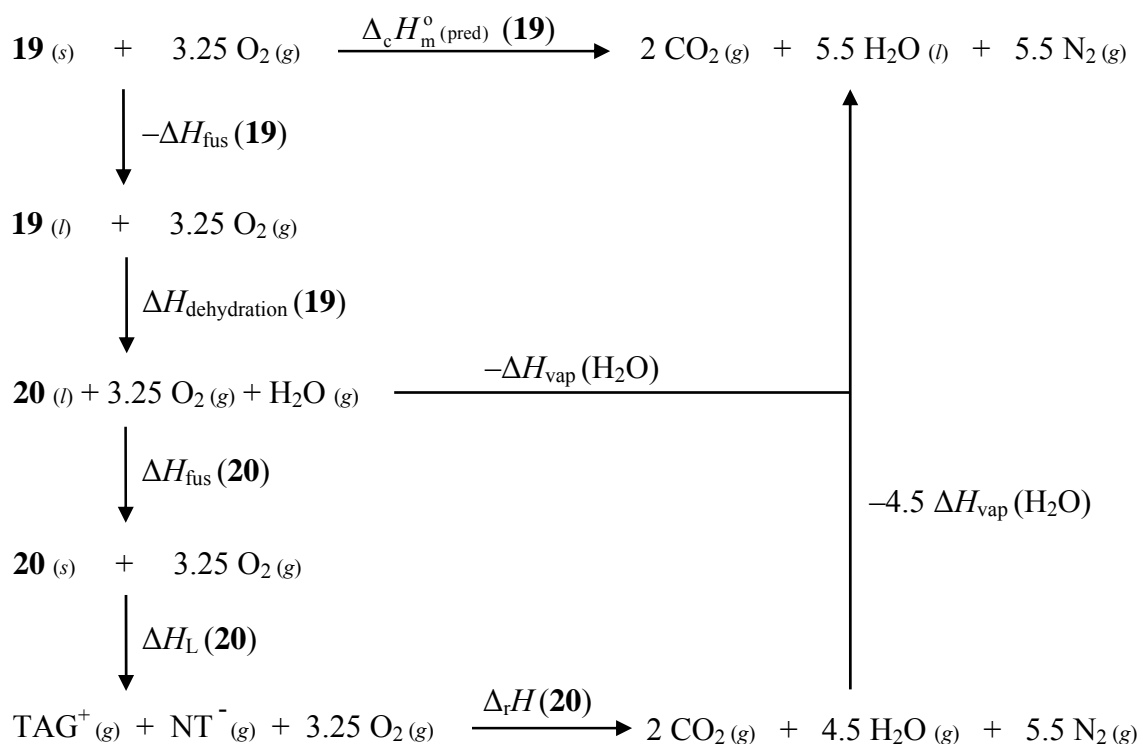
Scheme 2.8. Born-Haber energy cycle for the prediction of the combustion enthalpy of **19**.

The EXPLO5 code, using the following values for the empirical constants in the Becker-Kistiakowsky-Wilson equation of state (BKWN-EOS): $\alpha = 0.5$, $\beta = 0.176$, $\kappa = 14.71$ and $\theta = 6620$, was used, on the basis of experimentally determined data (except for **21**, for which computed data were used), to predict the detonation parameters (detonation velocity and pressure) for each non-halogen containing compound. The results of the calculations are shown in Table 2.26 for **6**, **9**, **11**, **12** and **21**, in Table 2.30 for TNT, RDX and analogous salts of **2** and **3** and in Table 2.27 for salts of the NT anion. From the EXPLO5 predictions made using the BKWN-EOS parameters given above and the known data for TNT and RDX, it would seem that detonation velocity and most likely pressure as well are slightly overestimated. Taking into account this systematic overestimation, the estimated performance of all of the compounds assessed in this study fall between those of TNT (7100 m/s, 20.5 GPa) and RDX (8900 m/s, 34.0 GPa). Previously reported detonation pressure and

velocity predictions of salts of **2** and **3** made using the empirical equations of Kamlet and Jacobs[67-69] are also shown in Table 2.30 for comparison to the EXPLO5 results. Compounds **9** and **11** are predicted to perform as well as the analogous MDAT salts and compounds **6** and **11** should show slightly lower performance than the analogous DAT and MDAT salts, but therefore much lower sensitivities. The better performance (and higher sensitivity) of the DAT salts is most likely due in large part to the higher densities of DAT and MDAT salts.

Table 2.30. EXPLO5 Predicted performance of TNT, RDX and CHNO salts of DAT (**2**) and MDAT (**3**).[c]

	P_{det} (GPa)[a]	D (m/s)[b]
TNT	20.5	7100 (6900)
RDX	34.0	8900 (8700)
2a[d]	31.0 [33.3]	8700 [8800]
3b[e]	20.3 [23.4]	7500 [7700]
3d[f]	21.9 [20.8]	8200 [7400]
3e[g]	28.4 [33.6]	8400 [8800]

[a] Detonation pressure. [b] Detonation velocity. [c] Experimental values in curved brackets () and Kamlet and Jacobs predictions from reference 7 in square brackets []. [d] 1,5-diamino-1*H*-tetrazolium nitrate. [e] 1,5-diamino-4-methyl-1*H*-tetrazolium nitrate. [f] 1,5-diamino-4-methyl-1*H*-tetrazolium azide. [g] 1,5-diamino-4-methyl-1*H*-tetrazolium dinitramide.

In comparison to other 5-nitro-2*H*-tetrazole salts for which predicted performance data are reported, the salts in this study (excepting **16**) are predicted to perform as well as or outperform substituted triazolium salts (7500 – 7900 m/s, 20 – 25 GPa)[20, 21, 40] and methylated aminotetrazolium salts (6200 m/s, 15.5 GPa)[11] and with the exception of **15** underperform amino- and diaminotetrazolium salts (8840 m/s, ~31 GPa).[21] Lastly, it is important to point out that the data used to predict all literature performance values are based solely on theoretical heat of formation values predicted by the above discussed methods. As shown in Gao et al. and here these methods tend to systematically overestimate heat of formation values. Overestimation of heat of formation should lead to slightly exaggerated performance values. On the other hand, experimentally determined heats of formation, like those used in this study, tend to be underestimated for the above mentioned reasons and therefore performance predictions based on experimental data should thus be slightly underestimated.

Therefore, it seems that the compounds in this study should certainly perform as well as, or slightly better than commonly used energetic materials.

2.3 Conclusions

In the course of this chapter, two families (**6 - 12** and **13 - 20**) of simple, heterocycle based energetic salts and a compound combing the cation of the first family and the anion of the second (**21**) have been synthesized and analyzed spectroscopically, structurally and energetically. All of the compounds in this study are easily synthesized from readily available, low-cost materials in moderate to excellent yields. The syntheses presented and suggested are also potentially scalable to enable larger scale production and testing.

Spectroscopic and structural analyses showed efficient use of hydrogen bond donors and acceptors resulting in the formation of extensive hydrogen bonding networks in many of the compounds studied. Simple, characteristic hydrogen bond patterns, such as the dimers found in compounds **8**, **10** and **11** and the helical chains identified in **9**, **12** and **21** could be identified for salts of **5** whereas more complex three dimensional networks are formed in nearly all other cases. In addition, the packing of salts of the NT⁻ anion seems to show strong similarities to analogous nitrate salts, also resulting from efficient hydrogen bonding networks.

The result of the effects observed spectroscopically and in structure determinations of the ionic materials lead to two families of nitrogen rich (up to 70% nitrogen in the case of **20**) energetic compounds that show promising physical and energetic properties. All compounds show significant thermal stability (up to 300 °C in the case of **10**) and are predicted to perform at least as well as the current standards in the energetic materials industry. The majority of the compounds studied are also less sensitive to physical stimuli than commonly used secondary explosives. Although several compounds are sensitive materials (**7**, **15** and **20**), the potential performance of these materials should not be overlooked as it may be possible to adjust these sensitivities by mixing or compounding these materials with desensitizing agents.

2.4 Experimental

2.4.1 Caution

Although no significant difficulties with the compounds described herein were experienced, silver azide, dinitramides, aminotetrazoles and their derivatives and 5-nitro-2*H*-tetrazole, and its derivatives are energetic materials and may explode under certain conditions. Appropriate safety precautions should be taken, especially when these compounds are prepared on a larger scale. Laboratories and personnel should be properly grounded, and safety equipment such as Kevlar gloves, leather coats, face shields, and ear plugs are highly recommended. In addition, special care should be taken when mixing and grinding (to generate KBr pellets for IR measurements or benzoic acid pellets for bomb calorimetry) the compounds in this study.

2.4.2 General

All chemical reagents and solvents were obtained from Sigma-Aldrich Inc. or Acros Organics (analytical grade) and were used as supplied. Silver azide and silver bis-pyridine dinitramide[26] were prepared according to known procedures. ^{1}H, ^{13}C, and $^{14/15}$N NMR spectra were recorded on a JEOL Eclipse instrument in DMSO-d_6 at or near 25 °C operating at 400 MHz for ^{1}H measurements, 100 mHz for ^{13}C measurements, 29 MHz for ^{14}N and 45 MHz for ^{15}N. The chemical shifts are given relative to tetramethylsilane (^{1}H, ^{13}C) or nitromethane (^{15}N) as external standards and coupling constants are given in Hertz (Hz). Infrared (IR) spectra were recorded on a Perkin-Elmer Spectrum One FT-IR instrument as KBr pellets at 20 °C. Transmittance values are qualitatively described as "very strong" (vs), "strong" (s), "medium" (m) and "weak" (w). Raman spectra were recorded on a Perkin-Elmer Spectrum 2000R NIR FT-Raman instrument equipped with a Nd:YAG laser (1064 nm). The intensities are reported as percentages of the most intense peak and are given in parentheses. Elemental analyses were performed with a Netsch Simultaneous Thermal Analyzer STA 429. Melting points were determined by differential scanning calorimetry (Perkin-Elmer Pyris 6 DSC instrument, calibrated with standard pure indium and zinc). Measurements were performed at

a heating rate of 10 °C/min in closed aluminum sample pans with a 1 μm hole in the top for gas release under a nitrogen flow of 20 mL/min with an empty identical aluminum sample pan as a reference.

2.4.3 Bomb Calorimetry

For all calorimetric measurements, a Parr 1356 bomb calorimeter (static jacket) equipped with a Parr 207A oxygen bomb for the combustion of highly energetic materials was used.[70] A Parr 1755 printer, furnished with the Parr 1356 calorimeter, was used to produce a permanent record of all activities within the calorimeter. The samples (~200 mg each) were carefully mixed with ~800 mg analytical grade benzoic acid and pressed into pellets, which were subsequently burned in a 3.05 MPa atmosphere of pure oxygen. The experimentally determined heats of combustion were obtained as the averages of five single measurements with standard deviations calculated as a measure of experimental uncertainty. The calorimeter was calibrated by the combustion of certified benzoic acid in an oxygen atmosphere at a pressure of 3.05 MPa.

2.4.4 X-ray Crystallography

Crystals were obtained as described in the preparative section below. The X-ray crystallographic data for **6**, **14**, **15** and **16** were collected on an Enraf-Nonius Kappa CCD diffractometer. Data sets for **7**, **9**, **11** - **13** and **18** - **21** were collected on an Oxford Diffraction Xcalibur 3 diffractometer equipped with a CCD detector. Data for **8**, **10** and **17** were collected on a STOE IPDS diffractometer. All data were collected using graphite-monochromated Mo Kα radiation ($\lambda = 0.71073$ Å). No absorption corrections were applied to data sets collected for **6** - **8**, **10** - **19** or **21**. Multi-scan numerical absorption corrections were applied to data collected for **9** and **20** using the ABSPACK[71] software supplied by Oxford Diffraction. All structures were solved by direct methods (SHELXS-97 and SIR97)[72, 73] and refined by means of full-matrix least-squares procedures using SHELXL-97.[72] In the cases of **9**, **12**, **18** and **20** which crystallize in the non-centrosymmetric space groups $P2_12_12_1$ (**9**, **12**
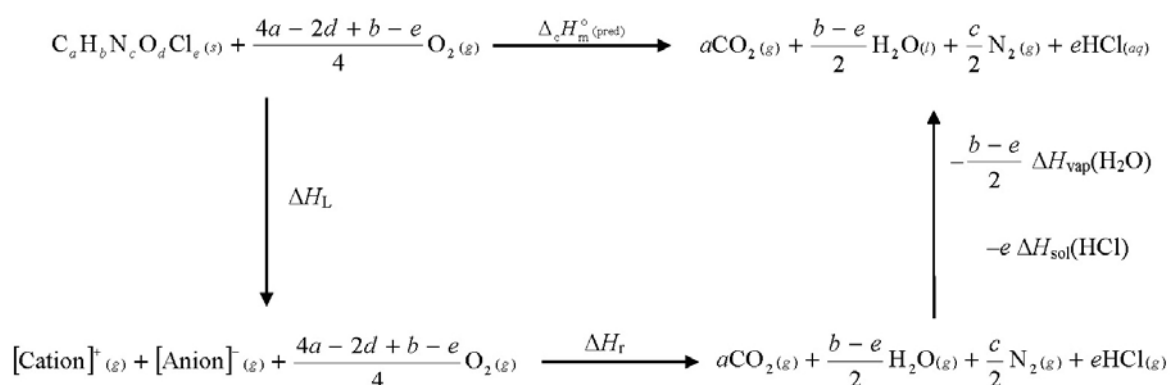
and **20**) and $P2_1$ (**18**), the Friedel pairs were averaged since no meaningful information about absolute structure configuration was obtained. Crystallographic data are summarized in Table 2.3, Table 2.4 and Table 2.5. Selected bond lengths and angles are reported in Table 2.6 and Table 2.7 and hydrogen-bonding geometries in Table 2.8, Table 2.9, Table 2.11, Table 2.13, Table 2.15, Table 2.17, Table 2.19, Table 2.20 and Table 2.22. All non-hydrogen atoms were refined anisotropically. For **6 - 11**, **13 - 17** and **19 - 21** all hydrogen atoms were located from difference Fourier electron-density maps and refined isotropically. In the case of **12**, the hydrogen atoms of the methyl groups were inserted at idealized positions and were subsequently refined riding on the atom to which they were bonded (fixed isotropic temperature factors with the value of 1.5 Beq). For **18** the positions of the hydrogen atoms were refined, but fixed isotropic temperature factors with the value of 1.2 Beq were used.

2.4.5 Computational Methods

All quantum chemical calculations were carried out with the Gaussian03W software package.[74] Vibrational (IR and Raman) frequencies of the 5-nitrotetrazolate anion were calculated using Becke's B3 three parameter hybrid function with an LYP correlation function (B3LYP)[75] and were scaled by a factor of 0.9614 as described by Radom et al.[35] Electronic energies for all cations, anions molecular oxygen and combustion products were calculated using Møller-Plesset perturbation theory truncated at the second order (MP2)[76] and were used unscaled. The results of the MP2 electronic energy calculations are tabulated in Appendix Table 1. For all atoms in all calculations, the correlation consistent polarized double-zeta basis set cc-pVDZ was used.[77, 78]

The standard molar enthalpies of combustion ($\Delta_c H^\circ_{m\,(pred)}$) of each compound were predicted on the basis of the computed electronic energies following the general Born-Haber energy cycle shown in Scheme 2.9. First the lattice enthalpy (ΔH_L) of each salt was predicted using the method described in reference [61]. Then the electronic energies calculated for the gaseous cations anions, molecular oxygen and appropriate combustion products are converted

into enthalpies by application of the zero point energy correction supplied in the *Gaussian03* output and internal energy corrections for rotational (U_{rot}), vibrational (U_{vib}) and translational (U_{trans}) motions as described in reference [79]. The reaction enthalpy (ΔH_r) of the cations in the gas-phase with gaseous O_2 to form gaseous CO_2, H_2O, N_2 and HCl (combustion) can then computed on the basis of the enthalpies determined from the corrected the *Gaussian03* outputs. The final step utilizes the known enthalpy of vaporization (ΔH_{vap} = 44.0 kJ/mol)[66] of water and enthalpy of solution (ΔH_{sol} = -74.8 kJ/mol)[66] of HCl to compute the predicted standard molar enthalpy of combustion for each compound.

$$C_aH_bN_cO_dCl_{e\,(s)} + \frac{4a - 2d + b - e}{4}O_{2\,(g)} \xrightarrow{\Delta_cH_m^\circ\,(pred)} aCO_{2\,(g)} + \frac{b - e}{2}H_2O_{(l)} + \frac{c}{2}N_{2\,(g)} + eHCl_{(aq)}$$

$$\Delta H_L \downarrow \qquad\qquad\qquad \uparrow \begin{array}{l} -\dfrac{b - e}{2}\Delta H_{vap}(H_2O) \\[2mm] -e\,\Delta H_{sol}(HCl) \end{array}$$

$$[Cation]^+_{\,(g)} + [Anion]^-_{\,(g)} + \frac{4a - 2d + b - e}{4}O_{2\,(g)} \xrightarrow{\Delta H_r} aCO_{2\,(g)} + \frac{b - e}{2}H_2O_{(g)} + \frac{c}{2}N_{2\,(g)} + eHCl_{(g)}$$

Scheme 2.9. Born-Haber energy cycle for the prediction of the combustion enthalpies of energetic salts.

2.4.6 Syntheses
1-Methyl-5-aminotetrazole (4)[9]

Compound **4** was prepared according to literature[9] mp 226-229 °C; IR (KBr, cm^{-1}) $\tilde{v}$ = 3328(s), 3151(s), 2950(w), 2805(w), 2741(w), 2454(w), 2380(w), 2262(w), 2203(w), 2157(w), 1679(s), 1666(s), 1595(s), 1483(m), 1321(m), 1279(w), 1236(w), 1121(w), 1090(m), 1043(w), 970(w), 789(m), 742(w), 688(w), 679(m), 538(w); Raman (200 mW, 25 °C, cm^{-1}) $\tilde{v}$ = 3150(13), 3042(5), 2951(32), 2888(4), 2809(4), 1661(13), 1594(20), 1484(10), 1411(13), 1319(28), 1278(22), 1119(17), 1093(10), 1043(8), 973(7), 789(100), 680(19), 478(10), 313(23), 218(16); ^{1}H NMR (DMSO-d_6, 25°C) δ 6.65 (s, -NH_2), 3.70 (s, -CH_3); ^{13}C NMR (DMSO-d_6, 25 °C) δ 156.4 (C_{arom}), 32.0 (-CH_3); ^{15}N NMR (DMSO-d_6, 25 °C) δ 2 (N2,

q, $^3J = 1.5$ Hz), -23 (N3), -93 (N4, t, $^2J = 1.5$ Hz), -185 (N1, q, $^2J = 1.7$ Hz), -339 (N5, t, $^1J = 87.0$ Hz); MS (EI+, 70 eV, >5%) m/z (%) 100(10) [M+], 99(100) [M+], 57(29), 43(90), 42(77), 28(60), 27(14), 15(34); $C_2H_5N_5$ (99.01) calcd.: C 24.2, H 5.1, N 70.7%; found: C 24.2, H 5.0, N 70.5%.

1,4-Dimethyl-5-iminotetrazole (5)

To a solution of 4.82 g (20.0 mmol) **8** in ~10 mL methanol in a large sublimation vessel under a steady stream of nitrogen were added 1.2 g (21.2 mmol) potassium hydroxide. The solution was stirred until all potassium hydroxide had dissolved. The solvent was then removed in vacuo and the residue was then sublimed at 90º C under static vacuum to yield 2.04 g (18.0 mmol, 90 %) of colorless hygroscopic needles. mp 106 ºC; IR (KBr, cm^{-1}) $\tilde{v}$ = 3314(m), 2996(w), 2945(w), 2919(w), 1649(s), 1456(m), 1429(m), 1390(m), 1347(w), 1277(w), 1251(w), 1199(m), 1138(w), 1047(m), 1034(m), 976(m), 799(w), 783(w), 711(w), 695(w); Raman (200 mW, 25 °C, cm^{-1}) $\tilde{v}$ = 3315(14), 2999(19), 2986(15), 2969(16), 2948(22), 2891(4), 1652(28), 1471(11), 1391(17), 1346(19), 1278(7), 1247(6), 1201(9), 1052(12), 982(6), 800(18), 786(100), 700(5), 599(30), 532(7), 307(30), 288(10), 232(6); ^{1}H NMR (DMSO-d_6, 25 °C) δ 5.0 (s, -NH) 3.4 (s, -CH_3); ^{13}C NMR (DMSO-d_6, 25 °C) δ 148.8 (C_{arom}), 31.3 (-CH$_3$); $C_3H_7N_5$ (113.12) calcd.: C 31.9, H 6.2, N 61.9%; found: C 31.5, H 6.3, N 61.7%.

1-Methyl-5-aminotetrazolium nitrate (6)[80]

To 2 mL concentrated nitric acid were added 1.620 g (10.0 mmol) of solid crystalline **4**. The clear, colorless reaction mixture was stirred until all **4** had dissolved. The solution was then cooled to 4 ºC overnight resulting in the formation of clear colorless crystals suitable for X-ray analysis, which were filtered off cold and washed until dry and acid free with diethyl ether. No further purification was necessary (1.206 g, 7.4 mmol, 74%). mp 162-164 °C; IR (KBr, cm^{-1}) $\tilde{v}$ = 3357(s), 3306(s), 3236(s), 3159(s), 2873(w), 2623(b), 2358(b), 1760(w), 1687(s), 1487(w), 1363(s), 1312(s), 1256(s), 1231(s), 1088(w), 1032(m), 965(m), 901(w),

775(w), 716(m); Raman (200 mW, 25 °C, cm^{-1}) $\tilde{v}$ = 2961(22), 1685(11), 1597(8), 1515(10), 1426(21), 1273(17), 1049(100), 778(89), 717(16), 665(18), 461(14), 302(22), 230(18), 136(25); ^{1}H NMR (DMSO-d_6, 25 °C) δ 9.1 (s, N-H, -NH_2), 3.9 (s, CH_3); ^{13}C NMR (DMSO-d_6, 25 °C) δ 153.6 (C_{arom}), 32.9 (-CH$_3$); ^{15}N NMR (DMSO-d_6, 25 °C) δ -11.5 (N6), -13.5 (N3), -24.0 (N2, q, ^{3}J = 1.5 Hz), -129.8 (N4), -184.0 (N1, q, ^{2}J = 1.9 Hz), -331.4 (N5); m/z (FAB^{+}, xenon, 6 keV, m-NBA matrix), 100 [MAT+H]$^{+}$; $C_2H_6N_6O_3$ (162.11) calcd.: C 14.9, H 3.7, N 51.8%; found: C 14.7, H 3.6, N 51.6%.

1-Methyl-5-aminotetrazolium perchlorate (7)

0.142 g (1.4 mmol) of **4** were dissolved in a minimal amount of concentrated (72%) perchloric acid The mixture was layered with ether and cooled in the fridge overnight to yield colorless plates, which were filtered off and washed with ether. No further purification was necessary. Alternatively, ether can be diffused into the mixture over 2 days yielding colorless crystals suitable for X-ray analysis (0.204 g, 1.0 mmol, 70%). mp 125-128 °C; IR (KBr, cm^{-1}) $\tilde{v}$ = 3411(s), 3300(s), 3269(s), 3187(s), 3043(w), 1702(s), 1684(s), 1603(w), 1325(m), 1280(w), 1072(s), 1033(s), 935(w), 724(w), 697(m); Raman (200 mW, 25 °C, cm^{-1}) $\tilde{v}$ = 3265(7), 3044(9), 2965(22), 1706(16), 1605(11), 1518(14), 1455(12), 1430(27), 1331(12), 1282(27), 1230(9), 1149(12), 1088(16), 1052(19), 1022(9), 974(11), 938(100), 782(88), 671(17), 632(25), 468(27), 457(33), 298(24), 226(18); ^{1}H NMR (DMSO-d_6, 25 °C) δ 8.4 (N-H, -NH_2) 3.7 (-CH_3); ^{13}C NMR (DMSO-d_6, 25 °C) δ 155.2 (C_{arom}), 31.6 (-CH$_3$); ^{15}N NMR (DMSO-d_6, 25 °C) δ -17.3 (N3), -24.2 (N2, q, ^{3}J = 1.9 Hz), -138.4 (N4), -183.8 (N1, q, ^{2}J = 1.9 Hz), -329.4 (N5); ^{35}Cl NMR (DMSO-d_6, 25 °C) δ 1.0 (Cl); m/z (FAB^{+}, xenon, 6 keV, m-NBA matrix) 100 [MAT+H]$^{+}$; $C_2H_6N_5O_4Cl$ (199.56) calcd.: C 12.0, H 3.0, N 35.1%; found: C 12.0, H 3.0, N 35.1%.

1,4-Dimethyl-5-aminotetrazolium iodide (8)

To a suspension of 20.0 g (0.2 mol) **4** in 250 mL of acetonitrile were added 50 mL (0.8 mol) of methyl iodide. The suspension was heated under reflux overnight yielding a red-brown

solution from which white crystals precipitated upon cooling. The off-white solid was filtered off (acetonitrile solution was set aside) and washed with diethyl ether until no traces of yellow remained. The remaining acetonitrile solution was reduced in volume on a rotary evaporator until further material precipitated. This material was again filtered off and washed until white with diethyl ether. The combined yield of colorless crystalline material was 44.0 g (183 mmol, 91%). mp 227 °C; IR (KBr, cm^{-1}) $\widetilde{v}$ = 3291(m), 3249(m), 3216(m), 3080(s), 3006(m), 2780(w), 1675(s), 1535(m), 1451(s), 1428(m), 1392(m), 1261(w), 1184(m), 1051(s), 1002(m), 782(s), 687(s), 612(w), 580(w), 567(w); Raman (200 mW, 25 °C, cm^{-1}) $\widetilde{v}$ = 3243(12), 3094(20), 3008(38), 2941(76), 2837(11), 1691(13), 1612(7), 1540(12), 1447(29), 1382(15), 1358(21), 1050(15), 786(100), 603(27), 518(8), 303(35), 267(18); ^{1}H NMR (CD$_3$OD, 25 °C) δ 9.1 (s, -NH_2) 3.9 (s, -CH_3); ^{13}C NMR (CD$_3$OD, 25 °C) δ 149.1 (C_{arom}), 34.7 (-CH$_3$); ^{15}N NMR{^{1}H} (CD$_3$OD, 25 °C) δ -29.6 (N2, N3), -182.8 (N1, N4), -318.0 (N5); m/z (FAB$^+$, xenon, 6 keV, m-NBA matrix) [DMAT]$^+$ 114; C$_3$H$_8$N$_5$I (241.01) calcd.: C 15.0, H 3.2, N 29.0%; found: C 14.9, H 3.4, N 29.0%.

1,4-Dimethyl-5-aminotetrazolium nitrate (9)

To a solution of 2.41 g **8** (10 mmol) in 10 mL methanol were added 1-2 drops of concentrated nitric acid and 1.70 g (10.0 mmol) solid silver nitrate. The resulting methanolic suspension was stirred for 3 hrs under exclusion of light, then filtered through a ~2 cm plug of wet (methanol) packed celite to remove the precipitated silver iodide. The remaining solid was washed twice with methanol. The solution was evaporated to dryness. The resulting solids were recrystallized from 3 mL of boiling methanol (1.2 g, 6.8 mmol, 68%). mp 181-183 °C; IR (KBr, cm^{-1}) $\widetilde{v}$ = 3276(s), 3223(s), 3166(s), 3040(s), 2824(w), 2753(w), 2690(w), 2340(w), 1685(s), 1543(m), 1424(m), 1396(m), 1307(s), 1196(m), 1058(w), 1038(m), 781(m), 709(w); Raman (200 mW, 25 °C, cm^{-1}) $\widetilde{v}$ = 3041(17), 3013(16), 2959(52), 1699(9), 1544(12), 1457(18), 1428(20), 1400(19), 1359(26), 1259(9), 1041(96), 1011(9), 947(5), 853(7), 792(100), 716(11), 681(7), 631(11), 598(32), 429(11), 325(28), 270(16), 128(17); ^{1}H NMR

(DMSO-d_6, 25 °C) δ 9.2 (s, -NH_2) 3.8 (s, -CH_3); ^{13}C NMR (DMSO-d_6, 25 °C) δ 148.9 (C_{arom}), 34.2 (-CH_3); ^{15}N NMR (DMSO-d_6, 25 °C) δ 4.3 (N6), -29.6 (N2, N3, q, ^3J = 1.9 Hz), -182.8 (N1, N4, q, ^2J = 2.0 Hz), -320.3 (N5); m/z (FAB$^+$, xenon, 6 keV, m-NBA matrix) [DMAT]$^+$ 114; $C_3H_8N_6O_3$ (176.13) calcd.: C 20.5, H 4.6, N 47.7%; found: C 20.5, H 4.3, N 48.0%.

1,4-dimethyl-5-aminotetrazolium perchlorate (10)

To 20 mL methanol were added 4.820 g (20.0 mmol) **8**. The solution was stirred until all the solid had dissolved. A second solution containing 4.140 g anhydrous silver perchlorate (weighed out in a dry-box) dissolved in 5 mL methanol was added to the solution of **8** in methanol. Yellow silver iodide precipitated immediately and the temperature of the reaction mixture rose to the boiling point of methanol. After stirring for 30 minutes under exclusion of light, the solution was filtered, divided into 12 equal portions and recrystallized by diffusion of ether into the methanol solutions yielding clear colorless crystals suitable for X-ray structure determination. No further purification was necessary (2.812 g, 18.0 mmol, 90%). mp 218-223 °C; IR (KBr, cm^{-1}) $\widetilde{v}$ = 3384(s), 3331(s), 3268(s), 3193(s), 2670(w), 2480(w), 2046(w), 1688(s), 1545(m), 1454(w), 1258(w), 1108(s), 1053(s), 934(w), 778(w), 625(m); Raman (200 mW, 25 °C, cm^{-1}) $\widetilde{v}$ = 3200(6), 3043(9), 3017(11), 2957(39), 1695(12), 1546(11), 1453(19), 1436(11), 1419(10), 1397(18), 1358(23), 1049(16), 935(100), 790(99), 626(13), 597(27), 461(23), 307(25), 273(15); ^{1}H NMR (DMSO-d_6, 25 °C) δ 9.1 (s, -NH_2) 3.8 (s, -CH_3); ^{13}C NMR (DMSO-d_6, 25 °C) δ 148.5 (C_{arom}), 34.0 (-CH_3); ^{15}N NMR (DMSO-d_6, 25 °C) δ 29.5 (N2, N3, q, ^3J = 1.9 Hz), -182.8 (N1, N4, q, ^2J = 1.9 Hz), -320.0 (N5); ^{35}Cl NMR (DMSO-d_6, 25 °C) δ 1.0(Cl); m/z (FAB$^+$, xenon, 6 keV, m-NBA matrix) [DMAT]$^+$ 114; $C_3H_8N_5O_4Cl$ (213.58) calcd.: C 16.9, H 3.8, N 32.8%; found: C 16.9, H 3.7, N 32.9%.

1,4-Dimethyl-5-aminotetrazolium azide (11)

Method 1

To a solution of 0.240 g (1.0 mmol) of **8** in 3 mL methanol were added 0.200 g (1.33 mmol) of silver azide. This suspension was stirred under exclusion of light for 1 hour and then

filtered. The remaining solution was divided into three 1 mL portions into which diethyl ether was allowed to diffuse over several days yielding identical clear, colorless, prismic crystals equally suitable for X-ray crystal structure determination. No further purification was necessary (0.122 g, 0.78 mmol, 78%).

Method 2

A 2.5 cm diameter glass column with sintered glass disc and a ground glass stopcock was wet packed with 50 g of Amberjet 4600-Cl (strongly basic ion-exchange resin). The resin was treated first with 10% sodium hydroxide solution in water and subsequently with 10% sodium azide solution as described in ref. 25. After azide loading was complete, the elution solvent was gradually changed to methanol. After rinsing the azide loaded column with ~500 mL of pure methanol, a solution of 4.820 g (20.0 mmol) **8** in 100 mL methanol was eluted slowly. As soon as the elution solvent exiting the column showed a precipitate when treated with nitric acid and silver nitrate (AgN_3) the elutant was collected and further methanol was passed through the column until no more precipitate formed upon treatment of the elutant with nitric acid and silver nitrate. The total elutant (~500 mL) was then evaporated to nearly to dryness and allowed to recrystallize overnight yielding 3.0 g (19.2 mmol, 96 %) large colorless prisms. mp 178-180 °C; IR (KBr, cm^{-1}) $\widetilde{v}$ = 3397(w), 3336(w), 2874(s,b), 2024(s), 1689(s), 1535(w), 1459(m), 1426(w), 1392(w), 1330(m), 1204(w), 1067(w), 1037(w), 1009(w), 787(m), 677(w), Raman (200 mW, 25 °C, cm^{-1}) $\widetilde{v}$ = 3016(38), 2947(63), 2829(12), 2027(4), 1711(7), 1658(6), 1536(10), 1451(21), 1395(13), 1356(32), 1331(77), 1263(6), 1238(7), 1131(4), 1061(9), 1010(6), 942(7), 792(100), 597(19), 522(10), 464(9), 328(50), 311(20), 289(15), 272(15), 165(29); ^{1}H NMR (DMSO-d_6, 25 °C) δ 8.4 (s, -NH_2), 3.8 (s, -CH_3); ^{13}C NMR (DMSO-d_6, 25 °C) δ 148.8 (C_{arom}), 33.4 (-CH_3); ^{15}N NMR (DMSO-d_6, 25 °C) δ -30.7 (N2, N3, q, ^3J = 1.9 Hz), -133.4 (N7), -185.8 (N1, N4, q, ^2J = 1.9 Hz), -277.1 (N6, N8), -307.2 (N5); m/z (FAB$^+$, xenon, 6 keV, m-NBA matrix) [DMAT]$^+$ 114; $C_3H_8N_8$ (156.15 g/mol) calcd.: C 23.1, H 5.2, N 71.8%; found: C 23.1, H 4.8, N 71.8%.

1,4-Dimethyl-5-aminotetrazolium dinitramide (12)

To a suspension of 0.370 g (1.0 mmol) of silver bis-pyridine dinitramide (Franek, et al) in 2 mL methanol were added 0.240 g (1.0 mmol) of **8**. The mixture was stirred under exclusion of light for 30 minutes, the silver iodide was then removed by filtration and the remaining clear, yellow solution was divided into two equal fractions and diethyl ether was allowed to diffuse into the solutions overnight yielding clear, colorless needles (0.157 g, 0.71 mmol, 71%). mp 120-122 °C; IR (KBr, cm^{-1}) $\tilde{v}$ = 3341(s), 3314(s), 3254(s), 3139(s), 1683(s), 1525(m), 1502(m), 1443(m), 1430(m), 1327(w), 1249(w), 1163(m), 1046(w), 1006(m), 758(w); Raman (200 mW, 25 °C, cm^{-1}) $\tilde{v}$ = 3049(11), 2963(41), 1689(13), 1526(16), 1425(24), 1397(16), 1353(25), 1329(82), 1252(10), 1182(11), 1046(12), 973(16), 955(15), 825(29), 787(100), 739(7), 594(22), 485(23), 396(12), 313(29), 273(21), 183(14); ^{1}H NMR (DMSO-d_6, 25°C) δ 9.1 (s, -NH_2), 3.9 (s, -CH_3); ^{13}C NMR (DMSO-d_6, 25 °C) δ 148.5 (C_{arom}), 34.0 (-CH$_3$); ^{15}N NMR (DMSO-d_6, 25 °C) δ -10.1 (N6,N8), -29.3 (N2, N3, q, ^3J = 1.9 Hz), -153.0 (N7), -182.6 (N1, N4, q, ^2J = 1.9 Hz), -320.1 (N5); m/z (FAB$^+$, xenon, 6 keV, m-NBA matrix) [DMAT]$^+$ 114; $C_3H_8N_8O_4$ (220.15) calcd.: C 16.4, H 3.7, N 50.1%; found: C 16.3, H 3.9, N 49.9%.

Ammonium 5-nitrotetrazolate hemihydrate (13).[27]

To a vigorously stirred mixture of 30 g of ice and 30 g of water in a 250 mL plastic beaker were added 5.5 g (22 mmol) copper(II)sulfate pentahydrate and 10.4 g (150 mmol) sodium nitrite. The temperature was maintained at ~2 ºC (ice water bath) and a previously prepared and cooled (~2 ºC) solution of 4.25 g (50 mmol) **1**, 2.8 mL (50 mmol) concentrated sulfuric acid and a 0.2 g (0.8 mmol) of copper (II) sulfate in 70 mL water (pale-blue solution). Addition resulted in vigorous gas evolution as well as the formation of a frothy, pale blue-green solid. After addition was completed (~30 mins) the dropping funnel was rinsed with ~20 mL water and removed. The resulting blue-green slurry was allowed to stir at room temperature for 1 hr. 4.1g (100 mmol) solid sodium hydroxide were then added under

vigorous stirring blue-green slurry resulting in a darkening of the mixture. The resulting dark-blue slurry was then heated to ~70 ºC for ~1 hr with vigorous stirring to convert the blue copper(II)hydroxide to black-brown copper(II)oxide. The resulting brownish-green suspension was then filtered hot through an approximately 2 cm thick plug of celite wet-packed in a 110 mm plastic Buechner funnel. The celite was subsequently washed twice with 50 mL hot (70 ºC) water. The filtrate (clear greenish-yellow solution) was then acidified with 1.6 mL (~27 mmol) concentrated sulfuric acid and treated with decolorizing carbon while warm. The addition of carbon resulted in gas evolution and the resulting suspension was then stirred for ~15 mins. The solution was filtered through a ~2 cm wet-packed plug of celite yielding a nearly clear (slightly yellow) solution. This solution was acidified with a further 1.6 mL (~27 mmol) concentrated sulfuric acid and then extracted with a solution of 12 mL (18.9 mmol) tridodecylamine in 150 mL of dichlorethane. The aqueous layer was set aside and the organic phase (clear light-yellow solution) was then dried over magnesium sulfate and placed in a wash bottle. Ammonia gas was slowly bubbled through the solution for ~15 mins at room temperature resulting in a slight change of color and the precipitation of a fine white crystalline solid. The solid was collected by vacuum filtration and washed twice with 20 mL fresh dichloroethane. The solvent collected was set aside and the white solid was allowed to dry overnight in air yielding 2.2 g (15.6 mmol) white crystalline powder (ammonium 5-nitrotetrazolate hemihydrate). The depleted dichloroethane was then transferred back to a wash bottle and treated with ammonia for a further 15 minutes. No additional solid precipitated. The remaining aqueous reaction solution was then extracted with a second solution of 12 mL (18.9 mmol) tridodecylamine in 150 mL of dichlorethane. The organic phase was dried, treated with ammonia gas and filtered as described above yielding 1.4 g (9.9 mmol) ammonium 5-nitrotetrazolate hemihydrate. The portions of solid collected were combined giving a total yield of 3.6 g (25.5 mmol, 51%). Crystals suitable for X-ray diffraction were prepared by slow evaporation of a methanolic solution of **13**. (Crystals of

anhydrous **13**, **14,** suitable for X-ray diffraction were prepared by slow diffusion of diethyl ether into an acetone solution of **13** which had been stored in finely powdered form in a desiccator for ~1 week prior to recrystallization.) mp 207 °C (decomp, DSC); IR (KBr, cm^{-1}) $\tilde{v}$ = 3396(m), 3179(w), 3141(w), 3044(s), 2900(m), 2856(m), 2732(w), 2080(w), 1823(wb), 1712(m), 1669(m), 1541(s), 1508(w), 1464(m), 1448(m), 1418(s), 1316(s), 1184(m), 1167(m), 1067(w), 1051(w), 1035(w), 834(m), 771(w), 736(w), 707(m), 669(m); Raman (200 mW, 25 °C, cm^{-1}) $\tilde{v}$ = 3063(3), 2837(1), 1875(1), 1689(1), 1555(8), 1445(5), 1421(100) 1318(6), 1185(2), 1168(4), 1071(63), 1053(21), 836(9), 775(4), 541(4), 454(3), 252(5), 197(3); ^{1}H NMR (DMSO-d_6, 25 °C) δ 7.11 (s, NH_4^+), 3.48 (s, H_2O); ^{13}C NMR (DMSO-d_6, 25 °C) δ 169.5 ($C5$); ^{14}N NMR (DMSO-d_6, 25 °C) δ 19 ($N2$, $v_{1/2}$ = 430 Hz), -22 ($N5$, $v_{1/2}$ = 60 Hz), -62 ($N1$ $v_{1/2}$ = 400 Hz), -359 (NH_4^+, $v_{1/2}$ = 10 Hz); m/z (FAB$^-$, xenon, 6 keV, m-NBA matrix) [NT]$^-$ 114; CH$_5$N$_6$O$_{2.5}$ (141.09) calcd.: C 8.5, H 3.6, N 59.6 %; found: C 8.5, H 3.6, N 59.6 %.

Hydrazinium 5-nitrotetrazolate (15)

To a suspension of 1.32 g **13** (9.4 mmol) in 3 mL EtOH were added 0.5 mL (0.5 g, 10.0 mmol) hydrazine hydrate. The solution was subsequently warmed to boiling with a heat gun to drive off the ammonia evolved. The resulting solution was allowed to cool to room temperature and was then refrigerated overnight. No material precipitated. The resulting yellowish solution was then divided into three 1 mL portions, each of which was evaporated to dryness individually. After removing the solvent, each portion was recrystallized from 2-3 mL boiling ethanol. Each portion of recrystallized material was vacuum-filtered and washed twice with diethyl ether. The total combined yield of colorless plates was 0.78 g (5.3 mmol, 56%). Crystals suitable for X-ray structure determination were obtained by slow diffusion of diethyl ether into a methanol solution of **15**. mp 135 °C (DSC); IR (KBr, cm^{-1}) $\tilde{v}$ = 3303(s), 3250(m), 3185(m), 3079(m), 2960(m), 2864(m), 2727(m), 2654(m), 2462(w), 2079(w), 1631(m), 1597(m), 1531(s), 1507(m), 1444(m), 1420(s), 1318(s), 1175(w), 1149(m), 1117(m), 1063(w), 1044(w), 1026(w), 979(m), 838(m), 771(w), 664(m), Raman (200 mW, 25

°C, cm^{-1}) $\tilde{v}$ = 3090(2), 2836(2), 2462(2), 1873(2), 1633(4), 1532(6), 1446(4), 1420(100), 1316(7), 1291(1), 1177(3), 1162(5), 1122(1), 1062(58), 1046(41), 1029(5), 980(7), 840(9), 773(3), 542(3), 454(3), 258(4), 174(2), 129(3); ^{1}H NMR (DMSO-d_6, 25 °C) δ 6.71 (s, N$_2$$H_5^+$); ^{13}C NMR (DMSO-$d_6$, 25 °C) δ 169.0 (C5); ^{14}N NMR (DMSO-d_6, 25 °C) δ 18 (N2, $v_{1/2}$ = 900 Hz), -23 (N5, $v_{1/2}$ = 110 Hz), -59 (N1 $v_{1/2}$ = 990 Hz), -338 (N$_2$H$_5^+$, $v_{1/2}$ = 1980 Hz); m/z (FAB$^-$, xenon, 6 keV, m-NBA matrix) [NT]$^-$ 114; m/z (FAB$^+$, xenon, 6 keV, m-NBA matrix) [N$_2$H$_5$]$^+$ 33; CH$_5$N$_7$O$_2$ (147.12) calcd.: C 8.2, H 3.4, N 66.7 %; found: C 8.3, H 3.3, N 66.6 %.

Guanidinium 5-nitrotetrazolate (16)

To a solution of 1.32 g **13** (9.4 mmol) in 3 mL water were added 1.22 g (10.0 mmol) guanidinium nitrate. The mixture was warmed with a heat gun until all solids dissolved and then allowed to cool to room temperature overnight yielding colorless crystals of guanidinium 5-nitrotetrazolate, which were vacuum-filtered and subsequently washed twice with diethyl ether. Yield 1.31 g (7.6 mmol, 81%). Crystals suitable for X-ray structure determination were obtained by slow diffusion of diethyl ether into a methanol solution of **16**. mp 212 °C (decomp., DSC); IR (KBr, cm^{-1}) $\tilde{v}$ = 3503(s), 3407(s), 3371(s), 3177(s), 2839(w), 2727(w), 2483(w), 2455(w), 2367(w), 2204(w), 2052(w), 1645(s), 1581(m), 1522(m), 1437(m), 1416(m), 1314(m), 1168(w), 1112(w), 1048(w), 1039(w), 1029(s), 838(m), 739(w), 664(w); Raman (200 mW, 25 °C, cm^{-1}) $\tilde{v}$ = 3203(1), 1643(1), 1569(3), 1541(5), 1419(100(1317(3), 1179(3), 1051(41), 1042(32), 1016(25), 843(6), 773(1), 545(9), 455(2), 268(3), 135(7), 116(3); ^{1}H NMR (DMSO-d_6, 25 °C) δ 6.89 (s, CH_6N$_3^+$); ^{13}C NMR (DMSO-d_6, 25 °C) δ 169.3 (C5), 158.4 (C1); ^{14}N NMR (DMSO-d_6, 25 °C) δ 20 (N2, $v_{1/2}$ = 490 Hz), -23 (N5, $v_{1/2}$ = 60 Hz), -62 (N1 $v_{1/2}$ = 390 Hz), -306 CH$_6$N$_3^+$, $v_{1/2}$ = 1460); m/z (FAB$^-$, xenon, 6 keV, m-NBA matrix) [NT]$^-$ 114; m/z (FAB$^+$, xenon, 6 keV, m-NBA matrix) [CH$_6$N$_3$]$^+$ 60; C$_2$H$_6$N$_8$O$_2$ (174.15) calcd.: C 13.8, H 3.5, N 64.4 %; found: C 13.8, H 3.5, N 64.4 %.

Aminoguanidinium 5-nitrotetrazolate (17)

A suspension of 4.23 g (30.0 mmol) **13** and 5.67 g (30.0 mmol) aminoguanidinium hydrogencarbonate in 50 mL ethanol was heated to reflux overnight under dry N_2. The clear, slightly yellow solution was allowed to cool slowly to room temperature under dry N_2 resulting in the precipitation of 2.72 g (14.4 mmol) of fine white solid aminoguanidinium 5-nitrotetrazolate. The precipitated material was filtered and washed with cold ethanol and then twice with diethyl ether. The ethanol was retained and reduced in volume on a rotary evaporator until further material precipitated. A second portion of 1.58 g (8.4 mmol) **17** was collected and the remaining ethanol solution was evaporated to dryness. The remaining white material was recrystallized once from ethanol and then washed with ether yielding a further 0.92 g (4.9 mmol) **17**. The total yield of **17** was 5.2 g (27.5 mmol, 92%). Crystals suitable for X-ray structure determination were obtained by slow diffusion of diethyl ether into a methanol solution of **17**. mp 147 °C (DSC); IR (KBr, cm^{-1}) $\tilde{v}$ = 3412(s), 3360(m), 3336(m), 3246(m), 3154(m), 3074(m), 2848(w), 2735(w), 2634(w), 2459(w), 2191(w), 2071(w), 1661(s), 1637(m), 1543(m), 1533(m), 1503(w), 1446(m), 1422(m), 1319(m), 1197(w), 1175(w), 1158(w), 1064(w), 1027(w), 940(m), 835(m), 757(w), 720(w), 668(w), 618(w), 583(w); Raman (200 mW, 25 °C, cm^{-1}) $\tilde{v}$ = 3293(2), 1869(1), 1674(1), 1630(2), 1533(7), 1490(2), 1422(100), 1319(5), 1285(1), 1204(2), 1177(3), 1159(4), 1063(45), 1041(44), 959(7), 838(8), 773(3), 626(3), 539(3), 497(4), 450(3), 348(4), 261(2), 243(4), 206(3), 133(7); ^{1}H NMR (DMSO-d_6, 25 °C) δ 8.53 (s, -N6*H*), 7.23 (broad s, -N8*H$_2$*), 6.71 (broad s, -N7*H$_2$*), 4.66 (s, -N9*H$_2$*); ^{13}C NMR (DMSO-d_6, 25 °C) δ 169.3 (*C*5), 159.3 (*C*1); ^{14}N NMR (DMSO-d_6, 25 °C) δ 15 (*N*2, $v_{1/2}$ = 720 Hz), -23 (*N*5, $v_{1/2}$ = 70 Hz), -62 (*N*1 $v_{1/2}$ = 460 Hz), -306 (CH$_7$N$_4^+$, $v_{1/2}$ = 2000 Hz); *m/z* (FAB$^-$, xenon, 6 keV, m-NBA matrix) [NT]$^-$ 114; *m/z* (FAB$^+$, xenon, 6 keV, m-NBA matrix) [CH$_7$N$_4$]$^+$ 75; C$_2$H$_7$N$_9$O$_2$ (189.14) calcd.: C 12.7, H 3.7, N 66.7 %; found: C 12.8, H 3.7, N 66.4 %.

Diaminoguanidinium 5-nitrotetrazolate (18)

A suspension of 0.35 g (2.5 mmol) **13**, 0.265 g (2.5 mmol) sodium carbonate and 0.468 g (2.5 mmol) 1-amino-3-ammonioguanidnium sulfate were suspended in ~20 mL ethanol. The mixture was refluxed under a flow of N_2 while stirring overnight. The resulting white suspension was then cooled under N_2 and filtered yielding 0.33 g of fine white powder solid (Na_2SO_4, after drying in an oven at 100 °C for 15 minutes). The remaining clear, slightly yellow solution was then reduced in volume to ~2 mL using a rotary evaporator (bath temp 50 °C). A white solid crystallized immediately upon removal from the rotary evaporator. ~2 mL ethanol were then added and the mixture was heated until all material had dissolved. After cooling, the white powder solid that precipitated was filtered and washed with ethanol (0.25 g, 1.2 mmol). Some material redissolved on washing and the filtrate was thus reduced in volume to ~2 mL and diethyl ether was diffused into the solution overnight resulting in the formation of a crystalline material. The solution was decanted off and the remaining solids were allowed to dry on air for ~15 mins. 0.11 g (0.54 mmol) additional material were recovered. Total yield 0.36 g (1.76 mmol, 71%). Crystals suitable for X-ray structure determination were obtained by slow diffusion of diethyl ether into a methanol solution of **18**. mp 108 °C (DSC); IR (KBr, cm^{-1}) $\widetilde{v}$ = 3412(s), 3349(s), 3295(s), 3233(s), 3196(s), 2843(w), 2455(w), 2207(w), 2071(w), 1663(s), 1633(m), 1532(s), 1503(m), 1441(m), 1417(s), 1373(m), 1316(m), 1187(m), 1176(m), 1055(w), 1029(w), 991(m), 941(m), 836(m), 771(w), 666(m), 580(w); Raman (200 mW, 25 °C, cm^{-1}) $\widetilde{v}$ = 3300(3), 2987(5), 2451(1), 1867(1), 1675(3), 1618(3), 1538(10), 1444(17), 1414(100), 1317(7), 1182(10), 1057(54), 1041(79), 1014(8), 929(11), 839(14), 773(5), 732(2), 659(2), 545(6), 451(3), 370(4), 271(5), 259(6), 242(5), 186(3), 133(5); ^{1}H NMR (DMSO-d_6, 25 °C) δ 8.52 (s, 2H, -N6/8*H*), 7.11 (s, -N7*H*$_2$), 4.56 (s, 4H, -N9/11*H*$_2$); ^{13}C NMR (DMSO-d_6, 25 °C) δ 169.3 (*C*5), 160.3 (*C*1); ^{14}N NMR (DMSO-d_6, 25 °C) δ 16 (*N*2, $v_{1/2}$ = 620 Hz), -23 (*N*5, $v_{1/2}$ = 70 Hz), -62 (*N*1 $v_{1/2}$ = 510 Hz); *m/z* (FAB$^-$, xenon, 6 keV, m-NBA matrix) [NT]$^-$ 114; *m/z* (FAB$^+$, xenon, 6 keV, m-NBA matrix)

[CH$_8$N$_5$]$^+$ 90; C$_2$H$_8$N$_{10}$O$_2$ (204.18) calcd.: C 11.8, H 4.0, N 68.6 %; found: C 11.8, H 3.8, N 68.7 %.

Triaminoguanidinium 5-nitrotetrazolate monohydrate (19)

To a solution of 1.41 g (10.0 mmol) **13** in a mixture of 4 mL water and 6 mL methanol were added 1.57 g (5.0 mmol) barium hydroxide octahydrate. The mixture was heated with a heat gun until all solids had dissolved. The volume was then reduced to ~5 mL on a rotary evaporator with heating to remove as much ammonia as possible. The pH was subsequently checked (7-8). Meanwhile, 1.62 g (5.0 mmol) triaminoguanidinium hemisulfate dihydrate were dissolved in ~5 mL deionized water. After cooling, the barium 5-nitrotetrazolate solution was added dropwise resulting in the formation of a white precipitate. The solution was stirred for ~1 hr and then filtered. The solvent from the resulting clear orange solution was then removed on a rotary evaporator, yielding an orange oil. The oil was redissolved in ~10 mL acetonitrile and filtered. The volume of the acetonitrile solution was then reduced to ~5 mL and the solution was cooled to 4 °C overnight yielding 1.2 g (5.1 mmol, 50%) colorless crystals. Crystals suitable for X-ray structure determination were obtained by slow diffusion of diethyl ether into an acetonitrile solution of **19**. mp 63 °C (DSC); IR (KBr, cm^{-1}) $\tilde{v}$ = 3339(s), 3225(sb), 2844(w), 2726(w), 2452(w), 2198(w), 2067(w), 1988(w), 1681(s) 1609(w), 1551(m), 1503(w), 1440(m), 1414(m), 1344(m), 1315(m), 1178(m), 1162(w), 1132(m), 1054(w), 1039(w), 943(m), 833(m), 667(w); Raman (200 mW, 25 °C, cm^{-1}) $\tilde{v}$ = 3340(1), 3240(3), 2454(0), 1861(1), 1685(2), 1645(1), 1553(3), 1536(6), 1441(4), 1416(100), 1341(3), 1318(4), 1198(1), 1179(2), 1163(4), 1137(3), 1056(52), 1040(35), 1028(11), 884(8), 838(7), 772(3), 637(2), 537(5), 447(2), 399(2), 257(5), 215(4), 140(5); ^{1}H NMR (DMSO-d_6, 25 °C) δ 8.57 (s, 3H, -N*H*), 4.46 (s, 6H, -N*H$_2$*), 3.49 (s, *H$_2$O*); ^{13}C NMR (DMSO-d_6, 25 °C) δ 169.1 (*C5*), 159.6 (*C1*); ^{14}N NMR (DMSO-d_6, 25 °C) δ 18 (*N2*, $v_{1/2}$ = 780 Hz), -23 (*N5*, $v_{1/2}$ = 90 Hz), -61 (*N1* $v_{1/2}$ = 670 Hz); *m/z* (FAB$^-$, xenon, 6 keV, m-NBA matrix) [NT]$^-$ 114; *m/z*

91

(FAB$^+$, xenon, 6 keV, m-NBA matrix) [CH$_9$N$_6$]$^+$ 105; C$_2$H$_{11}$N$_{11}$O$_3$ (237.18) calcd.: C 10.1, H 4.7, N 65.0 %; found: C 10.3, H 4.5, N 64.9 %.

Triaminoguanidinium 5-nitrotetrazolate (20)

Finely powdered **19** was stored in a desiccator over phosphorous pentoxide for 1 week. Crystals suitable for x-ray structure determination were obtained by slow diffusion of diethyl ether into an anhydrous acetonitrile solution of **20**. mp 96 °C (DSC); IR (KBr, cm^{-1}) $\widetilde{v}$ = 3369(m), 3334(s), 3295(s), 3260(m), 3197(m), 3127(m), 2839(w), 2721(w), 2451(w), 2212(w), 1685(s), 1590(m), 1536(s), 1507(w), 1438(m), 1414(m), 1375(m), 1311(m), 1212(w), 1180(w), 1143(m), 1132(m), 1039(m), 1028(m), 985(m), 927(m), 835(m), 740(w), 666(w), 632(w), 579(w); Raman (200 mW, 25 °C, cm^{-1}) $\widetilde{v}$ = 3294(3), 2986(5), 1688(4), 1638(2), 1534(9), 1439(4), 1415(100), 1316(7), 1204(2), 1181(3), 1153(6), 1054(43), 1042(30), 1029(12), 886(10), 839(12), 773(4), 639(2), 535(4), 447(4), 406(7), 330(3), 254(8), 197(6); C$_2$H$_9$N$_{11}$O$_2$ (219.20) calcd.: C 11.0, H 4.1, N 70.3 %; found: C 11.0, H 4.3, N 70.4 %.

1,4-dimethyl-5-aminotetrazolium 5-nitrotetrazolate (21)

To a stirred solution of 2.45 g (21.7 mmol) **5** in 25 mL THF in a 100 mL Schlenk flask were added 3.03 g (21.5 mmol) **13** and an additional 35 mL of THF. Ammonia was evolved immediately. The resulting suspension was then, under a gentle flow of nitrogen and a reflux condenser fitted with a paraffin oil bubbler, heated to reflux. The solution was refluxed carefully (so that no solvent was lost) for ~2 hrs under a gentle flow of nitrogen until no more ammonia was evolved. The flask was then allowed to cool to room temperature under nitrogen. The resulting fine white suspension was then vacuum filtered and dried on air yielding 4.72 g (20.7 mmol, 96%). Crystals suitable for X-ray diffraction were obtained by diffusing diethyl ether into a methanol solution of **21** overnight. mp 190 °C (DSC); IR (KBr, cm^{-1}) $\widetilde{v}$ = 3387(w), 3349(m), 3319(m), 3267(w), 3175(w), 3031(m), 1690(vs), 1531(s), 1505(w), 1439(m), 1418(m), 1392(m), 1314(m), 1257(w), 1185(w), 1164(w), 1152(w), 1056(m), 1028(m), 1006(w), 838(m), 790(w), 776(m), 680(m), 653(w); Raman (200 mW, 25

°C, cm^{-1}) $\tilde{v}$ = 3340(1), 3240(3), 2454(0), 1861(1), 1685(2), 1645(1), 1553(3), 1536(6), 1441(4), 1416(100), 1341(3), 1318(4), 1198(1), 1179(2), 1163(4), 1137(3), 1056(52), 1040(35), 1028(11), 884(8), 838(7), 772(3), 637(2), 537(5), 447(2), 399(2), 257(5), 215(4), 140(5); ^{1}H NMR CD$_3$OD, 25 °C) δ 4.98 (s, 2H, -NH$_2$), 3.85 (s, 6H, N-CH$_3$); ^{13}C NMR (CD$_3$OD, 25 °C) δ 167.9 (*C*10), 148.9 (*C*5), 33.3 (N-*CH*$_3$); ^{14}N NMR (CD$_3$OD, 25 °C) δ 8 (*N*6/9, $v_{1/2}$ = 430 Hz), -4 (*N*10, $v_{1/2}$ = 10 Hz), -26 (*N*2/3 $v_{1/2}$ = 30 Hz) -73 (*N*7/8 $v_{1/2}$ = 300 Hz), -182 (*N*1/4 $v_{1/2}$ = 1200 Hz), -318 (N5 $v_{1/2}$ = 950 Hz); *m/z* (FAB$^-$, xenon, 6 keV, m-NBA matrix) [NT]$^-$ 114; *m/z* (FAB$^+$, xenon, 6 keV, m-NBA matrix) [DMAT]$^+$ 114; C$_4$H$_8$N$_{10}$O$_2$ (228.2) calcd.: C 21.1, H 3.5, N 61.4 %; found: C 20.9, H 3.6, N 61.2 %.

2.5 References

(1)   Bellamy, A. J., FOX-7 (1,1-Diamino-2,2-dinitroethene). In *High Energy Density Materials*, 1st ed.; Klapötke, T. M., Ed.; Structure & Bonding; Springer-Verlag: Berlin, 2007; 125, 1-33.

(2)   Cady, H. H.; Larson, A. C., *Acta Crystallogr.*, **1965,** *18*, 485-496.

(3)   Xue, H.; Shreeve, J. M., *Adv. Mater. (Weinheim, Ger.)*, **2005,** *17*, 2142-2146.

(4)   Sikder, A. K.; Sikder, N., *J. Haz. Mater.*, **2004,** *112*, 1-15.

(5)   Xue, H.; Twamley, B.; Shreeve, J. M., *Inorg. Chem.*, **2005,** *44*, 7009-7013.

(6)   von Denffer, M.; Klapötke, T. M.; Kramer, G.; Spieß, G.; Welch, J. M.; Heeb, G., *Propellants, Explos., Pyrotech.*, **2005,** *30*, 191-195.

(7)   Galvez-Ruiz, J. C.; Holl, G.; Karaghiosoff, K.; Klapötke, T. M.; Löhnwitz, K.; Mayer, P.; Nöth, H.; Polborn, K.; Rohbogner, C. J.; Suter, M.; Weigand, J. J., *Inorg. Chem.*, **2005,** *44*, 4237-4253.

(8)   Galvez-Ruiz, J. C.; Holl, G.; Karaghiosoff, K.; Klapötke, T. M.; Löhnwitz, K.; Mayer, P.; Nöth, H.; Polborn, K.; Rohbogner, C. J.; Suter, M.; Weigand, J. J., *Inorg. Chem.*, **2005,** *44*, 5192.

(9)   Stadler, C.; Daub, J.; Kohler, J.; Saalfrank, R. W.; Coropceanu, V.; Schunemann, V.; Ober, C.; Trautwein, A. X.; Parker, S. F.; Poyraz, M.; Inomata, T.; Cannon, R. D., *J. Chem. Soc., Dalton Trans.*, **2001**, 3373-3383.

(10)   Percival, D. F.; Herbst, R. M., *J. Org. Chem.*, **1957,** *22*, 925-933.

(11)   Klapötke, T. M.; Karaghiosoff, K.; Mayer, P.; Penger, A.; Welch, J. M., *Propellants, Explos., Pyrotech.*, **2006,** *31*, 188-195.

(12)   von Herz, E. US Patent 2066954, 1937.

(13)   Redman, L. D.; Spear, R. J. Report MRL-R-901; Materials Research Laboratory: Australia, 1983; 1-27.

(14)   Gilligan, W. H.; Kamlet, M. J. Report NSWC/WOL/TR 76-146; White Oak Laboratory: Silver Spring, MD, USA, 1976; 1-15.

(15)   Gilligan, W. H. US Patent 4093623, 1977.

(16)   Spear, R. J.; Elischer, P. P., *Aust. J. Chem.*, **1982,** *35*, 1-13.

(17)   Huynh, M. H. V.; Hiskey, M. A.; Meyer, T. J.; Wetzler, M., *Proc. Natl. Acad. Sci. USA.*, **2006,** *103*, 5409-5412.

(18)   Koldobskii, G. I.; Soldatenko, D. S.; Gerasimova, E. S.; Khokhryakova, N. R.; Shcherbinin, M. B.; Lebedev, V. P.; Ostrovskii, V. A., *Russ. J. Org. Chem. (Engl. Trans.)*, **1997,** *33*, 1771-1783.

(19)   Boese, R.; Klapötke, T. M.; Mayer, P.; Verma, V., *Propellants, Explos., Pyrotech.*, **2006,** *31*, 263-268.

(20)   Gao, H.; Ye, C.; Piekarski, C. M.; Shreeve, J. M., *J. Phys. Chem.*, **2007,** *C111*, 10718-10731.

(21)   Xue, H.; Gao, H.; Twamley, B.; Shreeve, J. M., *Chem. Mater.*, **2007,** *19*, 1731-1739.

(22)   Xue, H.; Gao, H.; Twamley, B.; Shreeve, J. M., *Eur. J. Inorg. Chem.*, **2006,** *15*, 2959-2965.

(23)   Xue, H.; Gao, Y.; Twamley, B.; Shreeve, J. M., *Inorg. Chem.*, **2005,** *44*, 5068-5072.

(24)   Hammerl, A.; Hiskey, M. A.; Holl, G.; Klapötke, T. M.; Polborn, K.; Stierstorfer, J.; Weigand, J. J., *Chem. Mater.*, **2005,** *17*, 3784-3793.

(25)   Haiges, R.; Schroer, T.; Yousuffudin, M.; Christe, K. O., *Z. Anorg. Allg. Chem.*, **2005,** *631*, 2691-2695.

(26)   Ang, H.-G.; Fraenk, W.; Karaghiosoff, K.; Klapötke, T. M.; Mayer, P.; Nöth, H.; Sprott, J.; Warchhold, M., *Z. Anorg. Allg. Chem.*, **2002,** *628*, 2894-2900.

(27)   Lee, K. Y.; Coburn, M. D., *J. Energ. Mater.*, **1983,** *1*, 109-122.

(28)   Stierstorfer, J. Unpublished Results. Diploma, LMU, Munich, 2006.

(29)   Colthup, N. B.; Daly, L. H.; Wiberley, S. E., *Introduction to infrared and Raman spectroscopy*. Academic Press: Boston, 1990.

(30)   Williamson, K.; Li, P.; Devlin, J. P., *J. Chem. Phys.*, **1968,** *48*, 3891-3896.

(31)   Fernandes, J. R.; Ganguly, S.; Rao, C. N. R., *Spectrochim. Acta*, **1979,** *35A*, 1013-1020.

(32)   Cohn, H., *J. Chem. Soc.*, **1952**, 4282-4284.

(33)   Redlich, O.; Holt, E. K.; Bigeleisen, J., *J. Am. Chem. Soc.*, **1944,** *55*, 13-16.

(34)   Christe, K. O.; Wilson, W. W.; Petrie, M. A.; Michels, H. H.; Bottaro, J. C.; Gilardi, R., *Inorg. Chem.*, **1996,** *35*, 5068-5071.

(35)   Scott, A. P.; Radom, L., *J. Phys. Chem.*, **1996,** *100*, 16502-16513.

(36)   Jeffrey, G. A., *An Introduction to Hydrogen Bonding*. Oxford University Press: New York, 1997.

(37)   Bocian, W.; Jazwinski, J.; Kozminski, W.; Stefaniak, L.; Webb, G. A., *J. Chem. Soc., Perkin Trans. 2*, **1994**, 1327-1332.

(38)   Martin, G. J.; L., M. M.; Gouesnard, J.-P., *^{15}N-NMR Spectroscopy*. Springer: Berlin, Germany, 1981.

(39)   Bernhardt, S.; Crawford, M.-J.; Klapötke, T. M.; Radies, H. *Proceedings of The 10th New Trends in Research of Energetic Materials Seminar*, Pardubice, Czech Republic, Apr. 25-27, 2007; Ottis, J.; Krupka, M., Eds. University of Pardubice, 2007: Vol. 2, 532-540.

(40)   Darwich, C.; Klapötke, T. M.; Welch, J. M.; Suceska, M., *Propellants, Explos., Pyrotech.*, **2007,** *32*, 235-243.

(41)   Jeffrey, G. A.; Lewis, L., *Carbohydr. Res.*, **1978,** *60*, 179-182.

(42)   Grigoriev, M. S.; Moisy, P.; Den Auwer, C.; Charushnikova, I. A., *Acta Crystallogr.*, **2005,** *E61*, i216-i217.

(43)   Katrusiak, A.; Szafranski, M., *J. Mol. Struct.*, **1996,** *378*, 205-223.

(44)   Katrusiak, A.; Szafranski, M., *Acta Crystallogr.*, **1994,** *C50*, 1161-1163.

(45)   Steinhauser, G.; Crawford, M.-J.; Darwich, C.; Klapötke, T. M.; Miro Sabate, C.; Welch, J. M., *Acta Crystallogr.*, **2007,** *E63*, o3100-o3101.

(46)   Göbel, M.; Klapötke, T. M., *Z. Anorg. Allg. Chem.*, **2007,** *633*, 1006-1017.

(47)   Jin, X.; Shao, M.; Huang, H.; Wang, J.; Zhu, Y., *Huaxue Tongbao*, **1982**, 336-337.

(48)   Gaponik, P. N.; Ivashkevich, O. A.; Krasitskii, V. A.; Tuzik, A. A.; Lesnikovich, A. I., *Russ. J. Gen. Chem. (Engl. Transl.)*, **2002,** *72*, 1457-1462.

(49)   Morosin, B.; Dunn, R. G.; Assink, R.; Massis, T. M.; Fronabarger, J.; Duesler, E. N., *Acta Crystallogr.*, **1997,** *C53*, 1609-1611.

(50)   Charalambous, J.; Georgiou, G. C.; Henrick, K.; Bates, L. R.; Healey, M., *Acta Crystallogr.*, **1987,** *C43*, 659-661.

(51)   John, E. O.; Willett, R. D.; Scott, B.; Kirchmeier, R. L.; Shreeve, J. M., *Inorg. Chem.*, **1989,** *28*, 893-897.

(52)   Becker, T. M.; Krause-Bauer, J. A.; Homrighausen, C. L.; Orchin, M., *Polyhedron*, **1999,** *18*, 2563-2571.

(53)   Arp, H. P. H.; Decken, A.; Passmore, J.; Wood, D. J., *Inorg. Chem.*, **2000,** *39*, 1840-1848.

(54)   Graeber, E. J.; Morosin, B., *Acta Crystallogr.*, **1983,** *C39*, 567-570.

(55)   Ernst, V.; Klapötke, T. M.; Stierstorfer, J., *Z. Anorg. Allg. Chem.*, **2007,** *633*, 879-887.

(56)   Bernstein, J.; Davis, R. E.; Shimoni, L.; Chang, N.-L., *Angew. Chem., Int. Ed. Eng.*, **1995,** *34*, 1555-1573.

(57)   Motherwell, W. D. S.; Shields, G. P.; Allen, F. H., *Acta Crystallogr.*, **2000,** *B56*, 466-473.

(58)   RPLUTO. http://www.ccdc.cam.ac.uk/free_services/free_downloads/ (24.11.2007),

(59)   Motherwell, W. D. S.; Shields, G. P.; Allen, F. H., *Acta Crystallogr.*, **1999,** *B55*, 1044-1056.

(60)   Miró Sabaté, C.; Klapötke, T. M. *Proceedings of The 10th New Trends in Research of Energetic Materials Seminar*, Pardubice, Czech Republic, Apr. 25-27, 2007; Ottis, J.; Krupka, M., Eds. University of Pardubice, 2007: Vol. 2, 230-239.

(61)   Jenkins, H. D. B.; Tudela, D.; Glasser, L., *Inorg. Chem.*, **2002,** *41*, 2364-2367.

(62)   Jenkins, H. D. B.; Roobottom, H. K.; Passmore, J.; Glasser, L., *Inorg. Chem.*, **1999,** *38*, 3609-3620.

(63)   M. Suceska, *Propellants, Explos., Pyrotech.*, **1991,** *16*, 197-202.

(64)   Koehler, J.; Mayer, R., *Explosivstoffe*. Wiley-VCH: Weinheim, Germany, 1998.

(65)   *UN Recommendations on the Transport of Dangerous Goods, Manual of Tests and Criteria*. United Nations: New York, 2003.

(66)   http://webbook.nist.gov.

(67)   Kamlet, M. J.; Ablard, J. E., *J. Chem. Phys.*, **1968,** *48*, 36-42.

(68)   Kamlet, M. J.; Dickinson, C., *J. Chem. Phys.*, **1968,** *48*, 43-50.

(69)   Kamlet, M. J.; Jacobs, S. J., *J. Chem. Phys.*, **1968,** *48*, 23-35.

(70)   http://www.parrinst.com.

(71)   *ABSPACK, CrysAlis CCD and CrysAlis RED*, 1.171; Oxford Diffraction Ltd: Abingdon, Oxfordshire, England, 2006.

(72)   Sheldrick, G. M. *Programs for Crystal Structure Analysis (Release 97-2)*, Goettingen, Germany, 1998.

(73)   Altomare, A.; Burla, M. C.; Camalli, M.; Cascarano, G. L.; Giacovazzo, C.; Guagliardi, A.; Moliterni, A. G. G.; Polidori, G.; Spagna, R., *J. Appl. Crystallogr.*, **1999, *32*,** 115-119.

(74)   Frisch, M. J.; Trucks, G. W.; Schlegel, H. B.; Scuseria, G. E.; Robb, M. A.; Cheeseman, J. R.; Montgomery, J., J. A.; Vreven, T.; Kudin, K. N.; Burant, J. C.; Millam, J. M.; Iyengar, S. S.; Tomasi, J.; Barone, V.; Mennucci, B.; Cossi, M.; Scalmani, G.; Rega, N.; Petersson, G. A.; Nakatsuji, H.; Hada, M.; Ehara, M.; Toyota, K.; Fukuda, R.; Hasegawa, J.; Ishida, M.; Nakajima, T.; Honda, Y.; Kitao, O.; Nakai, H.; Klene, M.; Li, X.; Knox, J. E.; Hratchian, H. P.; Cross, J. B.; Bakken, V.; Adamo, C.; Jaramillo, J.; Gomperts, R.; Stratmann, R. E.; Yazyev, O.; Austin, A. J.; Cammi, R.; Pomelli, C.; Ochterski, J. W.; Ayala, P. Y.; Morokuma, K.; Voth, G. A.; Salvador, P.; Dannenberg, J. J.; Zakrzewski, V. G.; Dapprich, S.; Daniels, A. D.; Strain, M. C.; Farkas, O.; Malick, D. K.; Rabuck, A. D.; Raghavachari, K.; Foresman, J. B.; Ortiz, J. V.; Cui, Q.; Baboul, A. G.; Clifford, S.; Cioslowski, J.; Stefanov, B. B.; Liu, G.; Liashenko, A.; Piskorz, P.; Komaromi, I.; Martin, R. L.; Fox, D. J.; Keith, T.; Al-Laham, M. A.; Peng, C. Y.; Nanayakkara, A.; Challacombe, M.; Gill, P. M. W.; Johnson, B.; Chen, W.; Wong, M. W.; Gonzalez, C.; Pople, J. A. *Gaussian 03, Revision C.02*, Gaussian, Inc.: Wallingford, CT, 2004.

(75)   Miehlich, B.; Savin, A.; Stoll, H.; Preuss, H., *Chem. Phys. Lett.*, **1989, *157*,** 200-206.

(76)   Pople, J. A.; Seeger, R.; Krishnan, R., *Int. J. Quantum Chem., Symp.*, **1977, *11*,** 149-163.

(77)   Rick, A. K.; Dunning, T. H.; Robert, J. H., *J. Chem. Phys.*, **1992, *96*,** 6796-6806.

(78)   Kirk, A. P.; David, E. W.; Dunning, T. H., *J. Chem. Phys.*, **1994, *100*,** 7410-7415.

(79)   Klapoetke, T. M.; Schulz, A., *Quantum Chemical Methods in Main Group Chemistry*. Wiley: Chichester, 1998.

(80)   Garrison, J. A.; Herbst, R. M., *J. Org. Chem.*, **1957,** *22*, 278-283.

3   FOX-7

3.1   Introduction

Good performance (D = 8870 m/s, P_{det} = 34.0 GPa)[1] and low sensitivity (25 J BAM[2] impact, >350 N BAM friction and 4.5 J ignition electrostatic discharge) are two important properties of 1,1-diamino-2,2-dinitroethene, $C_2H_4N_4O_4$ (FOX-7), a recently developed low sensitivity energetic material.[1] FOX-7 (I) has the empirical formula $CH_2N_2O_2$, and thus has the same basic chemical composition as the widely used secondary explosives RDX (II) and HMX (III). However, at the structural level, as evidenced in Scheme 3.1 below, I differs substantially from II and III.

Scheme 3.1. Structural formulae of FOX-7 (I), RDX (II) and HMX (III)

The structural formula of I consists of highly polar amino and nitro groups bound to a two-carbon ethene backbone forming a "push-pull" compound in which the two electron donating amino groups form the "head" of the molecule and the two electron withdrawing nitro groups the "tail." On the other hand, compounds II and III are low polarity molecules composed of alternating secondary nitramine moieties and methylene groups. Due to these differences in molecular structure and their effects on solid-state structure, the properties of FOX-7 differ dramatically from those of HMX and RDX although their basic chemical compositions are the same.

Detailed structural and thermoanalytical investigations of FOX-7 can be used to clarify the physical grounds for its unusual insensitivity to physical stimuli. In addition to enhancing the understanding of one compound, it is hoped that insight gained from these investigations

might also find use in identifying other potential target molecules for synthesis as insensitive energetic materials. The single crystal X-ray structures of FOX-7 at low temperature (173 K)[3] and at room temperature (295 K)[4] have been determined by previous investigators. However, detailed information concerning changes in the structure of a material as it approaches the physical extremes of detonation (high temperature and pressure) should also provide significant insight into how the molecular properties of FOX-7 affect its energetic properties.

Initial investigations indicated that FOX-7 exists in several different forms in the solid state depending on temperature.[5-11] Different forms or molecular arrangements within crystals of the same material are known as polymorphs. Polymorphism is a common phenomenon in both organic and inorganic structures stemming from the small (with respect to chemical bonds) energetic differences between different organizations of molecules of a substance in the solid state. Energetic materials often crystallize in several different arrangements which in turn have different physical properties. Since differences in polymorph density can result in considerable differences in energetic performance as well as sensitivity to physical stimuli, thorough studies of all of possible forms of an energetic material are critical for both safety and performance considerations.[12]

Therefore, the structure of all observed polymorphs of FOX-7 and the energetics of transitions from one form to another were studied in depth using temperature resolved vibrational spectroscopy, temperature resolved X-ray diffraction (single crystal and powder) and thermal analysis. Thermal analysis by differential scanning calorimetry (DSC) provides information about transition temperatures, enthalpies and thus entropies, as well as transition nature (reversibility). Although, in the case of FOX-7, temperature dependent infrared (IR) measurements would seem to be an excellent tool for examining changes in hydrogen bonding with temperature and polymorph, sample preparation alone can affect the IR spectra of FOX-7. FT-IR spectra were measured using the attenuated total reflection method (neat

powder sample), as a KBr pellets and as a thin film on 2.0 mm NaCl plate. The spectra measured by these three methods are shown below in Figure 3.1 and it is reasonably clear that different sample preparations give different spectra.
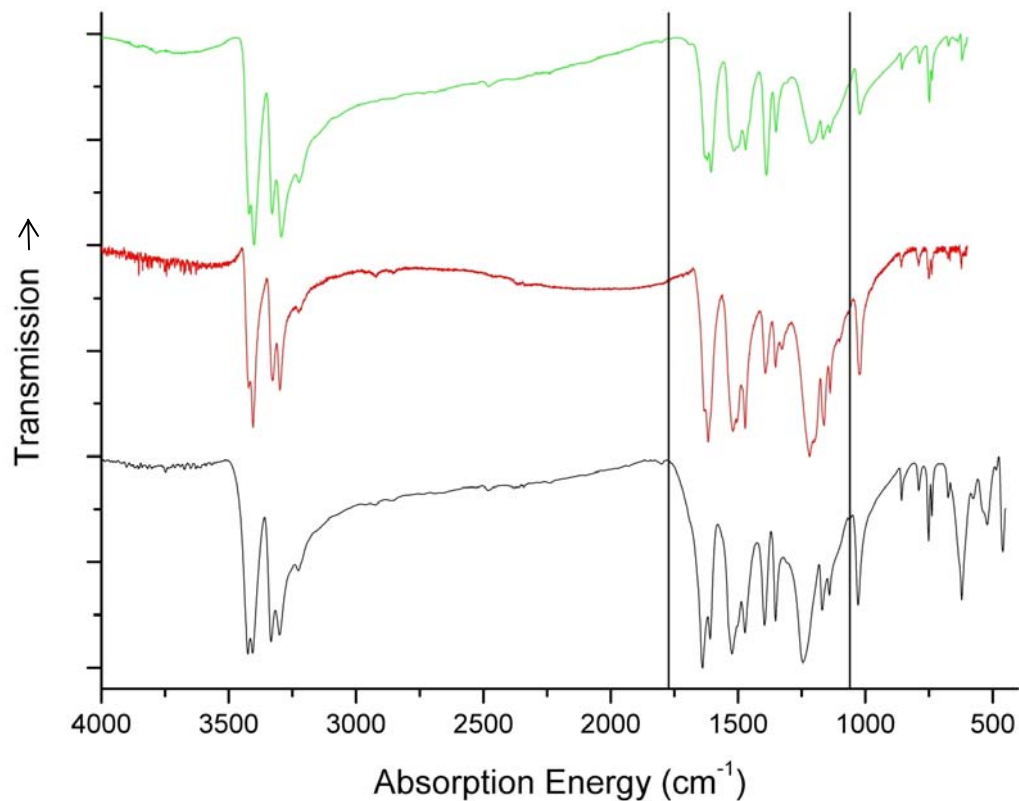
Figure 3.1. FT-IR spectra of FOX-7 at room temperature as a neat sample by ATR (green plot), as a thin film on a 2.0 mm NaCl plate (red plot) and as a KBr pellet (black plot). Note the subtle differences in absorptions in the region (1770-1060 cm^{-1}) bounded by the vertical black lines.

In addition, upon heating, the FTIR spectra of none of the samples show significant differences. Therefore, Raman rather than IR studies were utilized in this study. Raman spectra of neat material in crystalline form may be measured without any sample preparation making Raman spectra the more useful vibrational spectroscopic method for this study. Unfortunately the N-H stretching vibrations so characteristic to hydrogen bonding are only weakly observed in Raman spectra and are quickly obscured by infrared luminescence upon

heating above ~50 ºC. Diffraction methods are the classic means by which structural information is obtained in the solid state. Although microcrystalline powders are easier to obtain and measure, structural information is more difficult to extract from powder diffraction patterns, whereas single crystals of a suitable size may be more difficult to obtain but the structural information is often much more easily derived.[13] In this study, both temperature resolved powder and single crystal diffraction techniques were applied.

3.2 Results and Discussion

3.2.1   DSC

In preparation for temperature resolved spectroscopic and diffraction studies, FOX-7 was analyzed using differential scanning calorimetry (DSC) to confirm the properties (polymorphism and decomposition temperature) previously reported. [5, 7-9, 11] Additional studies were necessary at the beginning of this study due to considerable inconsistency in the literature concerning the behavior of FOX-7 upon heating. In the intervening time, several studies have appeared confirming the results of our and other initial DSC and DTA studies, thus clarifying and independently verifying the behavior of FOX-7 upon heating.[6, 10] In addition, information about the nature and energetics of the transitions was also obtained from the initial DSC measurements.

In the thermoanalytical studies, DSC traces from 323 to 573 K for a series of 16 samples of FOX-7 were acquired. Four small (~1-2 mg) samples of macrocrystalline (recrystallized) FOX-7 were placed in open aluminum sample pans. One sample was heated over the temperature range with $\beta = 1$ K/min, a second with $\beta = 2$ K/min, the third with $\beta = 5$ K/min and the fourth with $\beta = 10$ K/min. This series of measurements was repeated with samples of the same size and constitution but in sealed aluminum sample pans with 1 μm holes for gas evolution. The eight measurements described were then repeated with larger (~5 mg) samples of macrocrystalline material yielding a series of 16 measurements for which sample size, preparation and β were all varied. The results of the 16 DSC runs are tabulated in Appendix

Table 3, Table 4, Table 5 and Table 6. All measurements were made under a 20 mL/min flow of dry nitrogen with an empty aluminium sample pan (open or sealed depending on sample preparation) as reference. A full DSC trace (323 – 593 K) of a typical FOX-7 DSC curve is shown in Figure 3.2. A portion of a typical DSC trace focused on the two endothermic phase transitions (373 – 463 K) with temperatures and transition energies labeled is shown in Figure 3.3. The onsets and peak positions shown are averages of the appropriate values taken from all measurements of small samples made with $\beta = 1$ K/min or $\beta = 2$ K/min. The transition energies shown are again averages, but in this case of values obtained from measurements of large samples made with $\beta = 5$ K/min and $\beta = 10$ K/min. The data were treated in this way to extract the most precise temperature and energetic information possible, since smaller sample sizes and slower DSC heating rates give more accurate temperature information and large sample sizes and faster DSC heating rates give more accurate energetic information[14].
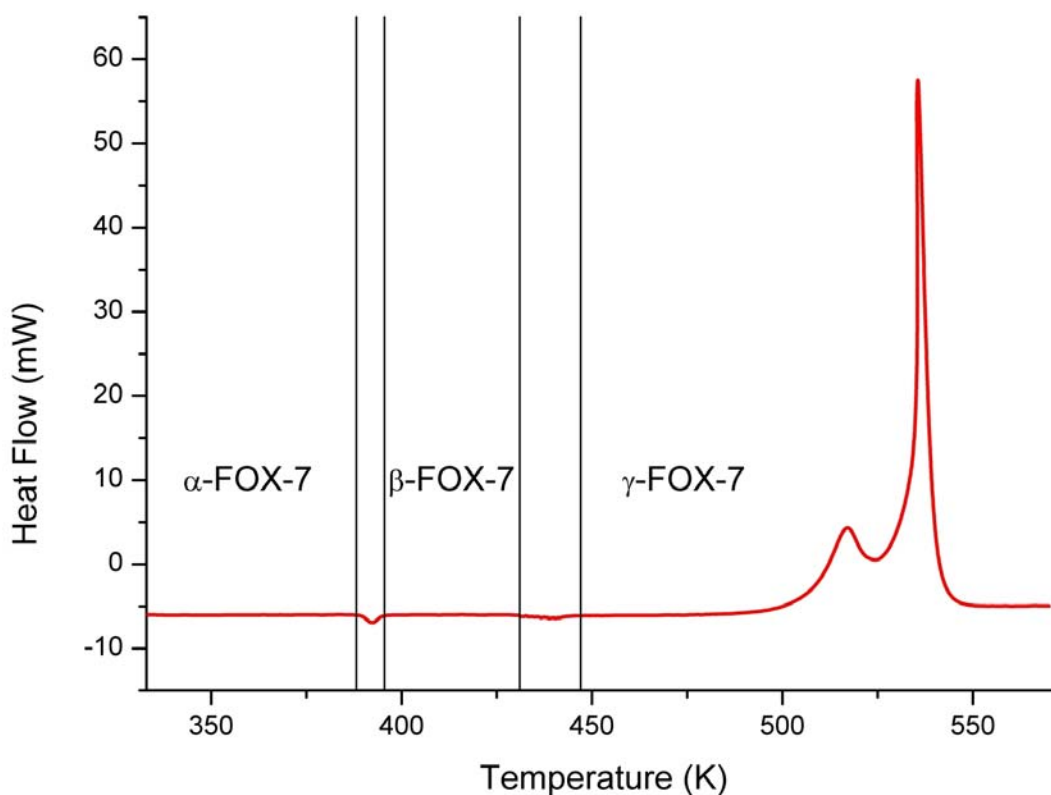
Figure 3.2. Full (323 K – 573 K) DSC trace measured for a large (~5 mg) sample of FOX-7 with β = 10 K/min.

The endothermic signal corresponding to the α – β phase transition occurs on average at 388(1) K with an onset of 387.1(4) K and an average $\Delta_{trs}H$ = + 18.1(4) J/g (2.68(8) kJ/mol) corresponding to an entropy increase, $\Delta_{trs}S = \Delta_{trs}H / T_{trs}$, = + 6.9 J/(K·mol). The β – γ phase transition occurs at ~435 K with an onset of ~430 K and $\Delta_{trs}H \approx$ + 20 J/g (3 kJ/mol) corresponding to an entropy change of ~ +7 J/(K·mole). Only approximate values for the transition temperature and energy are given for the β – γ phase transition because the DSC curves are not smooth at the β – γ transition temperature (see Figure 3.3). Therefore, neither the area between the heat flow curve and the baseline ($\Delta_{trs}H$) nor the inflection point of the heat flow curve during transition and therefore the onset temperature could be accurately

calculated. Regardless of heating rate, sample constitution (powder or crystals), size, or sample holder, a smooth curve at the β − γ transition temperature was not obtained.

The endothermic DSC peak for the α − β phase transition is sharp, smooth and highly symmetric. A slight change in the baseline heat flow is also observed on either side of the α − β phase transition due to heat capacity differences between the two polymorphs. Additionally previous studies have shown that the α − β transition is also reversible, indicating that the transition is mostly of displacive nature. The overall signal corresponding to the β − γ phase transition is broad, asymmetric and composed of a series of sharp, jagged endotherms, indicating a type of (reconstructive) transformation different than the displacive transition suggested for the α − β transformation. Also previous DSC studies have indicated that the β − γ phase transition is not fully reversible.

The roughness of the DSC curves during the β − γ transitions is likely a consequence of the "thermosalient effect," which causes crystals undergoing a phase transition to "jump" or "hop." In some cases crystals are reported to "jump" nearly 0.30 m.[12] The "thermosalient effect" in the β − γ phase transition of FOX-7 was observed using hotstage microscopy. During the α − β phase transition, small crystals of FOX-7 remained inert on the hotstage. However, the phase transition was clearly visible under the microscope since the crystals became increasingly clear as the transition from α- to β-FOX-7 progressed. When the crystals were heated to the β − γ transition temperature (~435 K, Figure 3), several larger crystals "jumped" sharply out of the field of magnification and several smaller crystals "jumped" from the center of the field of magnification to the edges. Although the motion of the crystals observed was at most ~0.01 m, this is certainly significant enough to effect a non-smooth DSC curve. When crystals undergoing β − γ transition move on the DSC sensor, a rapid change in thermal contact occurs and a spike in measured heat flow is consequently registered. Nevertheless, $\Delta_{trs}H(\beta − \gamma)$ and $\Delta_{trs}S(\beta − \gamma)$ can be approximated and are similar to the values determined for the α − β phase transition (see above). A full structural

investigation of all three polymorphs of FOX-7 should shed light on the differences in the DSC peaks and transition behaviors observed.
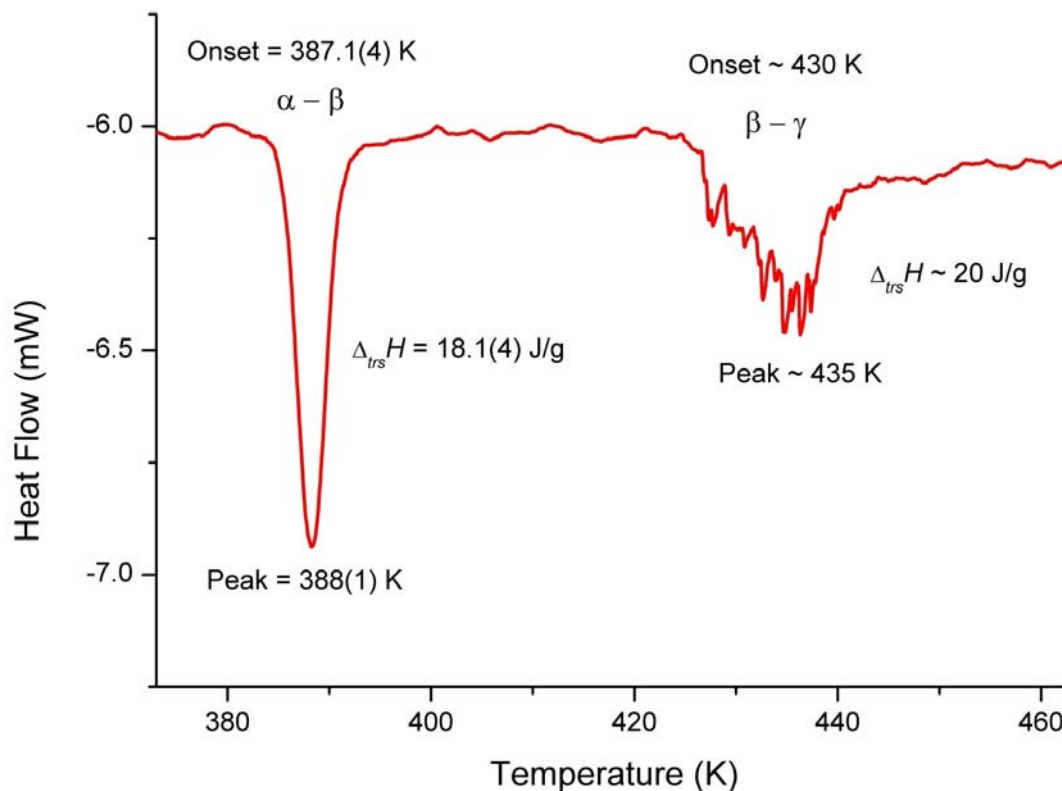
Figure 3.3. Typical DSC trace of FOX-7 between 373 and 463 K with endotherms corresponding to the α – β and β – γ phase transitions at 388(1) K and ~435 K, respectively.

3.2.2 Temperature resolved qualitative analysis of bulk material

The behavior of bulk (macrocrystalline and fine powder) FOX-7 was, as mentioned above, studied in situ upon heating using temperature resolved Raman spectroscopy and X-ray powder diffraction. A variety of both spectroscopic and diffraction experiments were carried out. Initially, Raman spectra of macrocrystalline samples of clear yellow α-FOX-7 were measured and the sample was then "tempered" in an oven overnight at ~490 K. The samples were removed from the oven, allowed to cool to room temperature at which point the crystals appeared no longer clear, but milky and slightly brownish. A Raman spectrum of this material was measured indicating subtle changes in the material. A comparison of the room

temperature Raman spectra of FOX-7 before and after heating is shown in Figure 3.4. The differences in Raman spectra before and after heating also seem to support the observation that the transition from β-FOX-7 to γ-FOX-7 is irreversible in nature as shown by previous thermal analyses.[10, 15] A "tempered" sample of γ-FOX-7 could therefore be quenched to room temperature (or below) for analysis. The process of measurement followed by tempering and remeasurement was repeated for finely powdered FOX-7 yielding the same result. Furthermore, any tempered sample which was submitted to physical stress (grinding) or recrystallized, yielded material with Raman spectra identical to those of the initial sample. Lastly, the ^{1}H and ^{13}C solution NMR spectra of the "tempered" material are also identical to those of the starting material, thus confirming that no irreversible chemical change had taken place during the heating process.[16]
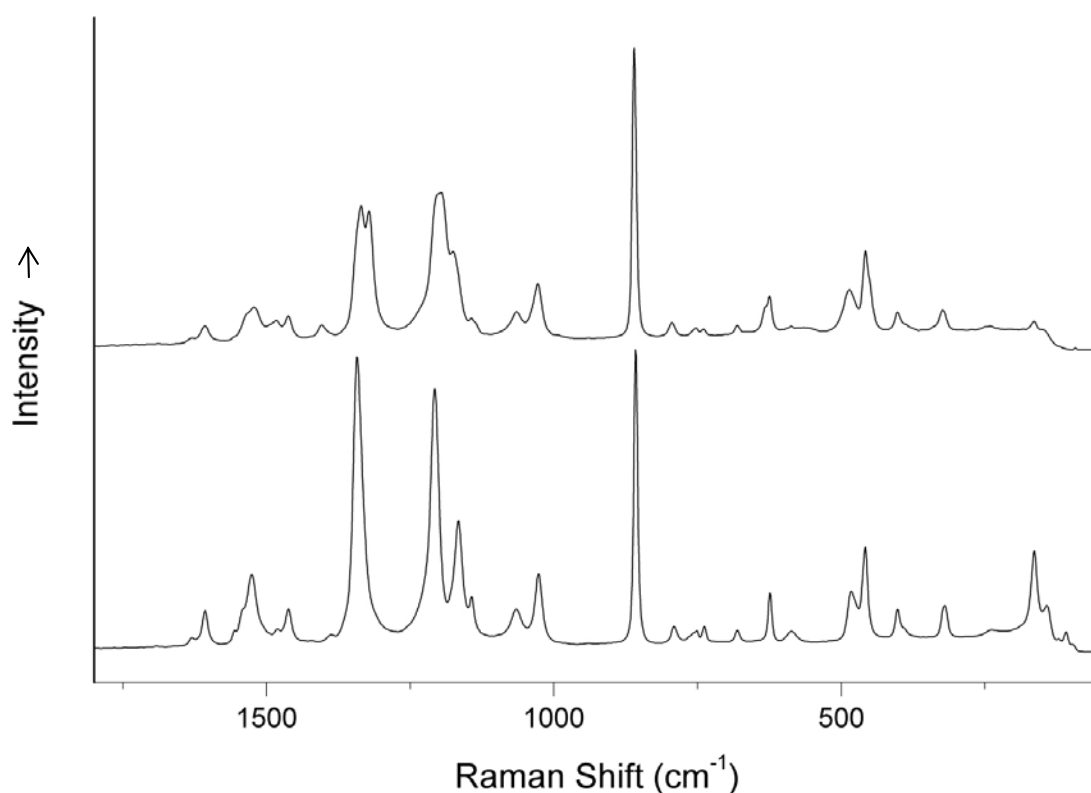
Figure 3.4. Raman spectra (1800-50 cm^{-1}) of tempered (γ-FOX-7, top) and untempered (α-FOX-7, bottom).

Initial powder studies were also carried out along similar lines. A sample of finely ground and sieved α-FOX-7 was loaded into a 0.5 mm Lindemann capillary. A diffraction pattern was measured using MoKα$_1$ (0.7093 Å) radiation. The capillary was then heated to ~490 K in an oven overnight and a second diffraction pattern was measured. Once again differences in the "tempered" and untempered material are observed. A second set of patterns was also measured using CuKα$_1$ (1.5406 Å) for attempts at a direct methods structure solution for γ-FOX-7. Comparisons of the CuKα$_1$ patterns before and after tempering are shown in Figure 3.5.
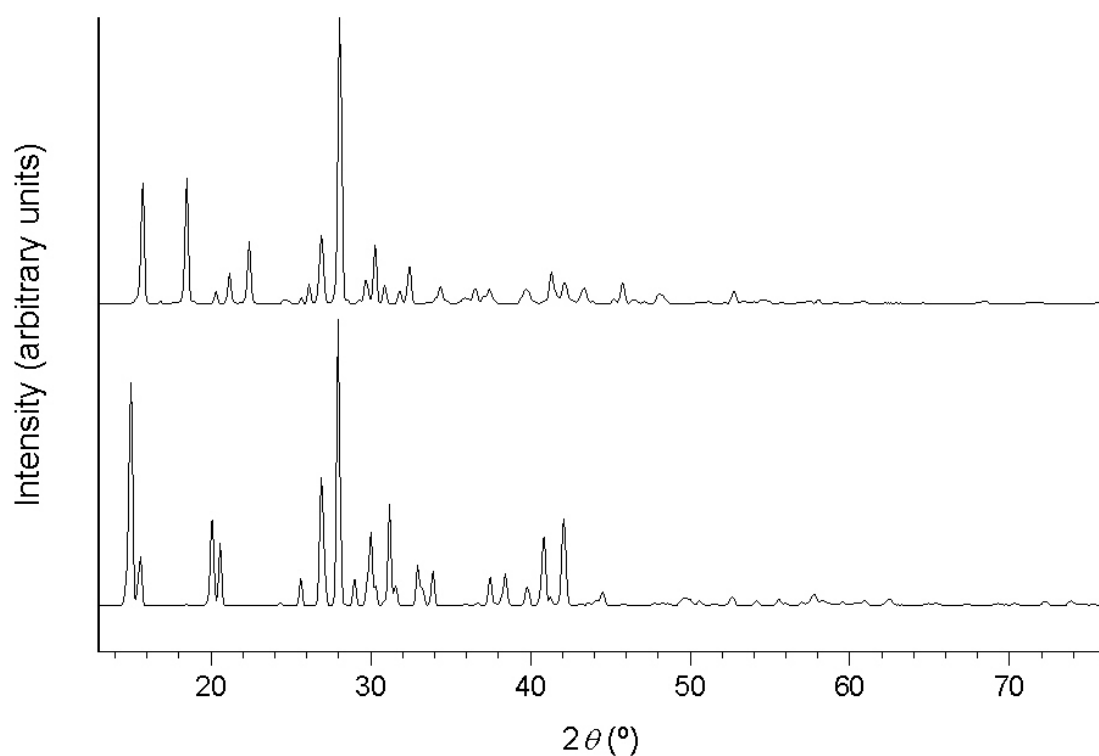
Figure 3.5. Guinier diffractograms (2θ = 13-76 °) of tempered (γ-FOX-7, top) and untempered (α-FOX-7, bottom) at room temperature measured with CuKα$_1$ radiation.

Following the initial room temperature Raman and powder diffraction studies of quenched γ-FOX-7, temperature dependent studies of FOX-7 starting at room temperature were undertaken. A series of Raman spectra were measured for samples of both macrocrystalline and finely powdered FOX-7 upon heating from 298 to 463 K. The spectra of

macrocrystalline and finely powdered material are nearly identical at all temperatures. The spectra also clearly show the α – β and β – γ phase transitions at the temperatures determined by DSC (Figure 3.6 and Figure 3.7).
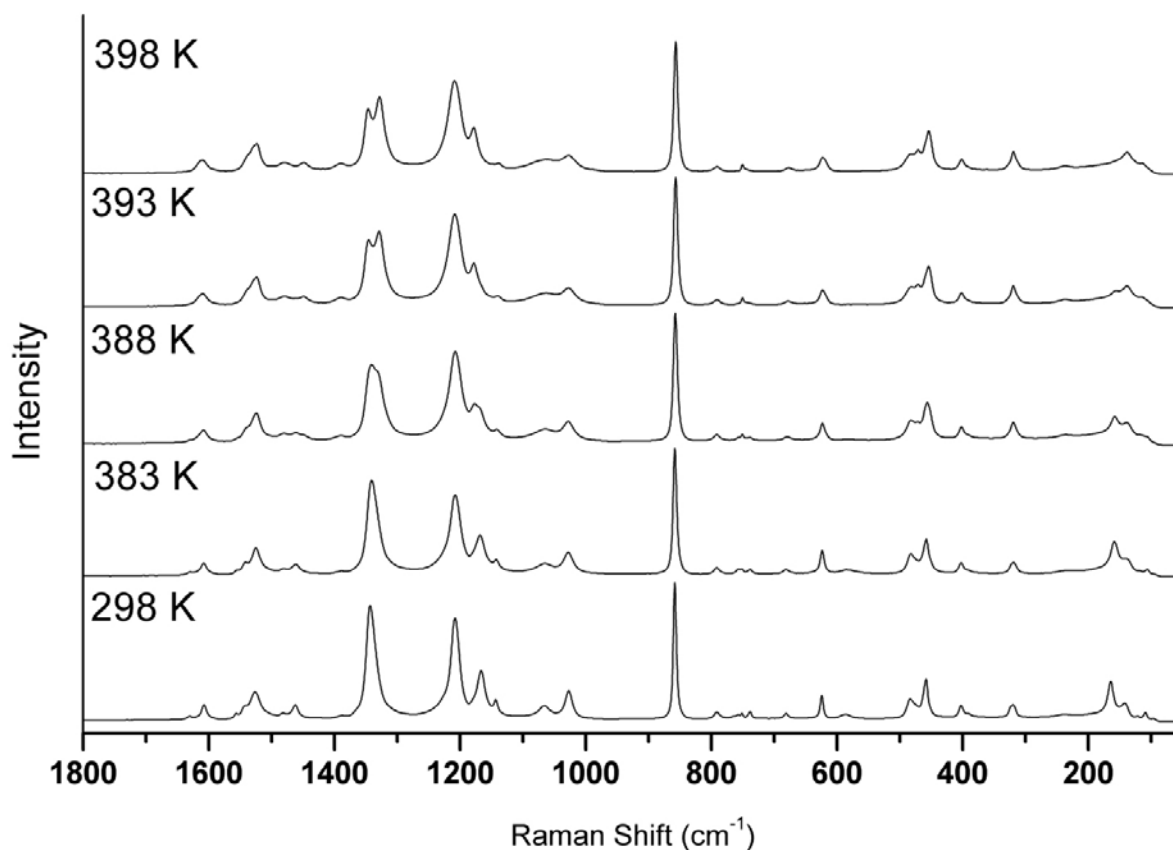
Figure 3.6. Stacked plots of Raman spectra of α- and β-FOX-7 over the temperature range 298 – 398 K.

Aside from the expected broadening ("softening") of the vibrations observed between the Raman spectra of FOX-7 upon heating, around the α – β transition temperature (388 K) determined by DSC, several distinct changes in the spectra are observed. The most obvious difference in the Raman spectra of α- and β-FOX-7 is the appearance of an intense peak at 1328 cm^{-1} in the spectrum of β-FOX-7. Many other subtle changes are observed in the Raman spectra of FOX-7 as it transforms from α- to β-FOX-7. These include the disappearance of the weak signals observed at 1556, 1461, 756 and 585 cm^{-1} in α-FOX-7 and

the appearance of new weak signals at 1450 and 471 cm^{-1} in β-FOX-7. Also, the apparent

shift of the medium strength signal at 1168 cm^{-1} in α-FOX-7 to 1178 cm^{-1} in β-FOX-7 seems

significant. Lastly, due to broadening the two lowest energy frequencies observed for α-

FOX-7 at room temperature are no longer observed for β-FOX-7 at 393 K.
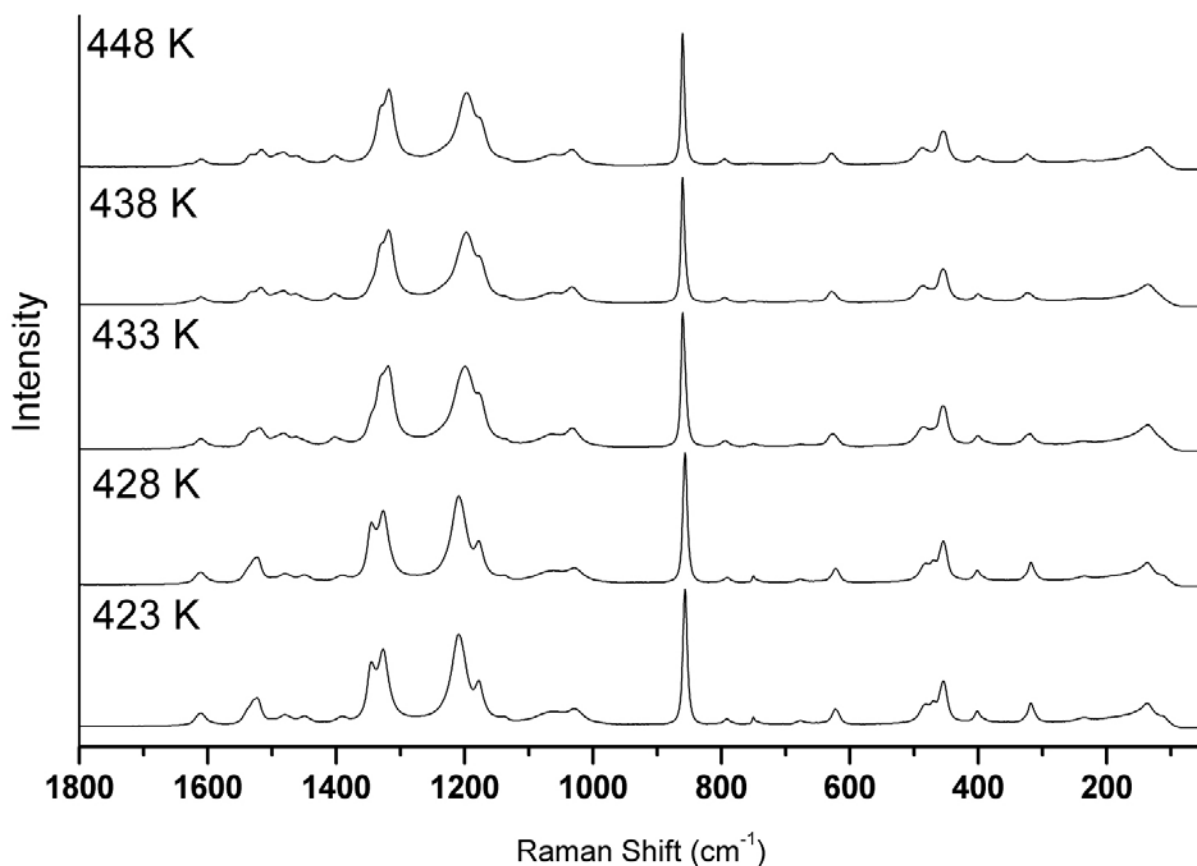
Figure 3.7. Stacked plots of Raman spectra of β- and γ-FOX-7 over the temperature range

423 – 448 K.

The β – γ phase transition in FOX-7 once again results in subtle changes in the Raman

spectra. Transition from β- to γ-FOX-7 results in an apparent decrease in the number of

Raman bands observed. The principal change observed is loss of the intense band at 1344

cm^{-1} in β-FOX-7 and the appearance of a shoulder on the intense band at 1327 cm^{-1} observed

at 1317 – 1319 cm^{-1} depending on temperature. More subtle changes include the apparent

shifting of the peak observed at 1209 cm^{-1} for β-FOX-7 to 1199 – 1197 cm^{-1} for γ-FOX-7

depending on temperature, the loss of low intensity signals at 1450, 1391 and 469 cm^{-1} in spectra of β-FOX-7 and the appearance and reappearance of weak signals at 1402 and 757 cm^{-1} in spectra of γ-FOX-7. Lastly several weak signals are not observed in spectra of γ-FOX-7 at 463 K due to broadening.

As a result of the initial studies and Raman data the behavior of FOX-7 on slow heating was also studied further using temperature resolved X-ray powder diffraction. Since $CuK\alpha_1$ radiation is more intense and therefore gives a better signal to noise ratio than $MoK\alpha_1$ radiation, more lines should be observed in diffractograms acquired using $CuK\alpha_1$ radiation. Therefore, more information should be available for quantitative structural analysis. Unfortunately, measurements at elevated temperature using $CuK\alpha_1$ radiation are complicated by the wide measurement angle ranges ($2\theta > 76$ °) necessitated by the longer wavelength of $CuK\alpha_1$ radiation. The heating element used to warm the sample surrounds the capillary to a certain degree and therefore two normalized measurements would be required at each temperature to assemble a diffraction pattern for the full measurable angle ranges. Since it is not possible to predict in advance whether or not a structural solution is possible from a given diffractogram and the process of measuring $CuK\alpha_1$ diffractograms for samples at elevated temperature is labor intensive, the temperature dependent studies were undertaken using $MoK\alpha_1$ radiation (Figure 3.8 and Figure 3.9).
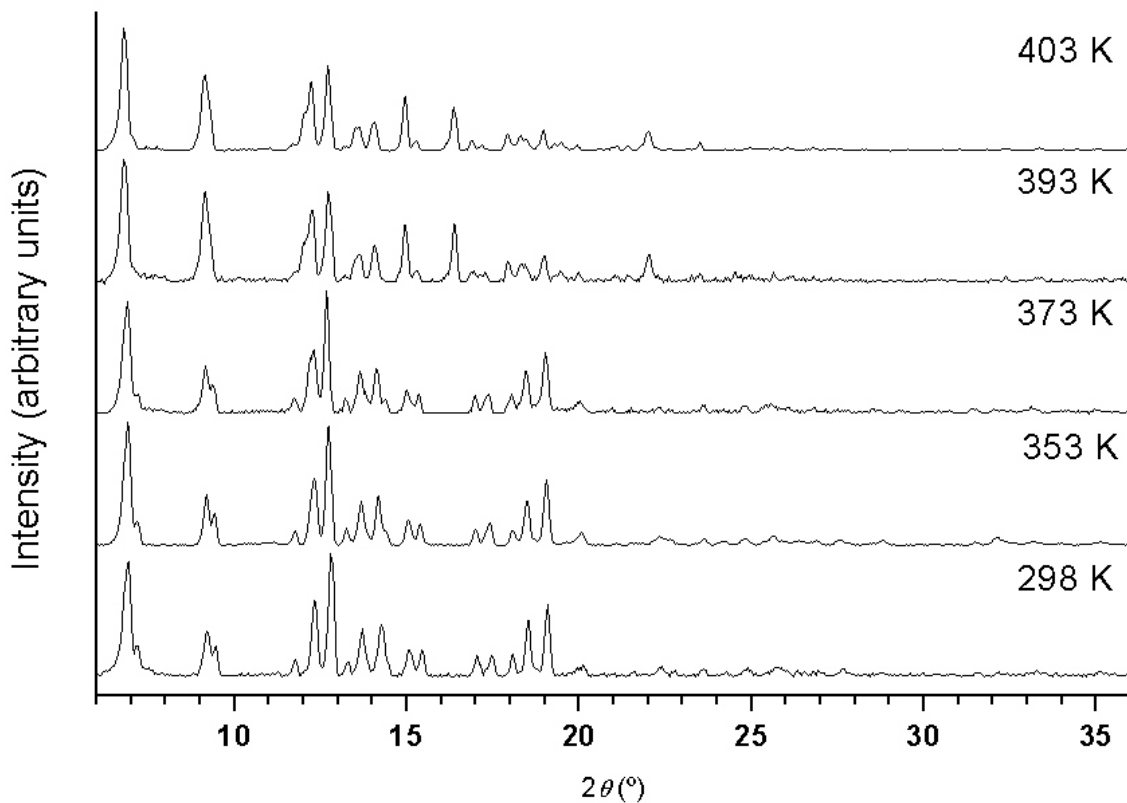
Figure 3.8. Stacked plots of Guinier diffractograms of α- and β-FOX-7 over temperature range 298 – 403 K measured with MoKα₁ radiation.

Upon initial inspection the low angle reflections observed for α- and β-FOX-7 appear very similar. However, close inspection shows differences in both the number of reflections and slight differences in reflection angle in the diffractograms of α- and β-FOX-7. Most notable in this range are the disappearances of the reflections found at 7.18 ° and 11.73 ° in the diffractograms of α-FOX-7. At wider angles a new set of reflections replaces those of α-FOX-7 above 388 K.
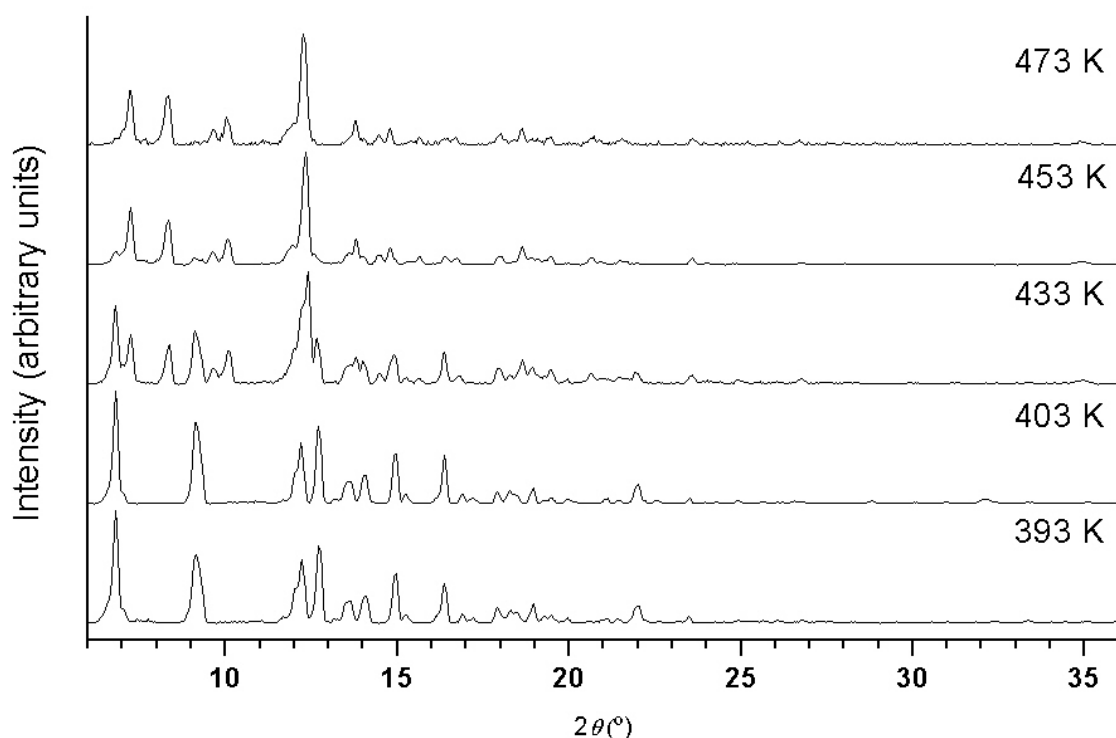
Figure 3.9. Stacked plots of Guinier diffractograms of β- and γ-FOX-7 as well as mixed β- and γ-FOX-7 (433 K) over the temperature range 393 – 473 K measured with MoKα₁ radiation.

The transition from β- to γ-FOX-7 results in more dramatic changes in the measured diffractograms than are observed as the result of transition from α- to β-FOX-7. Transition results in a new set of reflexes observed at both high and low 2θ ranges, suggesting that the crystallographic changes caused by the β – γ transition are more significant than those observed for the α – β transition. Lastly, the measurement made at 433 K shows reflections that can be assigned to both the β and γ polymorphs of FOX-7, indicating the simultaneous presence of both polymorphs. This phenomenon was not observed for the α – β transition and thus confirms the observation from DSC measurements that the β – γ transition takes place more slowly (in the case of DSC measurements over a greater temperature range) and less smoothly than the α – β transition.

The qualitative analysis of the polymorphic behavior of FOX-7 upon heating by Raman spectroscopy and X-ray powder diffraction seems to indicate several points. Firstly, the

similarities in the Raman spectra of α-, β- and γ-FOX-7 suggest that although the FOX-7 molecules may have slightly different conformations in the three different phases, the geometries (bond lengths and therefore strengths) should be very similar in each polymorph. The powder diffraction data on the other hand seem to indicate that more significant changes in the packing take place upon transition from α- to β-FOX-7 and then again upon transition from β- to γ-FOX-7.

3.2.3　Single crystal X-ray structures

Since, Raman spectroscopy and powder diffraction provide mainly qualitative information about the structural changes undergone by FOX-7 upon heating, the single crystal X-ray diffraction patterns of FOX-7 were measured over the temperature range from 200 – 490 K. From these patterns, more accurate and more precise information about the structures of α-, β- and γ-FOX-7 can be obtained. The unit cell parameters may be determined at elevated temperature with significantly higher precision than those obtained from the powder diffraction measurements. Space groups are also more easily assigned from single crystal data. Structural solutions which provide a plethora of information including, atomic positions and thus molecular geometries, thermal displacement parameters and packing and hydrogen bonding information, were also determined with reasonable reliability for all measurements except those at the highest temperatures >460 K.

Initial single crystal investigations were carried out along much the same lines as the initial Raman and powder diffraction studies. Several good quality single crystals of α-FOX-7 were tempered at ~470 K yielding in most cases low quality crystals of γ-FOX-7. Therefore, Weißenberg and precession X-ray photographs of low quality single crystals of the γ-phase were taken. The h0l equator Weißenberg photograph showed both single crystal reflections and powder lines, verifying the low quality of the crystal. However, in spite of the low crystal quality, it was possible to unambiguously determine the space group since h0l reflections occurred only with $h + l = 2n$. A precession photograph of the same crystal along

the 0kl equator showed that the 0k0 reflections occurred only for k = 2n. These reflection conditions resulted in the unequivocal assignment of the space group $P2_1/n$. With this information many attempts were made to find a structural solution for γ-FOX-7 from powder. However, none of these efforts met with any success.

At this point a good quality crystal of α-FOX-7 was mounted in a Lindemann capillary and cooled to 200 K. Data for α-FOX-7 were then acquired at 200, 298, 333 and 373 K. Somewhat unexpectedly, when the sample temperature reached 393 K, a clear diffraction pattern different than that of α-FOX-7, corresponding to β-FOX-7 was observed. A data set for β-FOX-7 was then collected at 393 K and the sample was cooled back to 293 K and a final data set was collected to confirm that the crystal had retransformed to α-FOX-7 on cooling. Solutions for all data sets in this run were obtained and the fits are of reasonably good quality. The crystallographic data and structure determination details for this first series of measurements and structure solutions are shown in Table 3.1.

Table 3.1. Crystallographic data and structure determination details for α- and β-FOX-7 (j069-j074).

Phase	α	α	α	α	β	α
Meas. code	j069	j070	j071	j072	j073	j074
T (K)	200	298	333	373	393	293
crystal system	monoclinic	monoclinic	monoclinic	monoclinic	orthorhombic	monoclinic
space group	$P2_1/n$	$P2_1/n$	$P2_1/n$	$P2_1/n$	$P2_12_12_1$	$P2_1/n$
a (Å)	6.9209(7)	6.9340(7)	6.9414(7)	6.9467(7)	6.9738(7)	6.9333(9)
b (Å)	6.5515(9)	6.6228(8)	6.6534(9)	6.6887(9)	6.635(1)	6.627(2)
c (Å)	11.2741(14)	11.312(1)	11.332(1)	11.350(1)	11.646(1)	11.316(2)
α (°)	90	90	90	90	90	90
β (°)	90.060(14)	90.07 (1)	90.08 (1)	90.14 (1)	90	90.03(2)
γ (°)	90	90	90	90	90	90
V (Å^3)	511.19(11)	519.47(3)	523.34(3)	527.37(3)	538.94(3)	519.9(2)
Z	4	4	4	4	4	4
ρ_{calcd} (g/cm^3)	1.924	1.894	1.880	1.865	1.825	1.892
μ (mm^{-1})	0.183	0.180	0.179	0.177	0.174	0.180
λ (Mo Kα, Å)	0.71073	0.71073	0.71073	0.71073	0.71073	0.71073
reflns collected	4257	4348	4397	4496	4538	4314
indep. reflns	1111	1135	1147	1172	1182	1130
R_{int}	0.0478	0.0583	0.0588	0.0605	0.0341	0.0489
obsd. reflns.	1065	1059	1052	1038	956	1025
F(000)	304	304	304	304	304	304
R_1[a]	0.0361	0.0402	0.041	0.0542	0.0359	0.0296
wR_2[b]	0.0926	0.0995	0.0977	0.1435	0.0878	0.0733
weighting scheme[c]	0.0691, 3.5456	0.0711, 0.0000	0.0629, 0.0000	0.1043, 0.0000	0.0537, 0.0000	0.0542, 0.0000
GOOF	1.080	1.041	1.065	1.069	1.019	1.022
parameters	108	108	108	108	107	108

[a] $R_1 = \Sigma \, ||F_o| - |F_c|| \, / \, \Sigma \, |F_o|$. [b] $R_w = [\Sigma \, (F_o^2 - F_c^2) \, / \, \Sigma \, w \, (F_o)^2]^{1/2}$. [c] $w = [\sigma_c^2 \, (F_o^2) + (xP)^2 + yP]^{-1}$, $P = (F_o^2 - 2F_c^2) \, / \, 3$.

With the knowledge that α-FOX-7 transforms smoothly to β-FOX-7, a second series of measurements of a good quality crystal of α-FOX-7 was made. The first pattern in this series was measured at 353 K, with subsequent points measured at 363, 373 (twice), 395, 403, 413 and 423 K. From these measurements a series of structures of β-FOX-7 were determined, although the quality of the fits is slightly lower than optimal as shown by the slightly elevated reliability statistics (R_1, wR_2). After further heating above the β – γ transition temperature the quality of the diffraction pattern was very low and severe twining was observed. The crystallographic data and structure determination details for the second series of measurements are shown in Table 3.2.

Table 3.2. Crystallographic data and structure determination details for α- and β-FOX-7 (jo025-jo032).

Phase	α	α	α	α	β	β	β	β
Meas. code	jo025	jo026	jo027	jo028	jo029	jo030	jo031	jo032
T (K)	353	363	373	373	395	403	413	423
crystal system	monoclinic	monoclinic	monoclinic	monoclinic	orthorhombic	orthorhombic	orthorhombic	orthorhombic
space group	$P2_1/n$	$P2_1/n$	$P2_1/n$	$P2_1/n$	$P2_12_12_1$	$P2_12_12_1$	$P2_12_12_1$	$P2_12_12_1$
a (Å)	6.9548(13)	6.9562(12)	6.9587(13)	6.9600(13)	6.9854(13)	6.9856(13)	6.9861(13)	6.9863(14)
b (Å)	6.6829(16)	6.6900(16)	6.7029(16)	6.7045(17)	6.6514(18)	6.6602(19)	6.6710(18)	6.6863(18)
c (Å)	11.356(3)	11.361(3)	11.370(3)	11.371(3)	11.670(3)	11.674(3)	11.681(3)	11.687(3)
α (°)	90	90	90	90	90	90	90	90
β (°)	90.016(17)	90.031(17)	90.145(17)	90.065(18)	90	90	90	90
γ (°)	90	90	90	90	90	90	90	90
V (Å^3)	527.8(2)	528.7(2)	530.4(2)	530.6(2)	542.2(2)	543.1(2)	544.4(2)	545.9(2)
Z	4	4	4	4	4	4	4	4
ρ_{calcd} (g/cm^3)	1.864	1.860	1.855	1.854	1.814	1.811	1.807	1.802
μ (mm^{-1})	0.177	0.177	0.176	0.176	0.173	0.172	0.172	0.171
λ (Mo Kα, Å)	0.7093	0.7093	0.70930	0.7093	0.7093	0.7093	0.7093	0.7093
reflns collected	2858	2858	2860	2865	2909	2897	2913	2902
indep. reflns	1097	1100	1101	1102	1125	1127	1127	1137
R_{int}	0.0391	0.0349	0.0375	0.0359	0.0353	0.0315	0.0335	0.0313
obsd. reflns.	1004	1008	996	1001	934	901	908	928
F(000)	304	304	304	304	304	304	304	304
R_1[a]	0.0406	0.0398	0.0396	0.0409	0.0586	0.0592	0.0600	0.0575
wR_2[b]	0.1036	0.0996	0.0974	0.1061	0.1654	0.1655	0.1698	0.1617
weighting scheme[c]	0.0683, 0.0601	0.0598, 0.0898	0.0572, 0.0883	0.0669, 0.0765	0.1086, 0.0000	0.1140, 0.0000	0.1178, 0.0000	0.1113, 0.0000
GOOF	1.053	1.058	1.063	1.049	1.138	1.096	1.118	1.117
parameters	109	109	109	109	108	108	108	108

[a] $R_1 = \Sigma \, ||F_o| - |F_c|| \, / \, \Sigma \, |F_o|$. [b] $R_w = [\Sigma \, (F_o^2 - F_c^2) \, / \, \Sigma \, w \, (F_o)^2]^{1/2}$. [c] $w = [\sigma_c^2 \, (F_o^2) + (xP)^2 + yP]^{-1}$, $P = (F_o^2 - 2F_c^2) \, / \, 3$.

Due to the slightly elevated reliability parameters of structural fits to the diffraction data measured in the second series of measurements of β-FOX-7 and the failure to produce crystal of a sufficient quality for determination of the structure of γ-FOX-7, a third series of measurements was made. A third crystal of α-FOX-7 was slowly heated to 403 K and a full diffraction pattern was measured, which led to slightly improved reliability statistics for structural fits for β-FOX-7. Further patterns were measured at 413 and 423 K and solutions were once again obtained. The crystallographic data and structure determination details for each of the third series of measurements are shown in Table 3.3.

Table 3.3. Crystallographic data and structure determination details for β-FOX-7 (ko033-ko035).

Phase	β	β	β
Meas. code	ko033	ko034	ko035
T (K)	403(2)	413(2)	423(2)
crystal system	orthorhombic	orthorhombic	orthorhombic
space group	$P2_12_12_1$	$P2_12_12_1$	$P2_12_12_1$
a (Å)	6.986(2)	6.989(2)	6.991(2)
b (Å)	6.662(2)	6.669(2)	6.680(2)
c (Å)	11.688(4)	11.694(4)	11.698(4)
α (°)	90	90	90
β (°)	90	90	90
γ (°)	90	90	90
V (Å^3)	544.0(3)	545.1(3)	546.2(3)
Z	4	4	4
ρ_{calcd} (g/cm^3)	1.808	1.805	1.801
μ (mm^{-1})	0.172	0.172	0.171
λ (Mo Kα, Å)	0.71073	0.71073	0.71073
reflns collected	2769	2786	2776
indep. reflns	1069	1075	1076
R_{int}	0.0397	0.0348	0.0346
obsd. reflns.	960	955	971
F(000)	304	304	304
$R_1{}^a$	0.0531	0.0526	0.0523
$wR_2{}^b$	0.1449	0.1463	0.1424
weighting	0.1087,	0.1117,	0.1007,
scheme^c	0.0267	0.0142	0.0687
GOOF	1.069	1.063	1.037
no. of parameters	107	107	107

^{a} $R_1 = \Sigma\, ||F_o| - |F_c|| / \Sigma\, |F_o|$. ^{b} $R_w = [\Sigma\, (F_o{}^2 - F_c{}^2) / \Sigma\, w\, (F_o)^2]^{1/2}$. ^{c} $w = [\sigma_c{}^2\, (F_o{}^2) + (xP)^2 + yP]^{-1}$, $P = (F_o{}^2 - 2F_c{}^2) / 3$.

The unit cell parameters determined by automatic indexing of the 298 K CuKα_1 diffraction patterns measured for quenched γ-FOX-7 and the space group assignment of $P2_1/n$ were eventually confirmed when a reasonable quality single crystal of γ-FOX-7 was produced by mounting good quality crystals in Lindemann capillaries and heating them slowly to 460 K on the diffractometer. Once the known diffraction pattern of β-FOX-7 was replaced by a good quality pattern of γ-FOX-7, the crystal was quenched rapidly to 200 K for data collection. Although this method eventually yielded a data set of reasonable quality, suitable for single crystal X-ray structure determination, the process of heating normally yielded low quality

crystals of γ-FOX-7. One crystal treated in this manner "disappeared" destroying the capillary. Initially, it was suspected that the sample had exploded. However, a more likely explanation is the above mentioned thermosalient effect. It would seem that upon heating to the β – γ transition temperature the crystal moved dramatically on transition to γ-FOX-7 and shattered the thin walled capillary.

The data collected for metastable (quenched) γ-FOX-7 at 200 K yielded a structural solution with significantly elevated reliability statistics and small amounts of residual electron density. However, all attempts to introduce split positions failed to yield improved reliability statistics (Table 3.4). With a structural model for γ-FOX-7 available, the process of heating crystals above the β – γ transition temperature until another γ-FOX-7 crystal of seemingly reasonably quality was repeated. Diffraction patterns were then measured at 460, 470, 480 and 490 K. At 500 K, no meaningful diffraction data could be collected indicating that the crystal had decomposed more or less completely. Refinements of the structural model of γ-FOX-7 determined at 200 K on the data measured at 460 and 470 K were possible but led to very poor reliability statistics and significant residual electron densities. Once again attempts to introduce split positions failed to improve the reliability statistics. No meaningful refinements were possible for the data set measured at 480 or 490 K. The crystallographic data and structure determination details for single crystal measurements of γ-FOX-7 are tabulated in Table 3.4. *ORTEP* representations of the asymmetric unit of α-, β- and γ-FOX-7 with accompanying atomic labeling schemes are shown in Figure 3.10.

Table 3.4. Crystallographic data and structure determination details for γ-FOX-7 at 200 K and 460-490 K (kn553, cx018_460-cx018_490).

Phase	γ	γ	γ	γ	γ
Meas. code	kn553	cx018_460	cx018_470	cx018_480	cx018_490
T (K)	200(2)	460(2)	470(2)	480(2)	490(2)
crystal system	monoclinic	monoclinic	monoclinic	monoclinic	monoclinic
space group	$P2_1/n$	$P2_1/n$	$P2_1/n$	$P2_1/n$	$P2_1/n$
a (Å)	13.354(3)	14.123(3)	14.162(3)	14.157(8)	14.22(2)
b (Å)	6.8946(11)	6.9570(8)	6.953(5)	6.943(2)	6.940(2)
c (Å)	12.050(2)	12.0615(19)	12.058(2)	12.055(4)	12.069(8)
$α$ (º)	90	90	90	90	90
$β$ (º)	111.102(8)	110.85(2)	110.93(2)	110.71(5)	109.63(13)
$γ$ (º)	90	90	90	90	90
V (Å^3)	1035.0(3)	1107.5(3)	1108.9(8)	1110.2(7)	1122(2)
Z	8	8	8	8	8
$ρ_{calcd}$ (g/cm^3)	1.901	1.776	1.774	1.772	1.754
$μ$ (mm^{-1})	0.181	0.169	0.169	0.169	0.167
$λ$ (Mo Kα, Å)	0.71073	0.71073	0.71073	0.71073	0.71073
reflns collected	3620	5537	11358	2920	18435
indep. reflns	2021	1840	1847		
R_{int}	0.0487	0.0507	0.0711	0.0809	0.324
obsd. reflns.	1308	915	950		
F(000)	608	608	608		
$R_1{}^a$	0.1117	0.184	0.1994		
$wR_2{}^b$	0.3386	0.5122	0.5448		
weighting	0.1867,	0.2000,	0.2000,		
scheme^c	4.2428	0.0000	0.0000		
GOOF	1.115	1.814	2.004		
Largest Residual Electron Density	+0.63 / -0.58	0.667 / -0.475	0.669 / -0.548		
no. of parameters	183	182	182		

$^a R_1 = Σ \, ||F_o| - |F_c|| \, / \, Σ \, |F_o|$. $^b R_w = [Σ \, (F_o{}^2 - F_c{}^2) \, / \, Σ \, w \, (F_o)^2]^{1/2}$. $^c w = [σ_c{}^2 \, (F_o{}^2) + (xP)^2 + yP]^{-1}$, $P = (F_o{}^2 - 2F_c{}^2) \, / \, 3$. ^{b} in e/Å^3.
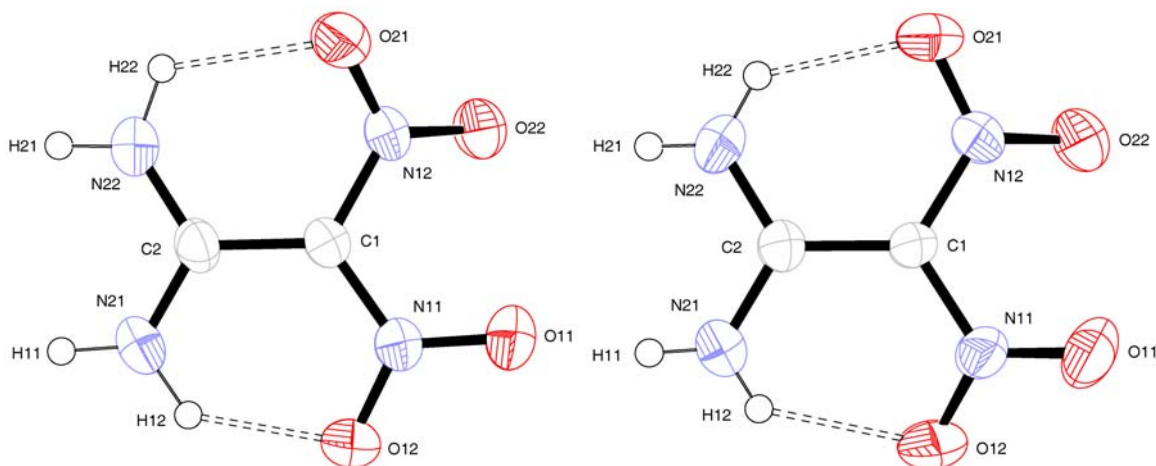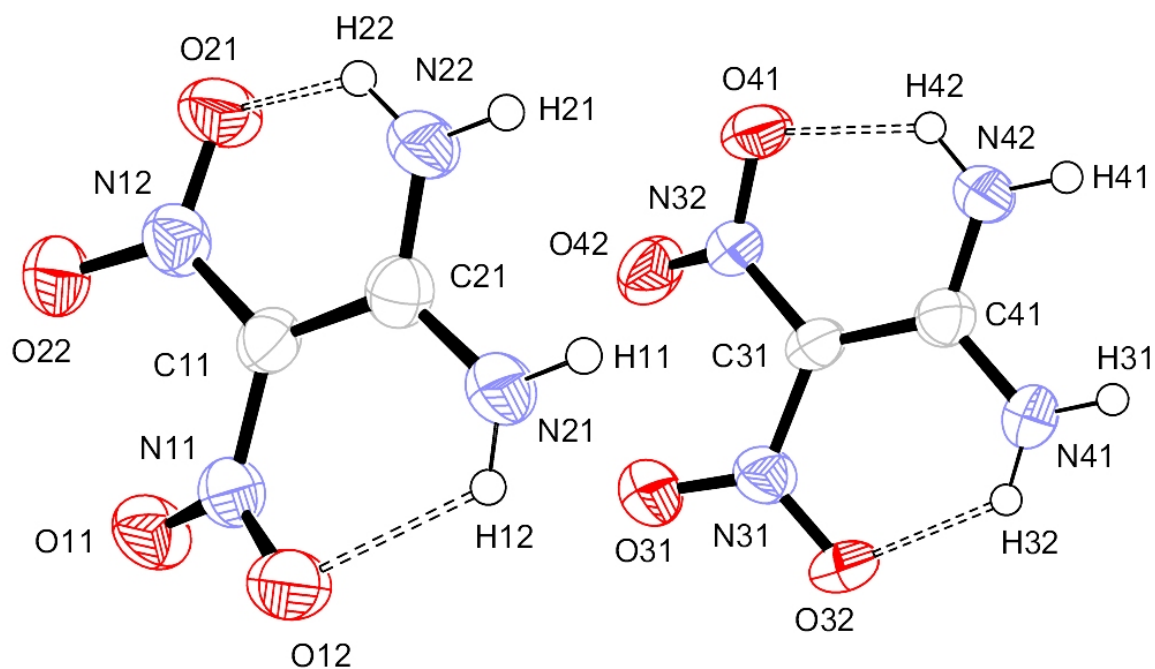
Figure 3.10. *ORTEP* projections of the asymmetric units of α- (373 K, upper left), β- (393 K, upper right) and γ-FOX-7 (200 K, bottom) with atom labels, thermal ellipsoids at 50% probability and intramolecular hydrogen bonds.

Since the reliability statistics (R_1 and wR_2) for nearly all of the structure determinations for β-FOX-7 are slightly higher than ideal, those for metastable γ-FOX-7 at 200 K are significantly elevated and those for γ-FOX-7 at high temperature are so large that the reliability of the structure would be considered suspicious under most normal circumstances, it seems that dynamic disorder (thermal motion within crystalline FOX-7) maybe the source of these fair to extremely poor structural fits. The isotropic thermal displacement parameters (U_{eq}) provide a simple gauge of the magnitude of the thermal motion (dynamic disorder) of each atom in a structure. A plot of the isotropic displacement parameters for all non hydrogen atoms in α-FOX-7 at 200, 298, 333, 353, 363 and 373 K, in β-FOX-7 at 393, 403, 413 and 423 K and γ-FOX-7 at 200 and 460 K is shown in Figure 3.11. From this plot several conclusions can be drawn. Firstly, it appears that in α-FOX-7 between 200 and 298 K dynamic disorder in the crystal is low, since an extrapolation of the plots to 0 K appears to

intercept the y-axis at ~0 Å^2. Secondly, above 298 K the slope of the U_{eq} vs. temperature plots increases suggesting the onset of dynamic disorder. Thirdly the U_{eq} values for the constituent atoms of the nitro groups (N11, N12, O11, O12, O21 and O22) are most affected by increasing temperature, with the oxygen atoms of the nitro groups suffering the most significant dynamic disorder in γ-FOX-7, both at 460 and 200 K. Lastly, increases in U_{eq} values observed for the oxygen atoms in FOX-7 upon phase transition from α- to β- and then β- to γ-FOX-7 may contribute to the entropy increases on transition of ~6 J/K·mol and ~7 J/K·mol respectively. Bearing these trends in mind, careful analysis of the large amount of information available from the single crystal X-ray measurements and subsequent structure determinations should still yield perfectly meaningful conclusions and possible explanations of the behavior of FOX-7 on heating.
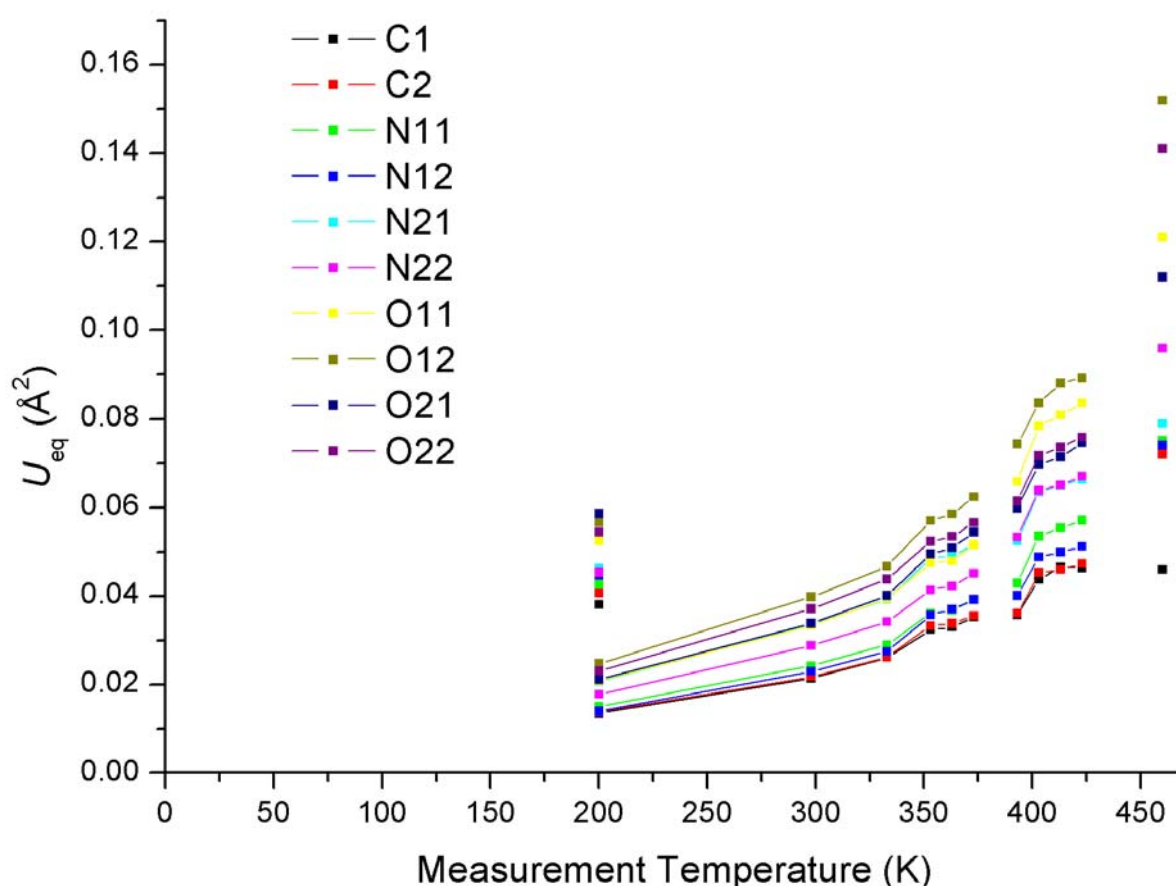

Figure 3.11. Plot of isotropic displacement parameters (U_{eq}) for α-, β- and molecule 1of the doubled asymmetric unit of γ-FOX-7 from 200 to 460 K. Data for molecule 1 of metastable

γ-FOX-7 measured at 200 K are also included. Data points from a structure determination of γ-FOX-7 at 460 are included only to exemplify the trend observed and should not be considered quantitatively.

Similarities in the unit cell parameters and space groups determined for α-, β- and γ-FOX-7 by single crystal X-ray diffraction suggest structural relationships between all three polymorphs. The relationship between α-FOX-7 and β-FOX-7 seems to be the most obvious since all three lattice parameters and angles are very similar for both sets of measurements for α-FOX-7 at 373 K and β-FOX-7 at either 393 or 395 K (See Table 3.1 and Table 3.2). The primary change observed upon transition from α- to β-FOX-7 is a change in crystallographic symmetry resulting from a change in space group from $P2_1/n$ to $P2_12_12_1$. Close similarity in the structures is also suggested by the reversibility of the α − β transition as well as the minimal loss of crystal quality upon transition. Furthermore, all three factors: the similarity in crystallographic axes and angles, the reversibility of the phase transition and the small loss of crystal quality upon transition suggests that the transition is of primarily diplacive nature as defined by Buerger[17], meaning that "a mere distortion from one network into another" is observed.

The relationship between the unit cell parameters of the α and β polymorphs of FOX-7 and the γ form appears to be more complex. However, close inspection of the observed crystallographic axes indicates $a(\alpha) \approx a(\beta) \approx b(\gamma)$, $b(\alpha) \approx b(\beta) \approx (\sin(180-\beta(\gamma))) a(\gamma)/2$ and $c(\alpha) \approx c(\beta) \approx c(\gamma)$ (see Table 3.1, Table 3.2 and Table 3.3). Since, the monoclinic angle observed for γ-FOX-7 (~111 °, depending on temperature) deviates significantly from the nearly 90 ° monoclinic angle observed for α-FOX-7 and the symmetry constrained β angle in orthorhombic β-FOX-7 the lengths of $a(\gamma)$ must not only be halved, but also corrected for this effect. The exchange, doubling of crystallographic axes and sharp increase in monoclinic angle upon transition from β- to γ-FOX-7, the decrease in space group symmetry, the irreversible nature of the β − γ phase transition and the significant loss of crystal quality upon

125

transition suggest that the transition is of reconstructive nature as defined by Buerger[17], meaning that major rearrangement of the crystal structure is observed.

Since both α- and γ-FOX-7 crystallize in the same space group it is possible to confirm these relationships between their crystallographic axes using Weißenberg X-ray photography. First, a Weißenberg X-ray photograph was taken of a good quality crystal of the α-phase. The crystal was then treated as in the initial studies (heating to ~490 K, followed by quenching to 298 K) yielding a crystal of the γ-phase. A Weißenberg X-ray photograph of the resulting crystal was then using the same goniometer head position as had been used for the α-phase photographs. Analysis of the reflections observed indicates precisely the axial relationships discussed above.

Taking into account the relationships between the crystallographic axes of α-, β-, and γ-FOX-7, several trends in axis lengths are observed for the transition from α- to β-FOX-7 and from β- to γ-FOX-7. The *a*-axis remains very nearly the same length upon transition from the α form to the β form of FOX-7, expanding only slightly. Upon further transition from β- to γ-FOX-7 the *a*-axis becomes the *b*-axis, as discussed above, and comparison of the *b*-axis found for γ-FOX-7 and the *a*-axis of β-FOX-7 shows that a slight decrease in axis length is observed upon transition. The length of *b*(α) decreases slightly but significantly upon transition to β-FOX-7. *b*(β) is related to *a*(γ) by (sin(180-*β*(γ))*a*(γ)/2 upon transition, and comparison of these two values again indicates a slight decrease in (sin(180-*β*(γ))*a*(γ)/2 as compared to *b*(β) on transition to γ-FOX-7. Lastly, modest, but important step-wise increases in the crystallographic *c*-axis are observed on transition from α- to β-FOX-7 and once again on transition from β- to γ-FOX-7. Overall, the changes in *a*(α), *a*(β) and *b*(γ) are minimal, changes in *b*(α), *b*(β) and (sin(180-*β*(γ))*a*(γ)/2 involve slight contractions for both transitions and the *c*-axis increases incrementally.
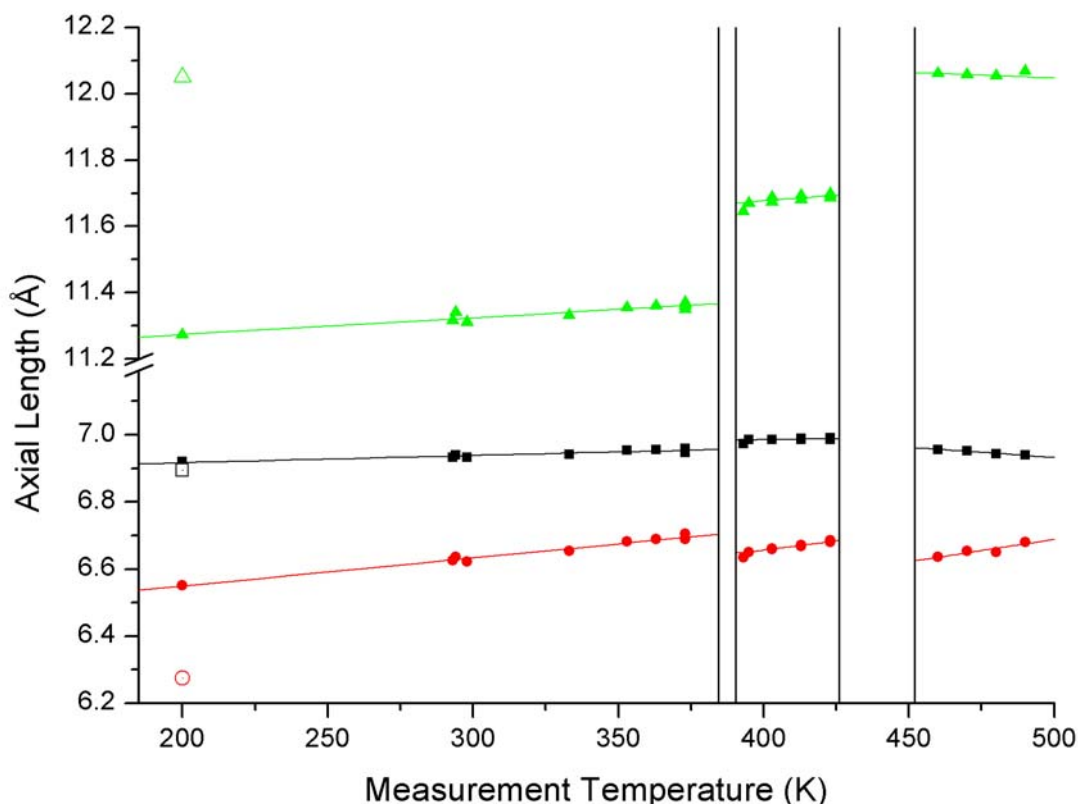
Figure 3.12. Plot of unit cell axis lengths with $a(\alpha)$, $a(\beta)$ and $b(\gamma)$ shown as black squares, $b(\alpha)$, $b(\beta)$ and $(\sin(180\text{-}\beta(\gamma))a(\gamma)/2$ as red circles and the c-axis for all three polymorphs shown as green triangles. Unfilled symbols with dots inside represent metastable γ-FOX-7 measured at 200 K. Vertical lines denote temperatures during which two phases are present. No crystallographic data were collected in these ranges. Linear least-squares regression lines are shown for the data for each axis in each phase in the appropriate color.

In addition to trends observed upon transition, several trends in the behavior of the axis lengths of individual phases on heating are apparent from the least squares regression data in Table 3.5. Within any given phase $a(\alpha)$, $a(\beta)$ and $b(\gamma)$ and the crystallographic c-axis of the α and γ polymorphs expand only slightly on heating as indicated by the very low slopes of the best fit lines (-0.00061(9) to 0.00051(7) Å/K). $c(\beta)$ seems to suffer slightly more thermal expansion than $c(\alpha)$ or $c(\gamma)$ (0.0007(2) Å/K) indicating that the intermolecular interactions are

weakest in this direction for β-FOX-7. However, $b(\alpha)$, $b(\beta)$ and $a(\gamma)$ expand the most significantly on heating as evidenced by the larger positive slopes (0.00084(5) to 0.0013(5) Å/K) of the red curves in Figure 3.12. This expansion seems to indicate that the weakest interactions in the structure occur along $b(\alpha)$, $b(\beta)$ and $a(\gamma)$, a suggestion that is confirmed by analysis of the packing and conformational differences in all three phases of FOX-7.

Table 3.5. Least squares regression parameters for the unit cell parameters (*a*, *b* and *c*) for α-, β- and γ-FOX-7 against temperature.

Cell Parameter	Slope (A/K)	Uncertainty	Intercept (Å)	Uncertainty	R	SD	N	P
$a(\alpha)$	2.12E-04	3.06E-05	6.87519	0.01008	0.92617	0.00508	10	1.19E-04
$a(\beta)$	1.28E-04	6.80E-05	6.93447	0.02792	0.64431	0.00177	7	0.11829
$b(\gamma)$	-6.10E-04	9.33E-05	7.238	0.04432	-0.97741	0.00209	4	0.02259
$b(\alpha)$	8.37E-04	4.33E-05	6.38225	0.01426	0.98948	0.00718	10	<0.0001
$b(\beta)$	0.00111	9.33E-05	6.21446	0.03831	0.98268	0.00243	7	<0.0001
$(\sin 110-\beta)a/2(\gamma)$	0.00134	4.25E-04	6.01943	0.20184	0.91238	0.0095	4	0.08762
$c(\alpha)$	5.05E-04	6.35E-05	11.17328	0.02092	0.94209	0.01054	10	<0.0001
$c(\beta)$	7.26E-04	2.80E-04	11.38644	0.11505	0.75718	0.0073	7	0.04872
$c(\gamma)$	-3.40E-04	2.31E-05	12.21777	0.01086	-0.9977	3.27E-04	3	0.04318

α-, β- and γ-FOX-7 form a layered structure in the solid state, in which the layers of α- and β-FOX-7 are "wave-shaped" and those of γ-FOX-7 are planar (See Figure 3.13). Simple visual comparison of the projections shown in Figure 3.13 shows that the layers become more planar upon transition from α- to β-FOX-7 and then completely planar on transition from β- to γ-FOX-7. These changes in structure are best quantified by measuring the "wave-shape" angle, that is the angle between molecular planes (plane defined by N21 – C2 – N22) of FOX-7 on opposite sides of a wave crest or trough. From 200 – 380 K (α-FOX-7) the "wave angle" increases only marginally from approximately 139 to 140 °. However, upon transition from α- to β-FOX-7, this angle increases to approximately 149º and then remains at 149º until transition to γ-FOX-7. Transition to γ-FOX-7 causes the interlayer angle to increase further to nearly 180º, resulting in the formation of planar layers as shown by Figure 3.14. Points for the low quality structures of γ-FOX-7 determined at 460 and 470 K are included in Figure 3.14, but should be considered only as substantiating evidence that the geometries of γ-FOX-7 at 200 K and >460 K are similar, since the reliability statistics for these structures are

extremely poor. Lastly, the wave angles used to generate Figure 3.14 were those taken from the 11 structures with the most reliable structural fits (j069-j071, jo025, jo026, jo028, j073, ko033-ko035 and kn553). This set of structure determinations will be used for all further discussion of molecular structure and no detailed discussion of the low quality high temperature structures of γ-FOX-7 will be undertaken.
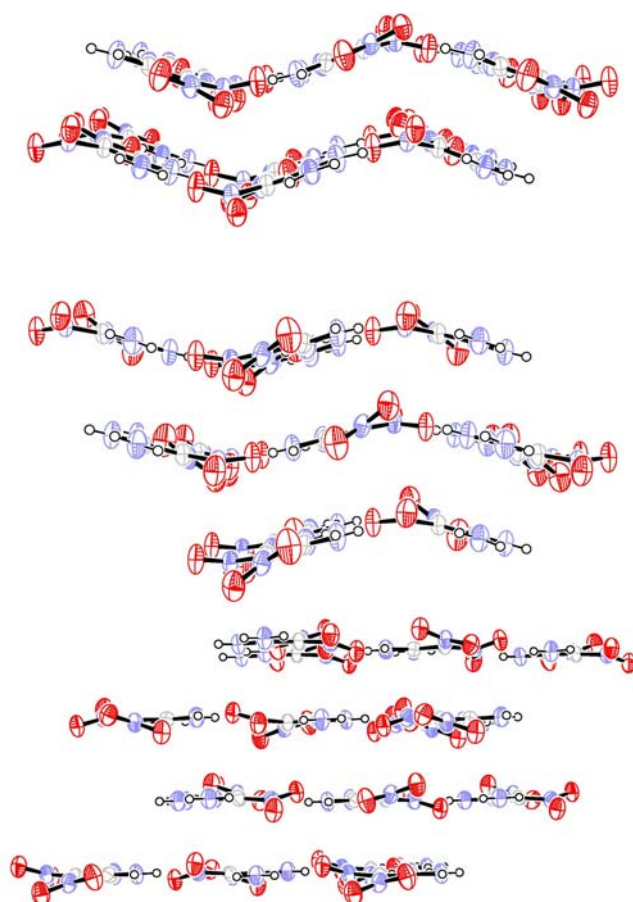
Figure 3.13. Ortep projections of the layers in the unit cells of α- (upper left), β- (upper right) and γ-FOX-7 (bottom).
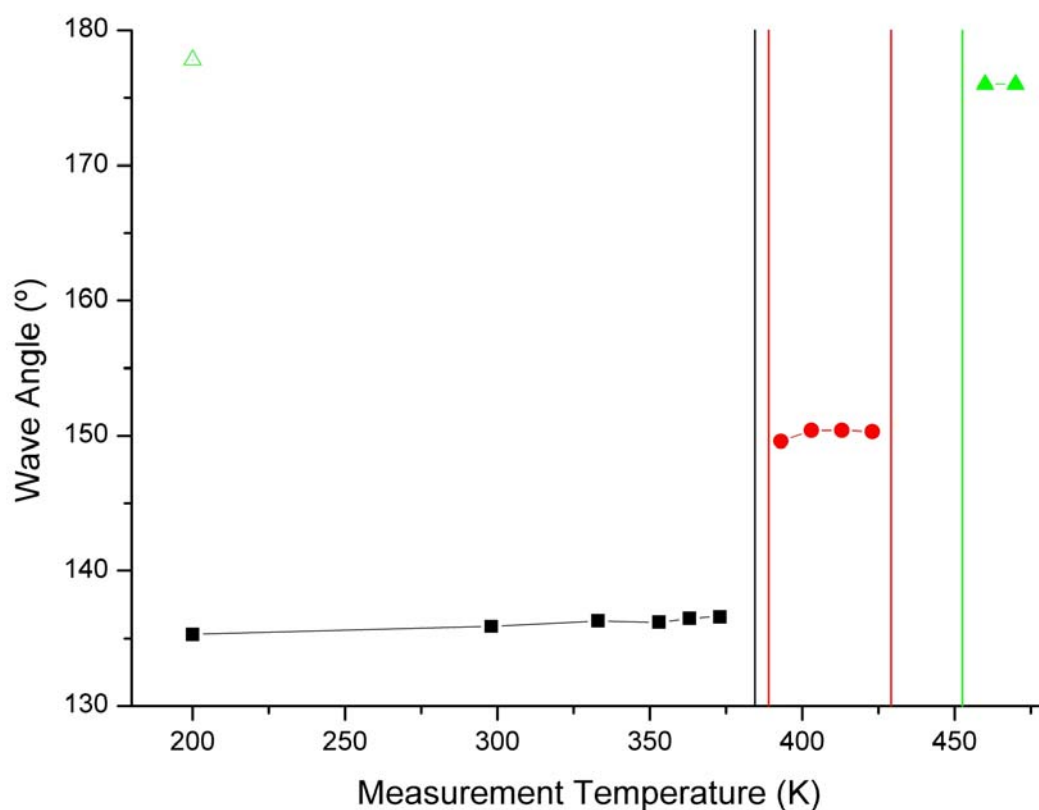
Figure 3.14. Plot of "wave angles" in α- (black squares), β-(red circles), and γ-FOX-7 (green triangles). The wave angle measured for metastable γ-FOX-7 at 200 K is shown as an unfilled green triangle with a dot in the center. The colored vertical lines represent temperatures at which a phase transition is taking place.

The layer structure of FOX-7 explains several of the trends and changes observed in the unit cell parameters upon heating. Firstly, the step wise expansion of the *c*-axis of FOX-7 by ~0.3 Å upon transition from α- to β-FOX-7 and ~0.3 Å again on transition from β- to γ-FOX-7 is explained by the fact that the *c*-axis is parallel to the layers but perpendicular to the wave fronts of the wave-shaped layers and thus expands as the layers are flattened. Both the positive slopes of the curves for of *b*(α), *b*(β) and *a*(γ) as well as the step-wise decrease in the *b*-axis length upon transition from α- to β-FOX-7 and step-wise relative decrease in the *b*(β) in becoming *a*(γ) (*b*(β) is comparable to $(sin(180-\beta(\gamma))a(\gamma)/2$ as described above) are

explained by the layered packing of FOX-7. Between the layers of FOX-7, the weakest intermolecular interactions (van der Waals interactions) predominate and therefore, since $b(\alpha)$, $b(\beta)$ and $a(\gamma)$ are all normal to the layers, FOX-7 should be most susceptible to thermal expansion in this direction. The highest positive slopes of the curves in Figure 3.12 (tabulated in Table 3.5) are calculated for $b(\alpha)$, $b(\beta)$ and $a(\gamma)$, thus showing that the greatest thermal expansion does occur in the direction normal to the layers. The slight decreases in b-axis length on transition from α- to β-FOX-7 and in relative b-axis ($b(\beta)$ compared to ($sin(180-\beta(\gamma))a(\gamma)/2$) on transition from β- to γ-FOX-7 is another effect due to the step-wise flattening of the wave-shaped layers of FOX-7. On transition (either α – β or β – γ) the wave angle increases (or becomes ~180 º) and the layers can thus rearrange into a more efficient packing arrangement, allowing the interlayer spacing to expand thermally (as shown in Figure 3.15) while maintaining the same relative b-axis lengths. Lastly the relative stability of $a(\alpha)$, $a(\beta)$ and $b(\gamma)$ is the result of only limited structural change along this axis which is parallel to the wave fronts in the wave-shaped layered structures (α- and β-FOX-7).
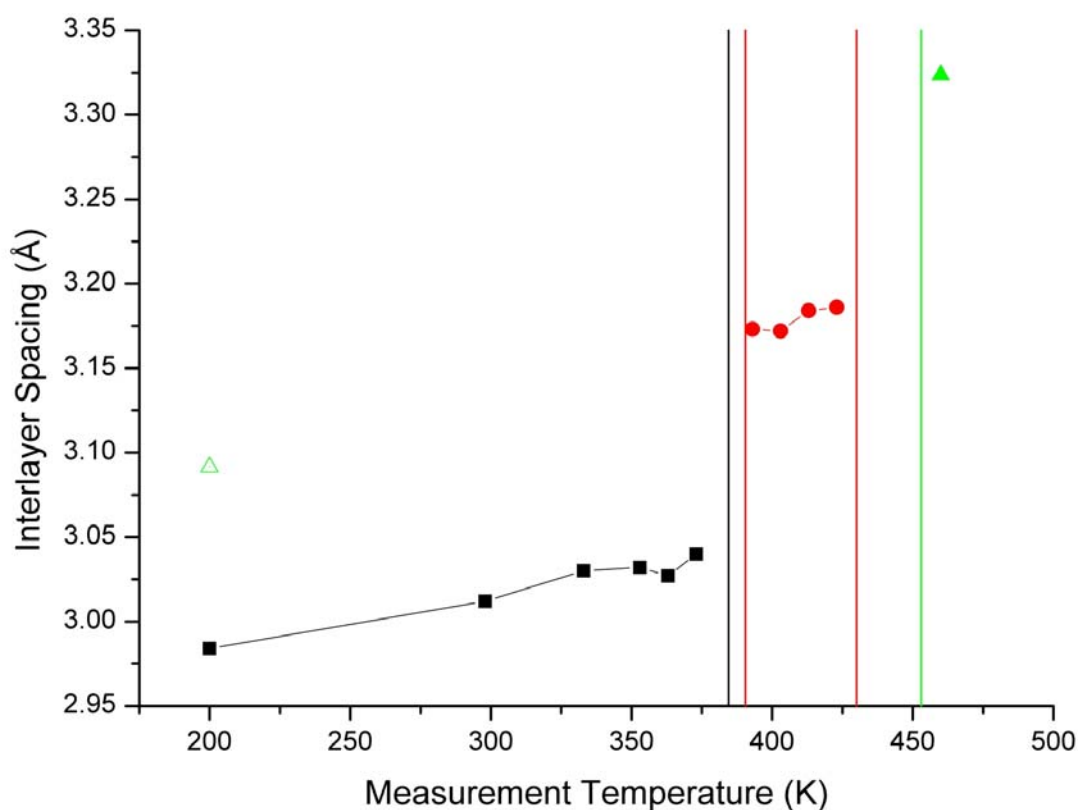
Figure 3.15. Plot of interlayer spacing in α- (black squares), β-(red circles), and γ-FOX-7 (green triangles). The interlayer spacing measured for metastable γ-FOX-7 at 200 K is shown as an unfilled green triangle with a dot in the center. The colored vertical lines represent temperatures at which a phase transition is taking place. A point representing the low quality structure determination from data at 460 K is shown only to demonstrate the trend in interlayer spacing and not for purposes of quantitative analysis.

The interlayer spacing discussed above and shown in Figure 3.15 is defined as the distance between the molecular planes of two parallel FOX-7 molecules not found in the same layer. This distance is best quantified for α-FOX-7 as the length of a line normal to the N21–C2–N22 (molecular) plane through C2^{sym} (Sym: -x, 1-y, 1-z), for β-FOX-7 as the length of a line normal to the N21–C2–N22 plane through C2^{sym} (Sym: 1/2+x, 3/2-y, 1-z) and for γ-FOX-7 as

the average length of lines normal to the N21–C21–N22 and N41–C41–N42 passing through C21^{sym} (Sym: 1/2-x, 1/2+y, 3/2-z) and C41^{sym} (Sym: 3/2-x, 1/2+y, 3/2-z), respectively.

Since the unit cell parameters generally increase with temperature in response to structural changes, so does the volume of the unit cell. For comparison to α- and β-FOX-7, the doubled unit cell of γ-FOX-7 was halved. Figure 3.16 shows a plot of nearly all single crystal unit cell volume data collected and available in the literature[4] along with linear least squares regressions for the expansion of each polymorph. The least squares best-fit lines are generally statistically sound with $R(\alpha) = 0.977$, $R(\beta) = 0.970$ and $R(\gamma) = 0.999$. Using the parameters derived by least-squares fitting (Table 3.6), the expansion trend for each polymorph was extrapolated to the transition onset and completion temperatures (determined from the DSC measurements made with a heating rate of $\beta = 1$ K/min) in order to determine the change in volume ($\Delta_{trs}V$) for both transitions. The change from α- to β-FOX-7 results in an increase in volume of 11.8 Å^3 and the change from β- to γ-FOX-7 in an increase of 6.6 Å^3 accounting for the doubled unit cell.
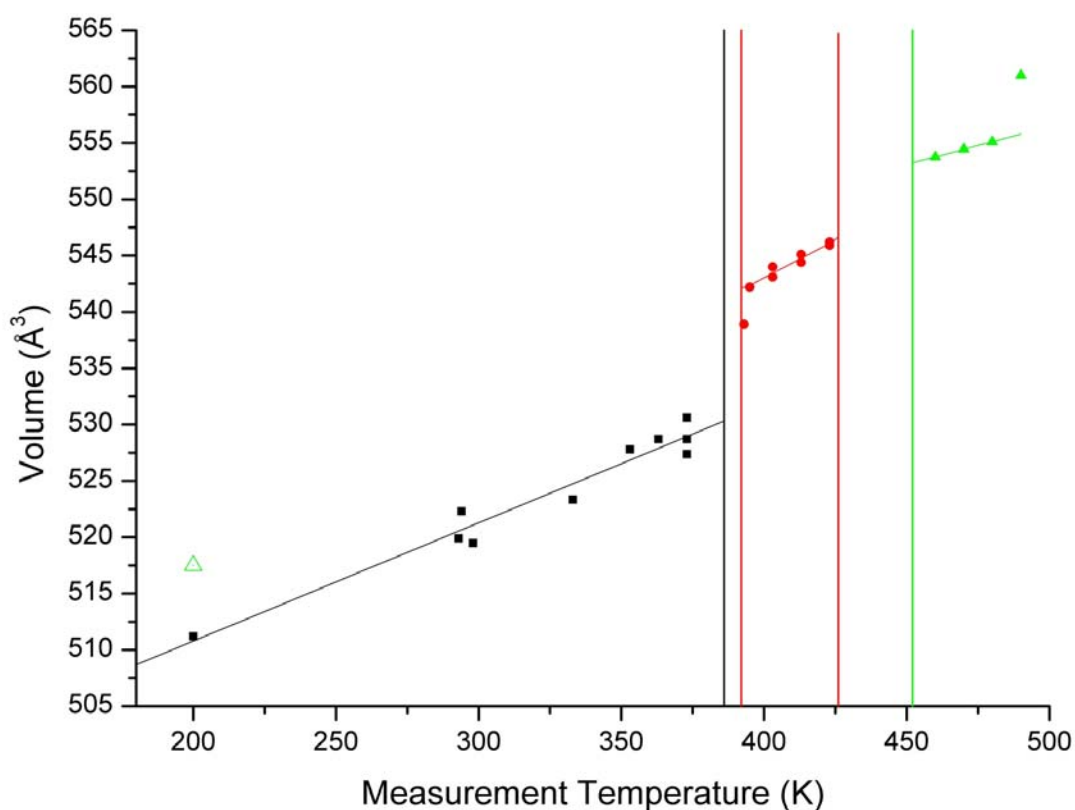
Figure 3.16. Plot of unit cell volume for α- (black symbols and lines), β- (red symbols and lines) and half of the unit cell volume (in order to account for the doubled unit cell of γ-FOX-7) of γ-FOX-7 (green symbols and lines) versus temperature. Unfilled symbols with dots inside represent metastable γ-FOX-7 measured at 200 K. Horizontal lines denote temperatures during which two phases are present. Linear least-squares regression lines are shown for the data for each phase in the appropriate color.

The slopes of the unit cell volume versus temperature lines provide information about the thermal expansion of each of the three polymorphs of FOX-7. The slopes of the unit cell volume versus temperature curves for α- and β-FOX-7 are of the same order of magnitude and are quite similar ($m(\alpha) = 0.105$ Å^3/K and $m(\beta) = 0.133$ Å^3/K). The slope of the line for γ-FOX-7 ($m(\gamma) = 0.0675$ Å^3/K) is about half of those of α- and β-FOX-7. These observations

seem indicate that of the three polymorphs of FOX-7, the molecules are in γ-FOX-7 are configured so as to absorb thermal strain with a minimum of physical change.

Table 3.6. Least squares regression parameters for (adjusted) unit cell volume for α-, β- and γ-FOX-7 against temperature.

Cell Parameter	Slope ($Å^3$/K)	Uncertainty	Intercept ($Å^3$)	Uncertainty	R	SD	N	P
$V(\alpha)$	0.10499	0.00816	489.78512	2.6896	0.97666	1.35464	10	<0.0001
$V(\beta)$	0.13259	0.01492	489.996	6.12628	0.96976	0.38847	7	3.00E-04
$V/2(\gamma)$	0.0675	0.00144	522.708	0.67849	0.99977	0.02041	3	0.01361

Analysis of the changes in unit cell parameters and volumes of α-, β- and γ-FOX-7 with temperature and their relationship to simple packing motifs (wave-shaped layers) strongly suggests that the overall packing of the three polymorphs should be related. Investigation of the relationships in the packing of α-, β- and γ-FOX-7 is facilitated by a thorough examination of the fractional atomic coordinates derived from the multiple single crystal X-ray structures determined in this study. Examination of the fractional atomic coordinates with relation to one another (molecular geometry) is also essential to establish relationships between α-, β- and γ-FOX-7 at the molecular level, as well as analyze how FOX-7 molecules react to thermal stress. For the analysis of packing relationships, fractional atomic coordinates derived from the X-ray data gathered at 373 K (jo028) and 393 K (j073) will be compared for α – β phase transition and for the β – γ transition the coordinates calculated for data collected at 393 K (β-FOX-7, j073) and 200 K (γ-FOX-7, kn553) will be discussed.

Inspection of Table 3.7 shows a simple relationship between the fractional atomic coordinates found for α-FOX-7 and those found for β-FOX-7. On average, transition from α- to β-FOX-7 results in a shift of +3/4 (or -1/4) along the *a*-axis, a shift of +1/4 along the *b*-axis and essentially no change along the *c*-axis. Therefore, the relationship between the coordinates of α- and β-FOX-7 can be summarized by the following simple expressions: $x(\alpha)$ – 1/4 ≈ $x(\beta)$, $y(\alpha)$ + 1/4 ≈ $y(\beta)$ and $z(\alpha) \approx z(\beta)$. The simplicity of the these relationships and their general nature (low standard deviation of mean shifts necessary to transform α- to β-

FOX-7) indicated once again that the α – β phase transition is primarily of displacive nature as discussed above.

Table 3.7. Fractional atomic coordinates for α- and β-FOX-7 from single crystal X-ray structure determinations at 373 K (jo028) and 393 K (j073), respectively.

atom	x/a(α)	x/a(β)	Δx/a	y/b(α)	y/b(β)	Δy/b	z/c(α)	z/c(β)	Δz/c
C1	-0.2303(3)	0.5326(3)	0.763	0.1726(3)	0.4369(3)	0.2643	0.6373(2)	0.63252(12)	0.00475
C2	-0.3107(4)	0.4329(2)	0.7436	0.2415(3)	0.4881(3)	0.2466	0.52564(19)	0.52753(14)	0.00189
N11	-0.0336(3)	0.7333(2)	0.7669	0.1491(3)	0.4206(3)	0.2715	0.65770(16)	0.63770(11)	0.02
N12	-0.3526(3)	0.4342(2)	0.7868	0.1335(3)	0.4049(2)	0.2714	0.73324(17)	0.73534(12)	0.0021
N21	-0.1999(4)	0.5277(3)	0.7276	0.2982(4)	0.5332(3)	0.235	0.4401(2)	0.43372(14)	0.00638
N22	-0.4990(4)	0.2454(3)	0.7444	0.2534(3)	0.4892(3)	0.2358	0.5105(2)	0.52365(18)	0.01315
O11	0.0241(3)	0.8084(2)	0.7843	0.0665(3)	0.3179(3)	0.2514	0.74928(17)	0.71229(13)	0.03699
O12	0.0801(3)	0.8285(2)	0.7485	0.2048(4)	0.5064(3)	0.3016	0.58103(19)	0.56336(14)	0.01767
O21	-0.5161(3)	0.2609(2)	0.777	0.0669(3)	0.3628(3)	0.2959	0.71285(14)	0.73342(12)	0.02057
O22	-0.2993(3)	0.5176(2)	0.8169	0.1692(3)	0.4235(3)	0.2543	0.83463(16)	0.82820(10)	0.00643
H11	-0.244(7)	0.479(4)	0.7232	0.328(5)	0.559(4)	0.2314	0.367(4)	0.374(3)	0.00732
H12	-0.069(6)	0.642(4)	0.7107	0.299(5)	0.548(3)	0.2493	0.456(3)	0.4379(18)	0.0181
H21	-0.534(6)	0.193(4)	0.7271	0.292(5)	0.527(4)	0.2352	0.445(4)	0.467(2)	0.02164
H22	-0.579(5)	0.180(4)	0.7587	0.209(4)	0.459(4)	0.2501	0.566(3)	0.584(3)	0.01796
μ[a]			0.7556			0.2567			0.013925
σ[b]			0.0293			0.022			0.009792

[a] Mean shift necessary to transform α-FOX-7 fractional atomic coordinates into β-FOX-7 fractional atomic coordinates. [b] Standard deviation of mean shift necessary to transform α-FOX-7 coordinates into β-FOX-7 coordinates.

Since the evidence found thus far suggests that the α – β phase transition is principally of displacive nature with relatively simple empirical relationships between the fractional atomic coordinates found for both phases, a group theoretical relationship between α- and β-FOX-7 might be expected. α-FOX-7 crystallizes in the centrosymmetric monoclinic space group $P2_1/n$ and β-FOX-7 in the non-centrosymmetric orthorhombic space group $P2_12_12_1$. Therefore a group theoretical relationship between the fractional atomic coordinates in both structures is only possible via a centrosymmetric supergroup. Comparison of the minimal *translationengleiche* supergroup entries in the *International Tables for Crystallography*, Volume A1[18] for $P2_1/n$ and $P2_12_12_1$ yields two potential supergroups (*Pbca* (No.61) and *Pnma* (No.62)) through which the space groups of α- and β-FOX-7 can be related. *Pbca* (No. 61) is related to the subgroup $P2_1/n$ by an exchange of crystallographic axes (*c*, *a*, *b*) and to $P2_12_12_1$ without any exchange of axes or shift of the crystallographic origin. As the crystallographic axes are not exchanged on transformation from α- to β-FOX-7 and the origin

is shifted, there seems to be no group theoretical relationship between α- and β-FOX-7 via *Pbca* (No. 61). The second possible supergroup, *Pnma* (No.62), also requires an exchange of axes to be transformed into $P2_1/n$ but not to $P2_12_12_1$. However, a shift of the origin (x, y, z + 1/4) is required to transform from *Pnma* to $P2_12_12_1$. This is also inconsistent with the observed shifts in the fractional atomic coordinates required for the transformation of α-FOX-7 into β-FOX-7 as observed in Table 3.7. Therefore no concrete group theoretical relationship between α- and β-FOX-7 can be established, thus suggesting that although the transition seems to be of mainly displacive character it does also have some reconstructive character.

Without a group theoretical relationship between α- and β-FOX-7, further inspection of the molecular packing of FOX-7 (Figure 3.17) found in both polymorphs seems to exemplify the empirical relationship between the two phases and explain the mechanism by which α-FOX-7 is transformed into β-FOX-7. In α-FOX-7 the molecular axes (defined by the C1–C2 bond) are all parallel within a single layer, where as in β-FOX-7 the molecular axes with a single layer form rows within which the molecular orientations are parallel but the orientations of the molecular axes in neighboring rows are no longer parallel. In order to transform the arrangement of molecular axes in α-FOX-7 to that of β-FOX-7 it appears that the "top" and "bottom" rows of FOX-7 molecules shown for α-FOX-7 in Figure 3.17 shift in opposite directions (the "top" shifts to the right and the "bottom" to the left). The molecules of the "middle" row appear to rotate as a result of the intermolecular hydrogen bonding and this "shearing" action. The relative simplicity of the motion necessary to produce β-FOX-7 from α-FOX-7 and vice versa not only demonstrates the largely displacive nature of the α − β phase transition, but also seems to explain its reversibility.
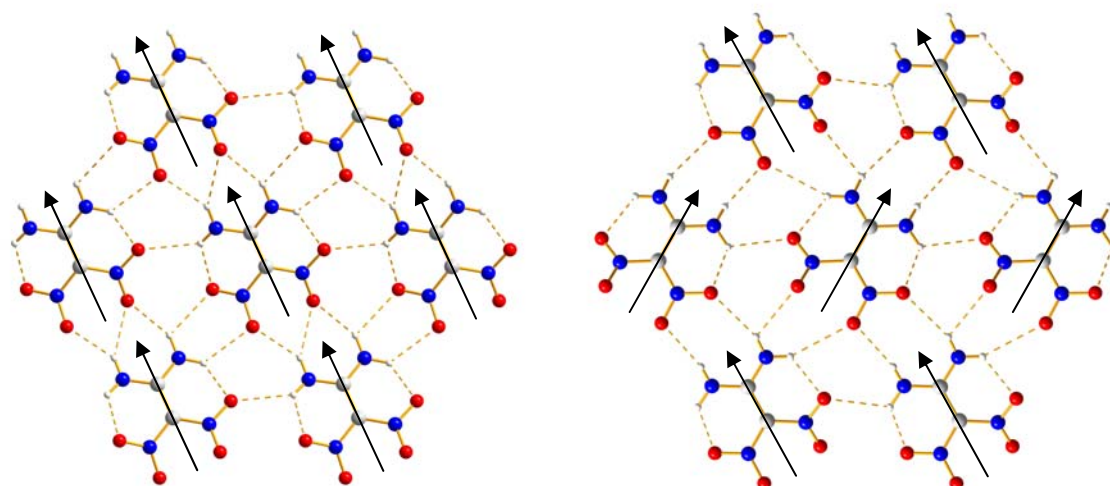
Figure 3.17. Ball and stick packing plots of one layer of α-FOX-7 (left) and β-FOX-7 (right). Arrows are drawn along the C1–C2 bond axis pointing from C1 to C2 in order to demonstrate differences in molecular orientation within the layers.

In order to compare the fractional atomic coordinates resulting from X-ray structure determinations for β- and γ-FOX-7 it is necessary once again to account for the formal exchange of the *a*- and *b*-axes, the approximate doubling of the *a*-axis in β-FOX-7 on transition to γ-FOX-7 and the 111.1 º monoclinic angle found for γ-FOX-7. Comparison of β-FOX-7 to molecule 1 (γ$_1$) of γ-FOX-7 is easily accomplished by comparing x/a(β) to y/b(γ$_1$), y/b(β) to $2(x/a$(γ$_1$))(sin180-*β*) and z/c(β) to z/c(γ$_1$). These comparisons shows that there is a high degree of similarity between the x/a(β) and y/b(γ$_1$) coordinates and z/c(β) to z/c(γ$_1$) coordinates and shifts of approximately +1/4 are observed in the y/b(β) and $2(x/a$(γ$_1$))(sin180-*β*) coordinates, which are due, most likely, to the "flattening" of the wave-shaped layers observed in the packing of α- and β-FOX-7.

atom	x/a(β)	y/b(γ₁)	Δx/a	y/b(β)	x/a(γ₁)ᵃ	Δy/b	z/c(β)	z/c(γ₁)	Δz/c
C1(1)	0.5326(3)	0.5591(10)	0.0265	0.4369(3)	0.23137(10)	0.2055	0.63252(12)	0.7175(6)	0.08498
C2(1)	0.4329(2)	0.4406(11)	0.0077	0.4881(3)	0.23828(12)	0.2498	0.52753(14)	0.6196(6)	0.09207
N11	0.7333(2)	0.7626(9)	0.0293	0.4206(3)	0.20637(10)	0.2142	0.63770(11)	0.7056(5)	0.0679
N12	0.4342(2)	0.4763(9)	0.0421	0.4049(2)	0.24406(10)	0.1608	0.73534(12)	0.8273(5)	0.09196
N21	0.5277(3)	0.5173(9)	0.0104	0.5332(3)	0.24705(10)	0.2862	0.43372(14)	0.5222(5)	0.08848
N22	0.2454(2)	0.2490(9)	0.0036	0.4892(3)	0.23361(10)	0.2556	0.52365(18)	0.6256(6)	0.10195
O11	0.8084(2)	0.8676(8)	0.0592	0.3179(3)	0.24630(10)	0.0716	0.71229(13)	0.7924(5)	0.08011
O12	0.8285(2)	0.8318(8)	0.0033	0.5064(3)	0.14815(10)	0.3582	0.56336(14)	0.6049(5)	0.04154
O21	0.2609(2)	0.3042(8)	0.0433	0.3628(3)	0.30190(10)	0.0609	0.73342(12)	0.8481(5)	0.11468
O22	0.5176(2)	0.5679(8)	0.0503	0.4235(3)	0.19443(10)	0.2291	0.82820(10)	0.8997(4)	0.0715
H11	0.479(4)	0.4420	0.037	0.559(4)	0.2497	0.3093	0.374(3)	0.4638	0.0898
H12	0.642(4)	0.6442	0.0022	0.548(3)	0.2504	0.2976	0.4379(18)	0.5151	0.0772
H21	0.193(4)	0.1782	0.0148	0.527(4)	0.2364	0.2906	0.467(2)	0.5654	0.0984
H22	0.180(4)	0.1924	0.0124	0.459(4)	0.2278	0.2312	0.584(3)	0.6897	0.1057
μᵃ			0.0244			0.23			0.0862
σᵇ			0.0193			0.0853			0.0183

ᵃ x/a(γ₁) coordinates adjusted to account for axis doubling and $\beta \neq 90$ ($2(x/a(\gamma_1))(sin180-\beta)$).
ᵇ Mean shift necessary to transform α-FOX-7 fractional atomic coordinates into β-FOX-7 fractional atomic coordinates. ᶜ Standard deviation of mean shift necessary to transform α-FOX-7 coordinates into β-FOX-7 coordinates.

Prior to analyzing the relationship between the fractional atomic coordinates found from single crystal X-ray structure determination for β-FOX-7 and molecule 2 (γ_2) of γ-FOX-7, it is useful to inspect the relationship between the two crystallographically inequivalent molecules (γ_1 and γ_2) found in the asymmetric unit of γ-FOX-7. As demonstrated by the data in Table 3.9, this relationship is quite simple with $x/a(\gamma_1)$ transformed into $x/a(\gamma_2)$ by a simple shift of 1/2, $x/b(\gamma_1) \approx x/b(\gamma_2)$ and $x/c(\gamma_1) \approx x/c(\gamma_2)$.

Table 3.9. Fractional atomic coordinates for molecules 1 and 2 in γ-FOX-7 from single crystal X-ray structure determination at 200 K (kn553).

atom	$x/a(\gamma_1)$	$x/a(\gamma_2)$	$\Delta x/a$	$y/b(\gamma_1)$	$y/b(\gamma_2)$	$\Delta y/b$	$z/c(\gamma_1)$	$z/c(\gamma_2)$	$\Delta z/c$
C11 / C31	0.1240(5)	0.6272(6)	0.5032	0.5591(10)	0.4987(10)	0.0604	0.7175(6)	0.7193(6)	0.0018
C21 / C41	0.1277(6)	0.6311(6)	0.5034	0.4406(11)	0.4009(10)	0.0397	0.6196(6)	0.6144(6)	0.0052
N11 / N31	0.1106(5)	0.6123(5)	0.5017	0.7626(9)	0.7055(9)	0.0571	0.7056(5)	0.7220(5)	0.0164
N12 / N32	0.1308(5)	0.6336(5)	0.5028	0.4763(9)	0.4005(9)	0.0758	0.8273(5)	0.8222(5)	0.0051
N21 / N41	0.1324(5)	0.6357(5)	0.5033	0.5173(9)	0.5010(9)	0.0163	0.5222(5)	0.5224(5)	0.0002
N22 / N42	0.1252(5)	0.6296(6)	0.5044	0.2490(9)	0.2109(8)	0.0381	0.6256(6)	0.6072(6)	0.0184
O11 / O31	0.1320(5)	0.5815(5)	0.4495	0.8676(8)	0.7784(8)	0.0892	0.7924(5)	0.7955(5)	0.0031
O12 / O32	0.0794(5)	0.6327(6)	0.5533	0.8318(8)	0.8044(8)	0.0274	0.6049(5)	0.6468(5)	0.0419
O21 / O41	0.1618(5)	0.6194(5)	0.4576	0.3042(8)	0.2200(8)	0.0842	0.8481(5)	0.8150(5)	0.0331
O22 / O42	0.1042(5)	0.6592(5)	0.555	0.5679(8)	0.4817(9)	0.0862	0.8997(4)	0.9197(5)	0.02
H11 / H31	0.1338	0.6376	0.5038	0.4420	0.4400	0.002	0.4638	0.4591	0.0047
H12 / H32	0.1342	0.6368	0.5026	0.6442	0.6286	0.0156	0.5151	0.5247	0.0096
H21 / H41	0.1267	0.6316	0.5049	0.1782	0.1538	0.0244	0.5654	0.5427	0.0227
H22 / H42	0.1221	0.6266	0.5045	0.1924	0.1407	0.0517	0.6897	0.6669	0.0228
μ^a			0.5036			0.0477			0.0146
σ^b			0.0280			0.0288			0.0126

^{a} Mean shift necessary to transform α-FOX-7 fractional atomic coordinates into β-FOX-7 fractional atomic coordinates. ^{b} Standard deviation of mean shift necessary to transform α-FOX-7 coordinates into β-FOX-7 coordinates.

Therefore, in addition to accounting for axis exchange and doubling as described for γ_1, a shift of $x/a(\gamma_2)$ by -0.5 is necessary to compare β-FOX-7 with γ_2 of γ-FOX-7. Table 3.10 shows the coordinates of β-FOX-7 and the transformed coordinates for γ_2 of γ-FOX-7. Just as in the case of γ_1 a comparison of the fractional atomic coordinates shows that there is a high degree of similarity between the $x/a(\beta)$ and $y/b(\gamma_2)$ coordinates and $z/c(\beta)$ to $z/c(\gamma_2)$ coordinates. Small but significant differences are observed and are most likely due to the "flattening" of the wave-shaped layers observed in the packing of α- and β-FOX-7. As was the case for γ_1 transformation of the $y/b(\beta)$ coordinates into the adjusted $x/a(\gamma_2)$ coordinates require shifts of approximately +1/4.

Table 3.10. Fractional atomic coordinates for β- and molecule 2 of γ-FOX-7 from single crystal X-ray structure determinations j073 (393 K) and kn553 (200 K).

atom	$x/a(\beta)$	$y/b(\gamma_2)$	diff	$y/b(\beta)$	$x/a(\gamma_2)^a$	diff	$z/c(\beta)$	$z/c(\gamma_2)$	diff
C11 / C31	0.5326(3)	0.4987(10)	0.0339	0.4369(3)	0.2373(12)	0.1996	0.63252(12)	0.7193(6)	0.08678
C21 / C41	0.4329(2)	0.4009(10)	0.032	0.4881(3)	0.2446(12)	0.2435	0.52753(14)	0.6144(6)	0.08687
N11 / N31	0.7333(2)	0.7055(9)	0.0278	0.4206(3)	0.2095(10)	0.2111	0.63770(11)	0.7220(5)	0.0843
N12 / N32	0.4342(2)	0.4005(9)	0.0337	0.4049(2)	0.2493(10)	0.1556	0.73534(12)	0.8222(5)	0.08686
N21 / N41	0.5277(3)	0.5010(9)	0.0267	0.5332(3)	0.2532(10)	0.28	0.43372(14)	0.5224(5)	0.08868
N22 / N42	0.2454(3)	0.2109(8)	0.0345	0.4892(3)	0.2418(12)	0.2474	0.52365(18)	0.6072(6)	0.08355
O11 / O31	0.8084(2)	0.7784(8)	0.03	0.3179(3)	0.1521(10)	0.1658	0.71229(13)	0.7955(5)	0.08321
O12 / O32	0.8285(2)	0.8044(8)	0.0241	0.5064(3)	0.2476(12)	0.2588	0.56336(14)	0.6468(5)	0.08344
O21 / O41	0.2609(2)	0.2200(8)	0.0409	0.3628(3)	0.2228(10)	0.14	0.73342(12)	0.8150(5)	0.08158
O22 / O42	0.5176(2)	0.4817(9)	0.0359	0.4235(3)	0.2971(10)	0.1264	0.82820(10)	0.9197(5)	0.0915
H11 / H31	0.479(4)	0.4400	0.039	0.559(4)	0.25675	0.3023	0.374(3)	0.4591	0.0851
H12 / H32	0.642(4)	0.6286	0.0134	0.548(3)	0.25526	0.2927	0.4379(18)	0.5247	0.0868
H21 / H41	0.193(4)	0.1538	0.0392	0.527(4)	0.24555	0.2814	0.467(2)	0.5427	0.0757
H22 / H42	0.180(4)	0.1407	0.0393	0.459(4)	0.23622	0.2228	0.584(3)	0.6669	0.0829
μ^b			0.0322			0.2234			0.0848
σ^c			0.0074			0.0587			0.0037

^{a} $x/a(\gamma_2)$ coordinates adjusted to account for asymmetric unit and axis doubling and $\beta \neq 90$ $(2(x/a(\gamma_2)-1/2)(sin180-\beta))$. ^{b} Mean shift necessary to transform α-FOX-7 fractional atomic coordinates into β-FOX-7 fractional atomic coordinates. ^{c} Standard deviation of mean shift necessary to transform α-FOX-7 coordinates into β-FOX-7 coordinates.

Attempts to establish a group theoretical relationship between β- and γ-FOX-7 on the basis of the observed shifts in coordinates were also unsuccessful. As γ-FOX-7 crystallizes in the centrosymmetric monoclinic space group $P2_1/n$, a group theoretical relationship between β-FOX-7 ($P2_12_12_1$) and γ-FOX-7 is once again only possible via the orthorhombic supergroups *Pbca* (No.61) and *Pnma* (No.62). Although the exchange of axes criteria of the β – γ phase transition is met, the doubling of the crystallographic axes is not possible via *Pbca* (No.61) or *Pnma* (No.62).

The packing of β- and γ-FOX-7 also seems to indicate significant similarity between the two polymorphs. The orientations of the molecules in the wave-shaped layers of β-FOX-7 are nearly identical to those found in the planar layers of γ-FOX-7. The alternating orientation between neighboring layers found in both α- and β-FOX-7 is also maintained in γ-FOX-7. With such apparent similarity between starting and ending points it seems unusual that the β – γ phase transition is irreversible and therefore ought to be reconstructive. The most likely explanation for the natures of the β – γ phase transformation is the following difference in the

packing of the two polymorphs: although the locations along the *c*-axis within the unit cell of the molecules in the layers of β-FOX-7 at y = 1/2 and those in the layers of γ-FOX-7 at x = 1/8 and x = 5/8 are similar, the position within the unit cell of the molecules of β-FOX-7 in the layer y = 0 and those γ-FOX-7 at x=1/4 and x= 3/4 along the *c*-axis are very dissimilar. A shift of ~0.4·c ≈ 5 Å is necessary to transform the two-dimensional arrangement of the β-phase (a-c plane) into that of the γ-phase (b-c plane) for these two layers. This change is most likely the result of the change in *β* from 90 º in β-FOX-7 to 111.1 º in γ-FOX-7 as a consequence of adjacent layers "sliding" over each other in the *c* direction.
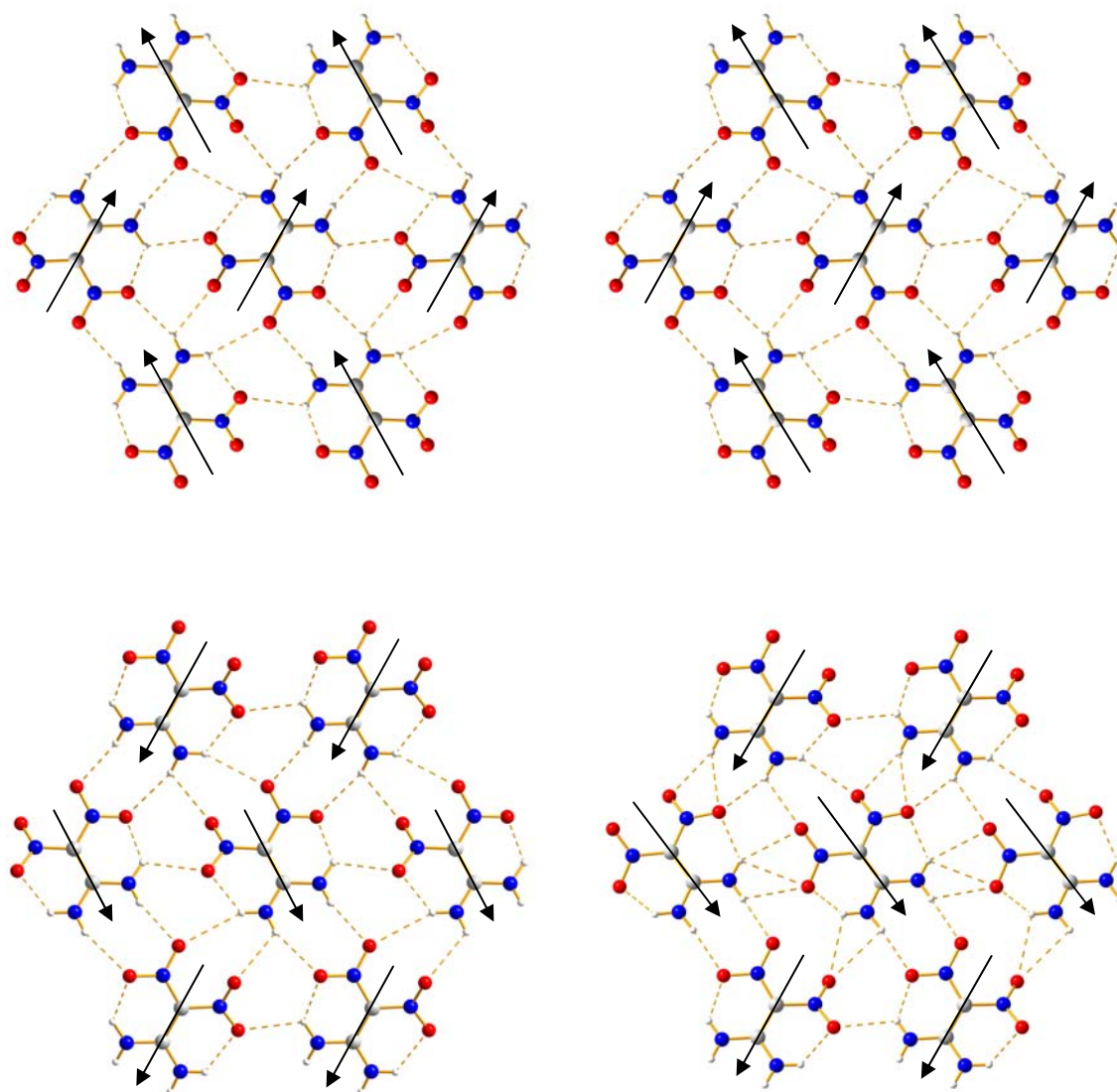
Figure 3.18. Ball and stick packing plots of one layer of β-FOX-7 (upper and lower left) and γ₁ (upper right) and γ₂ of γ-FOX-7 (lower right). Arrows are drawn along the C1(1)–C2(1) bond axis pointing from C1(1) to C2(1) in order to demonstrate similarities in molecular orientation within the layers.

Interestingly, inspection of Table 3.7, Table 3.8 and Table 3.10 shows that the largest deviations from the empirical rules for coordinate shifts required to transform one polymorph of FOX-7 into another are found for the oxygen atoms and to a lesser extent the nitro group nitrogen atoms (N11 / N31 and N12 / N41). In combination with the large U_{eq} values

observed for the atoms of the nitro groups (Figure 3.11), this suggests that the largest structural changes on transition and most significant vibrational motions in FOX-7 are found for the nitro groups and their constituent atoms. Analysis of the anisotropic thermal displacement parameters determined from the single crystal structure analysis confirms this suggestion.

For crystal systems in which all unit cell angles are 90º the ADPs U_{11}, U_{22} and U_{33} coincide directionally with the crystallographic *a*, *b* and *c* axes respectively. Since α-FOX-7 crystallizes with a monoclinic angle very close to 90º and β-FOX-7 crystallizes in an orthorhombic space group, a comparison of changes in the ADPs upon transition from α- to β-FOX-7 is straightforward. A complete set of ADPs for all non-hydrogen atoms in α-FOX-7 at 373 K and β-FOX-7 at 393 K are tabulated in Table 3.11 and Table 3.12. Firstly, inspection of Table 3.11 and Table 3.12 shows that U_{22} (parallel to the crystallographic *b* axis) generally has the largest values for both α- and β-FOX-7, with the oxygen atoms having the largest values followed by nitrogen and the smallest values are observed for the carbon atoms. Since the *b* axis is "normal" to the wave-shaped layers of FOX-7 molecules and the weakest interactions are observed between the layers, it is in keeping with the basic structure of FOX-7 in both the α and β forms that the largest thermal displacements are observed along the crystallographic *b* axis. Also, transition from α- to β-FOX-7 seems to induce a more significant increase in U_{22} over the temperature range 373 to 393 K than is observed as the temperature is increased from 353 to 373 K. This is possibly due to the increase in the "wave-shaped angle" discussed above for the transition from α- to β-FOX-7, which leads to a further weakening of inter-layer interactions.

Table 3.11. Anisotropic displacement parameters for α-FOX-7 at 373 K (jo028).

Atom Label	U_{11}	U_{22}	U_{33}	U_{23}	U_{13}	U_{12}
C1	0.0322(12)	0.0476(11)	0.0257(10)	0.0025(9)	-0.0004(10)	0.0006(9)
C2	0.0370(11)	0.0418(10)	0.0277(10)	-0.0017(8)	-0.0004(10)	0.0020(10)
N11	0.0321(10)	0.0530(11)	0.0327(11)	-0.0014(9)	-0.0017(8)	0.0004(8)
N12	0.0375(11)	0.0501(10)	0.0300(9)	0.0024(8)	0.0008(8)	0.0007(9)
N21	0.0437(14)	0.0800(15)	0.0309(10)	0.0119(10)	0.0020(10)	0.0013(11)
N22	0.0384(11)	0.0625(13)	0.0344(11)	0.0074(9)	-0.0057(11)	0.0027(11)
O11	0.0409(9)	0.0723(12)	0.0415(8)	0.0091(8)	-0.0091(8)	0.0069(9)
O12	0.0371(10)	0.1022(15)	0.0479(10)	0.0155(10)	0.0070(9)	0.0000(10)
O21	0.0429(10)	0.0820(14)	0.0383(9)	0.0016(8)	0.0007(8)	-0.0171(10)
O22	0.0449(11)	0.0973(15)	0.0276(8)	-0.0043(9)	-0.0022(8)	-0.0044(10)

Table 3.12. Anisotropic displacement parameters for β-FOX-7 at 393 K (j073).

Atom Label	U_{11}	U_{22}	U_{33}	U_{23}	U_{13}	U_{12}
C1	0.0263(10)	0.0517(10)	0.0292(7)	-0.0012(6)	0.0010(6)	0.0020(7)
C2	0.0336(11)	0.0456(9)	0.0292(7)	-0.0029(7)	-0.0024(6)	0.0000(7)
N11	0.0305(10)	0.0643(9)	0.0340(6)	-0.0073(6)	-0.0031(6)	0.0030(7)
N12	0.0394(10)	0.0510(8)	0.0297(6)	-0.0003(6)	0.0044(5)	0.0024(6)
N21	0.0444(13)	0.0824(13)	0.0304(7)	0.0061(7)	-0.0008(7)	-0.0043(9)
N22	0.0323(10)	0.0851(12)	0.0424(8)	0.0028(8)	-0.0081(7)	0.0064(8)
O11	0.0451(10)	0.0997(12)	0.0526(8)	-0.0015(7)	-0.0138(7)	0.0231(8)
O12	0.0316(11)	0.1295(15)	0.0618(9)	0.0118(9)	0.0096(6)	-0.0132(9)
O21	0.0347(9)	0.0960(11)	0.0484(8)	0.0053(7)	0.0104(6)	-0.0096(6)
O22	0.0578(10)	0.0989(11)	0.0274(6)	-0.0025(6)	0.0001(6)	-0.0007(8)

In order to compare the ADPs observed in β-FOX-7 before transition and in metastable γ-FOX-7 at 200 K, the exchange of crystallographic *a* and *b* axes and the ~110° monoclinic angle of γ-FOX-7 must be accounted for. Due to the exchange of the *a* and *b* axes, $U_{22}(\beta)$ is roughly comparable to $U_{11}(\gamma)$, but the orientation of $U_{11}(\gamma)$ is only approximately normal to the planar layers of FOX-7 molecules in γ-FOX-7. Inspection of Table 3.13 and

Table **3.14** show that as expected $U_{22}(\beta)$ and $U_{11}(\gamma)$ (normal and roughly normal to the layers in both structures) have generally the largest values and oxygen atoms have larger values than nitrogen atoms which have larger values than carbon atoms as observed above for α- and β-FOX-7. Also of note is that the amplitude of the ADPs observed for the γ-FOX-7 at 200 K are similar to those observed for β-FOX-7 at 423 K, over 200 K warmer. This seems to indicate the presence of dynamic disorder, especially in the oxygen atoms, in the structure of γ-FOX-7 at 200 K, which may be explained by the loss of rigidity resulting from the complete flattening of the wave-shaped layers.

Table 3.13. Anisotropic displacement parameters for β-FOX-7 at 423 K (ko035).

Atom Label	U_{11}	U_{22}	U_{33}	U_{23}	U_{13}	U_{12}
C1	0.0365(11)	0.0649(15)	0.0375(11)	-0.0006(10)	0.0027(8)	-0.0003(10)
C2	0.0437(11)	0.0604(14)	0.0379(11)	-0.0014(10)	-0.0015(8)	-0.0001(11)
N11	0.0410(11)	0.0847(16)	0.0455(10)	-0.0093(11)	-0.0051(8)	0.0030(11)
N12	0.0480(10)	0.0675(12)	0.0382(10)	-0.0008(10)	0.0050(8)	-0.0004(9)
N21	0.0573(13)	0.0994(19)	0.0424(11)	0.0068(11)	-0.0011(10)	-0.0031(14)
N22	0.0446(11)	0.1015(19)	0.0549(13)	0.0022(14)	-0.0101(10)	0.0075(12)
O11	0.0599(11)	0.1228(18)	0.0683(13)	-0.0022(12)	-0.0190(11)	0.0268(13)
O12	0.0443(10)	0.150(2)	0.0731(14)	0.0148(14)	0.0108(9)	-0.0146(15)
O21	0.0498(10)	0.1131(17)	0.0608(12)	0.0053(11)	0.0132(9)	-0.0107(10)
O22	0.0655(12)	0.1237(18)	0.0382(9)	-0.0033(11)	0.0003(9)	-0.0040(12)

Table 3.14. Anisotropic displacement parameters for molecules 1 and 2 of γ-FOX-7 at 200 K (kn553).

Atom Label	U_{11}	U_{22}	U_{33}	U_{23}	U_{13}	U_{12}
Molecule 1						
C1	0.042(4)	0.037(4)	0.038(4)	-0.003(3)	0.019(3)	-0.006(3)
C2	0.039(4)	0.044(4)	0.038(4)	0.001(3)	0.014(3)	0.001(3)
N11	0.056(4)	0.039(3)	0.037(3)	-0.006(3)	0.021(3)	0.000(3)
N12	0.050(4)	0.045(4)	0.039(3)	-0.004(3)	0.017(3)	0.003(3)
N21	0.063(4)	0.037(3)	0.043(3)	-0.006(3)	0.024(3)	0.002(3)
N22	0.062(4)	0.033(3)	0.044(3)	-0.005(3)	0.023(3)	0.002(3)
O11	0.068(4)	0.041(3)	0.048(3)	-0.014(2)	0.019(3)	0.000(3)
O12	0.084(4)	0.041(3)	0.048(3)	0.003(2)	0.027(3)	0.008(3)
O21	0.088(4)	0.042(3)	0.048(3)	0.006(2)	0.026(3)	0.013(3)
O22	0.074(4)	0.057(3)	0.043(3)	-0.005(3)	0.033(3)	0.005(3)
Molecule 2						
C31	0.048(4)	0.035(4)	0.036(4)	0.007(3)	0.018(3)	-0.001(3)
C41	0.040(4)	0.039(4)	0.042(4)	0.005(3)	0.017(3)	0.003(3)
N31	0.059(4)	0.035(3)	0.038(3)	-0.002(3)	0.016(3)	0.002(3)
N32	0.052(4)	0.037(3)	0.041(3)	0.003(3)	0.023(3)	-0.001(3)
N41	0.062(4)	0.044(4)	0.038(3)	0.002(3)	0.027(3)	0.002(3)
N42	0.076(5)	0.033(3)	0.043(3)	0.001(3)	0.029(3)	0.007(3)
O31	0.090(5)	0.047(3)	0.059(3)	-0.002(3)	0.040(3)	0.010(3)
O32	0.102(5)	0.036(3)	0.068(4)	0.015(3)	0.052(4)	0.002(3)
O41	0.078(4)	0.038(3)	0.047(3)	0.009(2)	0.027(3)	-0.003(3)
O42	0.074(4)	0.059(4)	0.039(3)	0.002(3)	0.024(3)	-0.007(3)

Although a quantitative comparison of the ADPs found for β-FOX-7 at 423 K and those found for γ-FOX-7 at 460 K is not particularly reliable due to the low reliability of the structure determination of γ-FOX-7 at 460 K (Table 3.4) a qualitative comparison using thermal ellipsoid plots (Figure 3.19) does serve to demonstrate the continuation of the trends discussed above. Inspection of Figure 3.19 confirms that the direction of maximum ADP amplitude in γ-FOX-7 at 460 K is roughly normal to the layers of FOX-7 and that once again a large jump in ADP amplitude in the direction of maximum amplitude for β-FOX-7 is observed upon transition to γ-FOX-7.
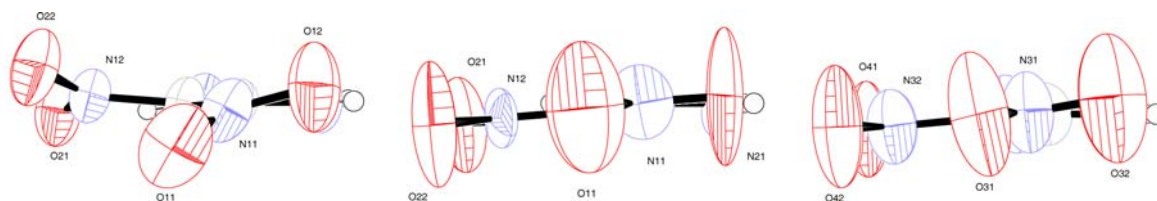
Figure 3.19. Ortep projections showing thermal ellipsoids at 50% probability for β-FOX-7 at 423 K (left), molecules 1 (center) and 2 (right) of γ-FOX-7 at 460 K.
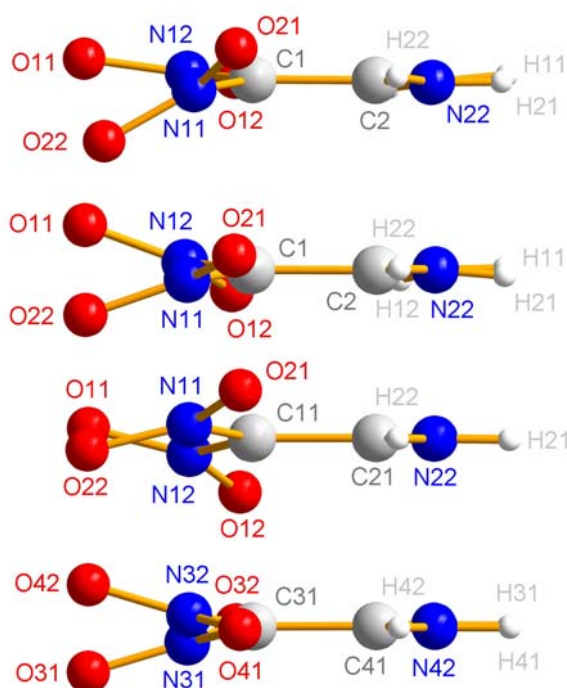
Figure 3.20. Comparison of the molecular structures of α-FOX-7 at 373 K (top), β-FOX-7 at 393 K (second from top) and molecules 1 (second from bottom) and 2 (bottom) of γ-FOX-7 at 200 K as ball and stick plots with atom labels.

Analysis of the fractional atomic coordinates and thermal displacement parameters (isotropic and anisotropic) established for α-, β- and γ-FOX-7 all indicate that the greatest structural changes within the FOX-7 molecule involve the nitro groups. Figure 3.20 shows two principal features of FOX-7 in all three phases. Firstly, C11, C21, N21 and N22 of the same FOX-7 molecule are always coplanar (the "molecular plane" is thus defined as the plane

formed by N21 , C21 and N22) and secondly the nitro group oxygen atoms all deviate from the "molecular plane" as a result of electrostatic repulsions previously described by Bemm et al [6]. Although this general observation is true for all three phases, subtle differences in the nitro group orientations are observed. In α-FOX-7 the N12 nitro group shows a substantial out of plane twist whereas the N11 nitro group lies nearly in the molecular plane. After the transition to β-FOX-7, both nitro groups are rotated out of the molecular plane, but to a lesser extent than is observed for the N12 nitro group in α-FOX-7. Provided that the atomic positions in γ-FOX-7 at high temperatures do not vary dramatically from those measured at 200 K (and brief inspection of the low quality structure determined, suggests that aside from the onset of serious disorder, very little else changes in the structure at 460 K) the transition to γ-FOX-7 should result in a further reduction in the out-of-plane twist of the nitro groups as observed in the structure of γ-FOX-7 measured at 200 K. Additionally, the degree to which each of the nitro groups deviate from the molecular plane in γ-FOX-7 seems to remain roughly the same as in β-FOX-7. Lastly, small deviations from the molecular plane in the nitro group nitrogen atoms are also apparent as shown in Figure 3.20.

The deviation of the nitro group nitrogen atoms from the molecular plane renders simple C-C-N-O torsion angles useless as a measure of the "out of plane twisting" of the oxygen atoms in asymmetric nitro groups. In order to mitigate the effect of the deviation of the nitro group nitrogen atoms from the molecular plane, the mid-point of a line connecting the two oxygen atoms was used instead of the nitrogen in a torsion (C – C – (O – O mid point) – O) angle calculation. These torsion angles were calculated three-dimensionally using the plotting program *DIAMOND*[19] and are summarized in Appendix Table 8. The data presented in Appendix Table 8 are plotted together in Figure 3.21. The plot in Figure 3.21 quantitatively confirms the qualitative observations made from Figure 3.20. In α-FOX-7 the torsion angles of +8º and –35º show the largest difference and the torsion of –35º shows the largest out of plane deviation observed in any polymorph of FOX-7. In β-FOX-7 the torsion angles are

+23º and −22º indicating a very similar out-of-plane twist of the nitro groups of medium amplitude. Finally, in γ-FOX-7, the torsion angles of +17º, + 19º and −16º, −18º are the smallest in trimorphic FOX-7 and are all quite similar to each other.
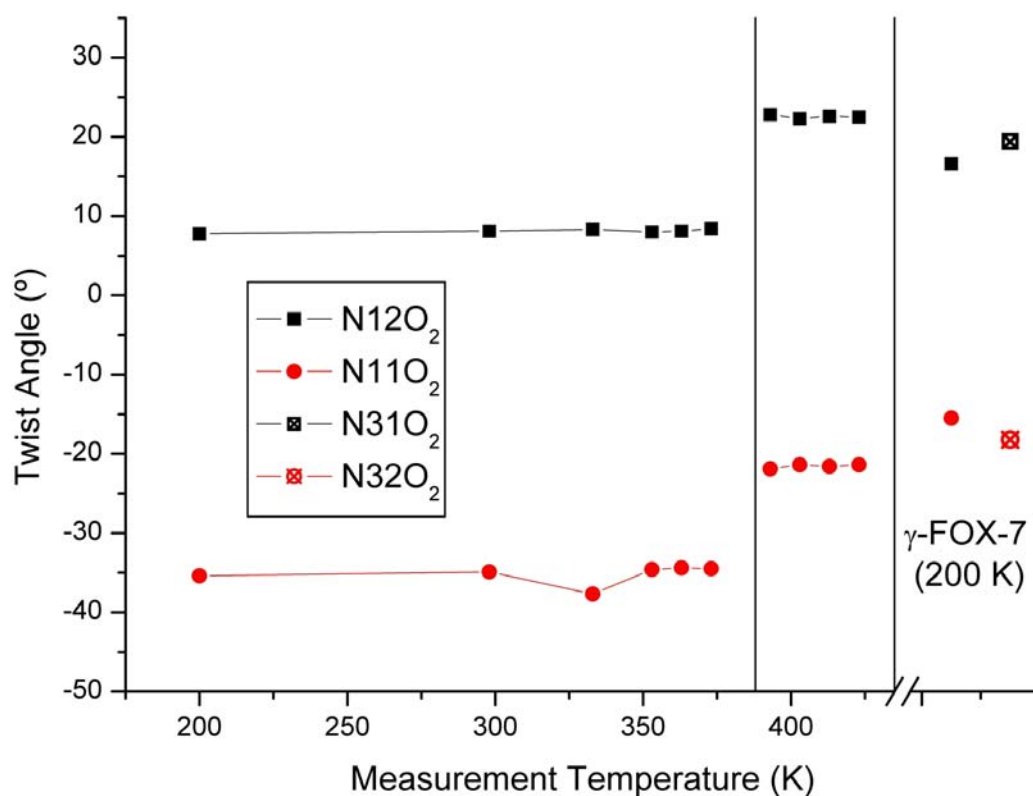
Figure 3.21. Out of molecular plane twist (º) of the nitro groups in α-, β- and γ-FOX-7.

In order to better understand the twist angles discussed above, the displacements of the nitro group oxygen and nitrogen atoms from the molecular planes of α-, β- and γ-FOX-7 for the series of 11 structures were calculated. The displacement from the molecular plane N21/N41–C2(1)/41–N22/N42) is measured as the length of a line normal to the molecular plane passing through the atom being analyzed. The results of the calculations are summarized in Appendix Table 9 Figure 3.22 shows that for α-FOX-7 at 200 K O22 and O21 have the largest out-of-molecular-plane displacements observed. Transition to β-FOX-7 results in smaller the oxygen atoms deviating to a lesser extent from the molecular plane, as

expected. It is interesting to note that for molecule 1 of γ-FOX-7 with essentially equal C-NO$_2$ bond lengths, the out-of-molecular-plane displacements of the oxygen atoms O12 (-0.66 Å) and O21 (+0.55 Å) are still larger than those of O22 (-0.47 Å) and O11 (0.54 Å) in β-FOX-7, despite the fact that the corresponding out-of-plane twist angles calculated for molecule 1 of γ-FOX-7 are less than those calculated for β-FOX-7.
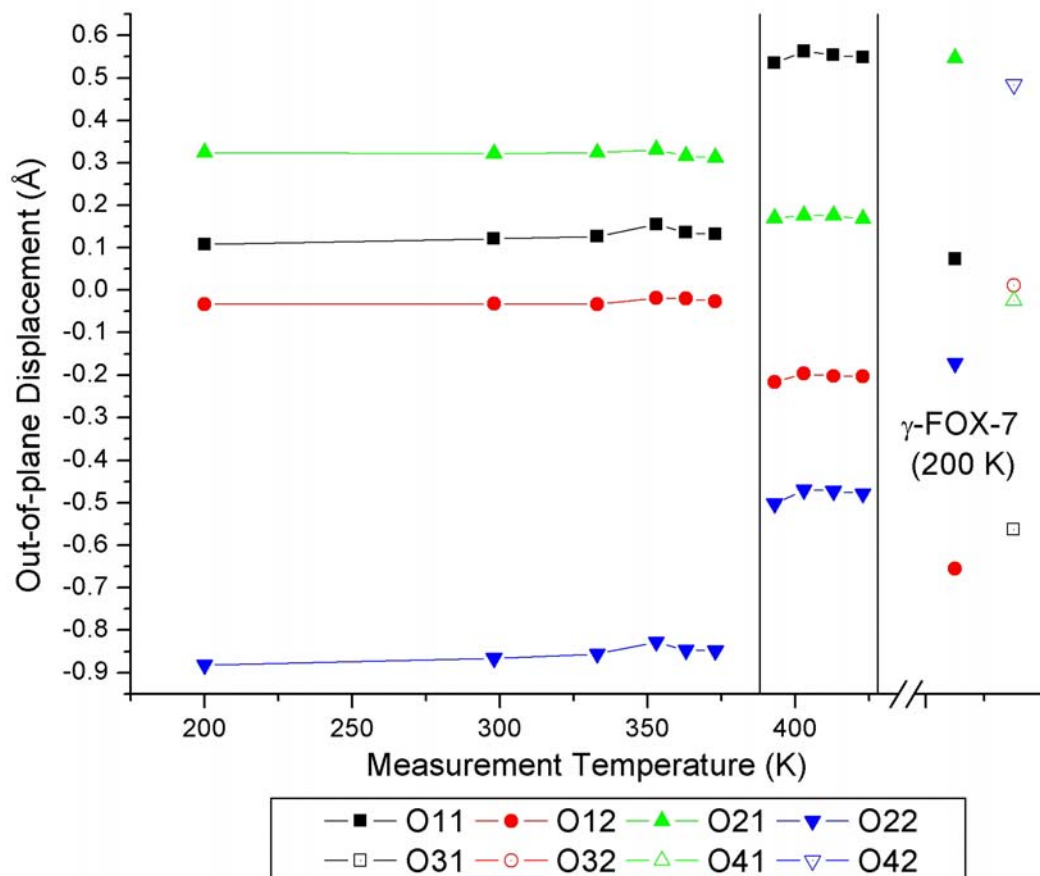
Figure 3.22. Displacement (Å) of oxygen atoms from the molecular planes (N21/N41–C2(1)/41–N22/N42) of α-FOX-7 (200 to 373 K), β-FOX-7 (393 to 423 K) and γ-FOX-7 (200 K). Values for molecule 2 of γ-FOX-7 are shown as unfilled symbols with dots at the center.

As well as being the most striking difference between the three polymorphs of FOX-7 at the molecular level, the nitro group twist angles and nitro group geometry in general play an essential role in the unusual physical properties of FOX-7. Firstly, cleavage of the C-NO$_2$ bond has been suggested as a possible detonation trigger for FOX-7[20]. Also, loss of NO$_2$ gas

is first step observed in non-explosive thermal decomposition of FOX-7. All of the above observations suggest that close inspection and detailed comparison of the nitro group geometries found in the three polymorphs of FOX-7 might yield interesting and potentially useful information.

The deviation of the nitro groups from the molecular plane should affect the degree to which the effects of π-conjugation are observed in FOX-7. In all polymorphs of FOX-7, the nitro groups are twisted substantially from the molecular plane and thus one might expect to observe weaker conjugation effects. However, considerable π-conjugation within the molecules is still evident from the bond lengths observed in the crystal structures. Bemm and Östmark[3] discussed the presence of π-conjugation in their work on α-FOX-7, and suggested that a combination of π-conjugation and extensive intra- and intermolecular hydrogen bonding was responsible for the low sensitivity and high activation energy barrier to decomposition observed for FOX-7. Examination of the carbon-carbon bond lengths from 18 single crystal structure determinations made over the course of this study along with the results of Bemm and Östmark and those of Gilardi, provides significant evidence for the presence of π-conjugation in all polymorphs of FOX-7. Firstly, quick inspection of Figure 3.23 indicates that the carbon-carbon bond in FOX-7 is not strongly affected by changes in temperature or polymorph. This is confirmed quantitatively by a linear least squares regression on all measured C-C bond lengths versus temperature showing a slope close to 0. Therefore, the average carbon-carbon bond length (1.45 Å) for all structures is useful to gauge the bond order (BO). Using average bond lengths for C-C double bonds and C-C single bonds of 1.33 Å and 1.54 Å, respectively[21], the bond order for a C-C bond with length 1.45 Å can be calculated[21] to be ~1.33, substantially less than 2 but still greater than 1, confirming that for all polymorphs of FOX-7 π-conjugation plays a substantial role.
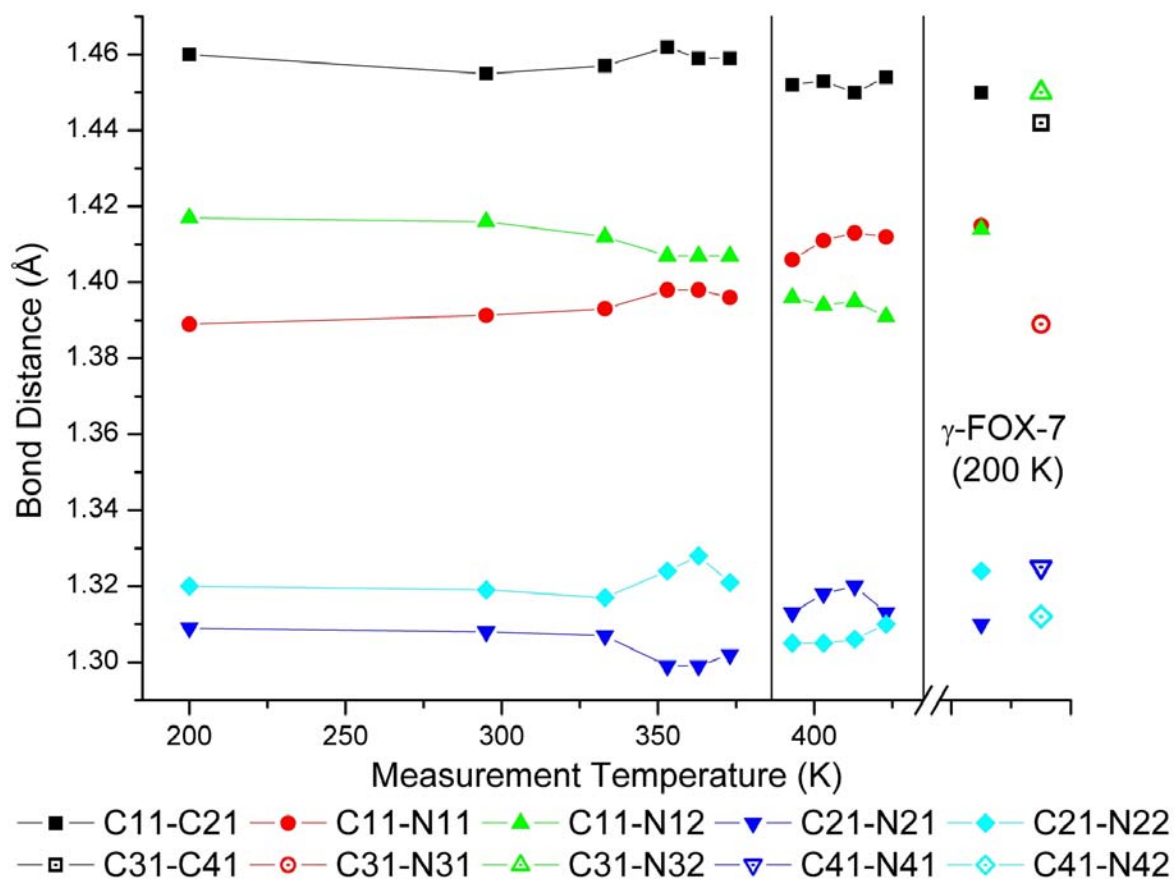
Figure 3.23. Plot of *TLS* corrected bond length (distance) observed against temperature for α-, β- and γ-FOX-7. Values for molecule 2 of γ-FOX-7 are shown as unfilled symbols with dots at the center.

Since FOX-7 shows both strong π-conjugation and considerable out-of-plane twisting of the nitro groups in all three polymorphs it seems that several bonds should be affected. It should then follow that the nitro group with the greatest out-of-plane twist should have the longest C-NO_2 bond length and vice versa. In α-FOX-7 this is observed with C11-N12 longer than C11-N11 and the C-$N12O_2$ twist angle greater than that of C-$N11O_2$ in all cases. However, the situation becomes more complex in both β- and γ-FOX-7 since the C-NO_2 twist angles are very similar but a significant difference in C-NO_2 bond length is observed in all cases for β-FOX-7 and for molecule 2 of γ-FOX-7 as seen in Figure 3.23. Perhaps the involvement of the

nitro groups in complex hydrogen bonding networks explains the discrepancies in bond length observed.

As stated in the general introduction and in the introductory section to Chapter 1, strong intermolecular hydrogen bonding plays several important roles in determining the properties of energetic materials. The molecular structure of FOX-7 containing both nitro (hydrogen bond acceptor) and amino (hydrogen bond donor) functional groups, suggests without any detailed analytical information that hydrogen bonding should be a defining element of the solid state structure of the material. Hydrogen-bonding is in fact the dominant feature of the solid state structures of all three polymorphs of FOX-7 as shown by X-ray structure analysis. However, for several reasons, quantitative assessment of hydrogen bonding from X-ray structures is a challenging task. The first and most obvious problem is to when to define a contact (or apparent contact) as a hydrogen bond. Defining a hydrogen bond is a much discussed topic in both the crystallographic[22] and spectroscopic literature[23]. The most common method used in the analysis of diffraction derived structural data is to use a set of geometric parameters, usually based on the van der Waals radii of either hydrogen (1.10 Å) or the donor atom (nitrogen, 1.55 Å in this case) and the acceptor atom (oxygen, 1.52 Å)[24]. The angle between donor (D), hydrogen atom (H) and acceptor (A) is also often constrained to be above 90º and in some cases 110º. Therefore, the working definition for a strong hydrogen bond contact used in this study is an H···A distance of less than 2.62±0.08 Å (sum of the van der Waals radii of H and O) with a D–H···A angle of greater than 110º.[25] However, when applying a geometric definition of hydrogen bonding it is important apply tolerances in the definition so that no possible contacts are excluded from the hydrogen bonding analysis on the basis of simple geometry. Therefore, all structures in this study were also searched for weaker contacts on the basis of a combination of believable donor acceptor distances and angles as discussed by Jeffrey et al.[22] The searches generally led to the identification of meaningful (but weak) contacts for angles greater than ~85º and H···A distances up to 3.0 Å.

In this manner all meaningful hydrogen bond contacts were identified and classified as either strong or weak.

A second problem with the analysis of hydrogen bonding from X-ray structural data are the large systematic errors involved in locating hydrogen atoms. These difficulties and their causes and remedies are well discussed in the crystallographic literature.[26] One simple solution that has been successful is to normalize D–H distances along the D–H bond axis determined to a mean distance determined for the particular donor-acceptor system by neutron diffraction.[25] Although significant uncertainty in the position of the hydrogen atom remains, the large systematic error can be accounted for by this method and thus, H⋯A distances can be used as reasonable barometers of hydrogen bond strength. In this work, geometric data for both normalized and non-normalized D–H distances are given, although primarily the normalized data have been analyzed.

As found by Bemm and Östmark for α-FOX-7 at 173 K, within the wave-shaped layers of α-FOX-7 at 373 K two strong intramolecular and six strong crystallographically independent intermolecular hydrogen bonds can be identified (see Table 3.15). Interestingly, no further weak contacts could be identified according to the search criteria mentioned above. The average intermolecular H⋯A distance for normalized N–H distances is 2.25(4) Å which is shorter, although not significantly, than the average H⋯A distance (2.30(2) Å) determined in the exhaustive study of N–H⋯O–N(O)–R hydrogen bonding by Allen et al.[25] This seems to suggest that on average the hydrogen bonding in α-FOX-7 is not remarkably strong and that hydrogen bond strength alone does not explain the exceptional energetic properties of FOX-7, rather that the number of contacts (six) and their three dimensional arrangement is responsible for its unusual stability.

Table 3.15. Hydrogen bonding geometry in α-FOX-7 at 373 K.[a]

	D–H		H•••A		D–A	D–H•••A	
	calculated	normalized	calculated	normalized	calculated	calculated	normalized
N21–H11•••O11[i]	0.88(4)	1.01(4)	2.22(4)	2.12(4)	3.033(3)	153(4)	149(4)
N21–H11•••O21[ii]	0.88(4)	1.01(4)	2.49(4)	2.42(4)	3.020(3)	119(3)	118(3)
N21–H12•••O12	0.93(4)	1.01(4)	1.86(4)	1.81(4)	2.600(3)	135(3)	132(3)
N21–H12•••O22[ii]	0.93(4)	1.01(4)	2.34(4)	2.29(4)	3.036(3)	131(3)	131(3)
N22–H21•••O22[i]	0.81(4)	1.01(4)	2.27(4)	2.11(4)	2.935(3)	139(4)	138(4)
N22–H21•••O11[i]	0.81(4)	1.01(4)	2.45(4)	2.29(4)	3.208(3)	155(4)	151(4)
N22–H22•••O21	0.91(3)	1.01(4)	1.99(3)	1.90(3)	2.620(3)	125(3)	126(3)
N22–H22•••O12[iii]	0.91(3)	1.01(4)	2.33(4)	2.30(4)	3.048(3)	135(2)	130(2)
average	0.92		2.35	2.25	3.047	138	136

[a] Symmetry codes: (i) -1/2+x, 1/2-y, -1/2+z; (ii) 1/2+x, 1/2-y, -1/2+z; (iii) -1+x, y, z. [b] Average of intermolecular distances.

A check of the hydrogen bonding found in β-FOX-7 further substantiates the conclusion that the stability of the α-polymorph is not merely a function of hydrogen bond strength but rather of highly efficient three dimensional organization of the FOX-7 molecules in space resulting from the combined effects of multiple, average strength hydrogen bonds. Applying the criteria for hydrogen bond identification and strength to β-FOX-7 at 393 K with normalized N–H bond distances, four strong intermolecular and two intramolecular hydrogen bonds, one borderline case and three weak contacts (see Table 3.16) can be identified. The average H•••A distance found for the strong intermolecular hydrogen bonds (excluding the borderline case) in β-FOX-7 is 2.32(3) Å, slightly longer than that found for the strong contacts in α-FOX-7. The loss of one strong contact and the presence of three additional weaker contacts also suggests a net weakening of the hydrogen bond network as well as a decrease in hydrogen bonding and packing efficiency upon transition from α- to β-FOX-7.

Table 3.16. Hydrogen bonding geometry in β-FOX-7 at 393 K.[a]

Strong Contacts	D–H		H···A		D–A	D–H···A	
	calculated	normalized	calculated	normalized	calculated	calculated	normalized
N21–H11···O21^i	0.79(3)	1.01(3)	2.40(3)	2.19(3)	3.158(3)	161(3)	159(3)
N21–H11···O11^{ii}	0.79(3)	1.01(3)	2.53(3)	2.44(3)	2.989(2)	118(3)	114(3)
N21–H12···O12	0.80(2)	1.01(2)	1.98(2)	1.84(2)	2.591(3)	133(2)	128(2)
N22–H21···O22^i	0.80(3)	1.01(3)	2.21(3)	2.00(3)	2.980(2)	164(2)	162(2)
N22–H22···O21	0.86(3)	1.01(3)	1.94(3)	1.84(3)	2.585(3)	131(3)	127(3)
N22–H22···O12^{iii}	0.86(3)	1.01(3)	2.48(3)	2.43(3)	2.946(3)	115(2)	111(2)
Borderline Contact							
N21–H12···O22^{ii}	0.80(2)	1.01(2)	2.70(2)	2.53(2)	3.413(3)	148(2)	146(2)
Weak Contacts							
N21–H12···O11^{ii}	0.80(2)	1.01(3)	2.8	2.78(3)	2.989(2)	96(2)	92(2)
N22–H21···O21^i	0.80(3)	1.01(3)	2.84	2.66(3)	3.521(3)	145(3)	144(3)
N22–H21···O12^{iii}	0.80(3)	1.01(3)	2.78	2.78(3)	2.946(3)	94(2)	90(2)
average	0.8143		2.46	2.32	3.097	141	138

^{a} Symmetry codes: (i) 1/2-x, 1-y, -1/2+z; (ii) 3/2-x, 1-y, -1/2+z; (iii) -1+x, y, z. ^{b} Average of strong intermolecular distances.

The packing and hydrogen bonding in β- and γ-FOX-7 are far more similar than those in α- and β-FOX-7. Most importantly, the molecular orientations within the layers are unchanged by the phase transition (although significant translational shifts are observed between the layers) and therefore the form of the hydrogen bonding network is also only slightly altered on transition from β- to γ-FOX-7. Direct comparison of the H···A distances observed in β- and γ-FOX-7 is complicated by several factors. Firstly, for γ-FOX-7 at 200 K it was only possible to determine the positions of seven out of eight hydrogen atoms from Fourier difference maps. Therefore, it was necessary to calculate the hydrogen atoms at idealized positions. However, inspection of the amino group geometries found in the multitude of structures determined for both α- and β-FOX-7 shows that deviations from ideal geometry are generally small and should have little or no effect on the hydrogen bond patterns and distances determined. The second complication that arises is the doubling of the asymmetric unit on transition from β- to γ-FOX-7. This problem is also, relatively simple to account for when analyzing the number of hydrogen bonds in the structure. Rather than averaging the lengths of the strong, crystallographically independent hydrogen bonds, for γ-FOX-7 it is necessary to average the lengths of all strong hydrogen bonds (regardless of symmetry dependence) surrounding a single molecule of FOX-7.

Taking both of these factors into account (using normalized N–H distances), both molecules of γ-FOX-7 found in the asymmetric unit are surrounded by nine strong intermolecular hydrogen bonds. The average H⋯A distance is 2.26(8) Å (assuming the uncertainty in H atom position, were they not calculated, would be approximately 10 times that of other interatomic distances), which is shorter, but not significantly, than that found for β-FOX-7 at 393 K (2.32(3) Å) and equal to that for α-FOX-7 at 373 K (2.26(4) Å) and slightly, but again, not significantly longer than the average H⋯A distance found for strong hydrogen bonds in α-FOX-7 at 200 K (2.22(4) Å). The hydrogen bonding surrounding both molecules of γ-FOX-7 is tabulated in Table 3.17 and Table 3.18 and shown graphically in Figure 3.26 and Figure 3.27.

Table 3.17. Hydrogen bonding geometry around molecule 1 of γ-FOX-7 at 200 K.[a]

	D–H		H⋯A		D–A	D–H⋯A	
Strong Contacts	calculated	normalized	calculated	normalized	calculated	calculated	normalized
N21–H12⋯O12	0.88	1.009	1.99	1.92	2.589(8)	124.5	121.3
N22–H22⋯O21	0.88	1.009	1.95	1.87	2.575(8)	127.1	123.9
N21–H11⋯O41[i]	0.88	1.009	2.06	1.93	2.936(8)	173.1	172.6
N22–H21⋯O42[i]	0.88	1.009	2.24	2.12	3.115(8)	170.1	169.5
N22–H22⋯O11[ii]	0.88	1.009	2.54	2.44	3.292(8)	143.9	142.2
N41–H31⋯O21[iii]	0.88	1.009	2.24	2.13	3.081(8)	158.6	157.3
N41–H31⋯O11[iv]	0.88	1.009	2.39	2.33	2.899(8)	117.5	114.7
N41–H32⋯O22[iv]	0.88	1.009	2.52	2.42	3.278(8)	144.4	142.6
N42–H41⋯O22[iii]	0.88	1.009	2.23	2.11	3.075(8)	159.9	158.7
N42–H41⋯O21[iii]	0.88	1.009	2.54	2.43	3.303(8)	146.2	144.5
Weak Contacts							
N21–H11⋯O31[iv]	0.88	1.009	2.70	2.69	2.927(9)	96.0	93.3
N21–H12⋯O31[iv]	0.88	1.009	2.54	2.50	2.928(9)	107.7	104.9
N21–H12⋯O42[iv]	0.88	1.009	2.89	2.77	3.729(9)	159.4	158.5
N22–H21⋯O12[ii]	0.88	1.009	2.56	2.53	2.933(8)	106.5	103.7
N22–H22⋯O12[ii]	0.88	1.009	2.67	2.65	2.933(9)	98.5	95.7
N41–H32⋯O11[iv]	0.88	1.009	2.77	2.78	2.899(9)	89.0	86.5
average			2.35	2.24	3.122	151.7	150.3

[a] Symmetry codes: (i) -1/2+x, 1/2-y, -1/2+z; (ii) x, -1+y, z; (iii) 1/2+x, 1/2-y, -1/2+z; (iv) 1/2+x, 3/2-y, -1/2+z. [b] Average of strong intermolecular distances.

Table 3.18. Hydrogen bonding geometry around molecule 2 of γ-FOX-7 at 200 K.[a]

	D–H		H•••A		D–A	D–H•••A	
Strong Contacts	calculated	normalized	calculated	normalized	calculated	calculated	normalized
N41–H32•••O32	0.88	1.009	1.92	1.84	2.582(8)	130.5	127.4
N42–H42•••O41	0.88	1.009	1.9	1.82	2.557(8)	129.9	126.8
N21–H11•••O41[i]	0.88	1.009	2.06	1.93	2.936(8)	173.1	172.6
N22–H21•••O42[i]	0.88	1.009	2.24	2.12	3.115(8)	170.1	169.5
N41–H31•••O21[iii]	0.88	1.009	2.24	2.13	3.081(8)	158.6	157.3
N41–H31•••O11[iv]	0.88	1.009	2.39	2.33	2.899(8)	117.5	114.7
N41–H32•••O22[iv]	0.88	1.009	2.52	2.42	3.278(8)	144.4	142.6
N42–H42•••O32[ii]	0.88	1.009	2.34	2.28	2.841(8)	116.6	113.7
N42–H41•••O22[iii]	0.88	1.009	2.23	2.11	3.075(8)	159.9	158.7
N42–H41•••O21[iii]	0.88	1.009	2.54	2.43	3.303(8)	146.2	144.5
Weak–Contacts							
N21–H11•••O31[iv]	0.88	1.009	2.70	2.69	2.927(9)	96.0	93.3
N21–H12•••O42[iv]	0.88	1.009	2.89	2.77	3.729(9)	159.4	158.5
N41–H32•••O11[iv]	0.88	1.009	2.78	2.78	2.899(9)	89.0	86.5
N42–H41•••O32[ii]	0.88	1.009	2.71	2.72	2.840(8)	89.2	86.5
N42–H42•••O31[ii]	0.88	1.009	3.11	2.99	3.93(1)	157.3	156.5
average			2.32	2.22	3.066	148.3	146.7

[a] Symmetry codes: (i) -1/2+x, 1/2-y, -1/2+z; (ii) x, -1+y, z; (iii) 1/2+x, 1/2-y, -1/2+z; (iv) 1/2+x, 3/2-y, -1/2+z. [b] Average of strong intermolecular distances.

Although examination of the average hydrogen bond contact distances (strength) carried out above is largely inconclusive on account of a lack of precision in the determination of hydrogen atom positions in X-ray structures, a combined careful examination of the changes in hydrogen bonding patterns and their connections to the above discussed changes in molecular geometry and packing, may provide further insight into the changes wrought by the phase transformation induced by heating FOX-7. In order to understand the changes caused by either phase transition completely, examination of not only the crystallographically independent surrounding of a FOX-7 molecule of any one given polymorph is necessary, but, due to the lack of group theoretical relationships between the three polymorphs, the entire surrounding of a molecule must be analyzed. The smallest section of packing that can thus be examined is a "hexagon" composed of 7 molecules of FOX-7. Figure 3.17 and Figure 3.18 show comparisons of such "hexagons" of FOX-7 molecules showing the relationship between the molecular orientations in α-, β- and γ-FOX-7. A similar concept is useful for comparison and analysis of the hydrogen bonding in α-, β- and γ-FOX-7.

The principal feature of the packing of α-FOX-7 is the lowest "wave angle" (140 °) observed for any polymorph of FOX-7. α-FOX-7 also has the most distinctive molecular feature of any polymorph of FOX-7 in that the N12 nitro group is twisted approximately -35° from the plane of the molecule. These features are dictated by the principal force at play in α-FOX-7, the highly efficient intermolecular hydrogen bonding network in which one molecule of α-FOX-7 is joined to six neighboring molecules by 12 strong hydrogen bonds (Figure 3.24). In order to achieve the most efficient combination of hydrogen bond donors and acceptors, the N12 nitro group is twisted so as to form the strong hydrogen bonds N21–H12···O22[ii] and N21–H12···O21[ii] (symmetry code (ii): 1/2+x, 1/2-y, -1/2+z) and which yield, within the graph-set formalism introduced by Bernstein et al.[27], a strong second level R 2,2(6) pattern. The out-of-plane twist of the N12 nitro group to form this interaction also results directly in the 140 ° wave angle observed, since a planar layer would have a wave angle of 180 ° and the out-of-plane twist of the N12 nitro group is -35 ° yielding a sum of 145 °. The 5 ° discrepancy in observed and predicted wave angle results from the 0.20 Å out-of-molecular plane displacement of N12. The resulting network not only makes highly efficient use of hydrogen bond donors and acceptors, but is also highly rigid due to the wave-shaped nature of the layers.

Figure 3.24. "Hexagon" of seven molecules of α-FOX-7 (373 K) viewed along the *b*-axis including graph-set characters for prominent hydrogen bond patterns.

In addition to the structure defining R 2,2(6) pattern, the three dimensional hydrogen bonding network of α-FOX-7 is composed of only C 1,1(6) motifs at the unitary level and a variety of intermolecular hydrogen bond patterns including C 2,2(X) chains in which X = 6, 8, 10 or 12, several of which integrate either an R 1,2(6) or R 2,2 (X) where X = 6 or 10 pattern. The network formed by the strong intermolecular hydrogen bonds in α-FOX-7 is fully described by the graph-set matrix in Table 3.19. The characteristic patterns observed are also highlighted graphically in Figure 3.24.

Table 3.19. Graph set matrix for intermolecular hydrogen bonding in α-FOX-7 at 373 K.[a]

	N21–H11•••O11^i a	N21–H11•••O21^{ii} b	N21–H12•••O22^{ii} c	N22–H21•••O11^i d	N22–H21•••O22^i e	N22–H22•••O12^{iii} f
a	C1,1(6)					
b	C2,1(6)	C1,1(6)				
c	C2,2(8)	C2,2(12)[R2,2(6)]	C1,1(6)			
d	C2,2(12)[R1,2(6)]	C2,2(10)	C2,2(10)	C1,1(6)		
e	C2,2(12)[R2,2(10)]	C2,2(8)	C1,2(6)	C2,2(12)[R2,1(6)]	C1,1(6)	
f	C2,2(8)	C2,2(10)	C2,2(10)	C2,2(6)	C2,2(8)	C1,1(6)

^{a} Symmetry codes: (i) -1/2+x, 1/2-y, -1/2+z; (ii) 1/2+x, 1/2-y, -1/2+z; (iii) -1+x, y, z.

As temperature and thermal motion in the crystal increase, maintaining the high rigidity of the tightly wave-shaped structure of α-FOX-7 is no longer possible and transition from α- to β-FOX-7 occurs. The transition seems to occur via the previously discussed "shearing" mechanism, resulting in the orientations of the C–C bond axes, "wave angle" and nitro group conformations observed in β-FOX-7. Once again all, of these structural features seem to be related by hydrogen bonding. The reduction of packing rigidity in the structure of FOX-7 on transformation from α- to β-FOX-7 is accomplished by a decrease in the efficiency of hydrogen bond donor–acceptor use, resulting in a smaller number of strong hydrogen bonds (four plus the borderline case) and the appearance of several weak contacts. Loosening of the hydrogen bond network results thus in the nitro groups of FOX-7 assuming lower energy conformations (out of plane twists of +23º and -22º for the N12 and N11 nitro groups, respectively), which in turn results in a higher wave-shaped angle (149 º) in β-FOX-7. In β-FOX-7 the wave angle is defined by an R 2,2(8) formed by N22–H21···O22^i and N21–H11···O21^i (symmetry code (i): 1/2-x, 1-y, -1/2+z)) rather than an R 2,2(6) observed for α-FOX-7 (see Figure 3.25). The expansion of the ring pattern is due to the changes in molecular orientation resulting from the phase transformation. Also, the angle between the "wave-shaped" layers suggested by the out-of-molecular-plane twist of the nitro group (180 – 23 = 157 ≈ 149) and that observed differs due to the out-of-molecular-plane displacement of N12.
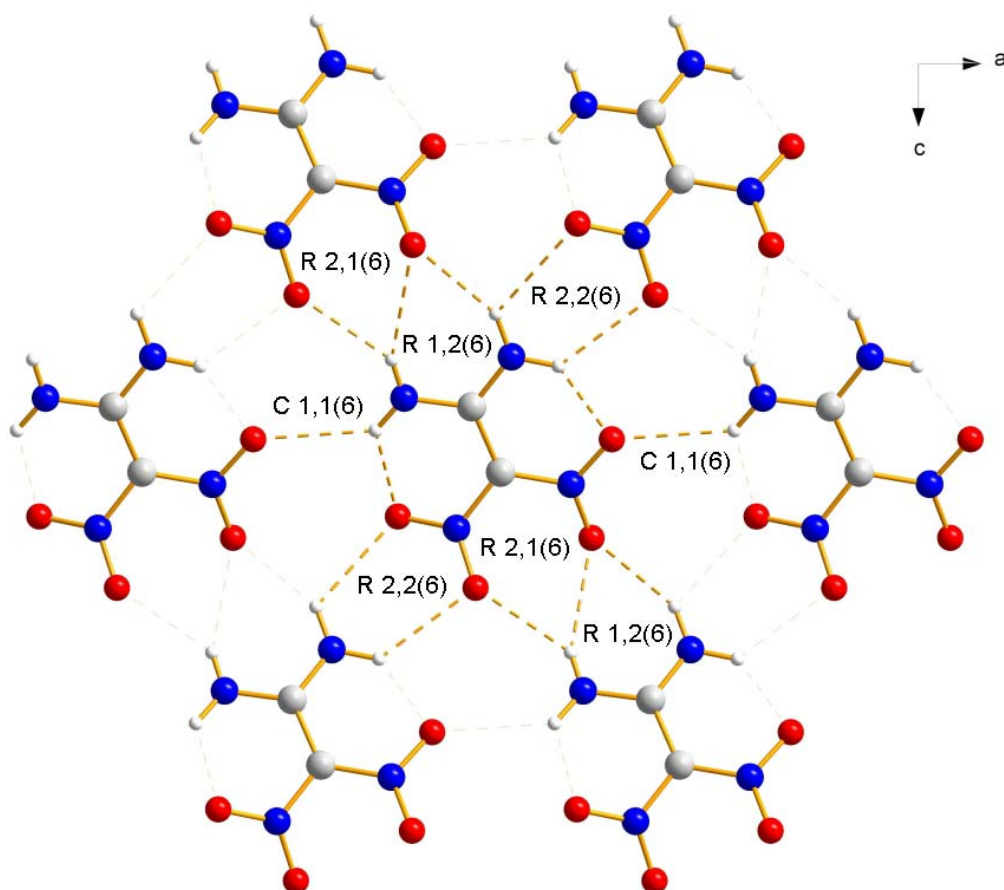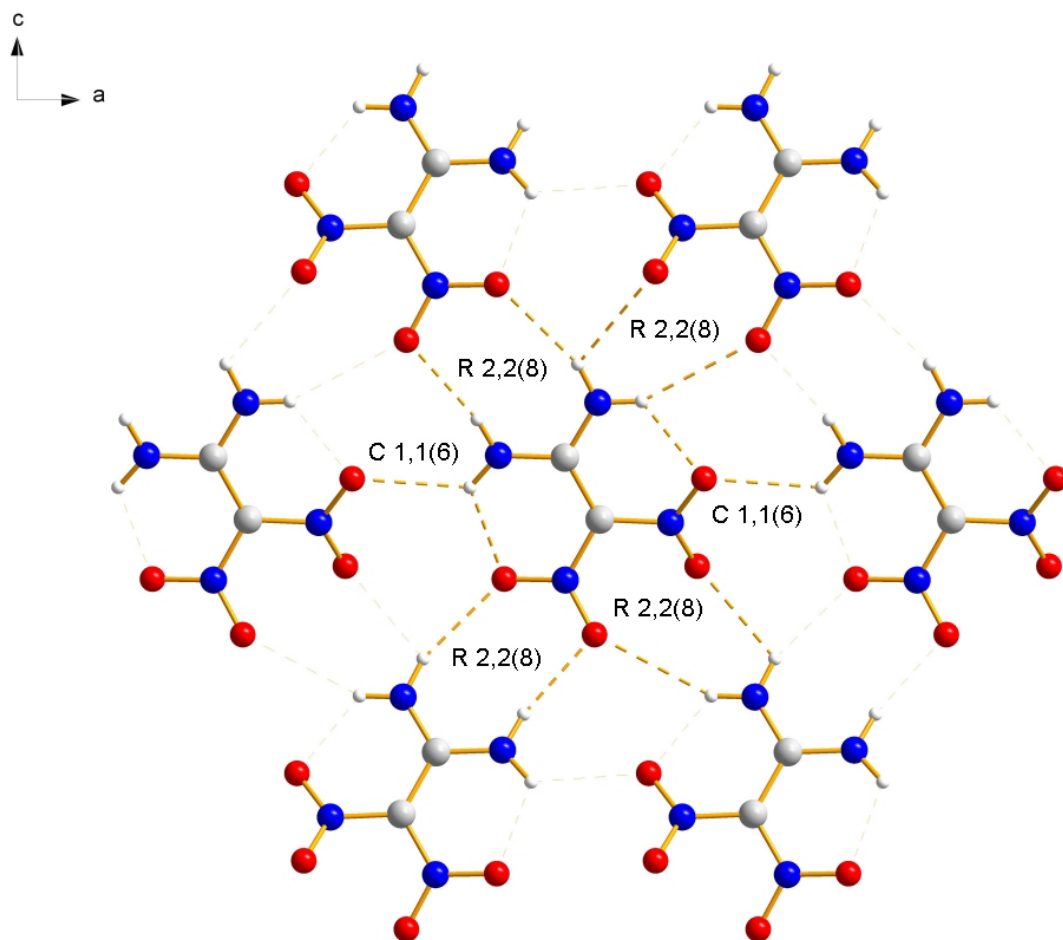
Figure 3.25. "Hexagon" of seven molecules of β-FOX-7 (393 K) viewed along the *b*-axis including graph-set characters for prominent strong hydrogen bond patterns.

As stated above, the changes in C–C bond axis orientations that result in the decrease in hydrogen bonding network efficiency also result in subtle changes in the overall network. Although several of the patterns observed in α-FOX-7 are maintained on transition to β-FOX-7 (principally the unitary C 1,1(6) motifs), a thorough graph set analysis (Table 3.20) reveals several subtle changes to the strong (and borderline) hydrogen bonding network. A graph set analysis was not carried out incorporating the weak contacts for the sake of simplicity. The majority of the weak contacts (Figure 3.26 and Figure 3.27) form R 2,1(4) or R 1,2(4) type patterns.

Table 3.20. Graph set matrix for strong intermolecular hydrogen bonding in β-FOX-7 at 393 K.[a]

	N21 H11 O11[ii]	N21 N11 O21[i]	N21 H12 O22[ii]	N22 H21 O22[i]	N22 H22 O12[iii]
	a	b	c	e	f
a	C1,1(6)				
b	C2,1(6)	C1,1(6)			
c	C2,2(12)[R2,2(8)]	C2,2(6)	C1,1(6)		
e	C2,2(10)	C2,2(12)[R2,2(8)]	C1,2(6)	C1,1(6)	
f	C2,2(8)	C2,2(10)	C2,2(10)	C2,2(8)	C1,1(6)

[a] Symmetry codes: (i) 1/2-x, 1-y, -1/2+z; (ii) 3/2-x, 1-y, -1/2+z; (iii) -1+x, y, z.

Several noteworthy changes in the binary strong hydrogen bonding network including the formation of an R 2,1(4) and R 2,1(6) patterns "within" the R 2,2(8) pattern involved in determining the angle of the wave-shaped layers are observed. All ring patterns observed in β-FOX-7 are also incorporated into chain patterns of various lengths, as observed for α-FOX-7. In addition, the same range of binary C 2,2(X) patterns in which X = 6, 8, 10 or 12 present in α-FOX-7 are present in β-FOX-7.

Further heating of β-FOX-7 induces the irreversible transition to γ-FOX-7. Although the wave-shaped layers of β-FOX-7 become planar layers of γ-FOX-7 on transition, the hydrogen bonding network is only slightly affected and the change in nitro group conformation is also only minor. Both crystallographically inequivalent molecules in the asymmetric unit of γ-FOX-7 are surrounded by 17 hydrogen bonds (including eight weak contracts around molecule 1 and seven weak and one extremely weak contact around molecule 2). Since graph-set analysis of a doubled asymmetric unit is complex and the relationship between the hydrogen bond networks in β- and γ-FOX-7 seems relatively simple, a rigorous graph-set analysis was not carried out for γ-FOX-7. Accounting for the exchange of crystallographic axes necessary to compare β- and γ-FOX-7, Figure 3.26 shows a comparison of the hydrogen bonding in β-FOX-7 and molecule 1 of γ-FOX-7 and Figure 3.27 β-FOX-7 and molecule 2 of γ-FOX-7.
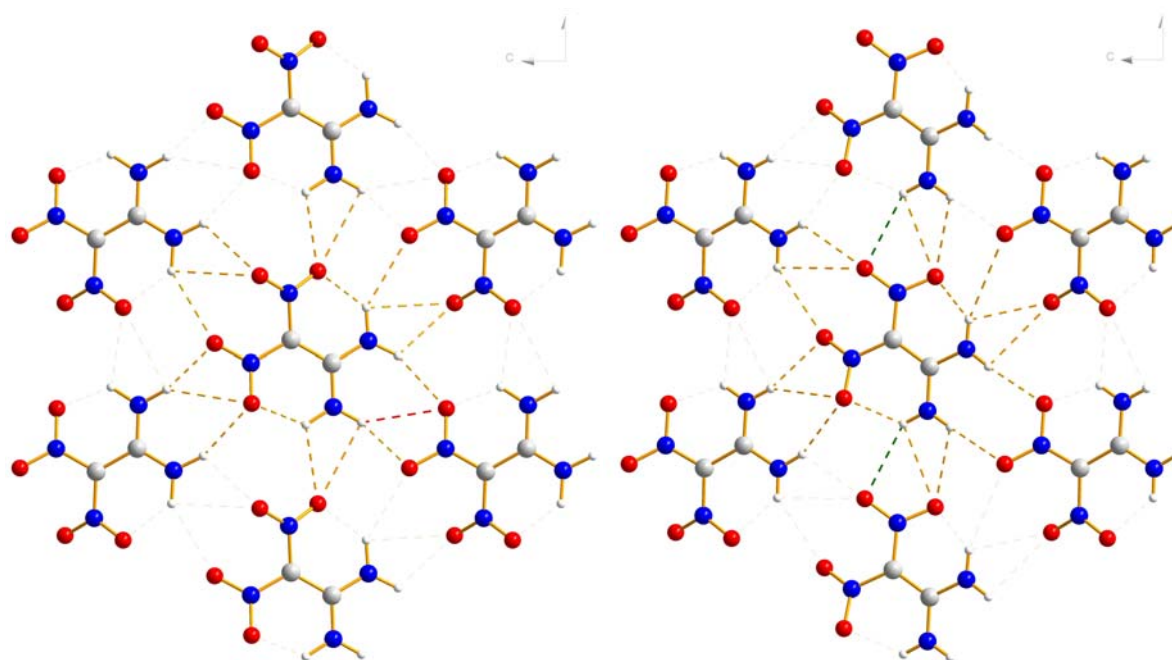
Figure 3.26. Ball and stick representations of seven-molecule hexagons of β-FOX-7 (left) and molecule 1 of γ-FOX-7 (right) showing hydrogen bonding around each central molecule. Hydrogen bonds lost upon transformation from β- to γ-FOX-7 are shown in red and new hydrogen bonds formed on transition are shown in green.
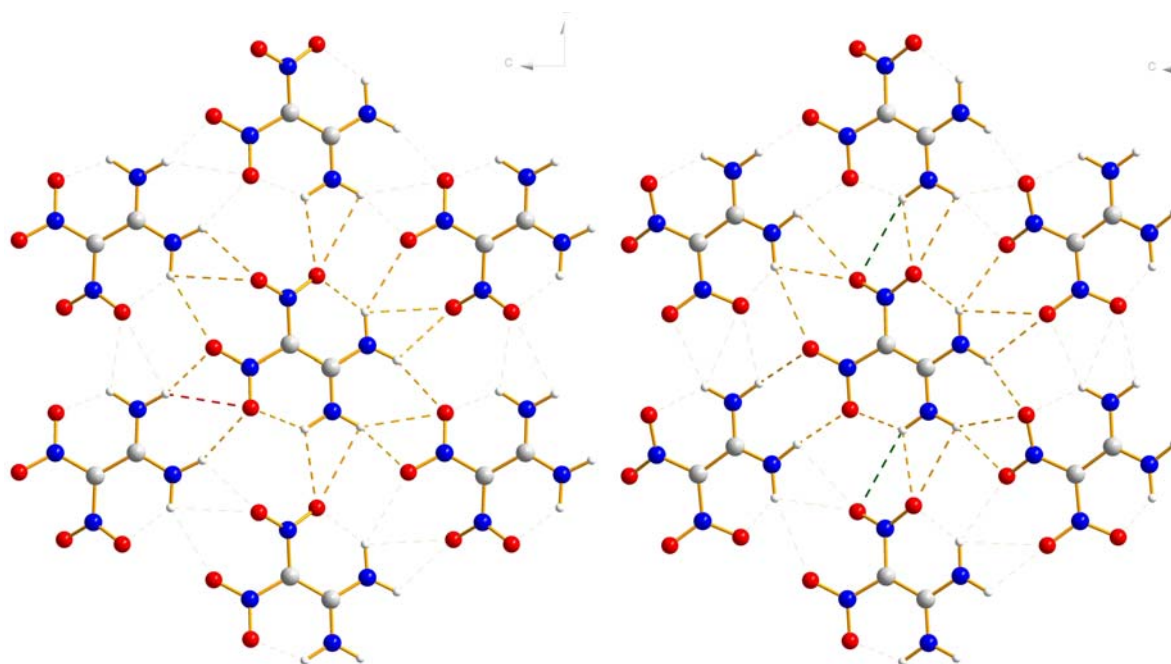
Figure 3.27. Ball and stick representations of seven-molecule hexagons of β-FOX-7 (left) and molecule 2 of γ-FOX-7 (right) showing hydrogen bonding around each central molecule. Hydrogen bonds lost upon transformation from β- to γ-FOX-7 are shown in red and new hydrogen bonds formed on transition are shown in green.

   As shown in Figure 3.26 and Figure 3.27 transformation from β- to γ-FOX-7 results in the loss of one weak hydrogen bond around each molecule in β-FOX-7 and the gain of two weak hydrogen bonds around each molecule (regardless of crystallographic differences) of γ-FOX-7 resulting in a net gain of one weak hydrogen bond. Interestingly, the additional new hydrogen bonds formed lie roughly along the crystallographic *b* axis in γ-FOX-7 and the hydrogen bond lost lies in both cases roughly perpendicular to that same axis. In α- and β-FOX-7 this corresponds to the *a* axis and upon transformation from the wave-shaped packing of β-FOX-7 to the planar layer packing arrangement found in γ-FOX-7 $a(\beta) = b(\gamma)$ contracts slightly, probably on account of the formation of the above mentioned new weak hydrogen bonds. The contraction of the crystallographic axis on transition may also explain the irreversible nature of the β – γ transition.

The wave-shaped layers of FOX-7 in α- and β-FOX-7 can be thought of as a folded sheet of paper, much like a paper fan. A paper fan is easily folded and unfolded (reversible α – β transition), as long as the creases are not pulled completely flat and the shape of the fan distorted roughly perpendicular to the folds. However, if the creases of the fan are pulled completely flat, resulting in not only flattening but a distortion in the paper perpendicular to the folds, the fan cannot refold itself. Since $a(\beta) = b(\gamma)$ are roughly perpendicular to the wave fronts of the layers of FOX-7, the complete flattening of the layers followed by contraction along the $b(\gamma)$ axis results in the layers effectively "jamming," rendering retransformation to β-FOX-7 impossible without either completely breaking down the intermolecular hydrogen bonding network (dissolving the material in a solvent) or mechanically stressing the material (grinding) such that the $b(\gamma)$ axis is distorted enough to allow reformation of the wave shaped layers.

Finally, in addition to providing the possible cause of the irreversible nature of the β – γ phase transition in FOX-7, analysis of the hydrogen bond networks in β- and γ-FOX-7 also seems to indicate increasing overall network strength on transformation from β- to γ-FOX-7.

3.3 Conclusions

Over the temperature range studied, FOX-7 has three distinct structural forms (polymorphs). α-FOX-7 which is stable from <200 to 388(1) K, β-FOX-7 from 392(1) to ~435 K and γ-FOX-7 from ~450 to decomposition. The transitions between polymorphs occur at reproducible temperatures with similar changes in enthalpy and entropy for both transformations (~3 kJ/mol and ~7 J/mol K, respectively). However, the transformation from α- to β-FOX-7 is fully and smoothly reversible, where as the transition from β- to γ-FOX-7 is not and therefore yields samples of metastable γ-FOX-7 on careful cooling. Retransition from metastable γ-FOX-7 directly to α-FOX-7 at room temperature can be induced by mechanical stimulus or recrystallization of the metastable material.

The nature and structural basis for the transitions are readily explained by comparison of the structures of each of the three polymorphs. The α to β transition seems to occur to decrease the overall rigidity of the "wave-shaped" layer structure (due to highly efficient hydrogen bond donor acceptor use in α-FOX-7) in response to the increasing thermal (vibrational) motion of the nitro groups as temperature rises. The transition occurs via a "shearing" action within the "wave-shaped" layers and results, as expected, in an increase in symmetry (change from monoclinic to orthorhombic space groups) and cell volume, but at the same time in a decrease in hydrogen bond network efficiency, which is accompanied by a decrease in packing efficiency. Changes in the packing of FOX-7 on transition from the α to the β polymorph also allow the molecules to assume an overall conformation very similar to the calculated gas-phase minimum energy conformation as calculated by Politzer et al.[28] Reformation of the highly efficient hydrogen bonding network of α-FOX-7 and the resulting decrease in unit cell volume and symmetry proceeds smoothly on cooling since no there is no significant structural barrier to the transition (i.e. the transition is of largely displacive nature).

The transition from β- to γ-FOX-7 eliminates the three dimensional rigidity of the structure, resulting in the formation of planar layers of FOX-7 molecules. The loss of three dimensional rigidity in the structure seems to be necessitated by further increases in the thermal motion of the nitro groups at high temperature. The transition seems to occur via simple flattening of the wave shaped layers followed by a substantial translation of neighboring layers with respect to one another. The flattening of the layers in response to increased nitro group thermal motion results in only minor changes in hydrogen bonding network efficiency and strength and thus only minor changes in molecular conformation. However, the translation or "sliding" of neighboring layers over one another in order to optimize the efficiency of the planar layer packing, results in far more significant structural changes. These changes include a dramatic increase in the unit cell β angle from 90 to 111 °, a decrease in overall symmetry (change from orthorhombic to monoclinic space group) and a relative decrease in

unit cell dimensions in both the *a* and *b* directions. The net result of these changes is a transition that is not only irreversible and appears to be of primarily reconstructive nature, but also explains the observed thermosalient behavior of the FOX-7 crystals upon heating (large changes in monoclinic angle, which result in substantial crystal deformation have been shown to result in thermosalient behavior[29]).

In conclusion, the results of this study have identified the changes and their causes and effects in the structure of FOX-7 as temperature approaches the its decomposition point. Interestingly, it seems that not only the strength of hydrogen bonding networks (or other intermolecular interactions) plays a significant role in the stability of insensitive energetic materials, but the efficiency of donor-acceptor use within the network is also critical. Taking FOX-7 as an example, the efficiency of the hydrogen bonding network suggested to be responsible for its insensitivity is most affected as temperature rises to the decomposition point. The overall strength of the network is not substantially affected. Therefore, for the design of future insensitive energetic materials, not only the ability of donors and acceptors (hydrogen bond or otherwise) to form strong interactions should be taken into account, but also the efficiency of their combination.

3.4 Future Work

Since detonation involves extremely high temperature and pressure, it also seems to be of considerable interest to study energetic materials, such as FOX-7 at elevated pressure. Previous work on FOX-7 documents the compressibility of the crystallographic axis of FOX-7 up to 8 GPa.[30] Although unit cell parameters and Raman spectra are reported in this study at a variety of pressures, no detailed structural information was derived and the Raman spectra are generally not well resolved so provide little insight into structural changes occurring in FOX-7 with increasing pressure.

Therefore, in collaboration with Dr. M. Eremets of the Max Planck Institute for Chemistry in Mainz, further studies of single crystals of FOX-7 under pressure have begun. The initial

Raman spectra were measured at 19 different pressures up to 21.5 GPa, although meaningful spectral changes are only observed in the 0 to 10 GPa range. Stacked plots of spectra in this range are shown in Figure 3.28 for the high frequency vibrations (3600 - 3000 cm^{-1}) and in Figure 3.29 for the lower frequency vibrations (1800 - 170 cm^{-1}).
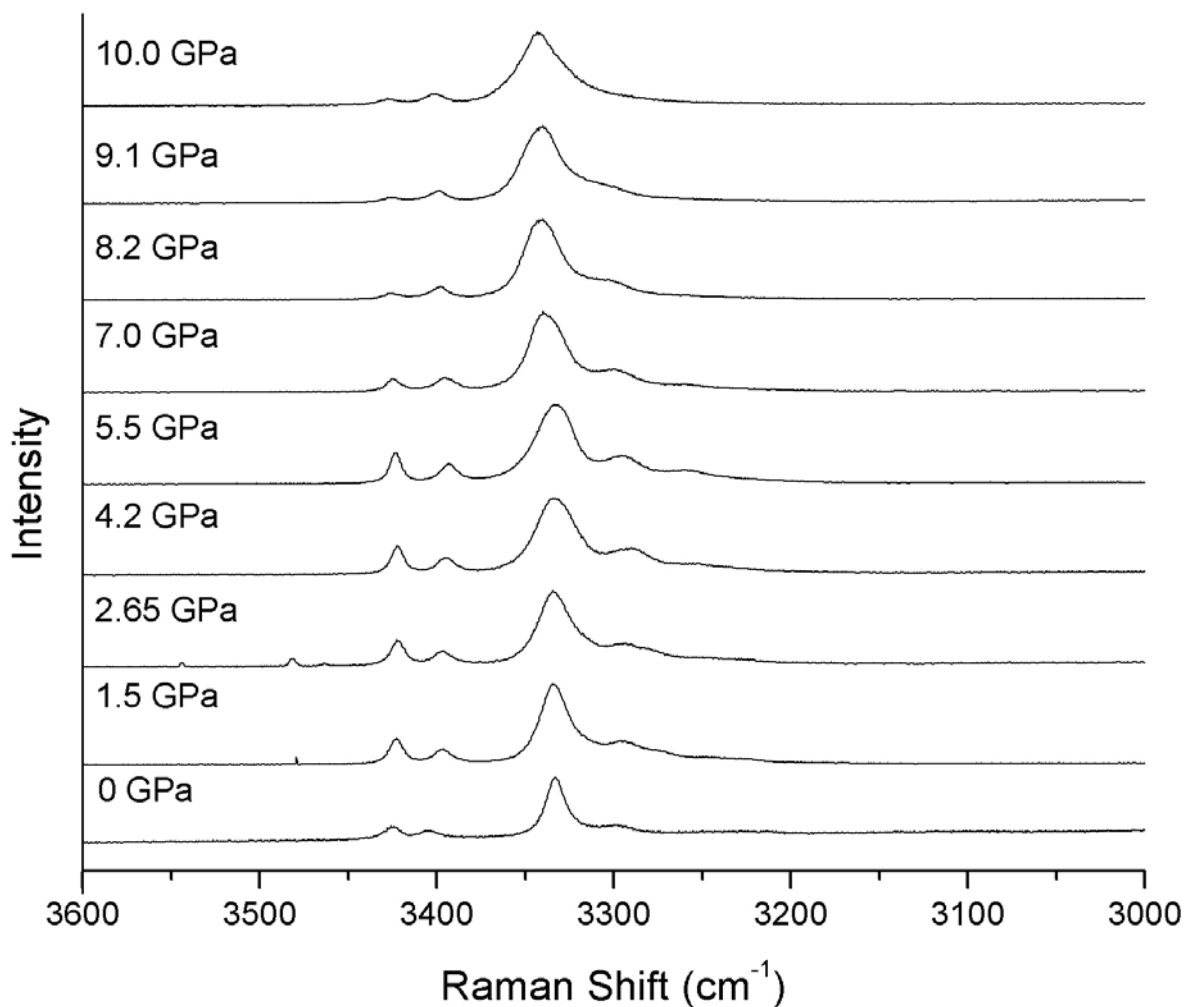
Figure 3.28. High frequency Raman vibrations observed for FOX-7 at 0 - 10.0 GPa.
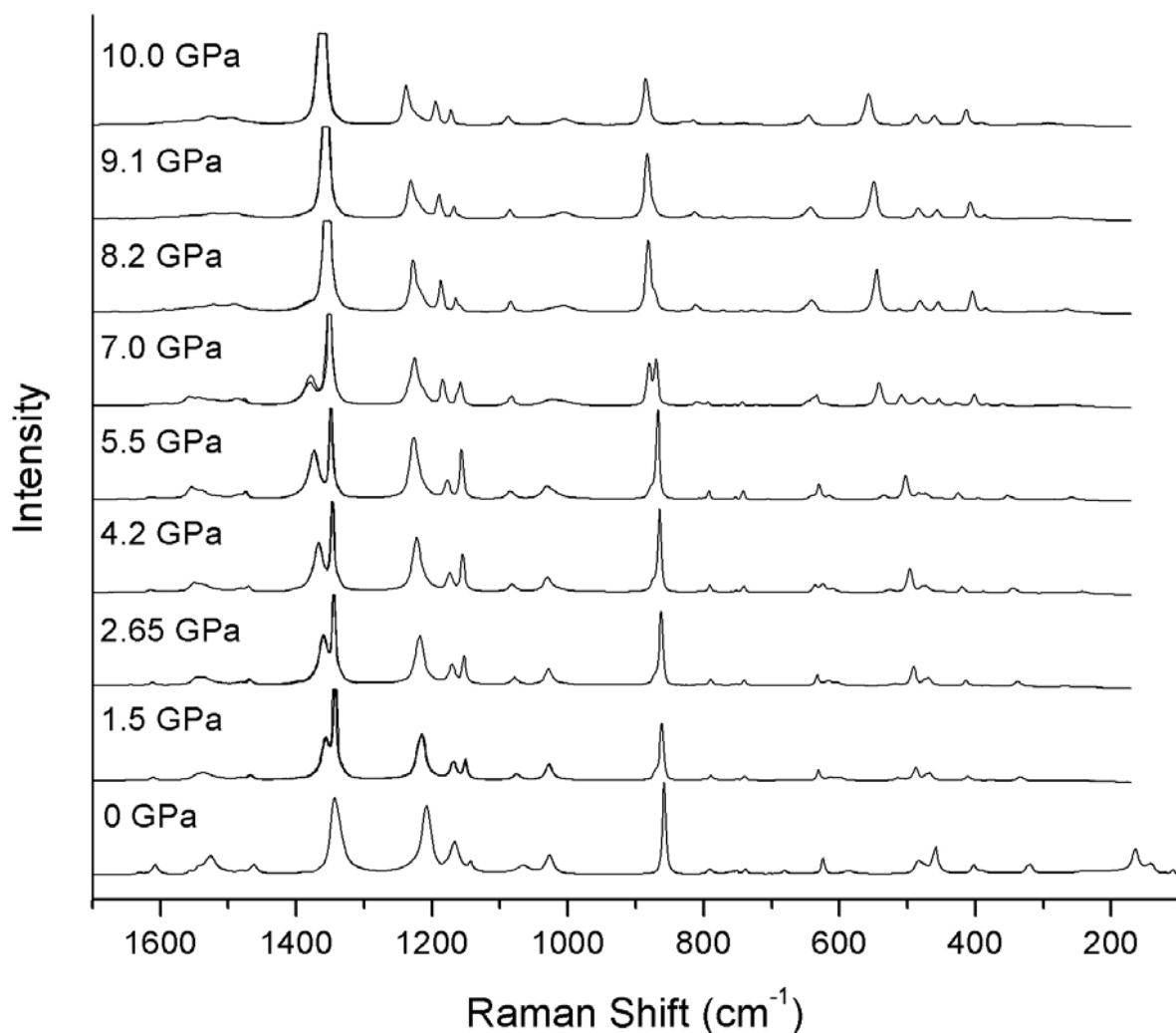
Figure 3.29. Low frequency Raman vibrations observed for FOX-7 at 0 - 10.0 GPa.

Brief inspection of Figure 3.28 and Figure 3.29 indicates the possibility of two further modifications of FOX-7 which are stable under pressure. One appears to be stable between 1.5 and 5.5 GPa and the second at 8.2 GPa and higher. Changes in the spectra as pressure is increased bear strong similarities to those observed on heating, suggesting structural changes that may be similar to those resulting from elevated temperature. Unfortunately, it seems that these further modifications of FOX-7 are not metastable at ambient pressure, since release of pressure results in Raman spectra identical to those measured prior to compression.

Since the initial Raman studies of FOX-7 under pressure indicate the possibility new modifications of FOX-7 it would be of considerable interest to determine the structures of

171

these polymorphs crystallographically. However, due to the complexity of measuring diffraction patterns at high pressure, no useable diffraction data have been collected to this point. Diffraction data which lead to detailed structural information for any new modifications of FOX-7 would be highly desirable and provide an even better understanding of the changes wrought in FOX-7 at near detonation conditions. A set of more closely spaced spectroscopic measurements (0.5 GPa or smaller intervals) over the 0 to 10 GPa range would also be of interest since they should more accurately indicate the pressure at which α-FOX-7 potentially transitions to the first higher pressure form.

Although the temperature dependent behavior of FOX-7 has largely been resolved over the course of this work and has supplied considerable insight into the properties of FOX-7, the behavior of FOX-7 under pressure remains largely unresolved. Future work in this area, will almost certainly yield further understanding of FOX-7, which may also be applied to the understanding of current and the design of new energetic materials.

3.5 Experimental Section

3.5.1 Caution
Although FOX-7 is classified as an insensitive energetic material and may, by and large, be handled in the same way as any laboratory chemical, it is nonetheless an energetic material and should be treated with care.

3.5.2 General
1,1-Diamino-2,2-dinitroethene (FOX-7) was purchased from Bofors and was dried under vacuum prior to use. Infrared (IR) spectra were recorded on a Perkin-Elmer Spectrum One FT-IR instrument as KBr pellets or as thin films deposited from acetone on a 2.0 mm NaCl plate at room temperature. Atenuated total internal reflection IR spectra were measured on a Perkin-Elmer Spectrum BX FT-IR System. Transmittance values are qualitatively described as "very strong" (vs), "strong" (s), "medium" (m) and "weak" (w). Raman spectra were recorded on a Perkin-Elmer Spectrum 2000R NIR FT-Raman instrument equipped with a

Nd:YAG laser (1064 nm) and a ventacon sample oven with an integrated temperature controller. The intensities are reported as percentages of the most intense peak and are given in parentheses. Differential scanning calorimetry measurements were made on a Perkin-Elmer Pyris 6 DSC instrument, calibrated with standard pure indium and zinc. Measurements were performed at the heating rates and with sample preparations described in the results and discussion section.

3.5.3 Single Crystal Experiments

Single crystals of α-FOX-7 were prepared by slow cooling of warm DMF or DMSO solutions of vacuum dried material. Crystals showing well-developed faces were selected under a polarization microscope and treated as described in the results and discussion section to produce crystals of β- and γ-FOX-7. Measurements j069 - j074 were made on a STOE IPDS diffractometer, jo025-jo032, ko033-ko035 and cx018_460-cx018_490 on an Oxford Diffraction Xcalibur 3 diffractometer equipped with a CCD detector and measurement kn553 was made on an Enraf-Nonius Kappa CCD diffractometer. All structures were solved using the *SHELX-97* program package[31], and thermal parameters for non-hydrogen atoms were refined anisotropically. For all measurements aside from kn553, the positions of the hydrogen atoms were determined experimentally from difference Fourier analyses and refined without geometric constraints. Unfortunately, for the γ-phase measurement at 200K (kn553) only seven of the eight hydrogen atom positions could be experimentally determined by difference Fourier analyses and therefore all hydrogen positions in the γ-phase were calculated using geometric constraints with the *SHELXL97* program package. In addition, since interatomic distances less than 2 Å are underestimated in structures with large anisotropic displacement parameters, a correction was applied to all structures of adequate precision by calculating the thermal tensors T, L and S^{32} using the program THMA11[33, 34]. The atomic labeling and coordinates of the asymmetric unit in α- and β-FOX-7 used here are

those used by Bemm and Östmark. This naming convention is slightly modified to describe both crystallographically independent molecules present in the asymmetric unit of γ-FOX-7.

3.5.4   Powder Diffraction Experiments

Finely ground α-FOX-7 was carefully sieved (140 mesh) in order to lower the effects of preferred orientation, filled into a 0.5 mm Lindemann capillary under an inert atmosphere and then sealed. The material was then investigated on a Huber G644 Guinier diffractometer with the angle calibrated using electronic grade germanium (a = 5.6575 Å). Sample temperatures were maintained on the diffractometer using a Huber heating attachment. The temperature was calibrated by measuring Guinier diffractograms of NaCl, for which the temperature dependence of the lattice parameters is well known[35], under the same heating conditions as the subsequently measured FOX-7 samples. Measurements with MoKα_1 radition were made over the 2θ range 6 - 36 ° with an increment of 0.04 ° and a counting time of 10 seconds per increment. Measurements with CuKα_1 radiation were made over the 2θ range 13 - 76 ° with an increment of 0.08 ° and a counting time of at least 60 seconds per increment.

3.6 References

(1)   Bellamy, A. J., FOX-7 (1,1-Diamino-2,2-dinitroethene). In *High Energy Density Materials*, 1st ed.; Klapötke, T. M., Ed.; Structure & Bonding; Springer-Verlag: Berlin, 2007; 125, 1-33.

(2)   *UN Recommendations on the Transport of Dangerous Goods, Manual of Tests and Criteria*. United Nations: New York, 2003.

(3)   Bemm, U.; Ostmark, H., *Acta Crystallogr.*, **1998,** *C54*, 1997-1999.

(4)   Gilardi, R., CCDC 127539. *Cambridge Crystallographic Data Centre*: Cambridge, U.K., 1999.

(5)   Burnham, A. K.; Weese, R. K.; Wang, R.; Kwok, Q. S. M.; Jones, D. E. G., *Proceedings of the NATAS Annual Conference on Thermal Analysis and Applications*, **2005,** *33rd*, 042 38 151/1-042 38 151/8.

(6)   Fan, X.-z.; Li, J.-z.; Liu, Z.-r., *J. Phys. Chem*, **2007,** *A111*, 13291-13295.

(7)   Garmasheva, N. V.; Chemagina, I. V.; Filin, V. P.; Kazakova, M. B.; Loboiko, B. G., *New Trends in Research of Energetic Materials, Proceedings of the Seminar, 7th, Pardubice, Czech Republic, Apr. 20-22, 2004*, **2004,** *1*, 116-122.

(8)   Kempa, P. B.; Hermann, M.; Metzger, F. J. M.; Thome, V.; Kjellstroem, A.; Latypov, N., *International Annual Conference of ICT*, **2004,** *35th*, 71/1-71/15.

(9)   Ostmark, H.; Bergman, H.; Bemm, U.; Goede, P.; Holmgren, E.; Johansson, M.; Langlet, A.; Latypov, N. V.; Pettersson, A.; Pettersson, M.-L.; Wingborg, N.; Vorde, C.; Stenmark, H.; Karlsson, L.; Hihkio, M., *International Annual Conference of ICT*, **2001,** *32nd*, 26/1-26/21.

(10)   Kempa, P. B.; Herrmann, M., *Part. Part. Syst. Char.*, **2006,** *22*, 418-422.

(11)   Burnham, A. K.; Weese, R. K.; Wang, R.; Kwok, Q. S. M.; Jones, D. E. G., *International Annual Conference of ICT*, **2005,** *36th*, 150/1-150/12.

(12)   Bernstein, J., *Polymorphism in Molecular Crystals*. Clarendon Press: Oxford, UK, 2002.

(13)   West, A. R., *Solid State Chemistry and its Applicaitons*. John Wiley and Sons Ltd.: Chichester, UK, 1998.

(14)   Sorai, M., *Comprehensive handbook of calorimetry and thermal analysis*. Wiley: Chichester, 2004.

(15)   Bemm, U.; Eriksson, L., *Insensitive Munitions & Energetic Materials Technology Symposium, Bordeaux, France, Oct. 8-11, 2001*, **2001,** *2*, 775-790.

(16)   Wild, R.; Teipel, U., *International Annual Conference of ICT*, **2004,** *35th*, 69/1-69/9.

(17)   Dunitz, J. D., *Acta Cryst.*, **1995,** *B51*, 619-31.

(18)   *Symmetry relations between space groups*. Kluwer Academic Publishers: Dordrecht, Netherlands, 2004; A1.

(19)   Brandenburg, K. *Diamond*, 3.0a; Crystal Impact GbR: Bonn, Germany, 2004.

(20)   Ju, X.-H.; Xiao, H.-M.; Xia, Q.-Y., *J. Chem. Phys.*, **2003,** *119*, 10247-10255.

(21)   Holleman, A. F.; Wiberg, E.; Wiberg, N., *Lehrbuch der Anorganischen Chemie*.
Walter de Gruyter: Berlin, Germany, 1985.

(22)   Jeffrey, G. A., *An Introduction to Hydrogen Bonding*. Oxford University Press: New
York, 1997.

(23)   Pimentel, G. C.; MacClellan, A. L., *The hydrogen bond*. Freeman: San Franciscon,
CA, USA, 1960.

(24)   Bondi, A., *J. Phys. Chem.*, **1964,** *68*, 441-451.

(25)   Allen, F. H.; Lommerse, J. P. M.; Hoy, V. J.; Howard, J. A. K.; Desiraju, G. R., *Acta
Cryst.*, **1997,** *B53*, 1006-1016.

(26)   Jeffrey, G. A.; Lewis, L., *Carbohydr. Res.*, **1978,** *60*, 179-182.

(27)   Bernstein, J.; Davis, R. E.; Shimoni, L.; Chang, N.-L., *Angew. Chem., Int. Ed. Eng.*,
1995, *34*, 1555-1573.

(28)   Politzer, P.; Concha, M. C.; Grice, M. E.; Murray, J. S.; Lane, P., *Theochem*, **1998,**
452, 75-83.

(29)   Crottaz, O.; Kubel, F.; Schmid, H., *J. Mater. Chem.*, **1997,** *7*, 143-146.

(30)   Peiris, S. M.; Wong, C. P.; Zerilli, F. J., *J. Chem. Phys.*, **2004,** *120*, 8060-8066.

(31)   Sheldrick, G. M. *Programs for Crystal Structure Analysis (Release 97-2)*, Goettingen,
Germany, 1998.

(32)   Dunitz, J. D., Thermal Motion Analysis. In *X-ray analysis and the structure of
organic molecules*, ed.; Ed.; VCH: Weinheim, Germany, 1995; 244-261.

(33)   Farrugia, L., *J. Appl. Crystallogr.*, **1999,** *32*, 837-838.

(34)   Trueblood, K., *Acta Cryst.*, **1978,** *A34*, 950-954.

(35)   Pathak, P. D.; Vasavada, N. G., *Acta Cryst.*, **1970,** *A26*, 655-658.

4 Appendices

4.1 Chapter 1
Brief description of the graph set description of hydrogen-bond patterns

A full description of the systematic use of graph set analysis is found in chapter 1, reference 56 and chapter 2 references 12 and 27 and is only paraphrased here. The patterns described in this work are either those formed by a single hydrogen bond and its symmetry equivalents (unitary or first order patterns, also know as motifs) or those formed by two hydrogen bonds and their symmetry equivalents (binary or second order patterns). All patterns composing a network may be described as rings (graph set descriptor **R**), chains (**C**), intramolecular (**S**) or dimer (**D**). Patterns are described by a full descriptor G a,d(n) in which G is the pattern descriptor described above, a is the number of hydrogen atom acceptors d is the number of hydrogen atom donors and n is the path length (number of atoms involved) of the pattern. For example a second order six remembered ring generated by two crystallographically independent hydrogen bonds involving two acceptors, two donors would have the complete descriptor R 2,2(6.)

Table 4.1. MP2/aug-cc-pVDZ computational results.

Ion / Compound	P. G.[a]	-E (a.u.)[b]	zpe (kcal/mol)[c]	NIMAG[d]
Ammonium	T_d	56.739780	31.2	0
Hydrazinium	C_s	111.912342	42.9	0
Guanidinium	D_{3h}	205.218050	55.3	0
Aminoguanidinium	C_1	260.403398	66.2	0
Diaminoguanidinium	C_1	315.588401	77.5	0
Triaminoguanidinium	C_3	370.773187	100.8	0
1-Methyl-5-amino-tetrazolium	C_1	352.3735075	65.1	0
1,4-dimethyl-5-aminotetrazolium	C_s	391.5687493	82.8	0
5-Nitrotetrazolate	C_{2v}	461.179216	24.1	0
Nitrate	D_{3h}	279.76175	9.0	0
Perchlorate	T_d	759.637931	9.4	0
Azide	$D_{\infty h}$	163.8588	6.3	0
Dinitramide	C_2	463.977162	17.9	0
Oxygen (O_2)	$D_{\infty h}$	150.004290	2.0	0
Carbon Dioxide	$D_{\infty h}$	188.169700	7.1	0
Water	C_{2v}	76.260910	13.4	0
Nitrogen (N_2)	$D_{\infty h}$	109.280650	3.1	0

[a] Point group. [b] Electronic energy. [c] Zero point energy. [d] Number of imaginary frequencies.

Table 4.2. Predicted thermochemical data.

Compound	ΔH_L (kJ/mol)[a]	ΔH_r (kJ/mol)[b]	$\Delta_\text{c} H^\text{o}_\text{m (pred)}$ (kJ/mol)[c]
6	538.4	-2177.8	-1771.4
7	519.0	-2467.6	-2058.6
9	517.8	-2774.1	-2432.4
10	502.3	-3063.9	-2640.9
11	520.4	-3231.9	-2887.5
12	490.2	-2958.1	-2643.9
13	567.2	-1635.0	-1155.8
15	558.4	-1899.4	-1451.1
16	527.4	-2230.2	-1834.8
17	517.4	-2457.7	-2094.3
18	501.8	-2687.8	-2362.0
20	493.1	-2968.7	-2673.6
21	483.8	-3587.4	-3279.6

[a] Predicted lattice enthalpy. [b] Gas-phase heat of reaction from calculated (MP2/aug-cc-pVDZ) electronic energies of ions and combustion products . [c] Predicted standard molar enthalpy of combustion.

4.2 Chapter 2

Table 4.3. DSC data from series measurements of FOX-7 (first endotherm, α – β transition)

Pan Type[a]	β (K/min)[b]	Mass (mg)[c]	Onset (K)	Position (K)[d]	Height (mW)	$\Delta_{trs}H$ (J/g)
Closed	10	1.649	389.31	391.88	1.3863	18.258
	5	1.170	388.36	390.59	0.9242	19.078
	2	1.741	387.76	389.3	0.4762	17.047
	1	1.958	386.82	388.16	0.2634	18.217
Open	10	2.144	389.13	392.05	2.0183	18.498
	5	2.476	388.35	390.67	1.5061	19.452
	2	2.099	387.21	389.17	0.5418	18.557
	1	2.005	387.33	387.51	0.3267	18.614
Closed	10	6.422	389.57	392.43	5.4262	18.958
	5	5.704	388.19	390.71	2.7330	17.057
	2	5.485	387.15	389.14	1.3302	17.450
	1	5.587	387.02	387.9	0.7202	17.399
Open	10	6.679	389.41	392.27	5.6119	18.288
	5	5.950	388.32	390.63	3.0870	18.259
	2	5.596	387.48	388.98	1.4862	19.323
	1	5.377	387.33	388.1	0.8745	19.646

[a] Sample pan type, "closed" are aluminium pans sealed by pressing as described in the experimental section and "open" are unsealed aluminium pans covered with an aluminium disk. [b] Heating rate. [c] Sample mass. [d] Peak position.

Table 4.4. DSC data from series measurements of FOX-7 (second endotherm, β – γ transition)

Pan Type[a]	β (K/min)[b]	Mass (mg)[c]	Onset (K)	Position (K)[d]	Height (mW)	$\Delta_{trs}H$ (J/g)
Closed	10	1.649	437.27	438.57	0.7238	15.511
	5	1.170	433.39	433.61	0.4812	16.777
	2	1.741		439.45	0.3623	17.792
	1	1.958		438.77	0.4455	19.816
Open	10	2.144		437.24	-	18.941
	5	2.476		435.27	1.0396	20.446
	2	2.099		438.37	0.6613	21.260
	1	2.005		437.29	0.5917	17.922
Closed	10	6.422	434.28	439	2.6319	18.811
	5	5.704	273.15	436.17	1.2141	15.647
	2	5.485	273.15	436.13	0.7628	16.763
	1	5.587	273.15	437.63	0.6908	17.509
Open	10	6.679	434.54	436.5	3.0735	18.03
	5	5.950		437.41	2.0491	17.70
	2	5.596		434.02	1.1992	19.543
	1	5.377		434.97	1.4657	20.540

[a] Sample pan type, "closed" are aluminium pans sealed by pressing as described in the experimental section and "open" are unsealed aluminium pans covered with an aluminium disk. [b] Heating rate. [c] Sample mass. [d] Peak position.

Table 4.5. DSC data from series measurements of FOX-7 (first exotherm, decomposition)

Pan Type[a]	β (K/min)[b]	Mass (mg)[c]	Onset (K)	Position (K)[d]	Height (mW)	$\Delta_{trs}H$ (J/g)
Closed	10	1.649	507.08	516.58	-16.1241	-700.93*
	5	1.170	499.15	512.82	-7.2696	-733.96*
	2	1.741	492.57	507.9	-3.4410	-732.60*
	1	1.958	485.82	501.32	-1.9380	-787.74*
Open	10	2.144	501.76	510.39	-18.4078	-552.71
	5	2.476	495.64	505.54	-9.6971	-600.14
	2	2.099	487.82	498.03	-4.3466	-794.23
	1	2.005	486.38	493.44	-2.3582	-898.507
Closed	10	6.422			-	-
	5	5.704	507.75	512.96	-49.8045	-698.75
	2	5.485	503.9	508.94	-16.2404	-655.73
	1	5.587			-	-
Open	10	6.679	508.15	513.44	-276.8058	-634.74
	5	5.950	497.03	504.38	-30.2846	-515.12
	2	5.596	488.8	498.25	-11.0636	-328.139
	1	5.377	483.73	493.35	-6.5952	-978.378

[a] Sample pan type, "closed" are aluminium pans sealed by pressing as described in the experimental section and "open" are unsealed aluminium pans covered with an aluminium disk. [b] Heating rate. [c] Sample mass. [d] Peak position. * Enthalpy change taken as a fraction of the total energy change, since the exothermic peaks are not completely resolved at some heating rates.

Table 4.6. DSC data from series measurements of FOX-7 (second exotherm, decomposition)

Pan Type[a]	β (K/min)[b]	Mass (mg)[c]	Onset (K)	Position (K)[d]	Height (mW)	$\Delta_{trs}H$ (J/g)
Closed	10	1.649	534.78	537.32	-101.9293	-2265.59*
	5	1.170	529.77	531.95	-60.8611	-2600.98*
	2	1.741	512.13	524.9	-10.4105	-2540.62*
	1	1.958	501.66	524.13	-2.5330	-2202.22*
Open	10	2.144	556.88	560.78	-166.2991	-554.786
	5	2.476	560.7	562.49	-83.4558	-336.668
	2	2.099	552.03	559.63	-1.7916	-261.66
	1	2.005	544.78	554.82	-0.7471	-324.745
Closed	10	6.422			-	-
	5	5.704	527.85	532.77	-278.8890	-2121.459*
	2	5.485	521.74	524.09	-57.3318	-2552.512*
	1	5.587	508.03	518.66	-21.6448	-2596.979*
Open	10	6.679			-	-
	5	5.950	553.38	557.89	-281.8366	-504.12
	2	5.596	555.46	556.67	-19.0703	-328.14
	1	5.377	537.88	552.81	-2.8800	-399.91

[a] Sample pan type, "closed" are aluminium pans sealed by pressing as described in the experimental section and "open" are unsealed aluminium pans covered with an aluminium disk. [b] Heating rate. [c] Sample mass. [d] Peak position. * Enthalpy change taken as a fraction of the total energy change, since the exothermic peaks are not completely resolved at some heating rates.

Table 4.7. Wave-shaped angles and interlayer spacings in FOX-7 determined by temperature resolved single crystal X-ray structure determinations

Measurement Temperature (K)	Measurement Code	Phase	Wave-shaped angle (°)	Interlayer Spacing (Å)
200	j069	α	135.3	2.984
298	j070	α	135.9	3.012
333	j071	α	136.3	3.03
353	jo025	α	136.2	3.032
363	jo026	α	136.5	3.027
373	jo028	α	136.6	3.04
393	j073	β	149.6	3.173
403	ko033	β	150.4	3.172
413	ko034	β	150.4	3.184
423	ko035	β	150.3	3.186
460	cx018_460	γ	176	3.3235
470	cx018_470	γ	176	
200	kn553	γ	177.8	3.0915

Table 4.8. Out-of-molecular-plane twist angles for $N11O_2$ and $N12O_2$ in FOX-7 determined by temperature resolved single crystal X-ray structure determinations

Measurement Temperature (K)	Measurement Code	Phase	$N11O_2$ out-of-plane twist angle (°)	$N12O_2$ out-of-plane twist angle (°)
200	j069	α	-35.4	7.8
298	j070	α	-34.9	8.1
333	j071	α	-37.7	8.3
353	jo025	α	-34.6	8
363	jo026	α	-34.4	8.1
373	jo028	α	-34.5	8.4
393	j073	β	-21.9	22.8
403	ko033	β	-21.4	22.3
413	ko034	β	-21.6	22.6
423	ko035	β	-21.4	22.5
200	kn553	γ	-15.5 / -18.2[a]	16.6 / 19.4[b]

[a] $N11O_2$ out-of-plane twist angle / $N31O_2$ out-of-plane twist angle. [b] $N12O_2$ out-of-plane twist angle / N32 out-of-plane twist angle.

Table 4.9. Out-of-molecular-plane displacement of N11, N12, O11, O12, O21 and O22 in FOX-7 determined by temperature resolved single crystal X-ray structure determinations

T (K)	Code	Phase	N11	N12	O11	O12	O21	O22
200	j069	α	-0.0113	-0.2047	0.1075	-0.0332	0.325	-0.8817
298	j070	α	-0.006	-0.1999	0.1212	-0.0317	0.3217	-0.8659
333	j071	α	-0.023	-0.1952	0.1265	-0.0333	0.3241	-0.8558
353	jo025	α	0.0182	-0.1795	0.1546	-0.0181	0.3313	-0.8275
363	jo026	α	0.0096	-0.1934	0.1356	-0.0202	0.3161	-0.8474
373	jo028	α	0.0043	-0.1971	0.1318	-0.0259	0.3126	-0.8485
393	j073	β	0.1036	-0.016	0.5354	-0.2164	0.1694	-0.502
403	ko033	β	0.1187	-0.0802	0.5629	-0.197	0.1763	-0.4693
413	ko034	β	0.1113	-0.0861	0.5542	-0.20257	0.1765	-0.4717
423	ko035	β	0.1095	-0.0924	0.5487	-0.2037	0.168	-0.4779
200	kn553	γ_1	-0.2152	0.1319	0.0733	-0.6557	0.5467	-0.1728
200[a]	kn553	γ_2	-0.213	0.1319	-0.5629	0.0111	-0.0248	0.4837

[a] Values for N31, N32, O31, O32, O41 and O42 are shown in the columns for N11, N12, O11, O12, O21 and O22 respectively for γ_2.

Table 4.10. Bond lengths, *TLS* corrections and corrected bond lengths in FOX-7 from temperature resolved single crystal X-ray structure determinations

code	α j069 200			α j070 298			α j071 333			α jo025 353			α jo026 363		
T(K)															
	Measured	TLS	Corrected	Measured	TLS	Corrected	Measured	TLS	Corrected	Measured	TLS	Corrected	Measured	TLS	Corrected
C1 - C2	1.460(2)	0.0031	1.463(2)	1.458(2)	0.005	1.463(2)	1.456(2)	0.006	1.462(2)	1.462(3)	0.0062	1.468(3)	1.459(3)	0.0062	1.465(3)
C1 - N11	1.389(3)	0.0034	1.392(3)	1.388(2)	0.005	1.393(2)	1.393(3)	0.006	1.399(3)	1.398(3)	0.0067	1.405(3)	1.398(3)	0.0068	1.405(3)
C1 - N12	1.417(2)	0.0045	1.421(2)	1.417(2)	0.007	1.424(2)	1.412(2)	0.008	1.420(2)	1.407(3)	0.0088	1.416(3)	1.407(3)	0.0091	1.416(3)
C2 - N21	1.309(2)	0.0042	1.313(2)	1.308(2)	0.006	1.314(2)	1.307(2)	0.007	1.314(2)	1.299(3)	0.0081	1.307(3)	1.299(3)	0.0083	1.307(3)
C2 - N22	1.320(3)	0.0033	1.323(2)	1.316(3)	0.005	1.321(3)	1.317(3)	0.006	1.323(3)	1.324(3)	0.0064	1.331(3)	1.328(3)	0.0066	1.334(3)
N11 - O11	1.254(2)	0.0028	1.257(2)	1.250(2)	0.004	1.254(2)	1.249(2)	0.005	1.254(2)	1.248(3)	0.0056	1.254(3)	1.249(3)	0.0056	1.254(3)
N11- O12	1.243(2)	0.004	1.247(2)	1.242(2)	0.006	1.248(2)	1.241(3)	0.007	1.248(3)	1.236(3)	0.0078	1.244(3)	1.237(3)	0.008	1.245(3)
N12 - O21	1.237(2)	0.0034	1.240(2)	1.235(2)	0.005	1.240(2)	1.237(2)	0.006	1.243(2)	1.239(3)	0.0065	1.245(3)	1.243(3)	0.0067	1.250(3)
N12 - O22	1.238(2)	0.003	1.241(2)	1.235(2)	0.005	1.240(2)	1.234(2)	0.006	1.240(2)	1.236(3)	0.0059	1.242(3)	1.237(3)	0.006	1.243(3)
σ_{av}		0.0022			0.0022			0.0024			0.003			0.003	

Phase code	α jo028 373			β j073 393			β ko033 403			α ko034 413		
T(K)												
	Measured	TLS	Corrected	Measured	TLS	Corrected	Measured	TLS	Corrected	Measured	TLS	Corrected
C1 - C2	1.458(3)	0.0067	1.465(3)	1.447(2)	0.01	1.457(2)	1.453(3)	0.0107	1.465(3)	1.450(3)	0.0104	1.461(3)
C1 - N11	1.396(3)	0.0073	1.403(3)	1.405(3)	0.013	1.418(3)	1.410(3)	0.0128	1.423(3)	1.414(3)	0.0131	1.427(3)
C1 - N12	1.407(3)	0.0096	1.417(3)	1.397(2)	0.012	1.409(2)	1.397(3)	0.0127	1.410(3)	1.397(3)	0.0128	1.410(3)
C2 - N21	1.303(3)	0.0089	1.312(3)	1.312(2)	0.012	1.324(2)	1.308(3)	0.0121	1.320(3)	1.309(3)	0.0122	1.321(3)
C2 - N22	1.326(3)	0.0071	1.333(3)	1.308(3)	0.012	1.320(3)	1.318(3)	0.012	1.330(3)	1.320(3)	0.0123	1.332(3)
N11 - O11	1.246(3)	0.0061	1.252(3)	1.222(2)	0.01	1.232(2)	1.225(3)	0.0103	1.235(3)	1.225(3)	0.0103	1.235(3)
N11- O12	1.240(3)	0.0085	1.249(3)	1.231(2)	0.012	1.243(2)	1.229(3)	0.0121	1.241(3)	1.225(3)	0.0122	1.237(3)
N12 - O21	1.244(3)	0.0071	1.252(3)	1.241(2)	0.012	1.253(2)	1.243(3)	0.0116	1.254(3)	1.244(3)	0.0119	1.255(3)
N12 - O22	1.234(3)	0.0064	1.240(3)	1.234(2)	0.009	1.243(2)	1.235(3)	0.009	1.244(3)	1.234(3)	0.0088	1.242(3)
σ_{av}		0.003			0.0023			0.003			0.003	

Phase	β			γ$_1$			γ$_2$		
code	ko035			jo031			jo032		
T(K)	423			413			423		
	Measured	TLS	Corrected	Measured	TLS	Corrected	Measured	TLS	Corrected
C1 - C2	1.454(3)	0.0111	1.465(3)	1.45(1)	0.0019	1.45(1)	1.450(9)	0.0019	1.452(9)
C1 - N11	1.408(3)	0.0138	1.422(3)	1.415(9)	0.002	1.417(9)	1.442(9)	0.002	1.444(9)
C1 - N12	1.393(3)	0.0133	1.406(3)	1.41(1)	0.0021	1.42(1)	1.39(1)	0.0021	1.39(1)
C2 - N21	1.310(3)	0.0127	1.322(3)	1.310(9)	0.0019	1.312(9)	1.325(9)	0.002	1.327(9)
C2 - N22	1.317(3)	0.0129	1.330(3)	1.324(9)	0.002	1.326(9)	1.312(9)	0.0019	1.314(9)
N11 - O11	1.226(3)	0.0107	1.237(3)	1.219(7)	0.0018	1.221(7)	1.212(8)	0.0012	1.213(8)
N11- O12	1.226(3)	0.0127	1.238(3)	1.229(8)	0.0019	1.231(8)	1.240(8)	0.0017	1.242(8)
N12 - O21	1.244(3)	0.0125	1.257(3)	1.252(8)	0.0017	1.254(8)	1.258(8)	0.0019	1.259(8)
N12 - O22	1.237(3)	0.0094	1.247(3)	1.228(8)	0.0013	1.230(8)	1.233(8)	0.0018	1.235(8)
σ$_{av}$		0.003			0.0087			0.0087	

<div align="center">CURRICULUM VITAE</div>

NAME	Jan Matthew WELCH
ADDRESS	Waldfriedhofstr. 72, 81377 München
TELEPHONE	Home: +49 89 71909681; Work: +49 89 2180 77503
DATE OF BIRTH	22.10.1981, Albany, NY, USA
NATIONALITY	United States Citizen
MARITAL STATUS	Single
EDUCATION	1987-1989: Guilderland Public Schools, Guilderland, NY, USA
	1989-1990: Hürstholz Schule, Zürich, Switzerland
	1990-1996: Guilderland Public Schools
	1996-2000: The Albany Academy, Albany, NY, USA
	June 2000: Highschool Diploma (cum laude), Albany Academy
	Aug. 2000-Dec. 2002: Bowdoin College, Brunswick, ME, USA
	Mar. 2003-Jul. 2003: Junior Year in Munich, Germany
	Aug. 2003-Dec. 2003 Bowdoin College
	May 2004: B.A. degree Chemistry and German, Bowdoin College
	Mar. 2004-: Doctoral studies in inorganic chemistry, LMU Munich
QUALIFICATIONS	B.A. degree in Chemistry and German (3.6 / 4.0 Grade Point Average), Bowdoin College, USA (May 2004)
PRESENT POST	Scientific Assistant, LMU Munich, Department of Chemistry and Biochemistry (Prof. Klapötke)
PREVIOUS EMPLOYMENT	Aug. 2000-Dec. 2003: Student, Bowdoin College
	Jan. 2004-Mar. 2004 Undergraduate Research Assistant, State University of New York at Albany Department of Chemistry
	Mar. 2004-Dec. 2004: Scientific Assistant, LMU Munich, Department of Chemistry and Biochemistry (AK Klapötke)
	Jan. 2005-Apr. 2008: Scientific co-worker (C1/2), LMU Munich, Department of Chemistry and Biochemistry (AK Klapötke)

ADDITIONAL EXPERIENCE	James Stacey Coles summer research fellow, Bowdoin College Department of Chemistry (Jun. 2001-Aug. 2001 and Jun. 2002-Aug. 2002)
	Undergraduate research assistant (Forschungspraktikant), AK Klapötke, LMU Munich (Apr. 2003-Jul. 2003)
	Introductory teaching lab instructor (Grundpraktikum), LMU Munich (Apr. 2005-Jul. 2005, Oct. 2005-Feb. 2006, Oct. 2006-Feb. 2007, Oct. 2007-Feb. 2008)
	Teaching lab instructor 2nd semester inorganic chemistry (AC I), LMU Munich (Apr. 2006-Jul. 2006)
	Teaching lab instructor 4th semester inorganic chemistry (AC II), LMU Munich (Apr. 2007-Aug. 2007)
	Teaching lab instructor advanced inorganic chemistry (AC III), LMU Munich (Mar. 2005, Sept. 2005, Mar. 2006, Sept. 2006, Mar. 2007, Sept 2007)
	Supervisor of 3 bachelor (honors project) students
	Supervisor of 2 undergraduate research students (Forschungspraktikanten)
LANGUAGE	English – native speaker
	German – fluent, attended Swiss primary school, instruction in secondary school, BA degree in chemistry and German with study abroad in Munich, 3.5 year resident of Munich, Germany
AWARDS AND SCHOLARSHIPS	CRC Press Freshman Chemistry Achievement Award (2001)
	Sarah and James Bowdoin Scholar (2001)
	James Stacey Coles summer research fellowship (2001, 2002)
	American Institute of Chemists Student Award Certificate (2004)
	Galen C. Moses Post Graduate Scholarship (2004)

Publications List

Articles in peer reviewed journals:

M. v. Denffer, T. M. Klapötke, G. Kramer, G. Spieß, J. M. Welch, G. Heeb, "Improved synthesis and X-Ray structure of 5-aminotetrazolium nitrate," *Propellants Explosives and Pyrotechnics*, **2005**, 30(3), 191 - 1195.

M-J. Crawford, T. M. Klapötke, J. Welch, "Energetic materials particle processing and characterization (Edited by Ulrich Teipel)," *Angewandte Chemie, International Edition*, **2005**, 44(13), 1909.

J. Evers, T. M. Klapötke, P. Mayer, G. Oehlinger, J. Welch, "α- and β-FOX-7, Polymorphs of a High Energy Density Material, Studied by X-ray Single Crystal and Powder Investigations in the Temperature Range from 200 to 423 K," *Inorganic Chemistry*, **2006**, 45, 4996 - 5007.

T. M. Klapötke, K. Karaghiosoff, P. Mayer, A. Penger, J. M. Welch, "Synthesis and Characterization of 1,4-dimethyl-5-aminotetrazolium 5-nitrotetrazolate," *Propellants, Explosives and Pyrotechnics*, **2006**, 31, 188 - 195.

C. Darwich, T. M. Klapötke, J. M. Welch, M. Suceska, "Synthesis and Characterization of 3,4,5-triamino-1,2,4-triazolium 5-nitrotetrazolate," *Propellants Explosives and Pyrotechnics*, **2007**, 32, 235 - 243.

G. Steinhauser, C. Darwich, T. M. Klapötke, C. Miró Sabaté, J. M. Welch, "The energetic double salt nitroguanidinium nitrate-guanidinium nitrate," *Acta Crystallographica Section E*, **2007**, 63, o3100 - o3101.

M-j. Crawford, J. Evers, M. Göbel, T. M. Klapötke P. Mayer, G. Oehlinger, J. M. Welch, "γ-FOX-7: the Structure of a High Energy Density Material Immediately before Decomposition," *Propellants, Explosives and Pyrotecinics*, **2007**, 32, 478 - 495.

K. Karaghiosoff, T. M. Klapötke, P. Mayer, C. Miró-Sabate, A. Penger, and J. M. Welch, "Energetic salts of methylated 5-aminotetrazoles," *Inorganic Chemistry*, **2008**, 47, 1007 - 1019.

T. M. Klapötke, P. Mayer, C. Miró Sabaté, J. M. Welch and N. Wiegand, "Simple, Nitrogen-rich, Energetic Salts of 5-Nitrotetrazole," *Inorganic Chemistry*, **accepted**.

T. M. Klapötke, C. Miró Sabaté and J. M. Welch, "1,5-Diamino-4-methyltetrazolium 5-Nitrotetrazolate – Synthesis, Testing and Scale-up," *Zeitschrift für Anorganische und Allgemeine Chemie*, **2008,** 634, 857 - 866.

Contributions to conference proceedings:

M. v. Denffer, T. M. Klapötke, G. Kramer, G. Spieß, J. M. Welch, G. Heeb, "Improved synthesis and X-ray structure of 5-aminotetrazolium nitrate," *New Trends in Research of Energetic Materials, Proceedings of the Seminar, 8th, Pardubice, Czech Republic, Apr. 19 - 21*, **2005**, 513 - 522 (indexed by chemical abstracts).

M. Göbel, K. Karaghiosoff, T. M. Klapötke, C. Miro, J. M. Welch, "Stable salts of methylated 5-aminotetrazoles," *New Trends in Research of Energetic Materials, Proceedings of the Seminar, 9th, Pardubice, Czech Republic, Apr. 19 - 21*, **2006**, 202 - 213 (indexed by chemical abstracts).

T. M. Klapötke, P. Mayer, K. Polborn, J. M. Welch, "Salts of 5-nitrotetrazolate," *New Trends in Research of Energetic Materials, Proceedings of the Seminar, 9th, Pardubice, Czech Republic, Apr. 19 - 21*, **2006**, 631 - 640 (indexed by chemical abstracts).

J. Evers, T. M. Klapötke, P. Mayer, G. Oehlinger, J. M. Welch, "The Three Ambient Pressure Polymorphs of FOX-7," *New Trends in Research of Energetic Materials, Proceedings of the Seminar, 10th, Pardubice, Czech Republic, Apr. 25 - 27*, **2007**, 368 - 375 (indexed by chemical abstracts).

Synthesis and Characterization of 3,4,5-triamino-1,2,4-triazolium 5-nitrotetrazolate. C. Darwich, T. M. Klapötke, J. M. Welch, *New Trends in Research of Energetic Materials, Proceedings of the Seminar, 10th, Pardubice, Czech Republic, Apr. 25 - 27*, **2007**, 546 - 560 (indexed by chemical abstracts).

Oral Presentations:

M. v. Denffer, T. M. Klapoetke, P. Mayer, C. Miró Sabaté, A. Penger and J. M. Welch, "Energetic Salts of 5-aminotetrazole, 1-methyl-5-aminotetrazole and 1,4-dimethyl-5-iminotetrazole," *4th Swiss Snow Symposium*, Grindelwald, Switzerland, Feb. 24 - 26, **2006**.

M. Göbel, K. Karaghiosoff, T. M. Klapötke, C. Miro, J. M. Welch, "Stable salts of methylated 5-aminotetrazoles," *9th New Trends in Research of Energetic Materials Seminar*, Pardubice, Czech Republic, Apr. 19 - 21, **2006**.

T. M. Klapötke, M. Göbel, M.-J. Crawford, J. M. Welch, J. Stierstorfer, V. Verma, J. J. Weigand, A. Hammerl, "New Highly Energetic Materials Based on C-N and P-N Heterocycles," *IRIS-11*, Oulu, Finland, Jul. 30 - Aug. 4, **2006**.

T. M. Klapötke, P. Mayer, C. Miro, A. Penger, J. M. Welch, "New tetrazole based energetic materials," *233rd ACS National Meeting*, Chicago, IL, United States, March 25 - 29, **2007**.

J. Evers, T. M. Klapötke, P. Mayer, G. Oehlinger, J. M. Welch, "The Three Ambient Pressure Polymorphs of FOX-7," *10th New Trends in Research of Energetic Materials Seminar*, Pardubice, Czech Republic, Apr. 25 - 27, **2007**.

J. Evers, T. M. Klapötke, P. Mayer, G. Oehlinger, J. M. Welch, "FOX-7 (1,1-diamino-2,2-dinitroethene): a polymorphic energetic material," *235th ACS National Meeting*, New Orleans, LA, United States, April 6 - 10, **2008**.

Poster Presentations:

M. v. Denffer, T. M. Klapötke, G. Kramer, G. Spieß, <u>J. M. Welch</u>, G. Heeb, "Improved synthesis and X-ray structure of 5-aminotetrazolium nitrate," *8th New Trends in Research of Energetic Materials Seminar*, Pardubice, Czech Republic, Apr. 19 - 21, **2005**.

G. Holl, M. Kaiser, T. M. Klapötke, P. Mayer, K. Polborn and <u>J. M. Welch</u>, "Synthesis and characterization of nitrated triphenylamines found in explosive compositions," *230th ACS National Meeting*, Washington, DC, Aug. 28 - Sept. 1, **2005**.

T. M. Klapötke, P. Mayer, K. Polborn, J. M. Welch, "Salts of 5-nitrotetrazolate," *9th New Trends in Research of Energetic Materials Seminar*, Pardubice, Czech Republic, Apr. 19 - 21, **2006**.

C. Darwich, T. M. Klapötke, J. M. Welch, "Synthesis and Characterization of 3,4,5-triamino-1,2,4-triazolium 5-nitrotetrazolate," *10th New Trends in Research of Energetic Materials Seminar*, Pardubice, Czech Republic, Apr. 25 - 27, **2007**.

T. M. Klapötke, P. Mayer, J. M. Welch, "Nitrogen-rich Salts of 5-nitrotetrazole," *Fall Meeting of the Swiss Chemical Society*, Lausanne, Switzerland, Sept. 12, **2007**.

T. M. Klapötke, C. Miró Sabaté, and J. M. Welch, "Alkali and alkaline-earth metal salts of 5-nitrotetrazole as primary explosives," *235th ACS National Meeting*, New Orleans, LA, United States, April 6 - 10, **2008**.

T. M. Klapötke, C. Miró Sabaté, and J. M. Welch, "Energetic salts containing the nitrogen-rich 2-methyl- and 1,3-dimethyl-5-amino-1H-tetrazolium cations," *235th ACS National Meeting*, New Orleans, LA, United States, April 6 - 10, **2008**.